

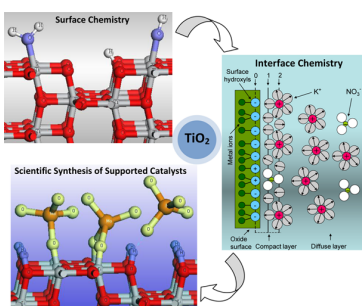
Titanium Dioxide (Anatase and Rutile): Surface Chemistry, Liquid–Solid Interface Chemistry, and Scientific Synthesis of Supported Catalysts

Kyriakos Bourikas,[†] Christos Kordulis,^{‡,§} and Alexis Lycourghiotis*,[‡]

[†]School of Science and Technology, Hellenic Open University, Tsamadou 13-15, GR-26222 Patras, Greece

[‡]Department of Chemistry, University of Patras, GR-26500 Patras, Greece

[§]Institute of Chemical Engineering and High-Temperature Chemical Processes (FORTH/ICE-HT), P.O. Box 1414, GR-26500 Patras, Greece



CONTENTS

1. Introduction	9755
2. Surface Chemistry	9756
2.1. Bulk Structure of the Anatase and Rutile	9756
2.2. Crystal Terminations of Anatase Crystals	9757
2.2.1. Surface Atoms Exposed	9757
2.2.2. Surface Energies before and after Relaxation	9758
2.2.3. Geometrical Surface Relaxations	9759
2.2.4. Surface Reconstructions	9760
2.3. Reactivity of the Anatase Crystal Terminations with Respect to Water Molecules: The Majority (101) Surface	9760
2.3.1. Modes of Adsorption of Isolated Water Molecules on the Perfect (101) Termination	9760
2.3.2. Modes of Adsorption of Water Molecules for Various Temperatures and H ₂ O Surface Concentrations on the Perfect (101) Termination	9760
2.3.3. The Structure of Thin Water Overlays on the Perfect (101) Termination	9762
2.3.4. Modes of Adsorption of Isolated Water Molecules on the Defective (101) Termination	9763
2.3.5. The Structure of Thin Water Overlays on the Defective (101) Surface	9764
2.3.6. Mobility of the Adsorbed Water Molecules	9765
2.3.7. Steps on the (101) Termination	9765
2.3.8. Experimental Studies Devoted to the Interactions of Water Molecules with the (101) Crystal Face	9766
2.4. Reactivity of the Anatase Crystal Terminations with Respect to Water Molecules: The Minority (001), (100), and (110) Terminations	9767
2.4.1. The (001) Surface	9767
2.4.2. The (100) Surface	9768
2.4.3. The (110) Surface	9769
2.4.4. The Trend in the Surface Reactivity	9769
2.5. Investigation of the Anatase Surfaces by Infrared Spectroscopy	9769
2.6. Experimental Investigation of Morphology of the Anatase Nanocrystallites Using XRD, TEM, and FT-IR Techniques	9771
2.7. Calculated Morphology of the Anatase Nanocrystallites	9772
2.7.1. Introductory Remarks	9772
2.7.2. Morphology of Anatase Nanocrystals: "Wulff Constructions"	9772
2.7.3. Surface Chemistry and Morphology of Anatase Nanocrystals	9773
2.8. Recent Methods for Investigating and Manipulating the Morphology of Anatase Nanocrystals	9776
2.9. The (110) Crystal Face of Rutile	9777
2.9.1. Introductory Remarks	9777
2.9.2. Surface Structure	9778
2.9.3. Surface Energy	9778
2.9.4. Modes of Adsorption of Water Molecules	9778
2.9.5. Recent Works Devoted to the Modes of Adsorption of Water Molecules	9778
2.9.6. The Structure of the Water Molecules in the "Rutile (110)/Electrolyte Solution Interface"	9780
2.10. The (011) Crystal Face of Rutile	9781
2.10.1. Surface Structure, Energy, and Relaxations	9781
2.10.2. Surface Reconstructions	9781
2.10.3. Modes of Adsorption of Water Molecules	9783
2.11. The (100) Crystal Face of Rutile	9783

Special Issue: 2014 Titanium Dioxide Nanomaterials

Received: June 8, 2012

Published: September 25, 2014

2.11.1. Surface Structure, Energy, Relaxations, and Reconstructions	9783	4.2.1. Introductory Remarks	9809
2.11.2. Modes of Adsorption of Water Molecules	9784	4.2.2. Co(II) Aqua Complexes	9809
2.12. The (001) Crystal Face of Rutile	9785	4.2.3. Fe(II) Aqua Complexes	9810
2.12.1. Surface Structure, Energy, Relaxations, and Reconstructions	9785	4.2.4. Cu(II) Aqua Complexes	9810
2.12.2. Modes of Adsorption of Water Molecules	9786	4.2.5. Cr(VI) Oxo-species	9811
2.13. The (101) Crystal Face of Rutile	9786	4.2.6. Mo(VI) Oxo-species	9812
2.14. Surface Chemistry and Morphology of the Rutile Nanocrystals	9787	4.2.7. V(V) Oxo-species	9813
2.15. Charges Localized above the Surface Atoms Exposed by the Anatase and Rutile Surfaces Studied	9788	4.2.8. Recent Efforts Based on a Modern Mapping of the Titanium Oxide Protonation/Deprotonation Sites and the Three Plane Model	9814
2.16. Surface Chemistry and Phase Transitions of the Anatase and Rutile Polymorphs	9789	5. Closing Remarks	9815
3. Interfacial Chemistry	9791	Author Information	9816
3.1. A General Description of the Interfacial Region	9793	Corresponding Author	9816
3.1.1. The Music Model	9793	Notes	9816
3.1.2. Basic Stern Model	9795	Biographies	9816
3.1.3. Triple Layer Model (TLM)	9795	References	9817
3.1.4. Three Plane Model	9795		
3.2. Studies on the Rutile (110) Crystal Termination/Electrolytic Solution Interface: A Bridge between the Surface and Interface Chemistry	9796		
3.2.1. Introductory Remarks	9796		
3.2.2. Theoretical Calculations	9796		
3.2.3. X-ray Studies	9796		
3.2.4. Sodium Ions	9797		
3.2.5. Calcium Ions	9799		
3.2.6. Rubidium Ions	9799		
3.2.7. Strontium Ions	9799		
3.2.8. Yttrium Ions	9800		
3.2.9. Zinc Ions	9800		
3.2.10. Cobalt(II) Ions	9802		
3.2.11. Chloride and Bromide Ions	9802		
3.2.12. Final Remarks	9803		
3.3. The Polycrystalline Titanium Oxide/Background Electrolyte Solution Interface	9804		
3.3.1. Historical Remarks	9804		
3.3.2. Description in Terms of the Music/Basic Stern Model: A Bond Valence Approach	9804		
3.3.3. The Influence of Temperature	9804		
3.3.4. Investigation of the Subtitle Interface for Anatase of a Nanosized Structure and High Surface Area	9805		
3.3.5. Description in Terms of a Multisite/Three Plane Model: An Ab Initio Approach	9806		
4. Deposition of Transition Metal Ionic Species on the "Polycrystalline Titanium Oxide/Electrolyte Solution" Interface Related to the Synthesis of Supported Catalysts	9807		
4.1. Regulation of the Mode of Deposition for a Tailor-Made Synthesis of a Supported Catalyst Based on Titanium Oxide	9807		
4.2. Deposition of Transition Metal Ionic Species on the "Polycrystalline Titanium Oxide/Electrolyte Solution" Interface Containing Catalytically Active Elements	9809		

1. INTRODUCTION

Solid catalysts are very useful functional materials, which are used in 90% of industrial processes. The most important are the supported ones. In these catalysts, nanoparticles of an active element (metal, oxide, or sulfide) are dispersed on the surface of a carrier with high surface area. In most of the cases, the synthesis starts with the impregnation (immersion) of powder or preshaped bodies of a carrier with (inside) an electrolytic solution containing the precursor species of the active element to be deposited. The control of the impregnation step is, in effect, essential for preparing very active and selective catalysts. This control requires the understanding, at molecular level, of the deposition processes taking place at the interface developed between the carrier surface and the solution upon impregnation. The above can not be realized without the knowledge of the interface structure. Thus, interfacial chemistry can help toward a scientific synthesis of supported catalysts. On the other hand, the knowledge of the surface chemistry (surface science) of a solid used as a carrier is an essential prerequisite for understanding the relevant interfacial chemistry and then the fundamental deposition processes taking place upon impregnation. Thus, in view of the above requirement for a controlled synthesis of supported catalysts at molecular level, we realize that we need more chemistry to shift catalyst synthesis from the art to the science. We need three different disciplines to come in contact: surface chemistry, interface chemistry, and scientific synthesis of solid catalysts.

This is the goal of the present work concerning titanium oxide, which is of paramount technological importance. It is widely used in most of the photocatalytic processes and in photoelectrochemistry.^{1–12} Typical examples are the hydrogen production^{13–16} and the degradation of environmentally harmful organic compounds.^{12,17–21} Most photovoltaic cells are based on granular thin films of titanium oxide.^{12,22} Numerous studies have been performed in an effort to improve its physicochemical characteristics, concerning mainly its photocatalytic efficiency.^{11,23–28} A huge amount of studies has been also devoted to the synthesis of various forms of titanium dioxide nanomaterials.^{11,12,29,30} Moreover, titanium oxide is used in many other applications,^{12,31} among which medical applications such as dental and bone implants, because this oxide is chemically and biologically inert, stable to corrosion, and nontoxic.³² Most importantly, this oxide is used as catalytic carrier for preparing supported solid catalysts

used in classical catalysis. It is impregnated with aqueous solutions containing one or more transition metal ionic species (TMIS) of the element to be deposited.³³ The ultimate goal of this contribution is to illustrate how recent findings drawn from surface chemistry and liquid–solid interface chemistry are used for a scientific synthesis of catalysts supported on titanium oxide. It should be mentioned that the study of bulk, surface, and interfacial phenomena occurring during TiO₂ photocatalysis is out of the scope of the present work. An excellent review dealing with these issues has been recently published by M. A. Henderson.³⁴

This work is divided into three parts. In the first part, we review important works concerning the surface chemistry of TiO₂ as well as the adsorption of water molecules on important surface terminations of TiO₂, which is the first step for the development of the solid–liquid interface. We have emphasized anatase, one of the two important phases of TiO₂, although the recent works reported for rutile in the past decade have been also reviewed. Anatase is more widely used than rutile in many applications, among which is the synthesis of supported catalysts, due to its remarkably higher specific surface area. For example, it is the most popular carrier used for the synthesis of the catalysts for the selective catalytic reduction of NO by ammonia.^{35–41} Moreover, Mo and CoMo catalysts supported on anatase are more active in hydrodesulfurization (HDS) than those dispersed even on the industrially used γ -alumina.^{42–45} In addition, due to the lower specific surface area of anatase as compared to alumina as well as its poor thermal stability at high temperatures,⁴⁶ mixed oxides with anatase^{47–54} have been proposed as supports for HDS catalysts. These combine the high intrinsic activity obtained for titania with the good characteristics of the other component of the mixed support (excellent texture, mechanical and thermal properties). Anatase is used also in photovoltaic cells^{55–57} and, in general, is more active in photocatalysis than rutile, although mixtures of anatase with rutile show an increased rate of catalytic activity for some reactions. The superiority of anatase was well-known for TiO₂ powders, but recently it was verified by comparing photocatalytic activities of single-crystalline anatase (101) with single-crystalline rutile (110).³⁸

Despite what one may expect from the above, the largest majority of the surface chemistry studies^{3,59–63} as well as the relevant interfacial chemistry studies,^{64–73} has focused on the (110) face of rutile. The main reason is that synthetic monocrystals of rutile are readily available.⁷⁴ The surface chemistry studies reported up to 2001 practically for rutile have been presented in detail in an excellent review reported by Diebold.³ In contrast, experimental surface chemistry results devoted to anatase are not so abundant in the literature because sufficiently large synthetic monocrystals of anatase are for the moment quite difficult to produce,^{74–79} although this problem has been alternatively confronted by growing thin films on various substrates^{80–84} or by using mineral samples.^{79,81,85–87}

However, the situation has been changed considerably in the past decade. Excellent studies, mainly theoretical, published in the last 12 years allow the developing a rather clear picture concerning the structure, energetics, and reactivity of the low-index faces exposed by the anatase crystals and the adsorption of the water molecules on these faces. Most studies are focused on the most stable (101) anatase face. An excellent outline of these efforts has been very recently presented briefly by one of the leading groups in this area.⁸⁸ With this Review, we cover in detail the surface chemistry contributions of the last 12 years

concerning structure, energetics, and reactivity (with respect to the water molecules) of the low-index faces exposed by the anatase nanocrystals. The review articles reported in the past decade focus on the (110) face of rutile nanocrystals.^{3,59,89,90}

In the second part of this work, we reviewed important contributions concerning the liquid–solid interface chemistry relevant to the title oxide. Important progress has been pointed out in the general domain, mainly in the last decades. These concern the structure of the interface. Concerning the surface of oxides in contact with an electrolyte solution, an important evolution was the recognition that more than one kind of hydroxyl groups are developed on their surfaces. This resulted in the replacement of the hypothetical homogeneous (one site/two pK and one site/one pK) models^{91–94} with the more realistic multisite complexation model (music).^{95–97} The last was successfully applied to titanium dioxide.⁹⁸ Concerning the structure of the “solid–liquid” electrostatic interface, an important evolution was the shift from the concept of the point charges to the concept of charge distribution of the interfacial species.⁹⁹ This resulted in more realistic interfacial electrostatic models.⁹⁹ The elucidation of the protonation mechanism of solid oxides in aqueous media, achieved in the past decade,^{100,101} shed more light on the interfacial processes. Recent works reported in the literature in the past decade concern the “rutile (110) crystal termination/electrolyte solution” interface.⁶⁹ These studies deal with the structure of the water molecules and ionic species at the aforementioned interface using ab initio and molecular dynamic simulations as well as in situ synchrotron X-ray-based techniques. These studies offer a way to pass from the surface to the interface chemistry. Unfortunately, similar studies with respect to the anatase low-index surface terminations have not been reported so far. A recent work reported by our group¹⁰² has taken advantage of most of the above progress and attempted to elucidate the structure of the “the polycrystalline titanium oxide/electrolyte solution interface”.

In the third part of this work, we reviewed important contributions concerning the scientific synthesis of catalysts supported on titanium oxide. This Review focuses on contributions dealing with the critical impregnation step and the “mechanisms” of deposition of transition metal ionic species (containing catalytically active elements) on the “polycrystalline titanium oxide/electrolyte solution” interface. The mode of interfacial deposition, the interfacial speciation and its dependence on the impregnation conditions, the nature of the surface bonds between the deposited surface species and the receptor sites, and the structure of the deposited species have been recently elucidated for many transition metals. This was realized by taken into account the progress pointed out in the field of surface chemistry and liquid solid interfacial chemistry related to the titanium oxide.^{103–107} These achievements allow one to tailor the critical impregnation step related to the synthesis of a catalyst supported on titanium oxide.

2. SURFACE CHEMISTRY

2.1. Bulk Structure of the Anatase and Rutile

Both anatase and rutile crystals are formed by chains of distorted TiO₆ octahedra (Figure 1) where each Ti atom is surrounded by 6 oxygen atoms.

The tetragonal structure of anatase (space group: D_{4h}^{19} – $I4_1/amd$) is illustrated in Figure 2. In the anatase phase, the conventional unit cell contains four TiO₂ units, 12 atoms. Each

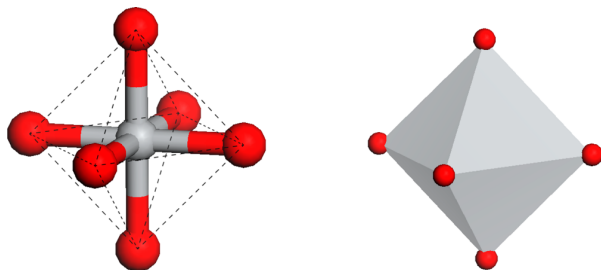


Figure 1. Schematic representation of the distorted TiO_6 octahedron of TiO_2 (anatase and rutile). Each Ti atom (gray ball) is coordinated to the six neighboring oxygen atoms (red balls) through two apical and four equatorial bonds of lengths 1.979 and 1.932 Å, respectively, for anatase (the corresponding lengths for rutile are 1.976 and 1.946 Å, respectively).

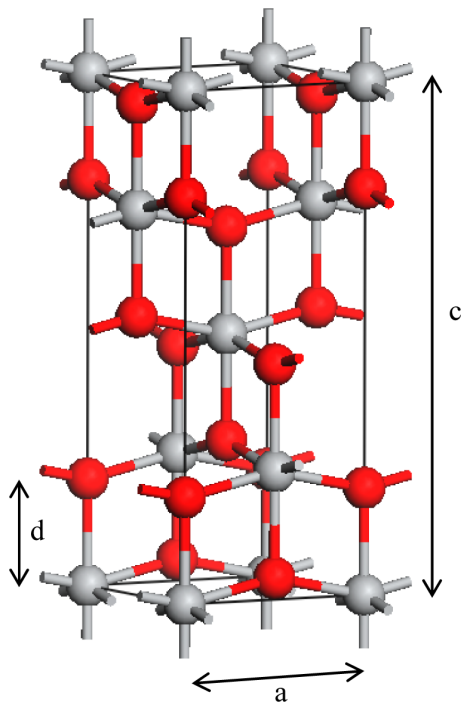


Figure 2. Tetragonal structure of anatase. It may be described using two cell edge parameters, a and c , and one internal parameter, d (the length of the Ti–O apical bond). The experimental values for a , c , and d are, respectively, equal to 3.782, 9.502, and 1.979 Å¹⁰⁸ whereas the experimental volume is equal to 135.25 Å³.^{109,110} The calculated values for these parameters are similar to the corresponding experimental ones.¹¹¹ Gray and red balls represent, respectively, Ti and O atoms. (The same representation stands for similar figures that follow.)

O atom is coordinated to three Ti atoms, lying in the same plane in the unrelaxed structure, through one long bond (apical) and two short bonds (equatorial).

The tetragonal structure of rutile (space group: D_{4h}^{19} – $P4_2/mnm$) is illustrated in Figure 3. In the rutile phase, the conventional unit cell contains two TiO_2 units, 6 atoms. Each O atom is coordinated to three Ti atoms, lying in the same plane in the unrelaxed structure, through one long bond (apical) and two short bonds (equatorial).

The stacking of the octahedra by which the bulk structures of rutile and anatase are being built is given in Figure 4. In the

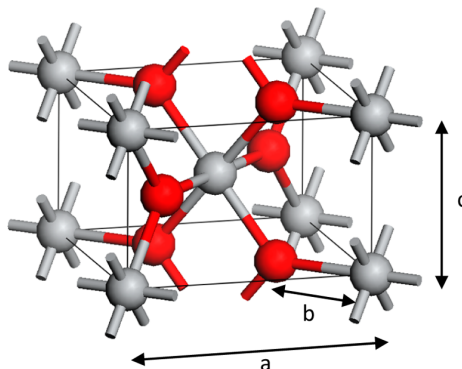


Figure 3. Tetragonal structure of rutile. It may be described using two cell edge parameters, a and c , and one internal parameter, d . The experimental values for a , c , and d are, respectively, equal to 4.587, 2.954, and 1.976 Å¹⁰⁸ whereas the experimental volume is equal to 62.07 Å³.^{109,110} The calculated values for these parameters are similar to the corresponding experimental ones.¹¹¹

rutile structure, each octahedron is in contact with 10 neighbor octahedrons (two sharing edge oxygen pairs and eight sharing corner oxygen atoms), while, in the anatase structure, each octahedron is in contact with eight neighbors (four sharing an edge and four sharing a corner).¹¹¹

It should be mentioned that a detailed analysis of bulk TiO_2 (both anatase and rutile) can be found in the work of Labat et al.¹¹² where the equilibrium geometries of bulk rutile and anatase have been calculated with different Hamiltonians.

2.2. Crystal Terminations of Anatase Crystals

2.2.1. Surface Atoms Exposed. The (101), (100), (001), (110), and (103) crystal surfaces are exposed by the anatase nanocrystals achieved following the usual preparation procedures.^{113–115} In most of the cases, the observed shapes exhibit the (101) and the (001) surfaces, although other crystal faces may be observed. These nanocrystals concern the most important applications, for instance, catalysis. Moreover, the (101) surface is the one mainly exposed by the natural anatase samples. The (001) is also exposed by these samples. Both surfaces are exposed in the Wulff construction, which corresponds to quite large crystals.⁷⁴ Schematic representations of the aforementioned surfaces are illustrated in Figure 5.

On the (101) face, both 5-fold- and 6-fold-coordinated Ti atoms (Ti_{5C} , Ti_{6C}) as well as 2-fold- and 3-fold-coordinated O atoms (O_{2C} , O_{3C}) are present. On the (100) face, both O_{2C} and O_{3C} atoms are exposed, whereas the outermost Ti atoms are 5-fold-coordinated. Moreover, Ti_{6C} atoms and O_{3C} atoms are present at the bottom of surface grooves. On the (001) face, Ti_{5C} atoms as well as O_{2C} and O_{3C} atoms are exposed. Ti_{4C} and O_{2C} atoms are exposed on the first layer of the (110) surface, whereas Ti_{6C} and O_{3C} atoms are on the second layer. The atoms of the first layer on the ideal surface form linear O–Ti–O units and are arranged in a rectangular structure. The (103) surface has two possible terminations called “faceted” ((103)_f) and “smooth” ((103)_s) terminations.¹¹¹ Ti_{5C} and Ti_{6C} atoms are exposed on the first termination, whereas Ti_{4C} and Ti_{6C} atoms are present on the second termination. In both cases, two inequivalent O_{2C} atoms as well as O_{3C} atoms are exposed. Table 1 compiles the surface density (sites per nm²) of the atoms exposed by the various crystal surfaces of anatase.

In view of the above, it is clear that the undercoordinated oxygen is always present on all surfaces as 2-fold-coordinated

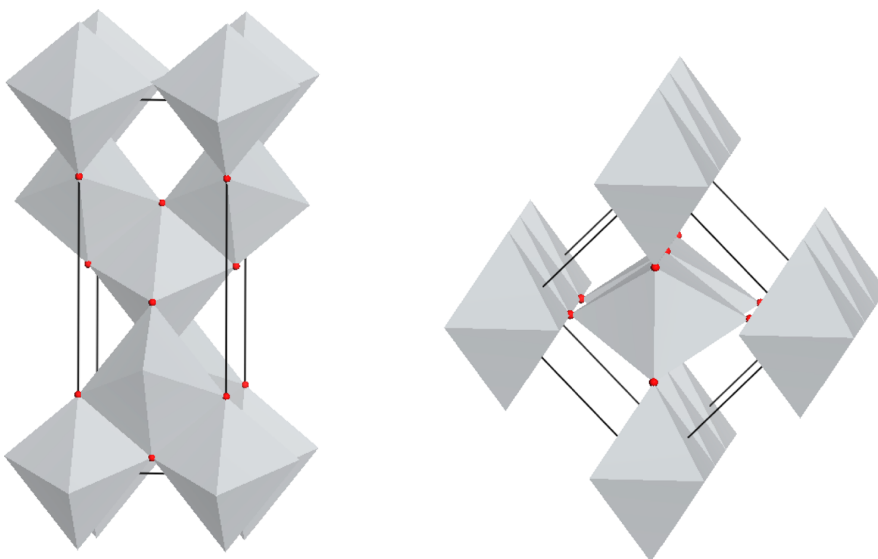


Figure 4. Bulk structures of anatase (left) and rutile (right).

oxygen. The 1-fold-coordinated oxygen does not appear. In contrast, the undercoordinated Ti atoms are present in two forms, as 5-fold-coordinated {(101), (100), (001), and “faceted” (103)} and 4-fold-coordinated {“smooth” (103) and (110)}.

2.2.2. Surface Energies before and after Relaxation. In the last 10 years, few theoretical studies have been devoted to the investigation of the stability of the aforementioned surfaces.^{111,116–121} The first theoretical study dealing with anatase surfaces was reported by Oliver et al.¹¹⁸ It was an atomistic simulation based on empirical interatomic potentials. This theoretical work suggested that the surface energies of anatase may be smaller than those of rutile. This, corroborated later by another theoretical study,¹²² explains why the experimentally synthesized crystalline nanoparticles are found to favor the anatase than the rutile structure for diameters up to about 14 nm.¹²³ Moreover, this study and another empirical approach¹²⁴ had attempted to determine the morphology of the anatase particles but without taking into account the surface relaxation energies.⁷⁴ It was suggested that the shape of the anatase nanocrystallites is a truncated bipyramid exposing the (101) and (001) surfaces.

Two important works devoted to the investigation of the structure and energetics of stoichiometric anatase surfaces were reported by Lazzeri et al.^{111,119} and by Arrouvel et al.¹¹⁶ In the first work, the energy of the anatase surfaces has been calculated using a plane-wave pseudo potential approach within density functional theory. Three different approximations were used: the local density approximation (LDA),^{125,126} the Perdew–Burke–Ernzerhof method (PBE),¹²⁷ and the Becke–Lee–Yang–Parr functional (BLYP).^{128,129} In the second work, the total energy calculations were performed within density functional theory and the generalized gradient approximation of Perdew and Wang (PW).¹³⁰ Moreover, in the frame of a study devoted to the morphology and the phase stability of the titanium oxide nanocrystallites, Barnard and Zapol calculated also the energy of the anatase surfaces.¹¹⁰ The first principle calculations have been performed using density functional theory within the generalized-gradient approximation with the exchange correlation functional of Perdew and Wang. The

values of energy of the anatase surfaces calculated before and after relaxation are compiled in Table 2.

In addition to these studies, a recent important theoretical work was published by Labat et al.,¹²¹ where the structural and electronic properties of the (101) and (100) surfaces of anatase were investigated using different Hamiltonians with all-electron Gaussian basis sets, within a periodic approach. Full-relaxations of the surfaces were carried out at the Hartree–Fock (HF) level and also using pure and hybrid DFT models, such as LDA, PBE, B3LYP, and PBE0.

Inspection of Table 2 shows that before relaxation the surface energy increases following the order: (001), (101), (103)_b, (100), (110), and (103)_s. The same trend concerning the (101) and (100) is also observed in the paper of Labat et al.¹²¹ The energy values of the unrelaxed anatase surfaces seem to be related to the form of the undercoordinated Ti atoms.¹¹¹ The surfaces with 4-fold-coordinated Ti atoms {(110) and (103)_s} have a larger energy than those with 5-fold-coordinated Ti atoms. On the other hand, it has been related to the number and the kind of the Ti–O bonds that must be broken to obtain a given surface.¹¹⁶ Thus, the formation of the surface (001), which exhibits the lowest energy value, requires the dissociation of only (Ti–O)_z apical bonds with energy smaller than that of the (Ti–O)_{x,y} equatorial bonds for about 30–35 kJ mol^{−1}. The lowest and highest value of the number of the broken (Ti–O) bonds has been reported for the (101) and (110) surfaces, respectively. This may be taken into account for the corresponding unrelaxed surface energies.

Table 2 shows also that the order mentioned above is considerably changed after relaxation, now following the increasing order: (101), (100), (103)_b, (001), (103)_s, and (110). The modification of the ranking is due to the different relaxation energy related to each crystal termination.^{111,116,131} The (001) surface exhibits the minimum relaxation energy, while the other surfaces are characterized by stronger relaxation effects. These effects render the (101), (100), and (103)_b surfaces more stable than the (001) surface. However, the (110) surface remains quite unstable even after relaxation. Finally, it may be observed that relatively low energy values have been calculated by Barnard and Zapol (Table 2, fourth

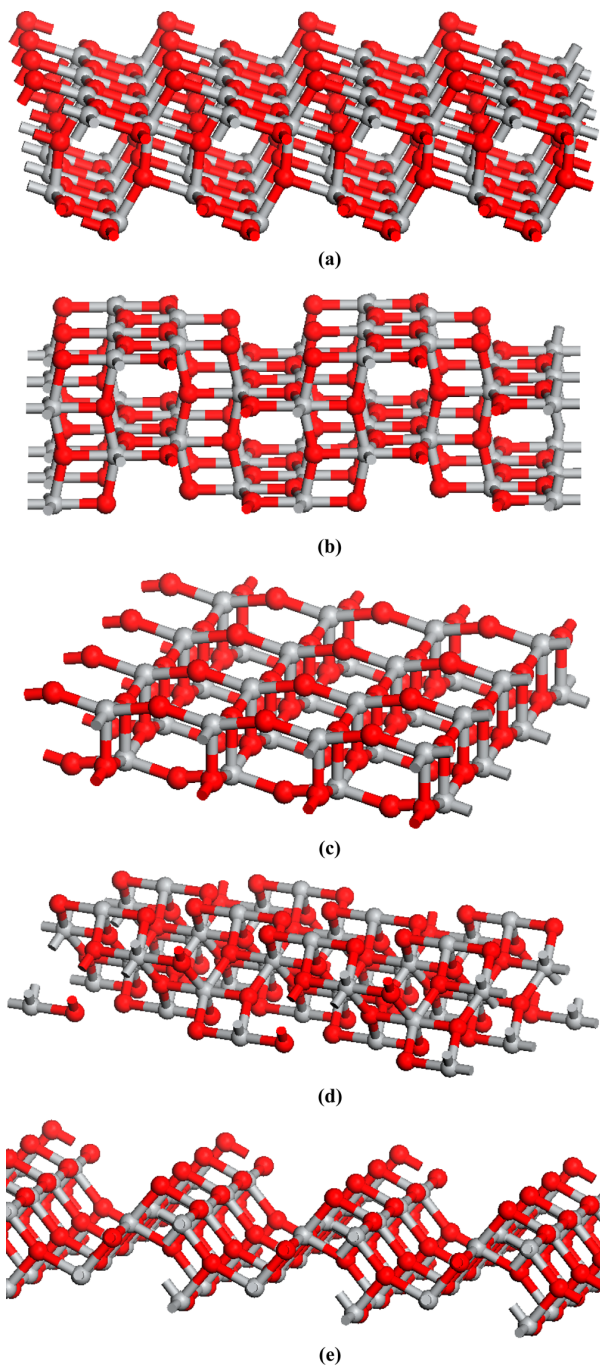


Figure 5. Schematic representation of the anatase (a) (101), (b) (100), (c) (001), (d) (110), and (e) (103) ideal crystal faces.

column, second values in parentheses). They attributed the differences of these energy values with the corresponding ones calculated in refs 111, 119 (Table 2, second column) to the significantly smaller convergence tolerance used for the structural relaxation as well as to the use of different generalized-gradient approximation with the exchange correlation functional of Perdew and Wang.¹²⁰ Lower energy values, as compared to those of the second and third columns of Table 2, were also calculated by Labat et al.¹²¹ for the unrelaxed (101)

and (100) surfaces. Strangely, a good agreement is observed concerning the energy of the relaxed (101) surface.

2.2.3. Geometrical Surface Relaxations. The patterns in the relaxation of the surface atoms of the aforementioned surfaces were, moreover, studied.^{111,116,120,121}

Concerning the (101) crystal face (Figure 5a), it was found that the fully coordinated surface Ti and O atoms are displaced about 0.2 Å outward, whereas the Ti_{SC} atoms are displaced inward (0.12 and 0.18 Å in refs 111, 116, and 120, respectively). The above displacements of the Ti atoms are related to the lateral displacement of the O_{2C} bonded with a Ti_{6C} and a Ti_{5C} atom through an apical and an equatorial bond, respectively. These are finally related to no negligible changes of the interatomic distances of the surface atoms.^{111,116} Labat et al.¹²¹ found also an outward displacement of 0.16 Å for the O_{3C} atoms, but in contrast to the above studies, they also found outward displacement of 0.13 Å for the Ti₅ atoms.

The (100) surface (Figure 5b) exhibits a similar relaxation pattern.^{111,116,120} In fact, it was found that the fully coordinated O atoms exposed on the surface displaced outward by 0.18 Å (0.17 Å in ref 121). The O_{2C} atoms exhibit also an outward relaxation (0.02–0.04 Å). In contrast, Ti_{SC} atoms relax inward (0.16 or 0.15 Å in ref 121), whereas the Ti_{6C} atoms relax outward (0.17 Å). Finally, relaxation brings about a decrease of the Ti–O–Ti bond distances of the 2-fold-coordinated oxygens.

Concerning the (001) surface (Figure 5c), it was found a distortion of the planar structure associated with the O_{3C} atoms.¹¹¹ The perpendiculars to the surface O–Ti–O–Ti rings become slightly skewed due to the relaxation. Moreover, the Ti–O–Ti angle of the O_{2C} atoms is reduced to 146°, and this is associated with the transformation of the two equivalent Ti–O bonds in the unrelaxed structure into strongly inequivalent. In fact, in the relaxed structure, the one bond is markedly shorter than the other (2.20, 1.76 Å). The above results^{108,113} are related to an inward displacement of the O_{3C} (0.02 Å) and Ti_{SC} (0.06 Å) atoms and an outward displacement of the O_{2C} atoms (0.08 Å). The calculations performed later by Barnard and Zapol suggested an outward displacement in all cases (0.20, 0.04, and 0.05 Å for O_{2C}, Ti_{SC}, and O_{3C}, respectively).¹²⁰

For the (110) termination (Figure 5d), it was found that the local structure is markedly modified upon relaxation.¹¹¹ Specifically, the O_{2C} atoms of the first layer displace differently, and thus these are no longer equivalent. This is related to the considerable contraction of the O–Ti–O and the reduction of the O–Ti–O angle. Inspection of Table 2 shows that the energy of the unrelaxed surface is very high. This may be attributed to the low coordination of the surface Ti and O atoms. Although this energy decreases considerably, it remains quite high after relaxation.

As to the (103)_f surface, it was found a decrease of the Ti–O–Ti angle from 102°, in the ideal structure, to 99° as well as a contraction of the Ti–O bonds.¹¹¹ Moreover, the other Ti–O–Ti angle, being equal to 156° in the unrelaxed surface (Figure 5e), decreases to 148°, whereas the relative equivalent Ti–O bonds become considerably inequivalent upon relaxation. On the other hand, the O_{3C} atoms are displaced outward for about 0.2 Å. The Ti–O–Ti angle formed by two fully coordinated Ti atoms and one fully coordinated oxygen renders equal to 102° after the relaxation of the (103)_f crystal termination, whereas the relative Ti–O–Ti bonds are shortened. Moreover, the Ti–O–Ti angle formed by an

Table 1. Surface Density (sites per nm²) of the Atoms Exposed by the Various Crystal Surfaces of Anatase^a

anatase crystal surface	Ti _{6C}	Ti _{5C}	Ti _{4C}	O _{3C}	O _{2C}
(101)	5.1 (5.2)	5.1 (5.2)		5.1 (10.4 ^b)	5.1 (5.2)
(100)	5.4 (5.6)	5.4 (5.6)		5.4 (11.2 ^c)	5.4 (5.6)
(001)		6.9 (7.0)		6.9 (7.0)	6.9 (7.0)
(110)	(7.9)		3.8 (4.0)	(7.9)	7.7 (7.9)
(103) _f	(3.6)	(7.2)		(10.7)	(7.2)

^aFirst values from ref 116; values in parentheses from ref 102. ^bThe O_{3C} atoms of both series have been counted. ^cBoth O_{3C} atoms located on the surface and at the bottom of surface grooves have been counted.

Table 2. Values of Energy of the Anatase Surfaces Calculated before and After^a Relaxation^{111,116,119,120}

anatase surface	E_{LDA}^b (J/m ²)	E_{PBE}^b (J/m ²)	E_{PW}^c (J/m ²)
(101)	1.56 (0.84)	1.28 (0.44)	1.139 (0.435, 0.35)
(100)	1.90 (0.96)	1.59 (0.53)	1.412 (0.533, 0.39)
(001)	1.46 (1.38)	1.12 (0.90)	1.034 (0.984, 0.51)
(110)		2.17 (1.09)	2.031 (1.024, 0.81)
(103) _f		1.50 (0.83)	
(103) _s		2.40 (0.93)	

^aValues in parentheses. ^bReferences 111, 119. ^cValues outside parentheses from ref 116; first and second values in parentheses from refs 116 and 120, respectively.

oxygen atom bonded with one Ti_{6C} and one Ti_{4C} atom via two equatorial bonds renders larger after relaxation. As on the (101), (100), and (103)_f surfaces, the fully coordinated oxygen atoms exhibited an important outward relaxation of about 0.5 Å. Finally, inspection of Table 2 shows that a relatively large decrease in the surface energy takes place upon relaxation. This may be attributed to the presence of the 4-fold Ti atoms on the (103)_s crystal termination.

2.2.4. Surface Reconstructions. Experimental surface chemistry results concerning the anatase crystal terminations are rather scarce in the literature. An excellent short overview has been recently reported by Diebold et al.⁷⁴ Preliminary surface chemistry experiments on a mineral sample using scanning tunneling microscopy (STM) have shown that the more stable (101) surface is the only one that does not reconstruct. It is notable that the O_{2C} atoms are presumably visible in the STM images taken with an unusually high tunneling current.

The (100) surface was investigated using a sample that was cut from a natural mineral crystal. Low energy electron diffraction of a sputtered/annealed surface indicated (1n) reconstruction,¹³² whereas the STM results suggested that this surface presumably reconstructs into (101) microfacets.

For the structural investigation of the (001) surface, thin films, formed by epitaxial growth on the SrTiO₃ (001) substrates, have been used.^{74,80,81,133} It was found that the aforementioned surface reconstructs exhibiting an 1 × 4 reconstruction^{133,134} and the high-resolution STM and NC-AFM images¹³⁵ are compatible with the “added molecule” model proposed by Lazzeri and Selloni¹³⁶ (Figure 6).

By comparing Figure 6 with Figure 5c, it may be seen that the 1 × 4 reconstructed (001) surface is derived by periodically replacing rows of O_{2C} atoms of the unconstructed (001) structure with “TiO₃ species”. On the bridging TiO₃ ridge, 4-fold-coordinated Ti atoms are present together with O_{2C} atoms. The reconstruction of the surface was verified later experimentally by Thomas et al.¹³⁸ by studying the electronic structure using synchrotron photoemission spectroscopy.

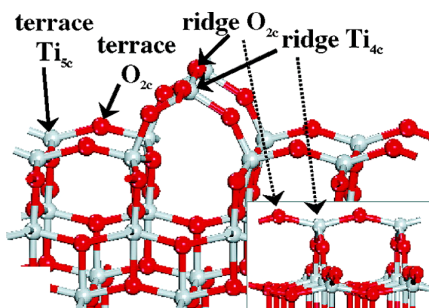


Figure 6. A 1 × 4 reconstructed (001) surface according to the added molecule model.¹³⁷ Reprinted with permission from ref 137. Copyright 2006 American Chemical Society.

Recently, Gong et al.¹³⁷ calculated the energy of reconstructed 1 × 4 (001) surface and found a value of about one-half of that calculated for the (001) surface (0.48 instead of 0.98 eV, see Table 2), indicating that reconstruction is energetically favorable. This was attributed to a strong relief of the surface stress.¹³⁶ In fact, the bonds between the Ti_{5C} and the O_{2C} atoms being on the terrace of the reconstructed surface have lengths of 1.80–1.85 Å, while these bonds in the unreconstructed (001) surface have a length equal to 1.96 Å. This indicates increasing strength of these bonds in the former structure, rendering the aforementioned surface atoms in the reconstructed surface much less reactive. This was confirmed by calculating the electronic densities of states.¹³⁶ In contrast, it has been reported that the O_{2C} and the Ti_{4C} atoms being on the bridging TiO₃ ridges are highly reactive.¹³⁶

LEED and STM have been used to study the (103) orientation using a natural mineral crystal cut in this direction.⁷⁴ It was found that this surface reconstructs producing ridges along the (010) direction.

2.3. Reactivity of the Anatase Crystal Terminations with Respect to Water Molecules: The Majority (101) Surface

2.3.1. Modes of Adsorption of Isolated Water Molecules on the Perfect (101) Termination. Concerning the most stable (101), surface only a few theoretical^{6,116,117,122,139–142} and experimental¹⁴³ studies have been devoted to the subject. Selloni et al.^{6,139–142} have studied the structure and energetics of water on the (101) surface by first-principles molecular dynamics using the Car–Parrinello approach^{144,145} and the generalized gradient approximation for the functional of exchange correlation.¹⁴⁶ They studied, first, the adsorption of water on a perfect (101) surface and at two surface coverages (θ : 0.25, 1.00) defined as the ratio between the number of adsorbed water molecules and the number of the surface 5-fold-coordinated Ti atoms. They started placing one water molecule with its O atom 2.7 Å above one of the four Ti_{5C} atoms of the surface cell studied (θ = 0.25). After

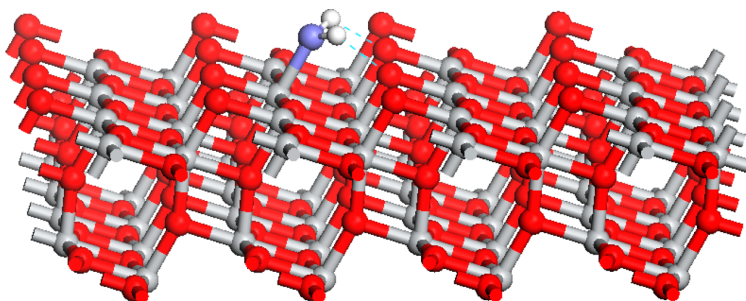


Figure 7. Representation of the structure of a water molecule adsorbed molecularly on the anatase (101) crystal face, according to the studies of Selloni et al.^{6,139–142}

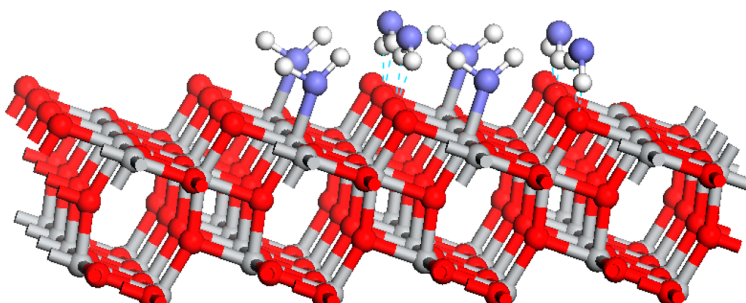


Figure 8. Local structures of water molecules adsorbed molecularly and through hydrogen bonds on the anatase (101) crystal face.¹¹⁶

relaxation, they performed a molecular dynamics run where the temperature was progressively raised to 450 K. Although the water molecule changed continuously its orientation during the run, it is not dissociated, remaining (with its oxygen) close to the same Ti_{5C} atom and forming two hydrogen bonds with the two neighboring O_{2C} atoms not directly bonded to the aforementioned uncoordinated Ti (Figure 7).

The calculated adsorption energy per water molecule was found to be equal to 0.74 eV in good agreement with the experimental values reported in the literature.^{143,147} To investigate further the mode of adsorption, they performed additional calculations starting from separated H^+ and OH^- ions. They attempted two configurations. In the first (second) configuration, the OH^- ion is bonded to a Ti_{5C} atom and the H^+ ion to the O_{2C} atom directly (neighboring but not directly) bonded to the aforementioned Ti atom. As the adsorption energy for the first and the second configurations was found to be, respectively, equal to 0.30 and 0.23 eV per water molecule, quite lower than that calculated for the molecular adsorption mentioned above (0.74 eV/ H_2O), it was concluded that the molecular adsorption is largely favored on anatase (101) surface at low coverages ($\theta = 0.25$).

For monolayer coverage ($\theta = 1$), the undissociated adsorption remains the energetically favorable case with respect to the fully dissociated one, although the difference in the adsorption energies has been decreased (0.72 eV/ H_2O for the molecular adsorption and 0.44 eV/ H_2O for the dissociative adsorption). This had provided evidence that the increase in the surface coverage could promote water dissociation upon adsorption on the (101) surface, thus keeping open this possibility at least under particular conditions (e.g., for the anatase aqueous suspensions). At this point, it should be stressed that adopting the picture illustrated in Figure 7 for the “(101) surface–water interactions”, taking into account the definition of θ and that the surface density of the Ti_{5C} atoms is

equal to that for the O_{2C} atoms (Table 1), it could be concluded that above a critical value of θ an O_{2C} atom interacts, through hydrogen bonds, with two water molecules. However, the two points mentioned above are fully clarified in more recent studies reported by Tiloca and Selloni.^{140,141} These works will be discussed later.

Selloni et al. have studied, moreover, the structure and energetics of H_2S and HI on the (101) surface.¹³⁹ It was found that the H_2S is also adsorbed molecularly with a surface structure identical to that proposed for water, although its adsorption energy is quite lower (0.49 eV/ H_2O). In contrast, dissociative adsorption is preferred for the strong acid HI . The maximum adsorption energy was obtained for the configuration where the I^- ion is bonded to Ti_{5C} atom and the H^+ ion to the O_{2C} atom directly bonded to the Ti_{5C} atom (0.67 eV/ H_2O).

Barnard et al.¹²² reported very recently theoretical results (DFT within the GGA with the exchange correlation functional of Perdew and Wang (PW91)) concerning the relaxations and the surface energies of the (101) terminations after water adsorption at monolayer coverage. Molecular adsorption was found to be energetically preferred on the (101) crystal face. However, the difference in the calculated values of the adsorption energy for the molecular adsorption (0.56 eV/ H_2O) and dissociative adsorption (0.48 eV/ H_2O) is considerably smaller as compared to that found by Vittadini et al. (0.72 eV/ H_2O for the molecular adsorption and 0.44 eV/ H_2O for the dissociative adsorption).⁶ The relaxation behavior is not identical to that found by the same group for the non-hydrated (101) crystal face. Thus, after hydration and upon relaxation, both the O_{2C} and the Ti_{5C} atoms were found to contract slightly inward (0.01 and 0.05 Å), whereas the O_{3C} atoms were found to relax upward (0.1 Å). The $Ti-O_{2C}$ bond length was found to be equal to 2.28 Å in full agreement with the value reported by Vittadini et al.⁶ The surface energy for the hydrated (101) crystal face was found to be considerably greater (1.03 J/

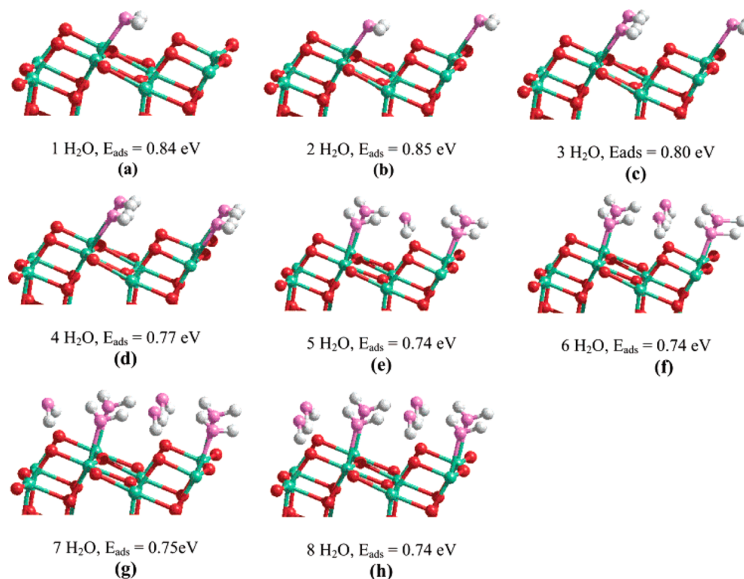


Figure 9. Stable configurations and corresponding adsorption energies for various coverages of water adsorption on the perfect (101) crystal face of anatase. Ti atoms, light green circles; O atoms from TiO_2 , red circles; O atoms from H_2O molecules, violet circles; H atoms, light gray circles.¹⁴⁸ Reprinted with permission from ref 148. Copyright 2007 American Chemical Society.

m^2) than that reported by the same group (0.35 J/m^2 , see Table 2 of this Review) for the nonhydrated crystal face.

2.3.2. Modes of Adsorption of Water Molecules for Various Temperatures and H_2O Surface Concentrations on the Perfect (101) Termination. By coupling ab initio calculations and a thermodynamic model, Arrouvel et al.¹¹⁶ studied not only the structure and energetics of stoichiometric anatase surfaces, but, in addition, the interactions of water with the low-index anatase faces mentioned above, for various temperatures and H_2O surface concentrations. Three configurations have been examined: chemisorbed water with dissociation, undissociated chemisorbed water, and physically adsorbed water.

Concerning the (101) face, it was found that at $\theta = 1$ the water molecules are chemisorbed without dissociation on the Ti_{5c} atoms.¹¹⁶ The adsorption energy, varying between 79 – 69 kJ mol^{-1} , is similar to those calculated by Selloni's group (0.72 eV/molecule , $1 \text{ eV/molecule} = 96.485 \text{ kJ mol}^{-1}$). For coverage higher than $\theta = 1$, the additional water molecules are adsorbed via hydrogen bonds with the O_{2c} atoms (Figure 8). As the concentration of the latter is equal to $5.0 \text{ atoms nm}^{-2}$, saturation is obtained at $\theta = 2$. The above implies that each water molecule covers one undercoordinated Ti_{5c} or O_{2c} atom, which is not in full agreement with the structure proposed initially by Vittadini et al.⁶ On the other hand, the calculations performed by Arrouvel et al.¹¹⁶ confirmed the finding mentioned above that the increase of the surface concentration of the water molecules and the increasing retention of these molecules by hydrogen bonds brings about an increase of the energy of adsorption of the chemisorbed water molecules, eventually enhancing dissociative adsorption. However, in contrast to that reported by Selloni's group, they found that at $\theta = 1$ the fully nondissociated state and the fully dissociated configurations compete in energy within less than 7 kJ mol^{-1} . As already mentioned, this could keep open the possibility for a dissociative water adsorption under particular conditions. The relatively low reactivity of this crystal face was attributed to the

relatively low $\text{Ti}-\text{O}$ bond energy of the surface bonds calculated after relaxation (26 kJ mol^{-1}).

The calculation of the surface energy at various temperatures at standard vapor pressure showed that the energy of the hydrated (101) surface increases linearly with temperature, whereas that of the dehydrated one remains constant.¹¹⁶ The slope of the linear curves increases with the water coverage in the range of θ 0.25 – 2.0 . This behavior is observed for all faces studied, the 1–4 ones illustrated in Table 2. As the surface energy for the hydrated (101) face is higher than the dehydrated one at temperature higher than 450 K , irrespective of the water coverage, it was concluded that above this temperature the (101) face is completely dehydrated at standard vapor pressure.¹¹⁶ At room temperature, the lowest energy is presented by the hydrated surface with the maximum water coverage ($\theta = 2.1$). This means that at room temperature the surface Ti_{5c} and O_{2c} atoms are fully hydrated.

The adsorption of water molecules on the perfect (101) crystal face of anatase was also recently studied at various temperatures by Hamraoui et al.,¹⁴⁸ using DFT calculations combined with thermodynamic analysis. A slab containing eight surface atoms (four Ti_{5c} and four O_{2c}) has been used.¹⁴⁸ A positive value for the adsorption energy reflects exothermic adsorption. The most stable configurations and the corresponding water adsorption energies for various degrees of hydration are illustrated in Figure 9. It may be seen that one water molecule is coordinated above a Ti_{5c} surface atom. In this structure, both hydrogen atoms of the coordinated water molecule form hydrogen bonds with the adjacent O_{2c} atoms. The water adsorption geometry is similar for coverage up to four molecules where all of the surface Ti_{5c} have been covered (Figure 9a,b). The additional water molecules, up to eight, can only be adsorbed through hydrogen bonds with the O_{2c} atoms. Thus, the monolayer involves four coordinated and four hydrogen-bonded water molecules. These results are in good agreement with those mentioned above.

The number of the water molecules present on the aforementioned slab was then calculated at various temperatures.¹⁴⁸ Eight water molecules are retained at room temperature covering all surface sites. Only one water molecule remains between 345 and 405 K, whereas the surface is completely dehydrated above 405 K. The above behavior concerns a partial water pressure equal to 0.01 bar. It is obvious that the temperature for complete dehydration increases with the partial pressure of water.

Finally, the structure of a water bilayer adsorbed on the same surface had been recently investigated by performing DFT total energy calculations and *ab initio* molecular dynamics simulations at different temperatures.¹⁴⁹ More specifically, the authors investigated the nature of the hydrogen bonds formed by water molecules in contact with the (101) surface. They showed that these bonds originate from a water/anatase interface effect, which induces an electronic charge transfer from surface Ti_{5c} atoms to surface O_{2c} atoms, mediated by the water molecules.

2.3.3. The Structure of Thin Water Overlays on the Perfect (101) Termination. As was already mentioned, the calculations performed by Arrouvel et al. suggested that the increase of the surface concentration of the water molecules and the increasing retention of these molecules by hydrogen bonds bring about an increase of the energy of adsorption of the chemisorbed water molecules enhancing dissociative adsorption. This is in general agreement with quite recent theoretical investigations devoted to the study of the influence of the intermolecular water–water interactions on the structure and reactivity of thin water overayers on solid surfaces.^{61,63,150–155} In fact, from these studies it can be concluded that the aforementioned interactions favor the dissociation of the adsorbed water molecules, although the intensity of the effect, if any, depends on the solid. These prompted Tiloca and Selloni to study systematically the structure and reactivity of thin water overayers on the (101) surface of anatase using the Car–Parrinello molecular dynamics simulations.^{140,141} Specifically, they studied the structural and dynamic properties of one, two, and three water monolayers adsorbed on the perfect (101) surface at 160 K.

The structure of the monolayer on the perfect surface is very similar to that obtained for the isolated water molecules.^{140,141} In fact, the monolayer is formed from a regular array of coordinative water molecules above the Ti_{5c} atoms. The molecules slightly rotate, upon relaxation, to form alternate rows in which the molecular dipoles point to different directions resulting in a zigzag pattern along the (101) direction. This induces a relatively low net dipole moment for the monolayer.¹⁴⁰ No dissociation of the water molecules has been observed during the whole simulation run. The adsorbed molecules are slightly tilted, with the molecular plane forming an angle close to 25° with the surface plane. The adsorption energy per water molecule was found to be 0.05 eV smaller than that for an isolated H₂O molecule.¹⁴⁰ Only very weak hydrogen bonds H₂O–O_{2c} are present. On the other hand, no H₂O–H₂O lateral H-bonds are formed. This is due to the relatively large distance (3.8 Å) between the Ti_{5c} surface atoms, which impose the same distance between the neighboring water oxygen atoms. This distance is indeed much larger than the O–O one in ice (2.75 Å). On this monolayer, the water molecules remain very close to their adsorption sites throughout the simulation with their oxygen atoms at a distance of about 2 Å from the surface. Thus, the

monolayer is highly ordered in registry with the underline lattice.¹⁴⁰

Concerning the structure of a water bilayer on the perfect (101) face, it was also found that no water dissociation takes place.¹⁴⁰ On the other hand, it was found that after adsorption of the second layer of water molecules the first water layer is changed.¹⁴⁰ The water molecules are still located on the Ti_{5c} surface atoms, but their orientation is less symmetrical and their plane is more tilted with respect to the monolayer. After formation of the first monolayer, all Ti_{5c} surface atoms are occupied. Thus, the additional water molecules may coordinate either to the surface O_{2c} atoms, being unoccupied, or to the Ti_{5c}–OH₂, or to both. To study these different possibilities, they performed two simulations starting from different initial configurations.¹⁴¹ Following the first configuration, the H₂O molecules of the second layer were arranged randomly.¹⁴¹ In this case, two, out of four, water molecules considered for the second layer move closer to the surface, forming hydrogen bonds with the bridging oxygens (H₂O–O_{2c}). These occupy an intermediate position between the first layer (Ti_{5c}–OH₂), located about 2 Å above the surface, and the two remaining second layer water molecules located at around 4 Å above the surface. In this intermediate position, the H₂O–O_{2c} molecules form, in addition, hydrogen bonds both with the H₂O–Ti_{5c} first layer water molecules and with the second layer water molecules. On the average, every water molecule is linked to two other water molecules, whereas every surface O_{2c} atom accepts one hydrogen bond come either from a H₂O–Ti_{5c} or from a H₂O–O_{2c}, not only from the latter. It was, moreover, found that the two O_{2c}–OH₂ species mentioned above are located at different distances from the surface, and the same is true for the two water molecules in the second layer.¹⁴¹ In this structure (BL1), every water molecule was involved in an extended network of hydrogen bonds, and this enhances the connectivity of the adsorbed water overlayer. Following the second initial configuration, they considered four H₂O–Ti_{5c} (first layer) and four H₂O–O_{2c} (second layer) water molecules.¹⁴¹ During the dynamical simulation, the one H₂O–O_{2c} molecule displaced with respect to the “regular” position dictated by the surface breaking one of the two hydrogen bonds linked with the O_{2c}. Therefore, in this quite stable configuration (BL2), we may distinguish two rows of H₂O–O_{2c}. In one row the H₂O molecules donate both hydrogens to O_{2c}, whereas in the other one of their hydrogens is pointing upward. The water molecules in the second row are at higher distance from the surface with respect to those of the first H₂O–O_{2c} row. There are not hydrogen bonds linking the H₂O–O_{2c} rows. An additional optimization showed that the arrangement where all H₂O–O_{2c} molecules are in the first row (BL3) has the same energy with BL2 and BL1 but is less probable due to the significant entropy differences favoring BL1 and BL2.¹⁴¹ It should be stressed that the structure BL1 is related to incomplete occupancy of the O_{2c} surface atoms. In view of the above, it may be concluded that a quite regular structure of the adsorbed bilayer is imposed by the (101) perfect anatase surface.

The starting configuration of a water trilayer on the perfect (101) surface was generated by adding a third water layer on the BL2 structure mentioned above.¹⁴¹ First, it was found that no water dissociation takes place. It was, moreover, found that the first two layers are very similar to the corresponding ones in the BL2 configuration.¹⁴¹ However, one H₂O–O_{2c} molecule of the second rows mentioned above appears to lose completely

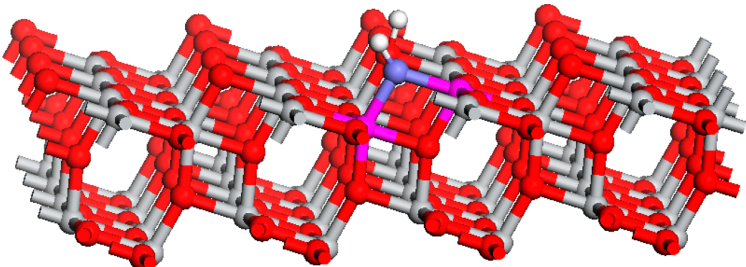


Figure 10. Dissociative adsorption of water on the defective (101) termination. The Ti atoms of the vacancy are marked with a different color.¹⁴²

its coordination to the bridging oxygen and tends to be located slightly above the second layer. It was inferred that the formation of such “vacancies” relieves the stress developed in the first bilayer when all undercoordinated titanium and oxygen atoms are occupied. There is an extended network of hydrogen bonds involving molecules in the three layers. It is notable that, in contrast to that found for the BL2, there are now developed hydrogen-bond bridges linking H₂O–O_{2C} rows. The water molecules in the third layer are distributed in the range 3.5–6.5 Å. These are quite mobile, whereas their average positions are only in part correlated with the surface Ti_{5C} and O_{2C} atoms. Therefore, the layering above the BL is not so pronounced.

2.3.4. Modes of Adsorption of Isolated Water Molecules on the Defective (101) Termination. In the above subsections, we presented the efforts done so far to study the structure of the water overlayers adsorbed on the undefective (101) crystal face. As was already mentioned, the surface reactivity with respect to water is quite low resulting in molecular rather than dissociative adsorption. However, Ti_{4C} atoms are present at the step edges of the (101) surface. These atoms, identified by STM, influence the chemical behavior of this surface. Surface Ti_{4C} atoms may be created by removal of the surface O_{2C} oxygen atoms. In fact, such a removal modifies the Ti_{5C} into Ti_{4C} atoms and the Ti_{6C} into Ti_{5C} atoms, resulting in a nonplanar ring Ti_{6C}–O_{3C}–Ti_{5C}–Ti_{4C}–O_{3C}–Ti_{5C}–O_{2C}–Ti_{6C} (Figure 10). Although the (101) surface shows relatively low tendency to form oxygen vacancies,^{156,157} Tiloccia et al. studied the adsorption of an isolated water on the defective (101) anatase surface.¹⁴² They found that the dissociative adsorption of the water molecules is thermodynamically favored with respect to the molecular one, although no spontaneous dissociation was observed in a simulation run of several picoseconds, indicating the presence of an energy barrier between the molecular and the dissociated states. Two configurations are very stable. In both configurations, the hydroxyl oxygen is located near the vacancy bonded to both Ti_{5C}–Ti_{4C} atoms and roughly replacing the missing O_{2C} atoms. Thus, a bridging hydroxyl group is formed. In the first, slightly more stable, configuration (adsorption energy 1.86 eV/H₂O), the proton is bonded to a non missing O_{2C} located to the adjacent ring whereas in the second (adsorption energy 1.85 eV/H₂O) to an O_{2C} located above the Ti_{5C} atom of the ring Ti_{6C}–O_{3C}–Ti_{5C}–Ti_{4C}–O_{3C}–Ti_{5C}–O_{2C}–Ti_{6C} mentioned before (Figure 10).

Moreover, in this work, the free energy profile along a possible dissociation path has been determined.¹⁴² The free energy barrier for dissociation was estimated to be equal to 0.1 eV. The above results allowed a mechanism for the water dissociation at coverages lower than a monolayer to be proposed.

Closing this subsection, it should be mentioned that, although the (101) surface shows relatively low tendency to form surface oxygen vacancies,^{156,157} it is characterized by the occurrence of predominant subsurface defects. This has been verified by both theoretical^{156,157} and a recent combined experimental and theoretical study on a reduced (101) crystal.¹⁵⁸ More specifically, the authors calculated the energetics and diffusion pathways of the oxygen defects, and they interestingly found that oxygen vacancies prefer to stay in subsurface rather than at the surface (the opposite situation has been found for rutile (110)). On the other hand, a very interesting experimental study¹⁵⁹ based on resonant photoemission and X-ray absorption spectroscopy had been found that the (101) surface of anatase shows the highest concentration of surface defects (as compared to those at the anatase (001) and the rutile (110) surfaces) resulting in an apparent contradiction with the DFT and STM studies mentioned before.^{156–158} However, taking into account that the oxygen vacancies detected by the resonant photoemission spectroscopy originate not only by the defects that are exactly at the surface but also by those in a few layers below, the increased number of oxygen vacancies at the anatase (101) surface detected by this spectroscopic technique¹⁵⁹ is mainly due to the occurrence of predominant subsurface defects as it has been found by the DFT calculations and STM measurements.^{156–158}

Although the subsurface defects are less reactive than the surface oxygen vacancies mentioned before (with respect to adsorption of water or other molecules of the environment), they are probably responsible for an increased photocatalytic activity.^{156,158} One year later, the same research group studied the adsorption of water on a reduced (101) surface with such subsurface defects.¹⁶⁰ They used scanning tunneling microscopy in combination with density functional theory calculations. The STM results showed that the presence of these defects leads to a higher desorption temperature of adsorbed water, indicating a stronger binding due to the defects. In accordance with the experimental results, the theoretical calculations showed a high selectivity for water binding to sites in the vicinity of the subsurface defects. Moreover, it was found that the water adsorption energy at these sites is considerably higher than that on the stoichiometric surface. A final very interesting prediction from the calculations was that the water dissociation at these sites is quite probable, confirming the important role of subsurface defects in the surface chemistry and reactivity of TiO₂.

Finally, a recent interesting work¹⁶¹ concerned the investigation of water adsorption on anatase model structures, consisting of ridges obtained by the intersection of orthogonal (101) surfaces. Such structures might exist in actual nano-

particles. By performing DFT calculations, the authors found that dissociation of water molecules is strongly enhanced in these ridges, on sites consisting of undercoordinated $\text{Ti}_{4c}-\text{O}_{2c}$ pairs.

2.3.5. The Structure of Thin Water Overlays on the Defective (101) Surface. Let us now examine the structure of a monolayer formed on the defective (101) surface.¹⁴⁰ In the most stable state, a portion of the water molecules is dissociated (1/6), whereas the remainder remains intact coordinated above the Ti_{5c} atoms. As in the case of an isolated water molecule adsorbed on the defective (101) structure, which was described in the previous subsection, the hydroxyl oxygen is located near the vacancy bonded to both $\text{Ti}_{5c}-\text{Ti}_{4c}$ atoms and roughly replacing the missing O_{2c} atoms (whereas the proton is bonded to an O_{2c} located above the Ti_{5c} atom of the ring $\text{Ti}_{5c}-\text{O}_{3c}-\text{Ti}_{5c}-\text{Ti}_{4c}-\text{O}_{3c}-\text{Ti}_{5c}-\text{O}_{2c}-\text{Ti}_{6c}$ mentioned before (Figure 10)). Thus, two bridging hydroxyl groups are formed. A slightly less stable state is very similar to that just presented. The only difference is that the hydroxyl oxygen located near to the vacancy is bonded only to the Ti_{4c} atom resulting, thus, in one terminal and one bridging hydroxyl. In this case, the terminal hydroxyl does not migrate to the vacancy. In both cases, the dissociation takes place spontaneously at 160 K, whereas, on the same time scale, no dissociation was observed at room temperature for an isolated water molecule. This suggests that the water–water interactions favor the dissociation by stabilizing the intermediate and/or product states. The dissociation involves the H_2O molecule coordinated to Ti_{4c} , which is more active due to its low coordination. In both cases, the dissociation mechanism involves three steps: the water adsorption on the $\text{Ti}_{5c}-\text{Ti}_{4c}$ or Ti_{4c} atoms, the formation of a hydrogen bond between the H_2O and the O_{2c} and the protonation of the O_{2c} .

The presence of defects causes another important effect on the monolayer.¹⁴⁰ While on the perfect surface all water molecules remain very close to their adsorption sites (about 2 Å above the surface), on the defect surface a water molecule breaks the $\text{Ti}_{5c}-\text{O}_{1c}$ bond leaving the Ti_{5c} site, and moves about 1 Å above the layer of the $\text{Ti}_{5c}-\text{OH}_2$ water molecules. It forms a strong hydrogen bond with an O_{2c} atom. Because $\text{H}_2\text{O}-\text{O}_{2c}$ is formed from the $\text{H}_2\text{O}-\text{Ti}_{5c}$, the coordination of surface Ti_{5c} is not complete for a monolayer in the defect structure. At variance to the monolayer on the perfect (101) anatase surface, almost every molecule in the monolayer on the defect structure is involved in a strong hydrogen bond with another water molecule. These hydrogen bonds are generally donated from a $\text{Ti}_{5c}-\text{OH}_2$ to a $\text{H}_2\text{O}-\text{O}_{2c}$.

As for the monolayer on the defective (101) surface, water dissociation takes place at the adsorbed water bilayer but following a different dissociation mechanism.¹⁴⁰ The water molecule chemisorbed on a Ti_{4c} atom transfers a proton to a water molecule located on the second layer forming a transient hydronium ion, which, in turn, donates the proton to the O_{2c} . Thus, larger coverages are likely to further increase the dissociation probability close to a surface vacancy by providing additional reaction paths through which the dissociation can proceed. As for the monolayer, the terminal hydroxyl formed by dissociation does not migrate to the vacancy. The mechanism resulting in two bridging hydroxyls is also tested.¹⁴⁰ The bridging hydroxyl remained in the vacancy site with its proton H-bonded to a water molecule and accepting another hydrogen bond from a second layer water molecule. The results indicated that the $\text{Ti}_{4c}-\text{OH}$ bond is weakened when the hydroxyl is

shared with a Ti_{5c} surface atom. As to the undissociated water molecules, three distinct kinds are inferred: $\text{H}_2\text{O}-\text{Ti}_{5c}$, $\text{H}_2\text{O}-\text{O}_{2c}$, and a second layer water molecule at a distance from the surface, respectively, equal to 1.5–2.5, 2.5–3.5, and 3.5–4.5 Å. The first two kinds are also inferred for the monolayer on the defect structure. However, there is a significant difference: the shifts $\text{H}_2\text{O}-\text{Ti}_{5c} \rightarrow \text{H}_2\text{O}-\text{O}_{2c}$ mentioned for the monolayer on the defect structure are not possible for the bilayer on the same structure because in that case the second layer water molecules are bonded to the surface O_{2c} atoms, as analytically described for the bilayer on the perfect surface. The above shows that besides water dissociation, the structure of the bilayer on the defective surface is rather similar to that on the perfect one. Thus, while the presence of oxygen defects changes considerably the local structure of adsorbed water at the monolayer, the differences are not so important at bilayer coverage.

2.3.6. Mobility of the Adsorbed Water Molecules. To estimate the mobility of the adsorbed water molecules, Tilocca et al.¹⁴⁰ calculated the mean square displacements of oxygen atoms. They concluded that the water molecules move mainly to a direction parallel to the surface. In any case, the mobility increases with the distance from the surface following the order: $\text{H}_2\text{O}-\text{Ti}_{5c} < \text{H}_2\text{O}-\text{O}_{2c} <$ second layer H_2O . The first layer becomes less mobile when the second layer is adsorbed. Finally, the mobility of the $\text{H}_2\text{O}-\text{O}_{2c}$ and second layer H_2O is considerably higher on the defective surface.

2.3.7. Steps on the (101) Termination. In the above subsections, we presented the theoretical works done so far to study the structure of the water overlays adsorbed on the perfect and defective (101) anatase surface. Concerning the defective (101) crystal face, the reviewed works concerned only the oxygen vacancies. This is the type of the surface defects of oxide surfaces that has been mainly studied. On the other hand, monatomic-height step edges at terraces are very common surface defects. A non-negligible fraction of the surface atoms are located at steps.¹⁶² Moreover, adsorption sites with a special reactivity are developed at steps, whereas most metals deposited on oxidic supports are nucleated preferentially at steps.¹⁶²

A theoretical (DFT) and experimental (STM) contribution devoted to the study of the steps developed on the anatase (101) crystal face has been very recently reported by the Selloni and Diebold groups.¹⁶² As the step edges at metal oxides have been studied far less extensively with respect to other types of surface defects, this contribution is actually very important for the surface chemistry of metal oxides. A step edge can be considered as a very narrow slice of a surface. The first principle calculations showed that the step formation energy of differently oriented step edges scales with the surface energy of the extended facet. More important is the finding that the reactivity of a step edge with respect to the adsorption of water molecules is similar to that of the corresponding flat surface.

Specifically, it was found¹⁶² that molecular adsorption is favored on the most stable type of step edge, but the difference between molecular (1.12 eV/ H_2O) and dissociative (1.04 eV/ H_2O) adsorption is much smaller than that previously mentioned for the flat surface. Moreover, these values are considerably higher than those mentioned before for the ideal (101) crystal termination.

Very similar adsorption energies were also found for the dissociative (0.67 eV/ H_2O) and molecular (0.65 eV/ H_2O) adsorption at a step edge with a surface structure similar to that

of the (100) crystal face for a surface coverage equal to $\theta = 0.5$.¹⁶² At monolayer coverage a mixed molecular/dissociative adsorption is favored (0.79 eV/H₂O). This finding is in agreement with that reported by Arrouvel et al.¹¹⁶ for this surface termination (see the subsection entitled “The (100) Surface”).

On the least stable step edge with a structure similar to that of the (001) crystal face, dissociative adsorption prevails with an adsorption energy (1.28 eV/H₂O)¹⁶² similar to that found for this crystal termination (see the subsection entitled “The (001) Surface”).

From the above results emerges, in effect, the very interesting relation between structure and reactivity mentioned before. When the local structure of a step is similar to that of an extended surface, the reactivity is also similar to that of the surface.¹⁶² This is eventually a general structure/reactivity relation valid in metal oxides.

2.3.8. Experimental Studies Devoted to the Interactions of Water Molecules with the (101) Crystal Face.

In the above subsections, we presented the theoretical works done so far to study the structure of the water overlayers adsorbed on the perfect and defective (101) anatase surface. The critical point is whether the main results of these theoretical studies are in agreement with relevant experimental results. Temperature-programmed desorption of the water molecules¹⁴³ and solid-state ¹H NMR experiments¹⁶³ proved very useful in this respect.

A very interesting experimental work published by Herman et al.¹⁴³ deals with the interactions of water with the (101) surface. They studied these interactions using temperature-programmed desorption and X-ray photoelectron spectroscopy. The experiments were conducted in an ultra high vacuum chamber. The samples were natural anatase single crystals. To reduce the influence of the impurities on the surface chemistry, a homoepitaxial anatase (101) film has been grown on top of the mineral sample. The surface studied was exposed to water using quasieffusive molecular beams of either D₂O or H₂O. The sample was dosed stepwise from 0 to 15.3 D₂O nm⁻² at temperatures lower than 130 K. Molecular water was the only species desorbed from the (101) surface. A broad peak centered at about 250 K was found to be maximized at about 5.0 D₂O nm⁻².¹⁴³ In line with the first theoretical work of Vittadini et al.,⁶ they assigned this peak to the chemisorbed water on the Ti_{5c} atoms proposing the surface configuration illustrated in Figure 10. It was, moreover, found¹⁴³ that the desorption energy shifts from 0.69 to 0.65 eV/D₂O as the coverage increases in the range 0–5.0 D₂O nm⁻² (corresponding to $\theta = 0$ –1) in quite good agreement with the theoretical results mentioned above. Later, Tiloca and Selloni recalculated the binding energy of the adsorbed water molecules for the same coverage range.¹⁴¹ They found a value equal to 0.74 eV/H₂O for the Ti_{5c}–OH₂ in the low coverage limit and a somewhat smaller value (0.69 eV/H₂O) at $\theta = 1$. Therefore, there is no doubt that the desorption peak at about 250 K confirms the formation of the Ti_{5c}–OH₂ groups in the range $\theta = 0$ –1 inferred by the ab initio calculations.

At coverage higher than 5.0 H₂O nm⁻² has been observed a second desorption peak at 190 K, which was maximized at about 10.0 D₂O nm⁻² (corresponding to bilayer).¹⁴³ This peak has been assigned to water nondissociated molecules bonded to O_{2C} atoms via hydrogen bonds, in general agreement with the suggestion of Arrouvel et al.¹¹⁶ and Tiloca and Selloni.^{140,141} On the basis of this peak, Herman et al.¹⁴³ determined the

desorption energy of these adsorbed water molecules. It was found to be equal to 0.5 eV/D₂O. This value is in general agreement with an average one (0.65 eV/H₂O) calculated by Tiloca and Selloni for the H₂O–O_{2C}, taking into account the structures BL1, BL2, and BL3 of the bilayer mentioned above. Therefore, the desorption peak at about 190 K confirms the formation of the H₂O–O_{2C} bilayer water molecules with their oxygens at a distance from the surface in the range 2.5–3.5 Å.

For coverage higher than 10.0 D₂O nm⁻², a third peak has been observed at 160 K.¹⁴³ This was assigned to water desorption from multilayers in agreement with previous work.⁵⁹ It is interesting to note that Tiloca and Selloni obtained a value equal to 0.56 eV/H₂O for the binding energy of the third-layer water molecules at a distance from the surface greater than 3.5 Å.¹⁴¹

It is, moreover, interesting to note that three desorption peaks, centered at about 180, 222, and 312 K, had been observed on the UHV-DPT curves derived by experiments performed on anatase powders.¹⁶⁴ The rather similar desorption pattern exhibited by the anatase particles and the anatase (101) surface has been attributed to that the fact that the (101) termination would be predominant in the nanocrystallites of the anatase powders. The anatase O 1s binding energy was found to be equal to 531 eV irrespective of the water coverage. In contrast, the binding energy of a second O 1s peak due to the water oxygens decreases almost linearly, from 535.2 to 534.2 eV, as the coverage increases from 0 to 10.0 D₂O nm⁻², indicating the influence of the surface coverage on the chemisorption energy mentioned before. However, in any case, the O 1s binding energy remained higher than that reported for the dissociated water,^{165–167} thus suggesting molecular adsorption.

In view of the above findings, one may conclude that the TPD curves of the water molecules provide a picture generally compatible with the DFT calculations for the water species formed on the (101) water overlayer. An approximately similar picture is also provided by the solid-state ¹H NMR experiments carried out, in air and room temperature, on anatase-abundant titania powders.¹⁶³ In fact, these experiments have shown the presence of three different layers of water molecules with increasing mobility from the innermost to the outermost layer, in general agreement with the trend of the “mean square displacements” values (0.045, 0.06, and 0.31 Å²) calculated by Tiloca and Selloni¹⁴¹ for the Ti_{5c}–OH₂, H₂O–O_{2C}, and water molecules located above the first two overlayer, respectively. The innermost layer is stable up to 358 K. In contrast, the water molecules of the layers above it are vaporized at that temperature. Moreover, the ¹H NMR experiments have indicated that the water molecules in the first layer are less involved in hydrogen bonds with respect to the water molecules in the second and the third layers, in full agreement with the theoretical calculations of Tiloca and Selloni.¹⁴¹ Finally, the above experiments confirmed the theoretical predictions mentioned in the previous paragraphs that the outermost layer is not significantly affected by the structure of the (101) anatase surface.

Very recently, He et al.¹⁶⁸ published an interesting combined experimental (scanning tunneling microscopy) and theoretical (density functional theory and first-principles molecular dynamics) study, which gives atomic-scale insights into the adsorption of water on anatase (101) surface. They found that the charge rearrangement at the molecule–anatase interface affects the adsorption of further water molecules, resulting in

short-range repulsive and attractive interactions along the (010) and $(1\bar{1}\bar{1})/(1\bar{1}\bar{1})$ directions, respectively, and a locally ordered (2×2) superstructure of molecular water. More specifically, they concluded that a surface oxygen atom can accommodate only one H-bond from an adsorbed water molecule, and after arrival of a second water molecule in its neighborhood, the competition between the two molecules for the same surface oxygen weakens the H-bond of the first one and effectively lowers its adsorption energy.

Closing this section, it should be mentioned that the recent efforts for preparing single crystal surfaces (e.g., the preparation of a pristine anatase (101) surface by the same research group⁷⁹) are expected to help obtain a clearer and secure picture about the surface structure and chemistry of anatase by allowing a more extensive use of advanced experimental techniques.

2.4. Reactivity of the Anatase Crystal Terminations with Respect to Water Molecules: The Minority (001), (100), and (110) Terminations

2.4.1. The (001) Surface. Studies devoted to the investigation of the reactivity of the anatase (001) surface are rare in the literature,^{6,116,136,169} although among the anatase single-crystalline surfaces investigated this surface has received considerable attention.¹⁴³ Bredow and Jug¹⁶⁹ studied the water–anatase (001) interactions using the semi empirical MO method (SINDO1) and proposed dissociative adsorption.

Vittadini et al.⁶ and Lazzari et al.¹³⁶ have studied the structure and energetics of water on the (001) surface, following the theoretical methodologies mentioned above, for three different values of the surface coverage (θ : 0.25, 0.50, and 1.00). For $\theta = 0.25$, it was found dissociative adsorption, with no activation barrier, associated with the breaking of two Ti–O–Ti bonds formed between two Ti_{SC} atoms and one O_{2C} atom along the (100) direction. Thus, two, singly coordinated, surface hydroxyls are formed along this direction (Figure 11a). These hydroxyls are bound one to another through a strong hydrogen bond. The adsorption energy is equal to 1.6 eV/ H_2O . For $\theta = 0.50$, the aforementioned dissociative adsorption (Figure 11a) was also found for the most favorable configuration (adsorption energy equal to 1.44 eV/ H_2O). Taking into account the definition of θ and the fact that the surface density of the Ti_{SC} atoms is equal to that for the O_{2C} atoms, it is understandable that at this state all of the Ti_{SC} atoms are bounded with a hydroxyl group, whereas one-half of the O_{2C} atoms remain intact. Starting with this favorable state and increasing the surface coverage to $\theta = 1.0$, they reached the most favorable state for the monolayer coverage (adsorption energy equal to 1.01 eV/ H_2O). At this “mixed state”, one-half of the water molecules are adsorbed dissociatively as before, whereas the other half are adsorbed molecularly via two hydrogen bonds: one with a terminal hydroxyl and one with an O_{2C} atom (Figure 11b).

A similar, if not identical, picture has been developed by Arrouvel et al. by applying the theoretical methodologies mentioned above.¹¹⁶ They studied the adsorption for water coverages in the range 0–6.9 H_2O nm⁻², namely $\theta = 0$ to $\theta = 1$, over a wide range of temperatures and for a standard water pressure equal to 1.013 bar. For values of $\theta = 0.25$ and $\theta = 0.5$, they reported entirely dissociative adsorption (associated with the breaking of the Ti–O–Ti bonds and the formation of strong hydrogen bonds between the surface hydroxyls mentioned above), whereas above this coverage a mixed

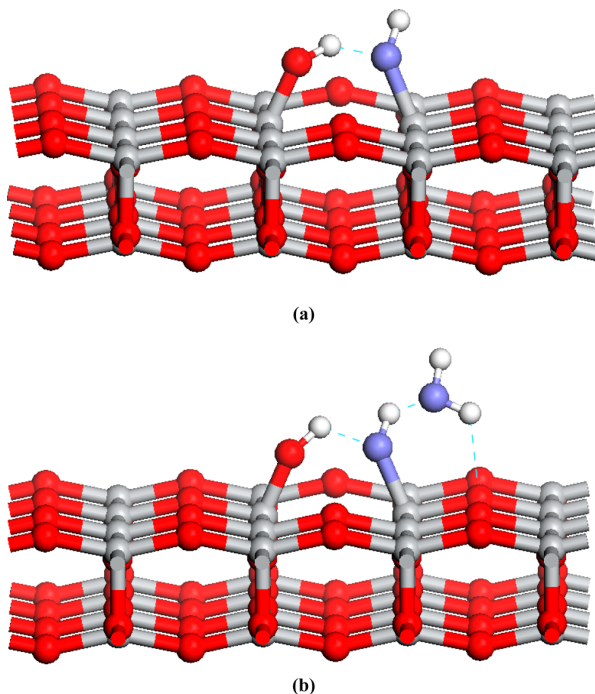


Figure 11. Representation of the structure of a water molecule adsorbed on the anatase (001) surface: (a) dissociative adsorption, $\theta = 0.5$, (b) “mixed”, dissociative and molecular, adsorption, $\theta = 1$.^{6,136}

adsorption mode involving both dissociative and molecular adsorption. Concerning the adsorption energies, they reported identical values with those reported by Selloni’s group for the same surface coverages. The very high reactivity of this crystal face was attributed to the high Ti–O bond energy of the surface bonds calculated after relaxation (43 kJ mol⁻¹).

On the basis of the “energy–temperature” linear curves (calculated at standard vapor pressure and mentioned in the previous section), it was predicted a progressive dehydration of the surface with temperature.¹¹⁶ At room temperature, the most stable state, among those examined, is that corresponding to $\theta = 1$, whereas at temperatures higher than 840 K the fully dehydrated state is the most stable one. For temperatures in the range 400–680 K, the hydrated surface corresponds to $\theta = 0.5$. The above are in line with the observation of a high temperature peak (723 K) in the TGA and TPD spectra as well as of peaks at 493–573 K in the TPD spectra of polycrystalline anatase samples.¹⁷⁰

The above results concerning the “anatase (001) surface–water” interactions have been generally confirmed in a very recent theoretical work done by Gong and Selloni (mainly devoted to the study of methanol adsorption),¹⁷¹ although somewhat different adsorption energy values have been reported (1.25, 1.1, and 1.17 eV/ H_2O respectively for θ equal to 0.17, 0.33, and 0.5). They, moreover, studied the influence of hydration on the energy of the (001) surface and found, in line with the findings of Arrouvel et al.,¹¹⁶ that hydration caused a considerable decrease in the surface energy at relatively low temperatures (0.98, 0.57, and 0.33 J m⁻² for θ equal to 0.0, 0.33, and 0.5, respectively). Thus, hydration may stabilize the (001)-1 × 1 surface. By comparing the energy values achieved for the hydrated (001) surface with that calculated for the nonhydrated reconstructed (001) 1 × 4 surface (0.48 J m⁻², see

the section “Surface Reconstructions”) and taking into account that reconstruction requires mass transport and thus quite high temperatures, it may be inferred that hydration may prevent reconstruction. Thus, they concluded that the (001) surfaces of the anatase nanoparticles grown in a wet environment are well described by the 1×1 (001) model.¹⁷¹

In agreement with the studies mentioned in previous paragraphs, Barnard et al.¹²² reported also dissociative water adsorption over the (001) anatase facet with H and OH terminations oriented perpendicular to the surface. The calculated energy for the dissociative adsorption is equal to 0.45 eV/H₂O. This value is significantly smaller as compared to the corresponding values reported by Gong and Selloni.¹⁷¹ As in the nonhydrated face, the O_{2C}, O_{3C}, and the Ti_{5C} surface atoms relax outward (0.03, 0.02, and 0.09 Å). However, as compared to the clean surface (0.20 and 0.05 Å), the outward displacement of the oxygen atoms was found to decrease after water adsorption. The effect of water is more significant for the O_{2C} surface atoms. In contrast, the outward displacement of the Ti_{5C} surface atoms was found to decrease slightly in the presence of water. In line with those reported by Barnard et al.¹²² for (101) and (100) crystal faces, the hydration of the (001) facet increased its surface energy from 0.51 J/m² (Table 2 of this Review) to 1.55 J/m². Two observations are important in this point. First, the trend of decreasing surface energy, (001) > (100) > (101), and thus of increasing face stability, is the same for the nonhydrated and the hydrated surfaces. Second, the increase in the surface energy due to the water adsorption reported by Barnard et al.¹²² does not agree with the aforementioned results of Arrouvel et al.¹¹¹ as well as with those reported by Gong and Selloni.¹⁷¹ The different results could be attributed to presumably different temperatures on which the surface energies of the hydrated surfaces have been calculated.

Finally, the adsorption of water molecules on the perfect (001) crystal face of anatase was also recently studied at various temperatures by Hamraoui et al.,¹⁴⁸ using DFT calculations combined with thermodynamic analysis. A slab containing eight surface atoms (four Ti_{5C} and four O_{2C}) has been used. A positive value for the adsorption energy reflects exothermic adsorption. The most stable configurations and the corresponding water adsorption energies for various degrees of hydration are illustrated in Figure 12. It may be seen that the first two water molecules are adsorbed through dissociation of both the water molecules and the Ti–O–Ti bonds resulting in terminal hydroxyl groups. For coverage greater than two H₂O molecules, mixed, dissociated, and nondissociated structures are formed. These findings are in good agreement with those described above. The adsorption energies obtained are significantly higher than those obtained on the (101) crystal face. The number of the water molecules present on the slab was then calculated at various temperatures. In the temperature range 300–500 K, the slab is covered by two water molecules. One water molecule remains on the slab when the temperature rises to 500 K. The surface is fully dehydrated above 600 K. The above concerns a water partial pressure equal to 0.01 bar. A configuration with six water molecules is stable for a water partial pressure equal to 0.1 bar.

2.4.2. The (100) Surface. To the extent of our knowledge, only the work of Arrouvel et al.¹¹⁶ deals systematically with the investigation of the reactivity of the anatase (100) surface. They studied these interactions for water coverages from $\theta = 0.25$ to $\theta = 1.5$. The reactivity of this orientation is similar to that of the

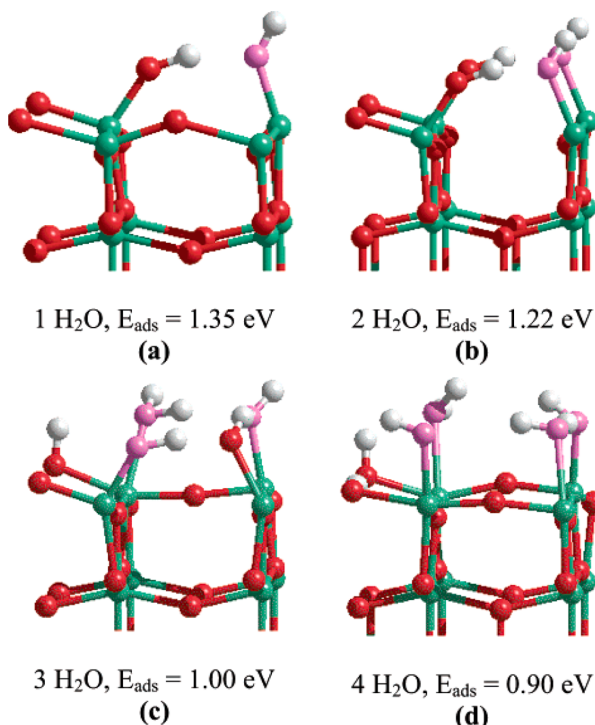


Figure 12. Stable configurations and corresponding adsorption energies for various coverages of water adsorption on the perfect (001) crystal face of anatase. Ti atoms, light green circles; O atoms from TiO₂, red circles; O atoms from H₂O molecules, violet circles; H atoms, light gray circles.¹⁴⁸ Reprinted with permission from ref 148. Copyright 2007 American Chemical Society.

(101) termination and much weaker than the reactivity of the (001) surface. This may be mainly inferred by the adsorption energies and the dehydration behavior with increasing temperature as well. In fact, the adsorption energies for the (101), (001), and (100) surfaces are in the range 70–79, 100–160, and 65–84 kJ/mol, respectively. On the other hand, on the basis of the “energy–temperature” linear curves mentioned in the previous section, it was predicted a progressive dehydration of the surface with temperature. At temperatures lower than 450 K, the most stable state, among those examined, is that corresponding to $\theta = 1.5$, whereas at temperatures higher than 450 K, the fully dehydrated state predominates. This picture is very similar to that obtained for the (101) termination and quite different from that achieved for the (001) orientation. The relatively low reactivity of this crystal face was attributed to the relatively low Ti–O bond energy of the surface bonds calculated after relaxation (30 kJ mol⁻¹).

As to the mode of water adsorption, the situation is not so clear.¹¹⁶ Dissociative adsorption takes place at relatively low water coverage, for example, at $\theta = 0.25$, where the hydroxyl binds to Ti_{5C} atom and the proton to the adjacent O_{2C} atom (Figure 13a). However, the dissociative adsorption is not related to the breaking of the Ti–O bond as is the case for the (001) surface, whereas the non dissociated configuration is only 5 kJ/mol less stable than the dissociated one. At higher water coverage, mixed dissociated and molecular configurations proved to be slightly more stable than the fully dissociated ones (Figure 13b).

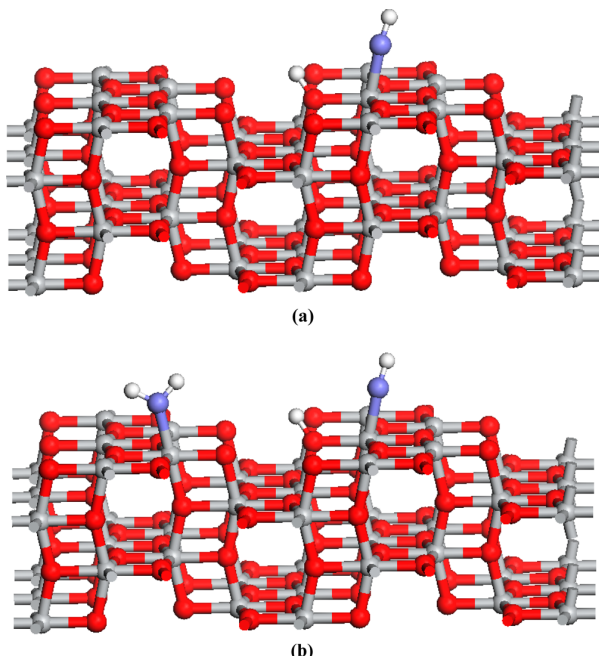


Figure 13. Representation of the structure of a water molecule adsorbed on the anatase (100) surface: (a) dissociative adsorption, $\theta = 0.25$, (b) “mixed”, dissociative and molecular, adsorption, for relatively high θ values.¹¹⁶

Barnard et al.¹²² reported very recently theoretical results (DFT within the GGA with the exchange correlation functional of Perdew and Wang (PW91)) concerning the relaxations and the surface energies of the (100) termination after water adsorption at monolayer coverage. Dissociative adsorption was found to be energetically favorable even on the (100) perfect crystal termination. The calculated values of the adsorption energy were found to be equal to 0.24 and 0.29 eV/H₂O for the molecular and dissociative adsorptions, respectively. An outward displacement of the O_{3C} (0.01 Å) and Ti_{5C} (0.10 Å) surface atoms and an inward displacement of the O_{2C} (0.02 Å) surface atoms take place upon relaxation. These displacements are different from the corresponding ones calculated for the non-hydrated (100) crystal face. The bending of the O–H bonds of the terminal hydroxyls toward each other is an interesting characteristic of this surface termination. In line with those reported by Barnard et al.¹²² for the (101) and (001) crystal faces, hydration of the (100) facet increases its surface energy from 0.39 J/m² (Table 2 of this Review) to 1.13 J/m².

2.4.3. The (110) Surface. It has been studied by Arrouvel et al.¹¹⁶ in water coverage in the range of θ 0.5–2.0. The water molecules are adsorbed dissociatively. The hydroxyls bind to the Ti_{4C} atoms and the protons to the adjacent O_{2C} atoms. At relatively low coverage, each Ti atom binds one hydroxyl group (Figure 14a). As the surface coverage increases more and more Ti atoms bind two surface hydroxyls per atom (Figure 14b). At $\theta = 2$, the surface is completely covered by surface hydroxyls, although at intermediate coverage mixed states involving both dissociated and molecular adsorption are the most favorable. The quite high reactivity of this surface is also manifested by the magnitude of the adsorption energy (138–109 kJ/mol) and the quite high value of temperature up to which the surface remains partially (460 K) or fully (710 K) dehydrated. The

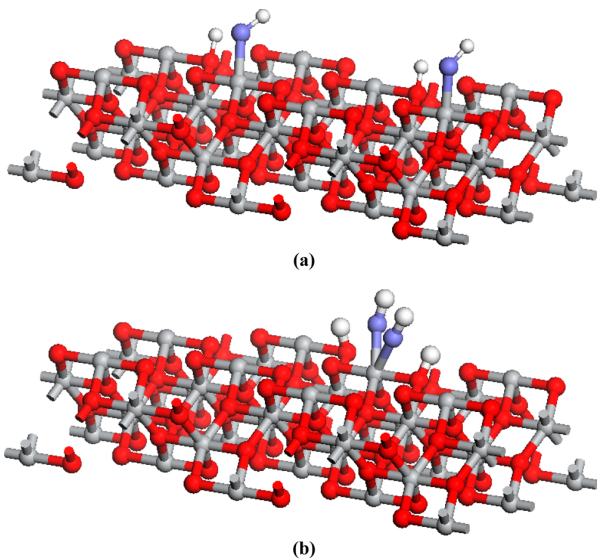


Figure 14. Representation of the structure of two water molecules adsorbed on the anatase (110) surface: (a) dissociative adsorption, $\theta = 0.5$, (b) dissociative adsorption, $\theta = 2$.¹¹⁶

relatively high reactivity of this crystal face was attributed to the relatively high Ti–O bond energy of the surface bonds calculated after relaxation (40 kJ mol⁻¹).

Barnard et al.¹²² reported that the (110) anatase crystal face is structurally unstable in the presence of water. It was found to deteriorate into a disordered structure by displacement of the Ti_{4C} surface atoms from their lattice positions and sometimes by the removal of the bridging hydroxyl.

2.4.4. The Trend in the Surface Reactivity. In view of the above, it is clear that the low -index surfaces mentioned above may be classified into two groups from the viewpoint of surface reactivity. The (001) and (110) surfaces belong to the high reactivity group. These dissociate the water molecules and retain the resulting surface hydroxyls up to relatively high temperatures (840 and 710 K, respectively). In contrast, the (101) surface chemisorbs water mainly molecularly, although dissociative adsorption cannot be completely excluded for high water coverages. On the other hand, on the (100) crystal face, the nondissociated configuration is only 5 kJ/mol less stable than the dissociated one at relatively low θ values, whereas at higher ones mixed dissociated and molecular configurations proved to be slightly more stable than the fully dissociated ones. Moreover, in both surfaces, the adsorbed water is desorbed at relatively low temperatures (450 K). As was already mentioned, the reactivity of the above surfaces was related to the Ti–O bond energy of the surface bonds calculated after relaxation. Therefore, it is not surprising that Arrouvel et al.¹¹⁶ found a linear dependence of the negative values of the inverse temperature, required for complete dehydration, on the Ti–O bond energy.

2.5. Investigation of the Anatase Surfaces by Infrared Spectroscopy

In Table 1, one may observe the various Lewis acidic (Ti atoms) and basic (O atoms) sites exposed on the dehydrated anatase surfaces. As was already mentioned, the interactions of the water molecules with the anatase terminations bring about, in addition, the formation of Bronsted sites (surface hydroxyls), whereas these decrease the concentration of the Lewis sites. It

is obvious that the types and the surface concentration of the Lewis and Bronsted sites developed on the various anatase surfaces depend on temperature and water pressure, which, as already mentioned, determine the hydration level of these surfaces. It is, moreover, obvious that the relative concentration of these sites in a polycrystalline anatase material is related to the contribution of each surface termination to the whole surface exposed by the anatase nanoparticles and thus to their morphology.

IR spectroscopy has been used many years ago to investigate the surface acidity of polycrystalline anatase materials.^{170,172–176} The numerous bands observed in certain IR spectra render quite difficult an unambiguous assignment of these bands to the different OH groups. However, the bands observed in the regions 3600–3750 cm⁻¹ (e.g., 3620–3680, 3690 3715, 3725, 3730–3742 cm⁻¹) and 3350–3500 cm⁻¹ had been attributed to the stretching vibrations of the OH groups, whereas a band at about 3300 cm⁻¹ had been related to the OH groups involved in hydrogen bonds. A quite strong band at 1600–1640 cm⁻¹ had been attributed to the bending vibrations of chemisorbed water molecules.^{116,170,172,173}

An assignment of the IR bands on the basis of fundamental theoretical findings mentioned above concerning the “water–anatase” interactions has been recently attempted.^{116,177} In the first article,¹¹⁶ the authors were based on experimental values collected from various published experimental works.^{170,172–176} In the second article,¹⁷⁷ the authors recorded FTIR spectra that characteristically show the presence of different types of OH groups on the surface. One of these spectra is shown in Figure 15.

More specifically, they calculated the IR frequencies for the low-index hydrated anatase surfaces at various water coverages. Studying the (101) surface at $\theta = 2.0$, they calculated two IR frequencies at 3646 and 3665 cm⁻¹ corresponding to the stretching modes of the free hydroxyl groups of the water molecules chemisorbed on the Ti_{SC} atoms. Therefore, they

assigned the experimentally observed bands at 3620–3680 cm⁻¹^{1170,173,174,176} to these groups. Moreover, they calculated one IR frequency at 2950–3253 cm⁻¹ corresponding to water molecules adsorbed physically (via hydrogen bonds with their hydrogens above the O_{2C} atoms) also in agreement with experimental observations (experimental value at 3300 cm⁻¹) and one IR frequency at 1565–1646 cm⁻¹ corresponding to the bending modes of the aforementioned chemically and physically adsorbed water molecules in agreement with the experimental values 1600–1640 cm⁻¹ mentioned above.^{116,170,172,173}

Concerning the (001) surface, they calculated two frequencies at 3760 and 3746–3751 cm⁻¹ for the free surface hydroxyls formed above the Ti_{SC} atoms, due to the dissociated water, at $\theta = 0.25$ and $\theta = 0.50$, respectively. It is interesting to note that these values are similar to certain experimental ones (3730–3742 cm⁻¹), although its calculation has not taken into account the formation of the strong hydrogen bonds mentioned in the previous section. In contrast, by considering these bonds, they calculated, for $\theta = 0.50$, a low-frequency mode at 2300 cm⁻¹, which had not been observed in the IR spectra. Despite the above, they assigned the experimentally observed absorption band at 3730–3742 cm⁻¹ to the OH groups developed on the (001) termination.

As to the (100) surface, they performed a vibrational analysis for a hydrated surface corresponding to $\theta = 1.5$. They calculated two frequencies at 3688 and 3710 cm⁻¹, respectively, for the surface hydroxyls formed above the Ti_{SC} atoms, due to the dissociated water, and to one surface hydroxyl belonging to a water molecule chemisorbed non dissociatively on the aforementioned Ti atoms. For the second hydroxyl, it is, moreover, calculating the bending mode frequency at 1578–1648 cm⁻¹. These frequencies, mainly the first and the second one, had been observed in the IR spectra of polycrystalline anatase materials (experimental values at 3690, 3715, and 1600–1640 cm⁻¹).

Finally, the vibrational analysis performed at the (110) surface for $\theta = 1$ resulted in the calculation of the stretching frequency of the surface hydroxyls bounded to the Ti_{SC} atoms. The calculated value, equal to 3728 cm⁻¹, is very close to the experimental one, 3725 cm⁻¹, which had been reported.¹⁷² This presumably indicates the presence of the (110) surface on the anatase nanoparticles of the given synthesis.

In view of the above assignments, it was very useful to investigate whether the IR spectra may be used for detecting a particular termination in the nanocrystallites of a given anatase polycrystalline sample. Table 3 compiles the characteristic frequencies, observed in the IR spectra or calculated by DFT and the corresponding anatase terminations drawn from the aforementioned assignments of Arrouvel et al.¹¹⁶ These assignments are corroborated by the thermal behavior of the polycrystalline samples.¹¹⁶ Thus, the almost complete disappearance of the experimentally observed band at 1620 cm⁻¹ after heating above 458 K,¹⁷³ assigned to the molecularly chemisorbed water molecules on the (101) and (100) surfaces (Table 3), is in excellent agreement with the DFT calculations of Arrouvel et al., which, as already mentioned, predicted complete dehydration of these surfaces after heating above 450 K. Moreover, the observation that the appearance of the band at 1620 cm⁻¹ upon increasing hydration is correlated with the band at 3620–3680 cm⁻¹, but not with the band at 3730–3742 cm⁻¹,¹⁷⁰ indicates that both bands concern the same (101) surface.

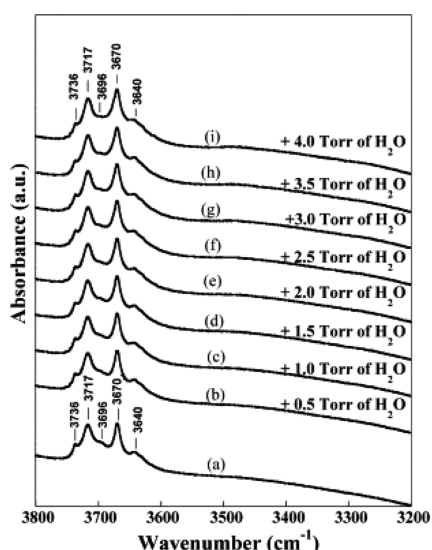


Figure 15. FTIR spectra of an anatase sample dehydrated under flowing oxygen at 693 K for 3 h, outgassed at 573 K for 1 h up to 10⁻⁶ Torr (a), and then hydrated with different water vapor doses at room temperature (b–i).¹⁷⁷ Reprinted with permission from ref 177. Copyright 2005 Elsevier.

Table 3. Anatase Terminations and the Characteristic Frequencies Observed in the IR Spectra or Calculated by DFT at Various Coverages θ^{116}

surface	characteristic frequencies (cm^{-1})	θ
(101)	3620–3680 (3646, 3665), ^a 3300 (2950–3253), 1600–1640 (1565–1646)	2.0
(001)	3730–3742 (3746–3751), (2300)	0.5
(100)	3690, 3715 (3688, 3710), 1600–1640 (1578–1648)	1.5
(110)	3725 (3728)	1.0

^aThe values in parentheses have been calculated by DFT.

Finally, it should be mentioned a recent theoretical study of the vibrational properties of OH groups for three oxides (γ -Al₂O₃, TiO₂-anatase, and MgO) published by the same research group.¹⁷⁸ By comparing results obtained by ab initio calculations in the frame of DFT, for the three aforementioned oxides, the authors identified the main geometric (hydrogen bonding, coordination, surface symmetry) and electronic parameters (strength and nature of the metal–oxygen bond (M–O)) that determine the vibrational properties of the OH groups. More specifically, they found a general linear correlation between the calculated anharmonic vibration O–H stretching frequencies and the O–H bond lengths, showing that the stretching frequency is closely linked to the O–H bond strength. The existence of hydrogen bonding is the most important parameter governing the O–H stretching frequency. Thus, isolated OH groups and hydrogen-bond acceptors exhibit higher frequencies than hydrogen-bond donors. Among isolated species and acceptors, O_{1C}–H groups vibrate at higher frequencies.

2.6. Experimental Investigation of Morphology of the Anatase Nanocrystallites Using XRD, TEM, and FT-IR Techniques

In a recent paper, Dzwigaj et al.¹⁷⁷ have taken advantage of the aforementioned DFT calculations of IR frequencies and used jointly the XRD, TEM, and FT-IR techniques to investigate the morphologies of the anatase nanoparticles prepared by two different methodologies. More specifically, they studied two different anatase samples: one prepared by a conventional synthesis route (sample A) and a second one prepared by a multigelation method^{179–181} (sample B). They observed a difference in the relative intensities in the XRD spectra of A and B (Figure 16). For sample A, the three peaks corresponding to (101), (004), and (200) Miller planes exhibited different intensities, whereas for sample B, the (004) and (200) peaks exhibit almost the same intensity. More importantly, the contribution of the (101) Miller plane is considerably more predominant in sample A than in sample B. These provided first evidence for different morphologies of the nanoparticles of the two samples. The dependence of the relative magnitude of the XRD peaks on the morphology of the nanoparticles (for example, spherical instead of faceted schemes) has been reported several times in the past [ref 11 and several references therein].

This first evidence is further corroborated by observing the TEM images taken for the samples (Figure 17).¹⁷⁷ The nanoparticles in sample A exhibit a rod-type morphology with sizes of 10 nm × 20 nm, whereas those of sample B exhibit more spherical nanoparticles of 10 nm diameter.

These findings were further investigated by IR measurements in conjunction with DFT calculations.¹⁷⁷ The relative intensities of the IR bands differ also significantly for the two samples. For sample A, two well-defined and predominant OH bands are detected at 3670 and 3717 cm⁻¹, whereas only weak

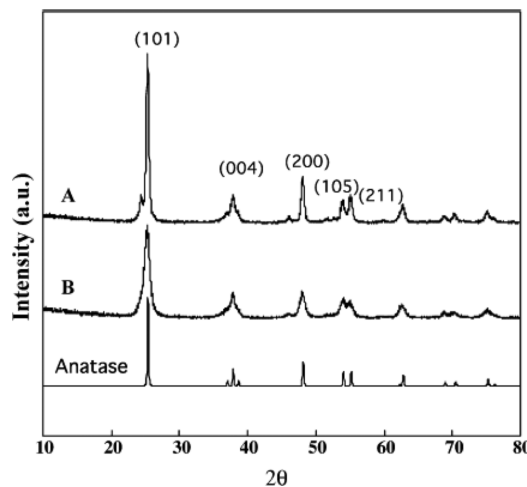


Figure 16. XRD patterns of samples A and B.¹⁷⁷ Reprinted with permission from ref 177. Copyright 2005 Elsevier.

peak contributions at 3640, 3696, and 3736 cm⁻¹ appear. In contrast, sample B exhibits a larger peak broadening; the most intense OH bands are located at 3736 and 3719 cm⁻¹ and a non-negligible contribution of the OH bands at 3676 and 3642 cm⁻¹. The two well-defined and predominant OH bands detected at 3670 and 3717 cm⁻¹ in sample A strongly indicated the considerable presence of the (101) and (100) orientations in the whole surface exposed by the nanoparticles, respectively. In fact, the DFT studies concerning the face (101) and (100) predict, respectively, strong absorption at 3670 and 3717 cm⁻¹ for the terminal and predominant OH₂ groups coordinated to the surface penta-coordinated Ti atoms. The appearance of the low intensity band at 3736 cm⁻¹ in the sample A indicates the minor contribution of the (001) crystal orientation in the whole surface of the nanoparticles of this sample. In fact, DFT calculations predict a strong absorption at this wavelength due to the presence of the terminal and predominant OH groups coordinated to the surface penta-coordinated Ti atoms in the (001) crystal orientation. In view of the above, Dzwigaj et al.¹⁷⁷ designed a rod-type morphology for the nanoparticles of sample A, which is compatible with the XRD, TEM, and IR findings (Figure 18a).

The more isotropic (spherical) nanoparticles observed by TEM in the sample B indicates the contribution of more crystal terminations in the whole surface of the nanoparticles, reflected in the larger peak broadening exhibited by sample B. Moreover, the increasing participation of the (001) crystal face as compared to the nanoparticles of sample A is reflected in the quite strong absorbance at 3736 cm⁻¹, which, as already mentioned, is the signature of this orientation. The participation of the crystal faces (100) and (101) is reflected, respectively, by the appearance of absorptions at 3719 cm⁻¹

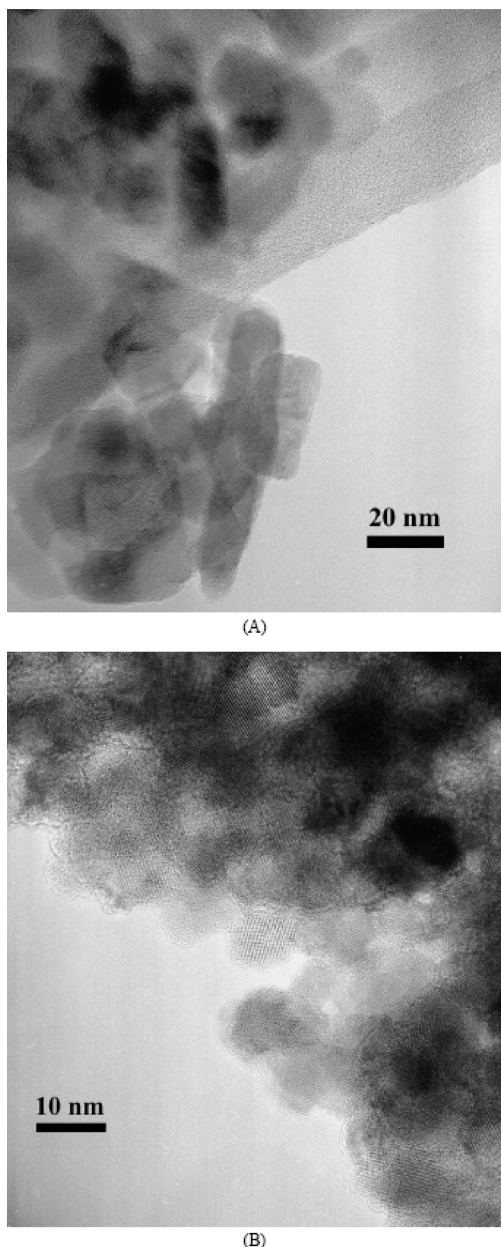


Figure 17. TEM images of samples A and B.¹⁷⁷ Reprinted with permission from ref 177. Copyright 2005 Elsevier.

(very near to 3717 cm^{-1}) and 3670 cm^{-1} (very close to 3676 cm^{-1}). Taking into account the above, Dzwigaj et al.¹⁷⁷ designed spherical-type morphologies for the nanoparticles of sample B, which are compatible with the XRD, TEM, and IR findings (Figure 18b,c). The contribution of Dzwigaj et al.¹⁷⁷ indicated how DFT calculations may be used for the morphologies of the anatase nanocrystallites to be more “visible” to IR spectroscopy.

2.7. Calculated Morphology of the Anatase Nanocrystallites

2.7.1. Introductory Remarks. The shape of nanocrystallites is strongly related to the relative contribution of the various crystal terminations to the whole nanoparticle area.

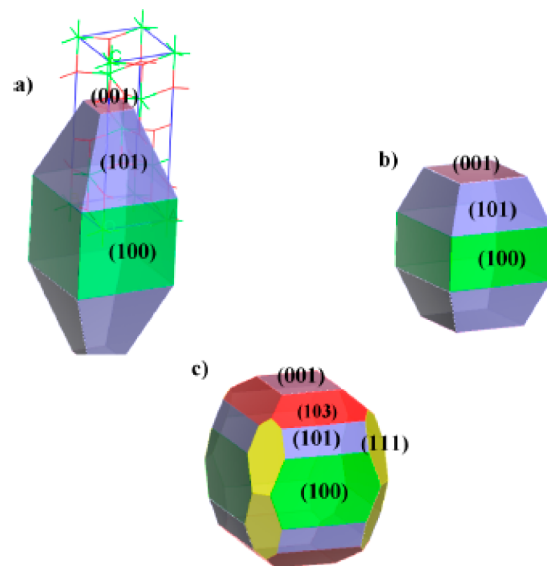


Figure 18. Proposed morphologies: (a) sample A with rod-type morphology and high anisotropy;¹⁷⁷ (b and c) sample B with spherical morphology and high isotropy.¹⁷⁷ Reprinted with permission from ref 177. Copyright 2005 Elsevier.

This may be manipulated.^{182–184} Thus, this shape may affect the chemical properties of the nanocrystallites, for example, reactivity and acid–base behavior. The equilibrium shape of the nanocrystallites generally varies with their size.¹⁸⁵ However, the description of the shape evolution with the particle size is very difficult. This is the reason for which in most of the cases the nanocrystallites are considered to be spherical.

The old approaches concerned crystal morphologies at the macroscale. These were independent of the crystal size. In this context, the morphology of a crystal of a certain volume may be determined following the Gibbs–Curie–Wulff law¹⁸⁶ where the relative stability of different crystal shapes is based on the minimization of the total free energy. The standard method for determining the equilibrium morphology of a material is to generate the so-called “Wulff construction”. However, this construction does not take into account the effects of surface tension. These may be significant at nanoscale. In other words, at the nanoscale, the surface/volume ratio influences considerably the actual atomic structure of the titania nanoparticles. Therefore, it is possible that the morphologies of nanocrystals may deviate from the corresponding Wulff constructions. Following the work of Wulff, criteria concerning the thermodynamic stability of various crystal shapes were developed by Herring.¹⁸⁷ An extensive literature is devoted to macroscopic crystal shapes.¹⁸⁵

2.7.2. Morphology of Anatase Nanocrystals: “Wulff Constructions”. As the morphology depends on the surface energy of each crystal termination, it is generally expected that different morphologies be obtained before and after relaxation. This is confirmed by the morphologies calculated by Arrouvel et al.¹¹⁶ on the basis of the energies compiled in the fourth column of Table 2 (figures outside parentheses and first figures inside parentheses) as well as by the morphologies calculated by Lazzari et al.¹¹¹ on the basis of the energies compiled in the third column of Table 2 (figures inside parentheses). However, in any case, it was found that the morphology is a truncated bipyramide with a square basis. In both relaxed and unrelaxed

structures, only the (101) and the (001) surfaces are exposed (Figure 19).

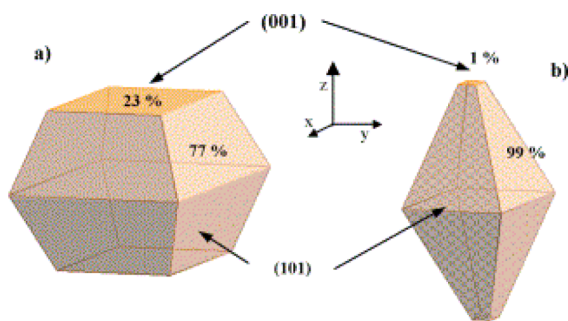


Figure 19. Morphologies for the anatase nanocrystallites according to the Gibbs–Curie–Wulff construction based on the energy values illustrated in Table 2.¹¹⁶ (a) Equilibrium shape obtained on the basis of the surface energy of the (101), (100), (001), and (110) unrelaxed surfaces (column 4¹¹⁶). (b) Equilibrium shape obtained on the basis of the surface energy of the (101), (100), (001), and (110) (column 4¹¹⁶) or the (101), (100), (001), (110), (103)_b, and (103)_s relaxed surfaces (column 3¹¹¹). Reprinted with permission from ref 116. Copyright 2004 Elsevier.

Concerning the unrelaxed structure, it was found that the (101) surface covers 77% of the whole crystal surface, whereas the (001) surface covers the remaining 23%.¹¹⁶ The contribution of the (001) surface to the whole crystal surface diminishes from 23% to 1%¹¹⁶ or 6%¹¹¹ upon relaxation. The morphology achieved taking into account relaxation (Figure 19b) agrees with experimental observations for natural anatase crystals¹⁸⁸ and in some cases with anatase nanocrystallites observed using electron microscopy.^{116,189} In fact, it has been reported that the (101) surface is the predominant face exposed on anatase minerals and the polycrystalline materials as well.¹¹⁸ In contrast, it has been reported that “in typical anatase preparations” these contain mainly two surfaces: the (101) and the (100)/(010) in approximately equal amounts, together with some (001).⁶

As was already mentioned, the hydration of an anatase surface causes a decrease in its surface energy. The magnitude of the effect is different for each orientation. Therefore, an influence of the hydration on the equilibrium morphology is expected. Arrouvel et al.¹¹⁶ calculated the equilibrium morphologies for two temperatures (400, 700 K) and two water pressures ($p_{\text{H}_2\text{O}}/p_0 = 0.01$, $p_{\text{H}_2\text{O}} = p_0$). They found that the crystals exhibit the (101) and (001) orientations (Figure 13), and only slight changes in the proportions of the (101) and (001) surface areas are induced by temperature and pressure effects. However, the above cannot exclude the formation of “non equilibrium” anatase nanocrystals under certain experimental conditions with morphologies allowing the appearance of the (110), (100), and (103) facets.¹⁷⁷

2.7.3. Surface Chemistry and Morphology of Anatase Nanocrystals. A thermodynamic model describing the relative stability of different shapes for nanoparticles as a function of their size has been recently reported by Barnard and Zapol.¹⁸⁵ This, based on the Gibbs free energy, was developed for arbitrary crystalline solids and tested for diamond, silicon, and germanium. An equation has been derived, which provides the free energy as a function of the bulk, surface, edges, and corners free energies (eq 12 of ref 185). These can be calculated by

non-empirical methods. For example, the surface energies of the aforementioned solids used in ref 185 were taken from previous density functional calculations in local density approximation with ultrasoft pseudopotentials of Stekolinkov et al.¹⁹⁰ Moreover, the model takes into account that the surface tension produces an effective pressure on the particle and thus affects the nanocrystal shape. Thus, a factor expressing the resulting change of the nanocrystal volume has been introduced in the aforementioned equation. Although this factor depends on the surface tension and the nanocrystal shape, it was found that the Laplace–Young equation (based on spherical shape) described satisfactorily the change of the volume caused by the surface tension. The model can be used for any type of material and any crystallographic system. This may be used, in addition, for predicting phase transitions as a function of shape and size by equating free energies for the most stable shapes of opposing phases. It was, moreover, predicted that edge and corner contributions to the total free energy rapidly decrease with the crystal size. They become negligible at sizes greater than 10^4 atoms corresponding to about 6 nm. It was finally mentioned that for crystals smaller than 2 nm, it is more appropriate to perform explicit calculations of isolated structures using methodologies in the frame of density functional theory.¹⁸⁵ The model is best applied to particles in the range 2–100 nm.

The above-described model was then applied by Barnard and Zapol to calculate the morphology of the anatase nanoparticles both before^{120,191} and after water adsorption¹²² over a wide range of particle size. The required surface tension and surface energy values for the application of the model were calculated, after relaxation, in the same works. The latter are also compiled in Table 2 (fourth column, second figures in parentheses) and mentioned in sections 2.3 and 2.4, which deal with the reactivity of the anatase crystal terminations with respect to water molecules.

First, the Wulff construction was generated, indicating the truncated tetragonal bipyramide morphology for the anatase nanocrystals. This morphology then has been defined in terms of two independent length parameters, A and B (Figure 20). By

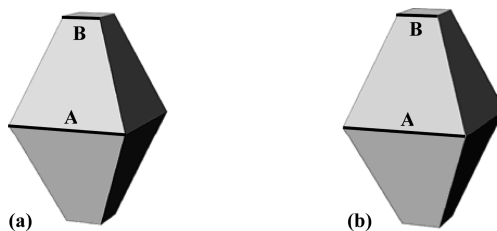


Figure 20. Effect of hydration on the morphology of the anatase nanocrystals calculated according to the model developed by Barnard and Zapol:¹⁸⁵ (a) morphology before hydration, (b) morphology after hydration.¹²² Reprinted with permission from ref 122. Copyright 2005 American Chemical Society.

expressing all of the geometric parameters such as the volume and surface area of the various crystal faces in terms of the ratio B/A , the energy was minimized with respect to this variable. Obviously, this ratio expresses the degree of truncation. Considering anatase crystals with nonhydrated faces, it was found that (at least in the range $A = 2$ –300 nm) this ratio is about 0.32, whereas the Wulff approach predicts a ratio equal to 0.47. As the size of anatase crystal increases, the effect of surface

tension is minimized, and the shape converges to that of the Wulff construction. It was found that this convergence occurs at about 10^8 TiO_2 units. Similar results were obtained for anatase crystals with hydrated surfaces. The ratio predicted by the model for nanocrystals in the aforementioned range is equal to 0.30, whereas the ratio predicted by the Wulff procedure is equal to 0.45. In conclusion, the application of the model developed by Barnard and Zapol predicts greater contribution of the (001) crystal termination to the whole surface area of the anatase nanocrystals with respect to that predicted by the Wulff approach. This contribution increased further due to the surface hydration. The influence of hydration on the morphology is illustrated in Figure 20.

Barnard et al.¹²⁰ studied the influence of the hydrogenation of the basic surface orientation of anatase nanocrystals on their shape. The subject is quite useful concerning catalyst preparation because the development of metallic supported catalysts involves hydrogenation of the oxic samples. The theoretical analysis was based on the minimization of the surface energy of basic faces ((001), (101), (100)) of the anatase nano crystals for clean, partially, and fully hydrogenated surfaces (Figures 21–24). In the case of partially hydrogenated

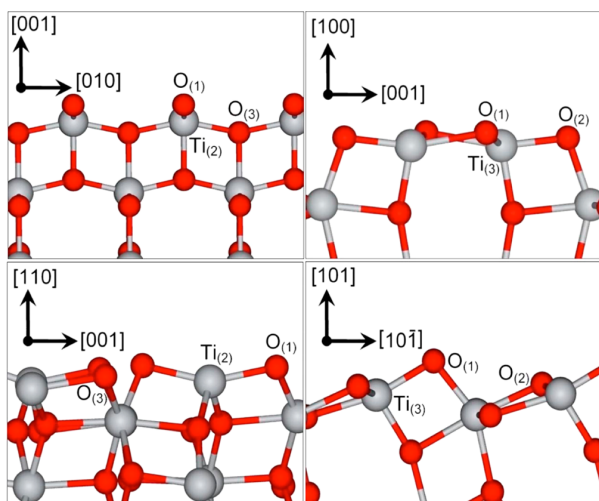


Figure 21. Relaxed anatase (001) surface (top left), (100) surface (top right), (110) surface (lower left), and (101) surface (lower right).¹²⁰ Reprinted figure with permission from ref 120. Copyright (2004) by the American Physical Society.

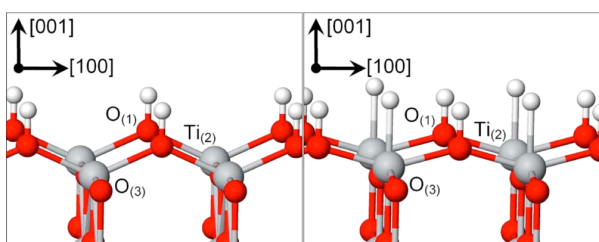


Figure 22. Relaxed, partially hydrogenated anatase (001) surface (left) and fully hydrogenated (001) surface (right).¹²⁰ Reprinted figure with permission from ref 120. Copyright (2004) by the American Physical Society.

surfaces, the hydrogen atoms are located above the $\text{O}_{2\text{C}}$ atoms, whereas in the case of the fully hydrogenated surfaces, the

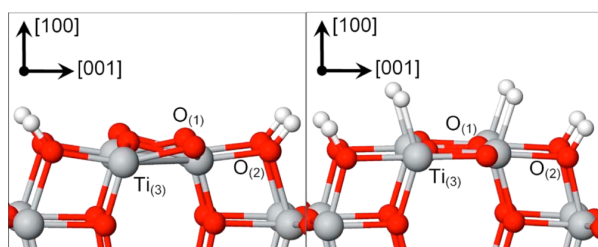


Figure 23. Relaxed, partially hydrogenated anatase (100) surface (left) and fully hydrogenated (100) surface (right).¹²⁰ Reprinted figure with permission from ref 120. Copyright (2004) by the American Physical Society.

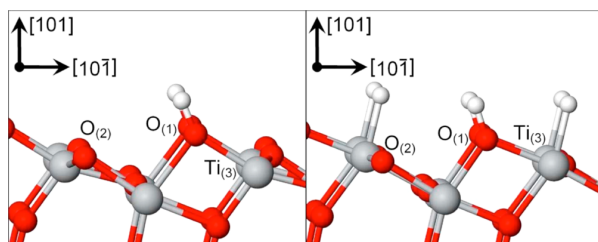


Figure 24. Relaxed, partially hydrogenated anatase (101) surface (left) and fully hydrogenated (101) surface (right).¹²⁰ Reprinted figure with permission from ref 120. Copyright (2004) by the American Physical Society.

hydrogen atoms are located above both the $\text{O}_{2\text{C}}$ and the Ti_{SC} atoms. It was predicted that the partial or full hydrogenation of these phases does not have any considerable effect on the Wulff construction of anatase nanocrystals (Figure 25).

Barnard et al. continued their theoretical studies on the morphology of the anatase nanoparticles by studying the influence of pH.^{192,193} It is well-known that in most of the cases titanium dioxide nanoparticles are prepared via sol–gel synthesis. The pH of the solution seems to affect particle size, shape, and agglomeration [refs 192,193 and many references therein]. The influence of pH on shape could be related to its influence on the faces of the generated-increased nanocrystals.

To approach the “highly acidic conditions”, it was assumed full hydrogenation of both the $\text{O}_{2\text{C}}$ and the Ti_{SC} atoms (Figure 26).¹⁹³ This corresponds structurally to the fully hydrogenated anatase surface mentioned before.

To represent moderately acidic conditions, the surface Ti_{SC} atoms have been capped with a water molecule, and the $\text{O}_{2\text{C}}$ atoms have been capped with hydrogen atoms (Figure 27).¹⁹³ Under these conditions, the crystal faces are rich in hydrogen.

Two surface configurations have been chosen to represent the neutral pH conditions. These correspond to molecular and dissociative adsorption. In the first configuration, each Ti_{SC} atom has been capped with a water molecule and the $\text{O}_{2\text{C}}$ atoms have been left uncovered. In the second configuration, the Ti_{SC} atoms were terminated with OH groups, and the $\text{O}_{2\text{C}}$ atoms were terminated with hydrogen atoms forming bridging hydroxyls. The most stable configuration was chosen for each crystal orientation (Figure 28).¹⁹³ The crystal faces in this case are simply hydrated.

To represent the “moderately basic conditions”, the Ti_{SC} atoms have covered by a OH group, and the $\text{O}_{2\text{C}}$ atoms were

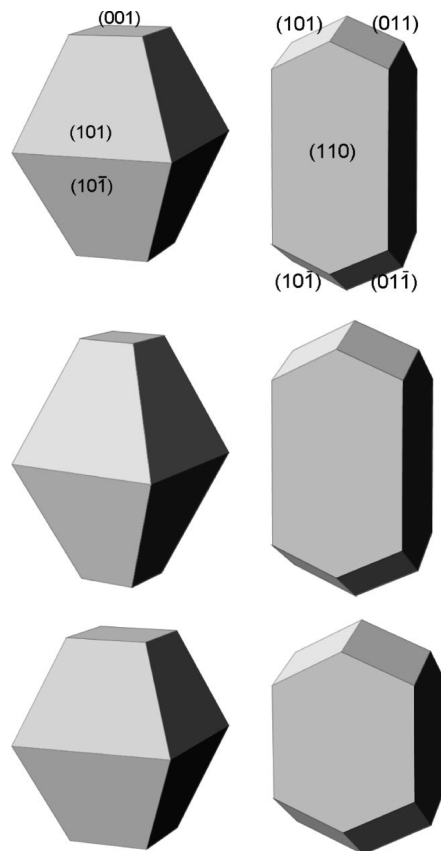


Figure 25. Calculated Wulff constructions for clean (top), partially hydrogenated (center), and fully hydrogenated (bottom) anatase (left) and rutile (right).¹²⁰ Reprinted figure with permission from ref 120. Copyright (2004) by the American Physical Society.

left uncovered (Figure 29).¹⁹³ The crystal faces in this case are hydrogen poor.

The highly basic conditions were represented by assuming that each Ti_{SC} atom is terminated with an oxygen atom and the $\text{O}_{2\text{C}}$ atoms are being uncovered (Figure 30).¹⁹³ The crystal faces in this case are oxygenated.

The authors calculated the surface relaxation, surface energy, and surface stress for each of the above-mentioned configuration and low-index surfaces of anatase.¹⁹³ Using these data, they predicted the morphology of the anatase nanoparticles for each configuration and for a constant size of the nanoparticles (side length $A \leq 15 \text{ nm}$).¹⁹² The effect of surface chemistry upon the shape of the anatase nanoparticles is illustrated in Figure 31.¹⁹²

We observe that the application of highly or moderately acidic conditions does not change considerably the shape of the anatase nanoparticles with respect to the shape predicted for the neutral conditions, with respect to the hydrated anatase surfaces. In contrast, under moderately or highly basic conditions, the anatase nanoparticles become elongated. This prediction is consistent with several experimental findings.^{114,115,183,194,195} It is worthwhile to note that the application of moderately or highly basic conditions leads to the development of the (100) crystal face causing a considerable change in the morphology of the anatase nanoparticles (Figure 31). We note that the lowest value for

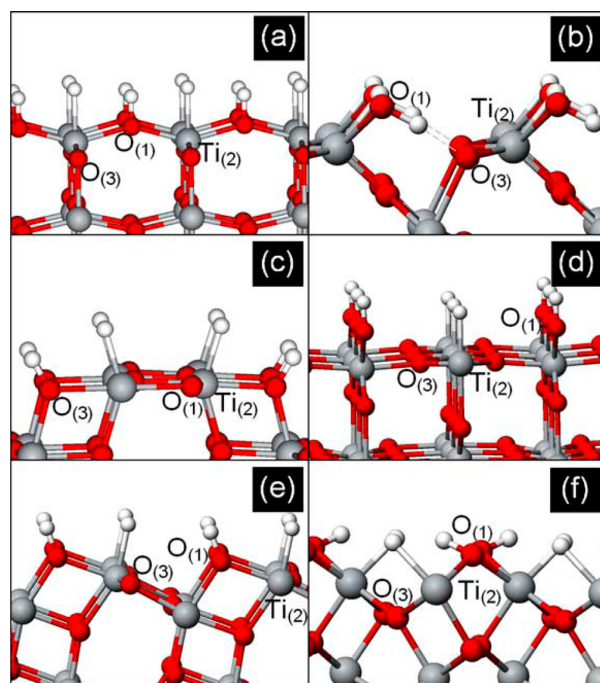


Figure 26. Relaxed low-index H-terminated stoichiometric surfaces of titanium dioxide, chosen to represent “highly acidic” conditions: (a) anatase (001), (b) rutile (100), (c) anatase (100), (d) rutile (110), (e) anatase (101), and (f) rutile (011).¹⁹³ Reprinted with permission from ref 193. Copyright 2005 Elsevier.

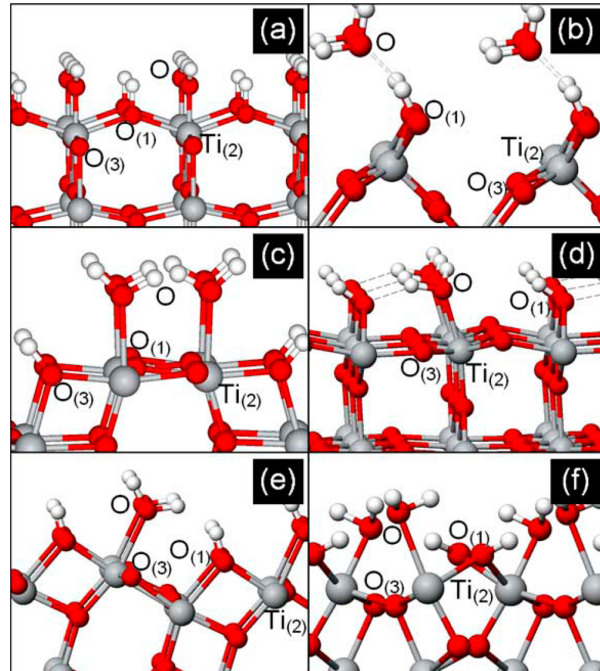


Figure 27. Relaxed low-index hydrogen-rich stoichiometric surfaces of titanium dioxide, chosen to represent “moderately acidic” conditions: (a) anatase (001), (b) rutile (100), (c) anatase (100), (d) rutile (110), (e) anatase (101), and (f) rutile (011).¹⁹³ Reprinted with permission from ref 193. Copyright 2005 Elsevier.

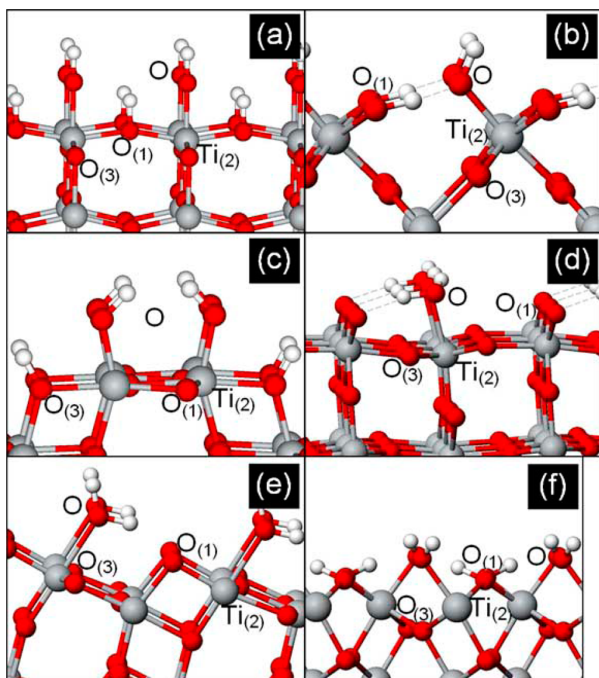


Figure 28. Relaxed low-index hydrated stoichiometric surfaces of titanium dioxide, chosen to represent “neutral” conditions (only the lowest energy configuration is shown): (a) anatase (001), (b) rutile (100), (c) anatase (100), (d) rutile (110), (e) anatase (101), and (f) rutile (011).¹⁹³ Reprinted with permission from ref 193. Copyright 2005 Elsevier.

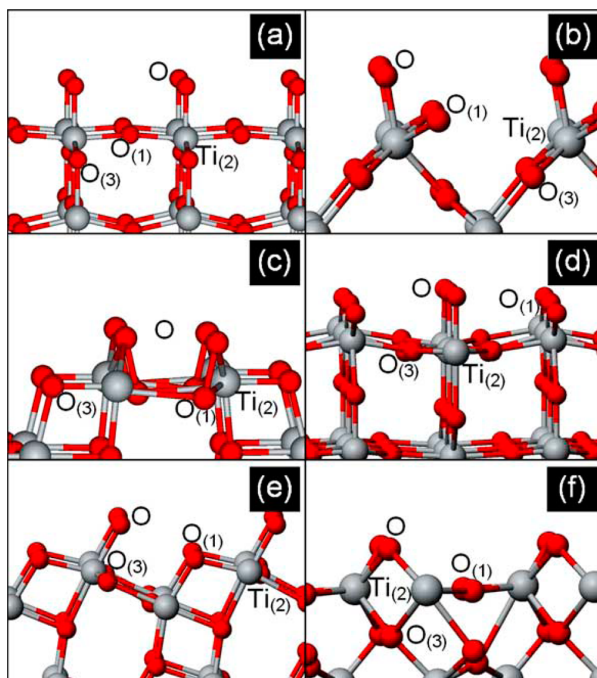


Figure 30. Relaxed low-index O-terminated stoichiometric surfaces of titanium dioxide, chosen to represent “highly basic” conditions: (a) anatase (001), (b) rutile (100), (c) anatase (100), (d) rutile (110), (e) anatase (101), and (f) rutile (011).¹⁹³ Reprinted with permission from ref 193. Copyright 2005 Elsevier.

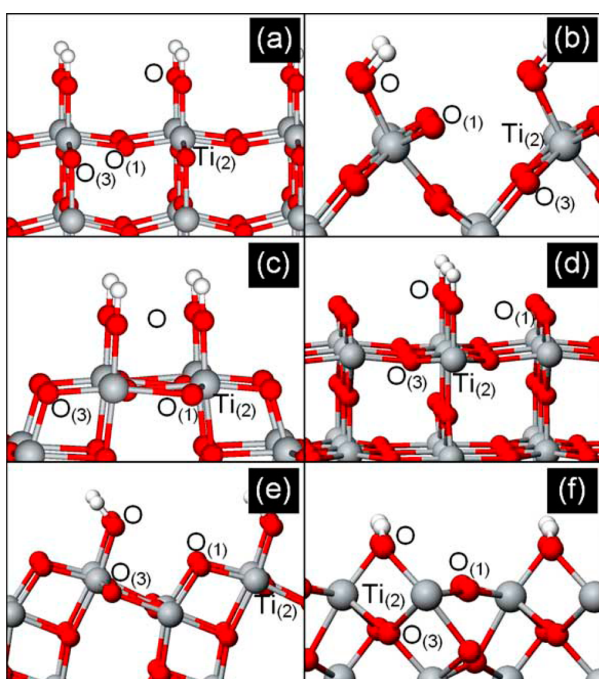


Figure 29. Relaxed low-index hydrogen-poor stoichiometric surfaces of titanium dioxide, chosen to represent “moderately basic” conditions: (a) anatase (001), (b) rutile (100), (c) anatase (100), (d) rutile (110), (e) anatase (101), and (f) rutile (011).¹⁹³ Reprinted with permission from ref 193. Copyright 2005 Elsevier.

the calculated surface free energy was obtained for the hydrated surfaces or surfaces with higher fraction of H. In contrast, the hydrogen-poor or oxygenated surfaces generally have the higher surface free energy value.¹⁹³

2.8. Recent Methods for Investigating and Manipulating the Morphology of Anatase Nanocrystals

Because the above-mentioned approaches become less reliable as the anatase crystallite size decreases, Barnard et al.¹⁹⁶ studied the structure and electronic properties of small anatase nanoparticles (105 atoms) using density functional theory as well as a self-consistent tight-binding (SCTB) method (a semiempirical method). More information about this method can be found in refs 197, 198. In DFT calculations, the initial nanocrystal structure was generated using a Wulff construction based on (101) surfaces only (bipyramidal) and surrounded by a 15 Å vacuum layer in all directions to create an isolated particle. After relaxation, the authors got again a bipyramidal nanocrystal characterized by a slight overall contraction. Concerning the SCTB method, similar results were found about the final structure and its contraction after relaxation, although some relatively small differences in the energies, geometries, and electronic properties of the nanoparticle between the SCTB and DFT methods are observed. Taking advantage of the fact that the SCTB method is much faster than the DFT one, the authors extended their study to other nanoparticles containing 99, 105, 417, 453, 495, and 1365 atoms. It is interesting that they found that some of these nanoparticles were bipyramidal and some truncated bipyramids with imperfect (001) facets truncating the two apexes of the pyramids, in general agreement with the approaches mentioned above.

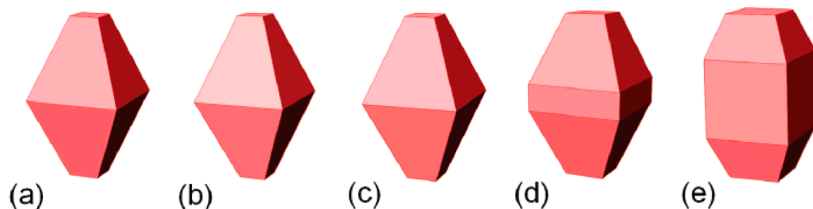


Figure 31. Morphology predicted for anatase with (a) hydrogenated surfaces, (b) hydrogen-rich surfaces, (c) hydrated surfaces, (d) hydrogen-poor surfaces, and (e) oxygenated surfaces.¹⁹² Reprinted with permission from ref 192. Copyright 2005 American Chemical Society.

Almost at the same period, Erdin et al.¹⁹⁹ extended the use of the SCTB method to study anatase nanoclusters in contact with water. The calculations showed a significant disorder and an expansion of the nanoparticle due to the presence of water molecules and a dissociation of some of these molecules close to the surface. The expansion is observed in the basal plane, and the dissociation is observed at the intersection of low-index planes of the nanocrystal surfaces. This is consistent with the increased reactivity observed in such edges (and mentioned above). Moreover, as the authors notice, it is very interesting from the catalytic point of view, because it appears that not only surface area but also the presence of defects and edges between low-index surfaces on the nanocrystals are important in the catalytic performance.

Closing this section, we should refer to a recent and very interesting work dealing with the manipulation of the morphology of anatase crystals. Yang et al.²⁰⁰ studied the anatase surface energies by performing first-principle quantum chemical calculations for a range of nonmetallic adsorbate atoms (H, B, C, N, O, F, Si, P, S, Cl, Br, I). The idea behind this was that a general approach for controlling the shape of the crystals is to grow them in the presence of species that bind with different adsorption energies to the different crystalline facets.²⁰¹ The adsorbed species affect the relative stabilities of the facets, resulting in shape that, ideally, is uniquely defined by the nature and the concentration of the adsorbate.²⁰² Using the above-mentioned thermodynamic model, they calculated an unusually high ratio B/A in the case of anatase crystals with fluorine as adsorbate atoms. This suggested that there would be a substantial increase of the fraction of (001) facets in fluorine-terminated anatase crystals. Thus, on the basis of these theoretical predictions, they synthesized uniform anatase single crystals with a high percentage (47%) of (001) facets, using hydrofluoric acid as a morphology controlling agent. A TEM image of these crystals is shown in Figure 32.

Taking into account the quite different reactivity of the (001) surface as compared to that of the dominant (101) surface, as presented in the previous sections, the crystals synthesized by Yang et al.²⁰⁰ are expected to have higher reactivity. This higher reactivity would be important in heterogeneous catalysis, where TiO_2 is widely used as an active support for transition metal particles. Moreover, these crystals may exhibit higher photocatalytic efficiency in comparison with currently used TiO_2 photocatalysts.²⁰² The question is whether these crystals can preserve their structure, morphology, and thus reactivity, even after the removal of fluoride atoms, which is necessary for use in photocatalysis or any other application. The authors suggest a simple heat treatment to clean the surfaces, without altering the crystal structure and morphology. However, as previously mentioned, the clean anatase (001) surface reconstructs, stabilizing the surface and reducing reactivity. A questionable alternative route in the aqueous environment is the

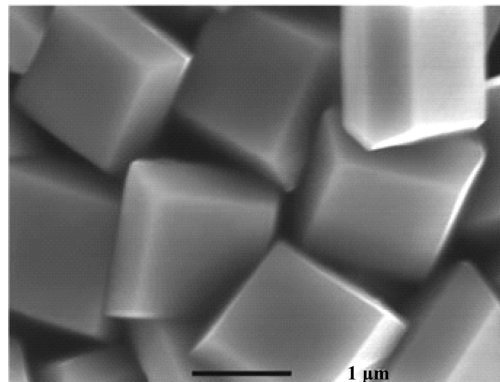


Figure 32. Anatase crystals exhibiting high percentage of (001) facets, as synthesized by Yang et al.²⁰⁰ Reprinted with permission from ref 200. Copyright 2008 Nature Publishing Group.

replacement of fluorine atoms by water or other functional moieties (e.g., photosensitizer molecules), before the surface reconstructs and thus becomes much less reactive.²⁰²

Finally, it must be mentioned that the above-described breakthrough has attracted the interest of many researchers in the direction of synthesizing and applying in various processes TiO_2 with exposed (001) facets. Yang and his coresearchers published very recently an excellent perspective article²⁰³ where they highlight the recent progress in this exciting field and mainly focus on the theoretical simulations and application explorations of the unusual properties of anatase exposed by highly reactive facets. Moreover, Liu et al.,²⁰⁴ in also an excellent concise review, presented the recent strategies for the synthesis of anatase TiO_2 micro- and nanosheets with exposed high-energy (001) facets and for the assembly of these nanosheets into various hierarchical structures. As the authors conclude, the presence of high-energy facets in titania improves significantly its adsorption, electronic, and photocatalytic properties, making this material attractive for various environmental and energy-related applications.

2.9. The (110) Crystal Face of Rutile

2.9.1. Introductory Remarks. In the above sections, we reviewed in detail the efforts done so far to investigate the structure, relaxations, and reconstructions as well as the energetics of the low-index surfaces of anatase. Moreover, we reviewed recent articles dealing with the interactions of these surfaces with adsorbed water molecules. The rather detailed presentation of these efforts was necessary because most of the main relevant articles have been very recently reported. In contrast, the most stable surface of rutile, the (110) crystal face, has been exhaustively examined in the last two decades. Most of the relevant papers have been presented in two excellent review articles published quite recently by Diebolt¹¹⁷ and Hender-

son.⁵⁹ In the former article, the structure, relaxations, reconstructions, and the energetics of the rutile (110) surface are presented in some detail, whereas in the second the interactions of this surface with the adsorbed water molecules are reviewed. Another review article reported earlier deals also with these interactions.⁸⁹ Moreover, another very interesting review article published very recently by Liu et al.⁹⁰ deals specifically with the interaction between adsorbed OH and O₂ or H₂O on TiO₂ (110) surfaces. Finally, a very recent review deals with the theoretical works concerning the low-index surfaces of titanium dioxide emphasizing the rutile (110) termination.²⁰⁵

In view of the above, we decided to present in this and the following four sections a rather concise treatment of the most important features of the rutile (110), (011), (100), (001), and (101) surfaces.

2.9.2. Surface Structure. A schematic representation of the rutile (110) ideal surface is illustrated in Figure 33. It may

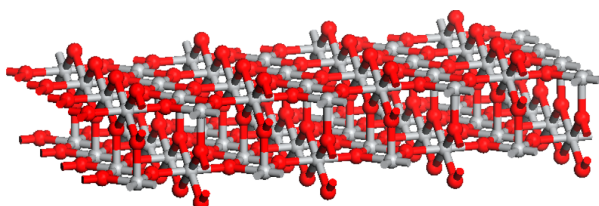


Figure 33. Schematic representation of the rutile (110) ideal surface.

be seen that on the rutile (110) surface two different kinds of Ti atoms are exposed. Rows of Ti_{6C} atoms, along the direction (001), alternate with rows of Ti_{5C} atoms having one dangling bond perpendicular to the surface. Moreover, two kinds of O atoms are exposed. Two rows of O_{3C} atoms within the main surface plane, along the direction (001), alternate with one row of O_{2C} atoms projected out of the surface plane. The O_{2C} atoms are thought to be removed relatively easily by thermal annealing resulting in point defects.

It may be, moreover, observed that the rutile (110) surface is similar to the anatase (101), also a stable surface. Thus, both surfaces have under-coordinated Ti_{5C} and O_{2C} atoms with a surface concentration of 5.2 atoms/nm². Moreover, the fully coordinated Ti_{6C} and O_{3C} atoms with a surface concentration, respectively, equal to 5.2 and 10.4 atoms/nm² make up the remainder of the sites for both surfaces. However, there are some significant differences. The anatase surface has a sawtooth profile (Figure 7a) in which the O_{2C} atoms are bound to both Ti_{5C} and Ti_{6C} atoms, while the rutile surface is flat with O_{2C} atoms bound exclusively to Ti_{6C} atoms (Figure 33). It is obvious that removal of one O_{2C} atom results in one Ti_{5C} and one Ti_{4C} atom in the case of anatase but in two Ti_{5C} atoms in rutile. Because the Ti_{4C} atoms are less stable than the Ti_{5C} atoms, the removal of O_{2C} is easier from the (110) surface of rutile. This explains why the number of oxygen vacancies observed by STM is much higher for the (110) face of rutile than for the (101) face of anatase.²⁰⁶ Xu et al. very recently proposed a new powerful method, called ultra high vacuum IR spectroscopy (UHV-FTIRS), which uses CO as a probe molecule, and they estimated the concentration of oxygen vacancies on the reduced rutile (110) surface at about 10% and on the powder rutile particles at about 8%.

2.9.3. Surface Energy. The value of surface energy calculated after relaxation for the perfect (110) crystal face of

rutile following the PBE method was found to be equal to 0.31 J/m²^{111,119} or 0.417 J/m².¹²¹ These values are lower even than the corresponding values calculated for the very stable (101) anatase surface (0.44 J/m², Table 2 or 0.495 J/m² in ref 121). In contrast, recent calculations performed by Barnard and Zapol,¹²² also after relaxation, indicate that the surface energy of the anatase (101) face (0.35 J/m² before hydration and 1.03 J/m² after hydration) is smaller than the surface energy of the (101) rutile face (0.47 J/m² before hydration and 1.08 J/m² after hydration). In addition, although Labat et al.¹²¹ found lower energy of the rutile (110) surface as compared to that of anatase using the PBE method, the order of the energy of the two surfaces was reversed when they used the HF and the LDA methods. Taking into account that the above terminations are the majority ones for anatase and rutile as well as the strong dependence of the phase stability on the surface energy at nanoscale, one may conceive why below a critical size the anatase nanocrystals are more stable than the rutile ones.¹²²

2.9.4. Modes of Adsorption of Water Molecules. Many experimental and theoretical studies, reported in the review articles mentioned above, have addressed the structure of the adsorbed water molecules on rutile (110) surface. Most experimental studies had suggested that these molecules do not dissociate on the undefective (110) surface of rutile. Water dissociation had been observed only on surface defect sites. In contrast, most theoretical studies had predicted dissociative adsorption even for the undefective (110) surface. Therefore, the situation remained controversial for years. Recently, STM experiments corroborated earlier experimental results that water dissociation takes place, in effect, exclusively on oxygen vacancies.^{208,209} This is in agreement with recent theoretical calculations, which showed that the water dissociation is exothermic on point defects (oxygen vacancies).²¹⁰

The reactivity of the undefective (110) surface would be interpreted on the basis of the structural model proposed by Henderson.²¹¹ According to this model, the water molecule is expected to be adsorbed on the Ti_{5C} surface atom with the O–H bonds pointing away from the surface. In this case, the distance between the oxygen of the adsorbed water molecule and the neighboring O_{2C} atom projected out of the surface plane is more than 3 Å. This does not allow the development of hydrogen-bonding interactions between the water hydrogen atoms and the bridging oxygen atoms. As stated in previous sections, these interactions facilitate the proton transfer, and thus it would be expected to promote water dissociation. On the other hand, the adsorption of a water molecule on Ti_{5C} atom located in an oxygen vacancy allows the development of the aforementioned hydrogen bonds, thus promoting water dissociation.

2.9.5. Recent Works Devoted to the Modes of Adsorption of Water Molecules. In two recent papers, reported after the publication of the aforementioned review articles, Bandura et al.^{65,66} studied the adsorption of water molecules on the rutile (110) surface using various theoretical methodologies. They modeled water adsorption at half-monolayer and monolayer coverage.

Concerning the first coverage, and studying first molecular adsorption, five different positions of the water molecule on the rutile (110) relaxed surface were considered. In the most stable non-dissociated state, they found that the water oxygen is coordinated to the Ti_{5C} surface atom, whereas a single H-bond is formed between a H atom in H₂O and an O_{2C} surface atom (Figure 34b), in contrast to the suggestion of Henderson

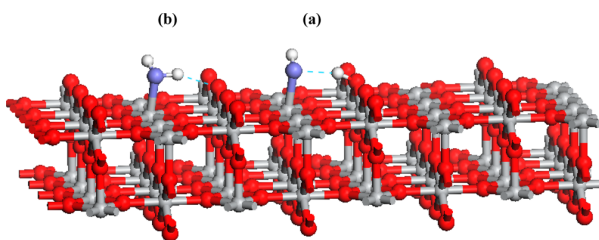


Figure 34. Representation of the structure of a water molecule adsorbed on the rutile (110) surface through (a) dissociative adsorption ($\theta = 0.5$), and (b) molecular adsorption ($\theta = 1$).^{65,66}

mentioned above.²¹¹ The adsorption energy corresponding to this state is equal to 97 kJ/mol. They found, moreover, that at half-monolayer coverage the dissociative adsorption is more favorable, than molecular adsorption, related to adsorption energy equal to 113 kJ/mol.^{65,66} In this state, the H atom is bonded to an O_{2C} atom next to the Ti atom retaining the terminal hydroxyl (Figure 34a). The neighboring hydroxyls may be configured either in a zigzag geometry or in line. In the latter case, there is the possibility of formation of H-bonds (O_{2C}—H···O_{1C}—H). Thus, the second configuration is more stable.

Going from one-half a monolayer to a monolayer coverage, the situation is changed completely. The molecular configuration described above (Figure 34b) is proved to be more stable than the dissociative one (adsorption energies of 104 and 96 kJ/mol for the molecular and the dissociative adsorption, respectively).^{65,66} This is in agreement with the experimental results mentioned above. However, in our opinion, the low difference of the adsorption energies, mainly that for the monolayer coverage, does not allow one to reach a definitive decision concerning the dissociative or nondissociative character of water adsorption on the perfect (110) rutile crystal phase. Moreover, Bandura et al.⁶⁶ calculated the charges of the bulk and surface Ti and O atoms of different coordination for the bare surface as well as for two additional surfaces resulting from the bare surface assuming dissociative and nondissociative adsorption of water molecules. On the other hand, on the basis of the aforementioned works,^{65,66} Predota et al.⁶⁷ calculated the charges localized above the surface atoms exposed by four rutile (110) model surfaces presented in the next subsections (Table 4).

Table 4. Model Rutile (110) Surfaces Studied⁶⁷

surface	ads H ₂ O on Ti _{5C}	terminal OH	unprotonated O _{2C}	protonated O _{2C}
1	144	0	144	0
2	0	144	0	144
3	108	36	144	0
4	0	144	36	108

Very recently, the same research group²¹² extended their work by studying the (110) surface of rutile with three structural layers of adsorbed water. Using ab initio molecular dynamics simulations at 280, 300, and 320 K, they studied the relation between the hydrogen bonding and the vibrational frequency spectra of the adsorbed water. They found that the first adsorbed layer consists of molecularly adsorbed water molecules above the Ti_{5C} surface atoms. These molecules form hydrogen bonds with adjacent water molecules, with O_{2C}

surface atoms, and with water molecules in the second adsorbed layer. The latter are hydrogen-bonded to the first layer adsorbed water molecules, to the O_{2C} surface atoms, and to water molecules in the third layer. The molecules of the third layer are hydrogen-bonded to other water molecules of the second or third layer. It should be mentioned that the authors determined, moreover, the strength of the above-mentioned hydrogen bonds by studying the stretching bands of the vibrational spectrum of water molecules.

In addition to the above-mentioned works, the structure and dynamics of hydration water on rutile were studied by Mamontov et al.^{213,214} using the quasielastic neutron scattering (QENS) and the new and powerful backscattering neutron spectroscopy in combination with Molecular Dynamics simulations. Their findings were in qualitative agreement with the above-mentioned works. Concerning their first article,²¹³ the MD simulations indicated three structurally distinct adsorbed water layers. The first layer (L₁) is the associated water molecules in direct contact with the surface. The second layer (L₂) is the water molecules hydrogen bonded to those of the first layer and the structural oxygen atoms of the surface. The third layer (L₃) is water molecules weakly bound to the surface. Accordingly, the QENS data indicated three hydration water diffusion components, which were attributed to various motions of the water molecules of the three layers. In their second work,²¹⁴ using the high energy resolution of a new backscattering spectrometer, they carried out QENS measurements down to 195 K. The results suggested that these experiments probe several types of molecular motion in the surface layers. More specifically, the slowest diffusion component exhibits non-Arrhenius behavior at higher temperatures and a dynamic transition at lower temperatures and originates from the translational jumps of the fully hydrogen-bonded water molecules of the L₂ layer. A faster component, which exhibited Arrhenius behavior down to at least 195 K, is attributed to the localized motions that take place in all hydration layers and require breaking fewer hydrogen bonds as compared to translational jumps. An even faster component is associated with the dynamics that take place in the L₃ layer, where the water molecules form on average only three hydrogen bonds.

Another interesting work that should be mentioned is that published by Kornherr et al.²¹⁵ The authors presented a model combining ab initio concepts and molecular dynamics simulations. Their aim was to bridge the gap between small supercells (accessible from ab initio calculations) and macroscopically observed representative surface regimes subjected to complex adsorption processes. They studied the energy, distance, and orientation of water molecules adsorbed on stoichiometric and reduced rutile TiO₂ surfaces at 140 K. They found that, on stoichiometric TiO₂, water adsorbs in two different geometries: (i) with O bound to the Ti_{5C} atoms (first monolayer) and (ii) with H bound to the O_{2C} atoms (second layer). The additional water molecules that form multilayers are not directly bound to the rutile surface and behave like those in the bulk water. In addition to the stoichiometric surface, the authors studied a weakly reduced surface by oxygen vacancies in the surface layer. This surface is shown to provide additional highly active adsorption sites (i.e., oxygen defects). As the authors claim, ab initio results showed that dissociation of water in the defect sites is even more exothermic by about 40 kJ mol⁻¹ than molecular adsorption.

Closing this subsection, we shall refer to a very interesting and integrated work on this subject published in the last years by Hammer and co-workers.^{216–219} Their work is concisely presented in a very recent article²²⁰ where they reviewed their studies and also presented some new results. They studied the interaction of water with the rutile (110) surface using STM experiments in combination with DFT calculations of low coverage water adsorption on mildly reduced and defective surfaces. From the high-resolution STM results, the following reactions have been revealed: molecular water adsorption over $\text{Ti}_{5\text{C}}$ atoms, water diffusion in the Ti troughs, dissociative water adsorption in bridging oxygen vacancies, assembly of adsorbed water monomers into rapidly diffusing water dimers, and formation of water dimers by reduction of oxygen molecules. In their recent article,²²⁰ the reader is suggested to see how interestingly the STM results were rationalized on the basis of the DFT calculations and revealed the bonding geometries and reaction pathways of the aforementioned water species.

2.9.6. The Structure of the Water Molecules in the “Rutile (110)/Electrolyte Solution Interface”. On the basis of the charges and the theoretical techniques developed in the previous works,^{65,66} Predota et al.⁶⁷ performed molecular dynamics simulations to model the “rutile (110)/electrolyte solution interface”. Concerning titanium oxide, this work can be considered as a pioneer one from the viewpoint of connection of the surface to the interface chemistry. Following the strategy adopted for the anatase, in this part we shall review their results concerning the structure of the water overlayers (this section). Their results concerning the surface charges will be presented in a common section for both rutile and anatase surfaces, whereas their results related to the location of the various cations inside the interface^{68–73} will be reviewed in the second part devoted to the interfacial chemistry.

2.9.6.1. Model Surfaces. Predota et al.⁶⁷ adopted a slab geometry with two parallel and identical surfaces based on the (110) rutile termination and water molecules (and ions if present) between them. The separation of the two surfaces was assumed to be equal to 50 Å. It was proved that it is sufficient to prevent the interference of the two identical interfaces. Thus, the properties reported are averages over both interfaces. To study the structure of the water overayers, they adopted four surfaces based on the (110) rutile termination, two neutral and two negatively charged (see Table 4).

Concerning the neutral surfaces, they adopted the perfect (110) surface, imposed to be neutral, assuming exclusively molecular adsorption of water molecules above the $\text{Ti}_{5\text{C}}$ (surface 1) and the same surface, but now assuming full dissociative adsorption of water (surface 2). Because the considered slab exposed 144 $\text{Ti}_{5\text{C}}$ and 144 $\text{O}_{2\text{C}}$ atoms, it was adopted that surface 1 is fully covered by the molecularly adsorbed water molecules over the $\text{Ti}_{5\text{C}}$ atoms, while surface 2 is fully covered by the terminal and bridging surface hydroxyls. Concerning the negatively charged surfaces they adopted, a surface originated from surface 1, but assuming that 25% of the $\text{Ti}_{5\text{C}}$ surface atoms are bonded with terminal hydroxyls instead of water molecules (surface 3), as well as a surface originated from surface 2, assuming that 25% of the $\text{O}_{2\text{C}}$ surface atoms are not protonated (surface 4). The simulations were mainly performed at room temperature assuming that 2048 water molecules are present in the whole interface. As was already mentioned, it was observed that 144 of them are adsorbed molecularly or dissociatively.

2.9.6.2. Height of the Oxygen Atoms from the Basal Plane of the Unrelaxed (110) Crystal Termination. The main goal of the study⁶⁷ was the calculation of the height of the oxygen atoms from the surface layer of the $\text{Ti}_{5\text{C}}-\text{O}_{3\text{C}}-\text{Ti}_{6\text{C}}$ atoms in the unrelaxed (110) crystal termination (Figure 33). Very recently, the theoretical results, which had been previously reported, were properly corrected.²²¹ Presenting this subsection, we have taken into account these corrections. Unlike in a vacuum, the relaxation in contact with the electrolytic solution is minimal.

The axial density profile of oxygen determined for the surfaces mentioned above shows two main peaks, one at about 2.0 Å and one at 3.8 Å. The first peak corresponds to the first layer of the adsorbed oxygen atoms, to the oxygen atoms of the terminal hydroxyls (all surfaces except surface 1) and to the oxygen atoms of the molecularly adsorbed water. The X-ray experiments⁶⁹ provided a distance equal to 2.12 Å in agreement with the theoretical results. The calculation of the number of terminal oxygens of the first layer showed full coverage, one oxygen atom per $\text{Ti}_{5\text{C}}$ surface atom. On the basis of molecular dynamics simulations, Predota et al.²²² have very recently reported that the first layer of the water molecules or hydroxyls coordinated above the $\text{Ti}_{5\text{C}}$ atoms is completely immobile at all temperatures. This was proved by the zero diffusivity and the zero streaming velocity of this layer. It should be noted that the structural $\text{O}_{2\text{C}}$ atoms are located at about 1.25 Å when unprotonated and at 1.4 Å when protonated, following the different Ti–O bond lengths. X-ray measurements⁶⁹ showed that these oxygens are located 1.17 Å from the basal plane.

The peak observed at 3.8 Å corresponds to the second layer of oxygen atoms, that is, to oxygen atoms of the second layer of the adsorbed water molecules. This was confirmed by X-ray experiments.⁶⁹ The experiments showed that these second layer adsorbed water molecules are located in ordered sites characterized as bridging between the surface oxygen sites. It was found that the number of water molecules per surface unit cell is equal to 0.92, 0.69, and 0.34 for the sites BO–TO (site between one bridging and one terminal oxygen), TO–TO (site between two terminal oxygens), and BO–BO (site between two bridging oxygens). The water molecules of the second layer interact through hydrogen bonds with the first layer of adsorbed water molecules as well as with terminal and bridging oxygens. The second layer water molecules are also immobile at room temperature, proved by the zero diffusivity and the zero streaming velocity of this layer.²²² However, it becomes increasingly mobile with increasing temperature.

In the axial oxygen distributions, additional small peaks appear: at 4.8 Å (surfaces 1 and 4), 5.8 Å (surface 4), 6.2 Å (surface 2), and around 8 Å. The structuring of the water is more pronounced for surfaces 2 and 4. In any case, the simulation results indicated that the structural properties of the water molecules become bulk like at a distance larger than 15 Å. In agreement with this finding, the diffusivity and viscosity profiles, calculated for the water molecules beyond the second layer,^{67,222} indicated an interfacial inhomogeneous region of additional 2–3 layers, where the diffusivity increases progressively with the distance from the surface, taking its bulk value at 15 Å. In fact, the calculated dynamic properties of the interface, represented by the shear viscosity and diffusivity, indicate that the bulk properties of the water molecules are recovered at a distance of 15–20 Å from the surface. However, it is significant to note that the X-ray measurements did not

provide any indication for the presence of ordered water beyond the hydration layer located at 3.8 Å.⁶⁹

2.10. The (011) Crystal Face of Rutile

2.10.1. Surface Structure, Energy, and Relaxations. An important minority orientation of the rutile nanocrystals is the (011) face. In a Wulff construction, a considerable part of the equilibrium shape crystal terminates with (011) orientation.²²³ In nano- and microcrystalline powder materials, this orientation is quite common. Nevertheless, this surface orientation has been much less studied with respect to the majority (110) surface of rutile. It exhibits an undulated topography by exposing O_{2C} atoms at the apexes, Ti_{5C} atoms, and O_{3C} atoms at valleys (Figure 35).

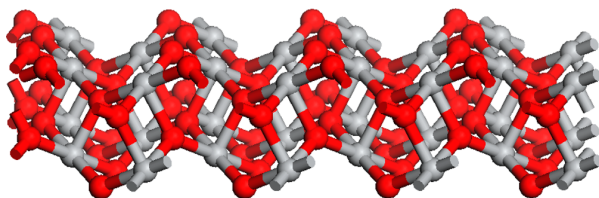


Figure 35. Schematic representation of the rutile (001) ideal surface.

Specifically, on the unrelaxed face, the Ti_{5C} atoms lie in a centered rectangular lattice with one basis vector along the (100) direction and the other along the (011). The octahedra of oxygen atoms around the Ti_{5C} are all truncated and lack an equatorial oxygen atom. The lengths of the bonds between the O_{2C} and the Ti_{5C} atoms fall into two symmetrical pairs of slightly different lengths. This creates the unmentioned topography, zigzag chains of surface oxygen atoms with the O_{2C} atoms at the highest level and O_{3C} atoms at a level below that of Ti_{5C} atoms. Thus, this arrangement makes the surface oxygen atoms lie in chains alternately along crests and troughs.^{120,223}

The relaxations of the surface Ti_{5C}, O_{2C}, and O_{3C} atoms have been studied by Ramamoorthy et al.²²³ They found that the relaxations of the Ti_{5C} atoms are in the surface plane along the (100) direction (0.4 Å) as well as along the surface normal inward (0.17 Å). This relaxation moves the Ti_{5C} atoms into the truncated oxygen octahedra. The relaxations of the surface oxygen atoms are equally distributed along the (100) and along the surface inward normal (0.14 Å). On the relaxed (011) face, the truncated oxygen octahedra around the Ti_{5C} atoms are rotated with respect to those in the bulk.²²³ The relaxations of the surface Ti_{5C}, O_{2C}, and O_{3C} atoms have been also studied by Barnard et al.¹²⁰ They found that the relaxations are dominated by outward relaxations of all atoms, in contrast to the aforementioned results of Ramamoorthy et al. (Ti_{5C}, 0.05 Å; O_{2C}, 0.09 Å; O_{3C}, 0.14 Å).

Concerning the energy of the rutile (011) face orientation, the surface energy values calculated by Barnard et al.¹¹⁹ are lower than those calculated previously by Ramamoorthy et al.²²³ More interesting are the differences reported from the above groups concerning the surface energy orders of the low-index rutile orientations (Barnard et al., (110) < (100) < (001) < (011); Ramamoorthy et al., (110) < (100) < (011) < (001)). According to the first group, the (011) face is the most unstable, whereas according to the second group the most unstable orientation is the (001). The above orders concern the unrelaxed and the relaxed surfaces as well.

2.10.2. Surface Reconstructions. The high reactivity of the (011) face is related to its reconstruction. The bulk terminated rutile (1 × 1) (011) orientation is reconstructed to (2 × 1) (011) orientation.²²⁴ The initial motivation for studying this reconstruction was related to the observation that the (011) facets of polycrystalline rutile samples are particularly active for certain photooxidations and the speculation that a particular atomic configuration on the (011) orientation affects either the efficiency for trapping photo generated carries or the rate at which they are transferred at the liquid–solid interface.²²⁵ Beck et al.²²⁴ studied this reconstruction both experimentally (STM, LEED, photoemission) and theoretically (ab initio calculations). Attempting to find out a model capable to explain their experimental observations, they performed DFT calculations constructing and optimizing different initial geometries. All resulting structures were found to have surface energies larger than the relaxed unreconstructed one. There was only one exception, that of the model proposed. This is illustrated in Figure 36a.

The main characteristic of the structure is the presence of O_{1C} atoms. The Ti–O_{1C} bond distances are 1.62 Å. Such a

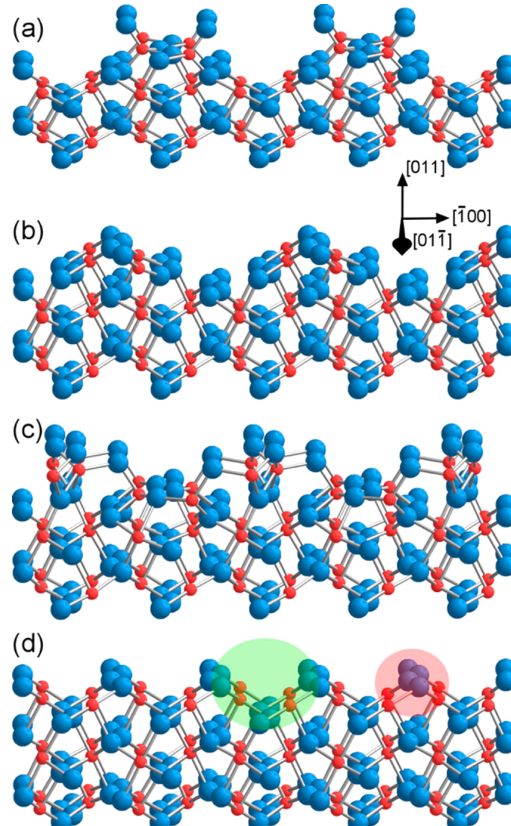


Figure 36. Ball-and-stick models of TiO₂ (011). Larger (smaller) spheres are oxygen (titanium) atoms. Parts (a) and (b) illustrate the structures proposed by Beck et al.²²⁴ and Kubo et al.,²²⁶ respectively, for the (2 × 1) reconstruction. Part (c) depicts the (2 × 1) geometry deduced in ref 227. Part (d) shows bulk-terminated TiO₂ (011) (1 × 1). The left (right) shaded area indicates the atoms lost from (1 × 1) surface during formation of (2 × 1) structure according to Beck et al.²²⁴ (Kubo et al.²²⁶). Figure is obtained from ref 227. Reprinted figure with permission from ref 227. Copyright (2008) by the American Physical Society.

distance is 0.3 Å shorter than the single Ti–O bond, suggesting the formation of a double bond $\text{Ti}=\text{O}_{\text{IC}}$. It is important to note that $\text{Ti}=\text{O}_{\text{IC}}$ groups (titanyl groups) had not been reported on the titanium dioxide surface orientations studied before the work of Beck et al.²²⁴ However, single Ti–O bonds had been reported for several Ti(IV)-containing compounds, for example, for complex oxides and titanosilicate materials.^{228,229} Moreover, such Ti–O single bonds had been reported to appear at the edges of the titanium dioxide nanoparticles.^{230,231} These bonds are frequently associated with a square -pyramidal coordination environment of Ti atoms like the topmost titanium atoms in the proposed structure. The above description refers to the so-called titanyl model (Figure 36a).

Dulub et al.²³² extended the previous study by examining the structure, defects, and impurities of the reconstructed face. The reconstructed surface was obtained upon sputtering and annealing in ultravacuum and supported by STM. The $\text{Ti}=\text{O}_{\text{IC}}$ sites were bright in empty states STM. A small fraction of the O_{IC} atoms are missing from the vacuum annealing surfaces of the bulk-reduced samples. It was found²³² that their density depends on the reduction state. Single vacancies, vacancies involving several oxygen atoms, and mainly double vacancies have been observed. The formation of defects can be suppressed by annealing a sputtered surface first in vacuum and then in oxygen. It was finally found²³² that segregation of calcium impurities from the bulk leads to an ordered over layer.

Following the work of Beck et al.,²²⁴ Kubo et al.²²⁶ studied further the reconstructed surface structure of the rutile (011) orientation using noncontact atomic force microscopy (NC-AFM), STM, and density functional calculations. NC-AFM and STM images showed that the surface exhibits row-like structures along the $(0\bar{1}1)$ direction (Figure 37).

We observe that for both (2×1) and (4×1) structures these are separated by dark rows running along the $(0\bar{1}1)$

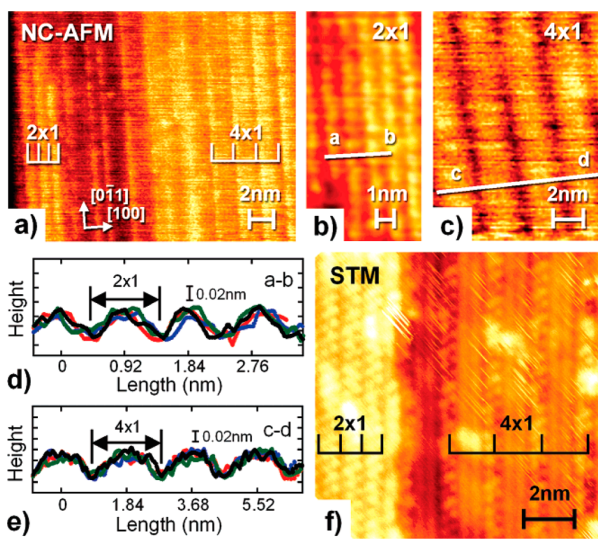


Figure 37. (a–c) NC-AFM and (f) STM images of rutile (011) after heating at 800 °C. The image sizes are (a) $25 \times 20 \text{ nm}^2$, (b) $6 \times 12 \text{ nm}^2$, (c) $8 \times 10.4 \text{ nm}^2$, and (f) $12 \times 12 \text{ nm}^2$. Height profiles along the (100) direction of the (d) (2×1) and (e) (4×1) surface structures.²²⁶ Reprinted with permission from ref 226. Copyright 2007 American Chemical Society.

directions. To explain the results of Beck et al.²²⁴ and Dulub et al.²³² as well as the NC-AFM results, they proposed microfaceting missing-row structural models in which the rows of the TiO_2 units are removed on the top of the surface (Figure 36d). In the missing rows the width of the (111) micro facets becomes wide and surface Ti_{SC} atoms are replaced by surface O_{2C} atoms.²²⁶ This is also illustrated in Figure 36b,d. The model proposed was also corroborated by DFT calculations.²²⁶

Torrelles et al.²²⁷ investigated further the geometry of the reconstructed (1×2) (011) rutile orientation using high precision surface X-ray diffraction and ab initio calculations. The experimental data were inconsistent with the previously proposed titanyl and microfaceting models.^{224,226} An entirely unanticipated geometry was emerged. The model proposed is illustrated in Figure 36c.²²⁷ According to this model, zigzag rows of O_{2C} atoms, bound asymmetrically to Ti_{SC} atoms, terminate the surface. Ab initio calculations demonstrated the energetic stability of the structure. The structure proposed does not contain titanyl groups.

The efforts for obtaining a model for the (2×1) reconstruction of the rutile (011) face were continued by Gong et al.²³³ They studied the reconstruction by using jointly DFT ab initio calculations, SXRD, and STM measurements. They identified several models by DFT calculations with much lower surface energies than the titanyl and microfaceting models mentioned above.^{224,226} The new structures proposed were tested using the aforementioned experimental techniques. The model with the lowest surface energy, similar to fully optimized brookite (001) face, was called “brookite (001)-like” model (Figure 38).

This exhibits two different structures of uncoordinated oxygen and titanium atoms. The “brookite (001)-like” model can be regarded as evolving from the titanyl model through insertion of a Ti_2O_4 unit between neighboring O_{IC} atoms. This converts the O_{IC} atoms into the more stable O_{2C} species. Moreover, it transforms the Ti_{SC} atoms in the deep valleys of

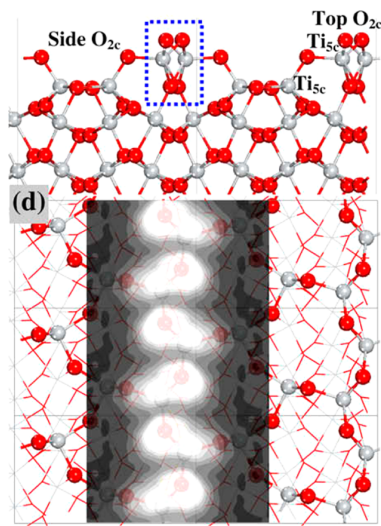


Figure 38. Side and top views (upper and lower parts, respectively) of the TiO_2 (011) (2×1) “brookite (001)-like” model. Atoms in deeper layers are represented as thin lines in the top view. The overlay shows a simulated STM image of the model.²³³ Reprinted with permission from ref 233. Copyright 2009 Elsevier.

the titanyl structure into a saturated bulk-like configuration. In the top view, the model is characterized by rings of under-coordinated surface atoms. This model is in best agreement with the SXRD results. Moreover, the calculated STM images agree with the experimental ones for appropriate tunneling conditions. We note that the structure proposed by Torrelles et al.²²⁷ and the “brookite (001)-like” model proposed by Gong et al.²³³ do not contain $\text{Ti}=\text{O}_{1\text{C}}$ groups.

2.10.3. Modes of Adsorption of Water Molecules. The effort for understanding the structure of the bulk terminated (1×1) (011) and the reconstructed (1×2) (011) rutile orientations proceeded in parallel with efforts of understanding the mode of water adsorption on these orientations. Barnard et al.¹²² reported on the water adsorption on the rutile unreconstructed (011) crystal face. They found that dissociative water adsorption is preferred. The hydrogen atoms and hydroxyl groups are bonded with the $\text{O}_{2\text{C}}$ and $\text{Ti}_{5\text{C}}$ atoms, respectively (Figure 39). It was also found that hydrogen bonds are developed between the hydrogen atoms connected to the bridging oxygens and the oxygen atoms of the OH groups (Figure 39).

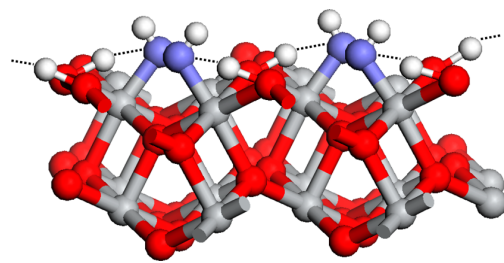


Figure 39. Dissociative adsorption of water on the (011) surface of rutile, according to Barnard et al.¹²²

Beck et al.²³⁴ and Di Valentin²³⁵ studied the water adsorption on the reconstructed (1×2) (011) rutile orientation with respect to the titanyl model described above, using DFT ab initio calculations, molecular dynamic simulations, ultraviolet photoemission spectroscopy, STM, and work function measurements. The ultraviolet photoemission experiments showed that water is absorbed in molecular form at 110 K. At the same time, the presence of 3σ state in the above spectra as well as work function measurements indicated a significant amount of hydroxyls within the first monolayer of water, indicating dissociative water adsorption in addition to molecular one. The presence of dissociative water adsorption was suggested by STM measurements performed at room temperature. These measurements indicated that about 30% of the surface sites are hydroxylated. The theoretical results confirmed the experimental observations, indicating a mixed molecular/dissociative layer at low temperatures and complete dissociation at 250 K. In the molecular adsorbed state, the water molecules are coordinated above the $\text{Ti}_{5\text{C}}$ atoms, whereas in the dissociative adsorption state the hydrogen atoms are bonded with the oxygen titanyl groups and the hydroxyl groups with the surface $\text{Ti}_{5\text{C}}$ atoms (Figure 40). Hydrogen bonds are developed between the adsorbed species (Figure 40).

He et al.²³⁶ studied the adsorption of water molecules on the reconstructed (1×2) (011) rutile orientation with respect to the “brookite (001)-like” model mentioned above, using STM and DFT ab initio calculations. The model proposed is

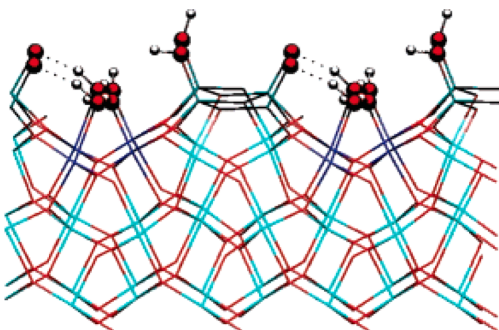


Figure 40. Calculated structure of one monolayer of water adsorbed on the (2×1) reconstructed rutile (011) surface (with respect to the titanyl model described above): mixed (molecular and dissociated) state.²³⁵ Reprinted with permission from ref 235. Copyright 2005 American Chemical Society.

illustrated in Figure 41.²³⁶ According to this model, water molecules are adsorbed weakly, through hydrogen bonds, on

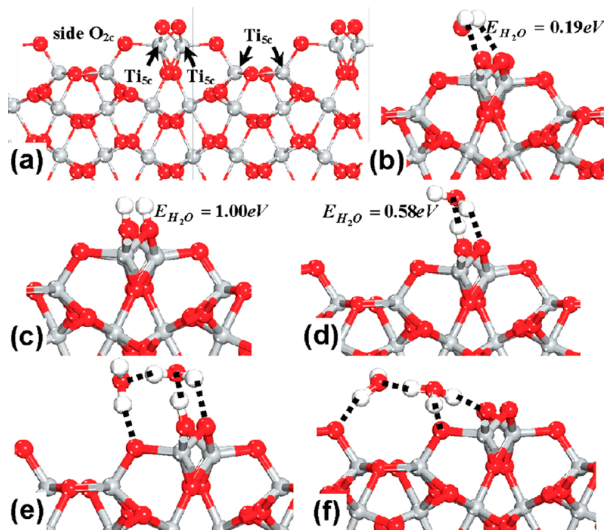


Figure 41. Calculated structures of the “brookite (001)-like” model of the rutile (011) (2×1) surface: (a) clean surface, (b) with a single adsorbed H_2O , (c) with paired hydroxyls from dissociated water at a top O vacancy, (d) a single and (e) two water molecules attached to the surface hydroxyl, and (f) a complex containing H_3O^{+} species. The dashed lines represent the H-bonds.²³⁶ Reprinted with permission from ref 236. Copyright 2009 American Chemical Society.

the stoichiometric nondefective face (Figure 41b). In contrast, dissociative adsorption occurs on a defective “brookite (001)-like” model face with oxygen vacancies (Figure 41c). The hydroxyls that resulted from this mode of adsorption act as nucleation sites for the growth of hydrogen-bond water clusters. These clusters are arranged in one dimension (Figure 41d–f).

2.11. The (100) Crystal Face of Rutile

2.11.1. Surface Structure, Energy, Relaxations, and Reconstructions. The rutile (1×1) (100) surface orientation exhibits a corrugated structure. It is more corrugated than the (110) orientation. It contains $\text{Ti}_{5\text{C}}$ atoms in the center of oxygen truncated octahedra, ridges of $\text{O}_{2\text{C}}$ atoms in the uppermost layers ((100) direction), and $\text{O}_{3\text{C}}$ atoms at a level

lower than that of the $\text{Ti}_{5\text{C}}$ atoms (Figure 42). This face looks like a periodic array of ridges and troughs parallel to the (001)

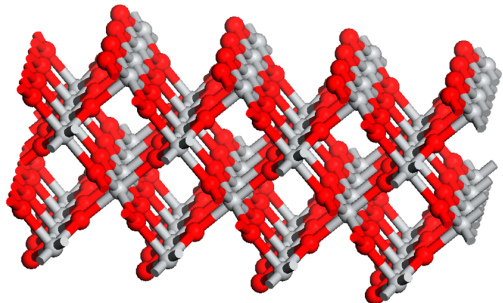


Figure 42. Schematic representation of the rutile (100) ideal surface.

direction. The surface unit cell is rectangular, with axes along bulk (010) and (001) directions. There is one TiO_2 unit per surface unit cell. The structure is consistent with LEED, ASTM, and noncontact AFM images.^{117,237–239}

Several earlier papers have been reported on the relaxations of this orientation.^{117,223,240,241} According to Ramamoorthy et al.,²²³ the dominant relaxations are along the (010) axis. The $\text{Ti}_{5\text{C}}$ and $\text{Ti}_{6\text{C}}$ atoms move, by 0.32 \AA , in opposite directions with respect to $\text{O}_{2\text{C}}$ and $\text{O}_{3\text{C}}$ atoms. Considerable inward relaxation occurs for the $\text{Ti}_{5\text{C}}$ atoms in the direction normal to the surface (0.14 \AA), whereas the relaxation is negligible for the oxygen atoms in this direction (0.01 \AA for the $\text{O}_{2\text{C}}$ and 0.03 \AA for the $\text{O}_{3\text{C}}$ atoms). The inward relaxation of the $\text{Ti}_{5\text{C}}$ atoms enables these atoms to sink below the equatorial plane of the truncated oxygen octahedra and shorten their bonds with the apical oxygen atoms lying below the surface. Purton et al.²⁴⁰ found similar trends for the relaxation. According to their calculations, the surface oxygen atoms relax toward the exposed surface, while the titanium atoms move into the bulk to increase their coordination and shielding. Rather different results have been reported more recently by Barnard et al.¹²² They reported rather negligible upward relaxations for the $\text{Ti}_{5\text{C}}$ atoms (0.06 \AA) and larger upward relaxations for the oxygen atoms (0.16 \AA for the $\text{O}_{2\text{C}}$ atoms and 0.15 \AA for the $\text{O}_{3\text{C}}$ atoms).

In a more recent paper, Labat et al.¹²¹ found that the largest relaxations occur along the (010) direction in the outermost plane with $\text{Ti}_{5\text{C}}$, $\text{O}_{2\text{C}}$, and $\text{O}_{3\text{C}}$ atoms moving in opposite directions. Furthermore, it was found an inward relaxation along the (100) direction for the $\text{Ti}_{5\text{C}}$ atoms, while $\text{O}_{2\text{C}}$ atoms relax outward. These relaxations result in an increase of the $\text{Ti}_{5\text{C}}$ coordination.

In addition to the rutile (1 \times 1) terminated (100) face, a rutile reconstructed (100) face, (1 \times 3), is formed upon annealing to high temperatures in UHV.¹¹⁷ Photoemission experiments have shown that this surface is partially reduced.^{117,242–245} A microfaceting model was developed to describe the rutile (100)-(1 \times 3) surface. A lot of experimental and theoretical works have been devoted to this reconstruction. These have been reviewed in detail by Diebold.¹¹⁷ As the adsorption of water molecules, presented in the next paragraphs, concerns almost exclusively the rutile (100) unreconstructed termination, we do not deal further with the rutile (100)-(1 \times 3) surface.

2.11.2. Modes of Adsorption of Water Molecules. The first papers dealing with the adsorption of water molecules on

the rutile (100) termination were reported by Lo et al.²⁴² and Suda and Morimoto.²⁴⁶ The experimental study of Lo et al.²⁴² used UPS, ELS, AES, and LEED techniques. It was concluded that water is adsorbed associatively on the stoichiometric (1 \times 3)-(100) rutile surface. In contrast, the water adsorption tends to be dissociative on a surface rich in Ti^{3+} ions.

The experimental study of Suda and Morimoto²⁴⁶ was performed using polycrystalline rutile and IR data. The sample was saturated by water vapor for establishing complete surface hydration. The IR spectra were obtained after degassing the sample disc at various temperatures in a vacuum of 1.33 mN m^{-2} for 4 h. The results obtained have corroborated the presence of molecularly adsorbed water on the rutile surface. On the basis of the above IR results and simple crystallographic data, including the geometry of the more important rutile terminations, they attempted to deduce a model for the adsorption of the water molecules on the rutile (100) crystal face. They supported the view for molecular adsorption of the water molecules on this crystal face. According to the model proposed on the basis of the aforementioned empirical approach, the water molecule is coordinated to the $\text{Ti}_{5\text{C}}$ atoms through oxygen. The hydrogen atoms of the coordinated water molecule form hydrogen bonds with the adjacent oxygen atoms. Thus, the oxygen atoms of the coordinated water molecules present 3-fold symmetry, as in the bulk crystal.

A theoretical investigation of water adsorption on titanium dioxide low-index surfaces was performed by Fahmi and Minot using a periodic Hartree–Fock method.²⁴⁷ Concerning the rutile (100) termination, it was concluded that both molecular and dissociative adsorption may occur. The energy of adsorption for the dissociative adsorption is slightly larger than that for the molecular adsorption ($1.8 \text{ kcal mol}^{-1}$). Thus, molecular adsorption becomes competitive with the dissociative one. This is due to hydrogen bonding, which is particularly important for molecular adsorption on the rutile (100) face. More precisely, they concluded that in the molecular adsorption one of the hydrogen atoms of the coordinated water molecule above a $\text{Ti}_{5\text{C}}$ atom is bonded with two adjacent oxygen atoms through hydrogen bonds.²⁴⁷ In this structure, this hydrogen atom is tricoordinated. This structure for the associatively adsorbed water is slightly different from that proposed by Suda and Morimoto.²⁴⁶ Concerning the slightly more favorable dissociative adsorption, it was inferred that a hydroxyl group is coordinated above a $\text{Ti}_{5\text{C}}$ atom and a proton above an $\text{O}_{2\text{C}}$ atom. Hydrogen bonds are developed between the hydrogen of the coordinated hydroxyl and the adjacent oxygen atoms. We note that molecular adsorption had been reported in experimental studies.^{242,246}

Ferris and Wang performed electronic structure calculations for the water adsorption on the rutile (100) surface.²⁴⁸ Their calculation results corroborated the view that water dissociation is favored. On the basis of the reaction coordinate for proton transfer, they were able to provide the reason for the water dissociation, in addition to the thermodynamic predictions.

A theoretical study for the water adsorption on the rutile (100) face has been reported by Langel²⁴² following a Car–Parrinello simulation methodology. He found that water is adsorbed associatively on the rutile nondefected (100) termination, forming a strong bond between the water oxygen and the $\text{Ti}_{5\text{C}}$ atoms. The hydrogens of the coordinated water form hydrogen bonds with the adjacent $\text{O}_{2\text{C}}$ atoms. In contrast, water is adsorbed dissociatively on the partially reduced rutile (100) termination in which oxygen vacancies are generated by

omitting one oxygen atom of four bridging oxygen atoms in the simulation cell. A water molecule in such a defect dissociates spontaneously within 0.3 ps. Thus, one single and one bridged hydroxyl group are formed (Figure 43).⁶² The hydrogen atoms

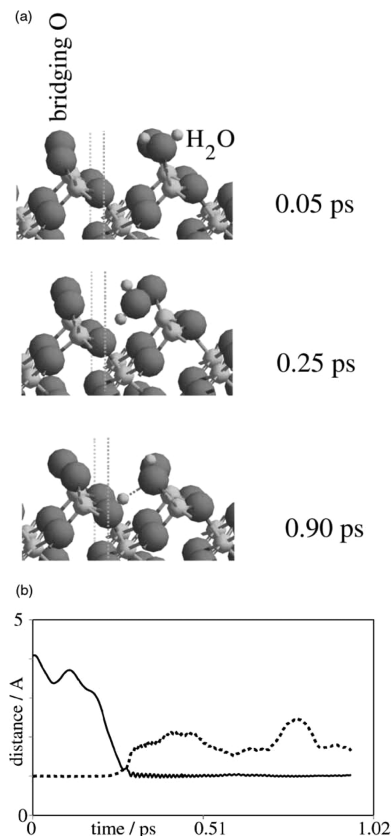


Figure 43. Dissociation of water in an oxygen vacancy on the partially reduced rutile (100) termination: (a) (from top) starting configuration, activated complex, and final state, (b) lengths of the opening (dashed line) and closing (solid line) O–H bonds as a function of time. The closed bond is vibrationally excited showing rapid oscillations in length.⁶² Reprinted with permission from ref 62. Copyright 2002 Elsevier.

on the simulation cell correspond to 3.8 hydroxyl groups/nm². In contrast, previous experimental data had indicated that 7.5 hydroxyl groups/nm² or 4 hydroxyl groups in the cell are possible. Such a high coverage may be generated by replacing

two O_{2C} atoms in the second row by the hydroxyl groups and inserting the water into the oxygen vacancy.

In a recent theoretical study, Barnard et al.¹²² concluded that the (100) surface prefers dissociative adsorption of water molecules. According to the proposed structure, the oxygen of a coordinated hydroxyl above a Ti_{5C} atom forms a weak hydrogen bond with the hydrogen atom connected with an adjacent O_{2C} atom.

In the context of a study devoted to the surface stress of rutile (110) and (100) surface terminations and the effect of water adsorbent, Kamisaka and Yamashita²⁴⁹ calculated the adsorption energies for three optimized adsorbed states of water molecules, molecular and dissociated water adsorption on the rutile nondefected (100) termination as well as dissociated water adsorption on a defect (100) structure above an oxygen vacancy. On the basis of the calculated adsorption energies, one may conclude that molecular adsorption is preferred on the nondefected surface, whereas the dissociated adsorption above an oxygen vacancy is the most favorable among the structures studied.

From the above considerations, we see that the mode of water adsorption on the rutile nondefective (100) surface is rather controversial; several studies favor molecular adsorption,^{62,242,246,249} some others dissociative adsorption,^{122,248} and one work both molecular and dissociated adsorption.²⁴⁷ For the defected (partially reduced) structures with oxygen vacancies, there is a general agreement for dissociative adsorption of water molecules.^{62,242,249} Despite the disagreement for the mode of the water adsorption on the nondefective (100) surface, there is a good agreement (with the exception of Fahmi and Minot²⁴⁷) concerning the surface structure of the rutile (100) termination after the associatively or dissociatively adsorbed water. Figure 44 illustrates the relevant structures.

2.12. The (001) Crystal Face of Rutile

2.12.1. Surface Structure, Energy, Relaxations, and Reconstructions.

This crystal termination is of choice for electrochemical studies as the electrical conductivity is the highest along the (001) direction.¹¹⁷ This is perhaps one of the reasons for which several studies reported in the past have dealt with this face. The structure of the rutile (001) surface is illustrated in Figure 45. We observe that the unrelaxed surface is rather flat. All of the surface titanium atoms are 4-fold coordinated (Ti_{4C}), and all of the surface oxygen atoms are 2-fold coordinated (O_{2C}).^{117,120,223,239,240,250} For this reason, the number of broken bonds in this surface is higher as compared to the titanium dioxide faces studied in the previous sections. On the unrelaxed surface, each Ti_{4C} atom is bonded to two oxygen atoms in its plane and to two oxygen atoms in the layer below the surface. The former bonds are 2% longer than the

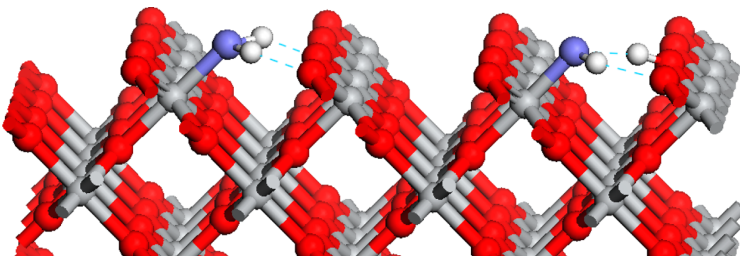


Figure 44. Representation of the structure of two water molecules adsorbed on the rutile (100) surface: (left) associative adsorption,^{62,242,246,247,249} (right) dissociative adsorption.^{122,247,248}

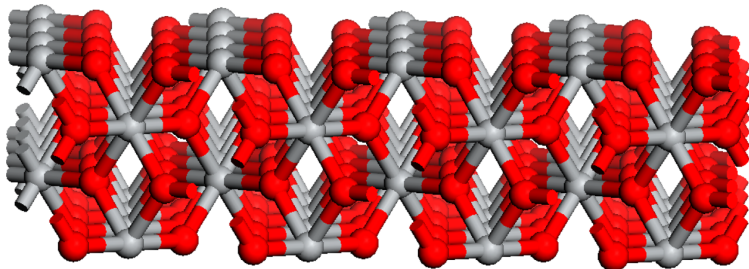


Figure 45. Schematic representation of the rutile (001) ideal surface.

later. The oxygen octahedra around the surface Ti_{4C} atoms have their equatorial planes perpendicular to the surface, and they are truncated.

The relaxation of the title face has been first studied by Ramamoorthy et al.²²³ Upon relaxation the surface, Ti_{4C} atoms move inward by 0.60 Å, while the Ti_{6C} atoms of the layer below move toward the surface by the same distance. These relaxations are a very significant fraction of the interlayer spacing of the unrelaxed surface and decay slowly with the distance below the surface. The relaxations of the oxygen atoms are relatively small. The relaxations mentioned above for the titanium atoms pucker the surface and lessen the O_{2C} atoms at the topmost level on the surface. The above results are very similar, although not identical, to those reported later by Barnard et al.,¹²⁰ who reported an inward relaxation for the surface Ti_{4C} atoms by 0.31 Å. The general trends of the relaxation results are also similar to those calculated by Muscat and Harrison²⁵⁰ using HF approximation and Schelling et al.¹⁹⁸ The relaxed (001) surface proposed by Barnard et al.¹²⁰ is illustrated in Figure 46. Labat et al.¹²¹ in a more recent paper

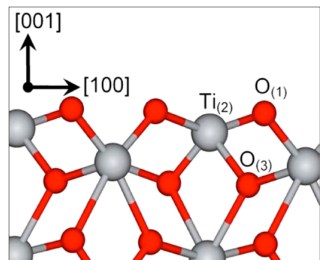


Figure 46. Relaxed rutile (001) surface proposed by Barnard et al.¹²⁰ Reprinted figure with permission from ref 120. Copyright (2004) by the American Physical Society.

found a similar downward relaxation for the surface Ti_{4C} atoms by 0.28 Å, with O_{2C} atoms moving laterally by 0.10 Å toward it. Purton et al.²⁴⁰ was the only study that found very small relaxations for both titanium and oxygen surface atoms.

The number of broken bonds in the rutile (001) face should be related to its high surface energy. This is confirmed by ab initio calculations; as was already mentioned in a previous section, there is no agreement concerning the relative stability of rutile (001) and (011) faces. Ramamoorthy et al.²²³ proposed the order $(110) < (100) < (011) < (001)$, whereas Barnard et al.¹²⁰ the order $(110) < (100) < (001) < (011)$. According to the first group, the (001) face is the most unstable, whereas according to the second group the most unstable orientation is the (011). In any case, the rutile (001) face is more unstable as compared to the rutile (110) and (100)

terminations. This is also in line with the surface energies calculated by Muscat et al.^{241,250,251} and Schelling et al.¹⁹⁸ More recently, Labat et al.¹²¹ confirmed the above-mentioned order for the (110), (100), and (001) rutile surfaces.

The high surface energy of the rutile (001) face would justify that this face does not belong to the three major faces present in the nanoparticles of powdered samples. Moreover, this justifies why this face tends to facet or reconstruct. Several studies have been devoted to reconstructions.^{252–258} Several facets have been identified using various experimental techniques (LEED, STM, AFM) for samples prepared using various methods (e.g., heating at various temperatures).^{252–258} The subject has been critically reviewed by Diebold.¹¹⁷

2.12.2. Modes of Adsorption of Water Molecules.

Studies directed to the adsorption of water molecules on the rutile (001) termination are rather scarce in the literature.^{247,259} Smith and Bernasek²⁵⁹ studied the adsorption of water on the rutile (001) termination using UPS, AES, ELS, and LEED. The study was performed on a rutile stoichiometric, well annealed (001) low temperature facet as well as on Ar^+ bombarded rutile (001) surfaces. It was found that water adsorbs dissociatively on the Ar^+ bombarded and nonbombarded surface.²⁵⁹ The authors attributed the high reactivity of the rutile (001) termination, as compared to that of (101) and (100) faces, to the excess of bonding sites and the greater Ti^{3+} ($3d^1$) availability relative to the aforementioned faces. It was inferred that Ti^{3+} surface atoms are involved in the dissociative adsorption of water. It was moreover found that reoxidation of the reduced surface sites occurs upon water adsorption.²⁵⁹

Fahmi and Minot²⁴⁷ studied the adsorption of water molecules on the title surface using a periodic Hartree–Fock method. It was found that water is adsorbed dissociatively. In fact, the calculated energy for the molecular and dissociative adsorption was found to be 34.07 and 77.77 kcal mol⁻¹, respectively. The oxygen of a surface hydroxyl forms a strong covalent bond with a Ti_{4C} surface atom. In the best configuration, the proton is asymmetrically bridging two surface oxygen atoms. It is bound to one of them and forms a hydrogen bond with the other one. The dissociative adsorption of the water molecules and the strong bond $Ti_{4C}–O$ were attributed to the poor coordination of the surface titanium atoms as compared to other terminations. A schematic representation of the dissociative adsorption of water molecules on the unrelaxed rutile (001) termination is illustrated in Figure 47.

2.13. The (101) Crystal Face of Rutile

The rutile (101) termination is the third face occurring naturally in rutile powder for about 20%. However, it is much less studied than the other low-index faces of rutile. Its structure is illustrated in Figure 48. It looks like the (100) termination.

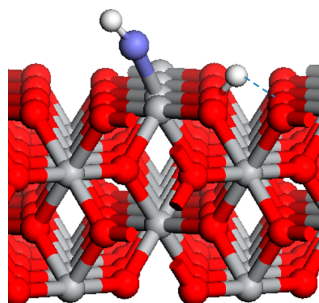


Figure 47. Representation of the structure of a water molecule adsorbed on the unrelaxed rutile (001) surface through dissociative adsorption.²⁴⁷

We observe that it exhibits two kinds of surface atoms, Ti_{5C} and O_{2C} atoms. Each O_{2C} atom is bonded to two Ti_{5C} atoms by two different bond lengths. The optimized $Ti-O$ bond lengths on this surface are very different from those of the bulk.²³⁹ More precisely,²⁶⁰ the title termination has Ti_{5C} atoms interconnected at the surface by two O_{2C} atoms. The Ti_{5C} atoms sit at the base center of TiO_5 square pyramids tilted from the surface normal. The $-O-Ti-O-Ti-$ chains that define the (101) surface are arranged in zigzag rows along the (101̄) direction, giving the TiO_5 square pyramids alternating tilt directions. The truncated octahedra that make up these (101) surface chains have alternately missing long and short $Ti-O$ bonds, originally axial and equatorial local directions in the bulk.²⁶⁰

Perron et al.²³⁹ calculated the surface energy values for four rutile terminations ((110), (100), (101), and (001)) using three different pseudo potentials, and they found the following order: (110) < (100) < (101) < (001). This means that the (101) termination is less stable than the (110) and (100) ones but more stable than the (001) termination. Taking into account that the energy calculated for (001) is similar to that calculated for the (011) (see section 2.10.1), it may be inferred that the (101) face is more stable than the (011) one. The relative stabilities of the above surfaces can be explained in terms of their unsaturation. The more the surface is unsaturated, the less it is stable. More specifically, a nearly linear correlation between the surface energies of the rutile low-index faces and their respective unsaturation has been reported.²³⁹ The unsaturation density was defined as the number of broken bonds per nm^2 of surface titanium and oxygen atoms relative to their bulk coordination (six and four for titanium and oxygen atoms, respectively). The values obtained for the (110), (100), (101), and (001) surfaces are, respectively, equal to 10.23, 14.47, 15.59, and 18.5, respectively.²³⁹

Works dealing with the adsorption of water on the rutile (101) surface are practically not reported in the literature. An

early work has been reported by Suda and Morimoto²⁴⁶ who studied the adsorption of water molecules on the (110), (100), and (101) terminations using polycrystalline rutile and IR data. The experimental details of this work were presented in the section dealing with the adsorption of the water molecules on the rutile (100) face. Concerning the (101) termination, they supported the view for molecular adsorption. According to the model proposed, the water molecule is coordinated to a Ti_{5C} atom through oxygen. The hydrogen atoms of the coordinated water molecule form hydrogen bonds with the adjacent oxygen atoms. Thus, the oxygen atoms of the coordinated water molecules present 3-fold symmetry, as in the bulk crystal. Figure 49 illustrates a schematic representation of a water

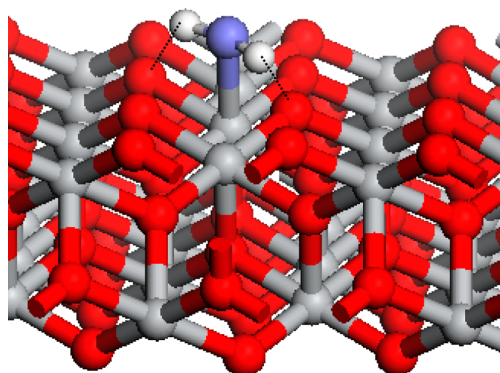


Figure 49. Representation of the structure of a water molecule adsorbed on the rutile (101) surface through molecular adsorption.²⁴⁶

molecule adsorbed molecularly on the rutile (101) termination. This must be considered as a tentative structure. Much more work is required to establish the mode of water adsorption on this termination.

2.14. Surface Chemistry and Morphology of the Rutile Nanocrystals

This section deals with the relation between surface chemistry and morphology of the rutile nanocrystals. The Wulff construction for rutile predicts a tetragonal prism bounded by the (110) surfaces and terminated by a pair of tetragonal pyramids bounded by (011) surfaces.¹²² Obviously, the variable A/B (Figure 50) expresses the “aspect ratio” of the rutile shape. At macroscale the shape of rutile may vary “from long acicular crystals to a short blocky habit”.¹²² The model developed by Barnard and Zapoli¹⁸⁵ has been also applied to study the rutile morphology at nanoscale.^{120,122,191} By expressing all of the geometric parameters, such as the volume and surface area of the various crystal faces, in terms of the ratio A/B , the energy was minimized with respect to this variable.

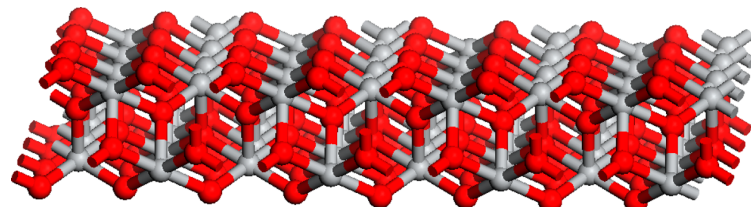


Figure 48. Schematic representation of the rutile (101) ideal surface.

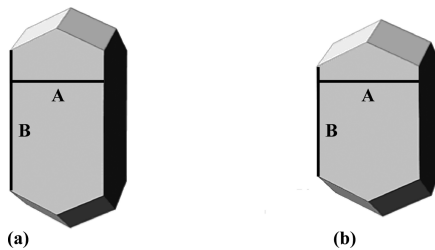


Figure 50. Effect of hydration on the morphology of the rutile nanocrystals calculated according to the model developed by Barnard and Zapol.¹⁸⁵ (a) morphology before hydration, (b) morphology after hydration.¹²² Reprinted with permission from ref 122. Copyright 2005 American Chemical Society.

In contrast to that mentioned in a previous subsection for the anatase, no lower energy shape was found than that predicted by the Wulff approach. This indicates that the Wulff construction prevails even at nanoscale. The optimization of rutile shape is quite complicated because B has no upper bound. Thus, B could increase rapidly with respect to A , producing long needlelike crystals but with higher energy per TiO_2 unit than the Wulff construction. Finally, it was found that the presence of water reduces the aspect ratio A/B . This is illustrated in Figure 50.

Barnard et al.¹²⁰ continued their studies on the shape of the rutile nanocrystals by investigating the influence of the hydrogenation of the basic surface orientation of rutile nanocrystals on their shape. As in the case of anatase, the analysis was based on the minimization of the surface energy of basic faces of the rutile nano crystals ((110), (100), (011)) for clean, partially, and fully hydrogenated surfaces (Figures S1–S4).¹²⁰ In the case of partially hydrogenated surfaces, the hydrogen atoms are located above the $\text{O}_{2\text{C}}$ atoms, whereas in the case of the fully hydrogenated surfaces, the hydrogen atoms are located above both the $\text{O}_{2\text{C}}$ and the $\text{Ti}_{5\text{C}}$ atoms.

The study predicts that the aspect ratio increases with hydrogenation and the rutile nanocrystals become squatter as

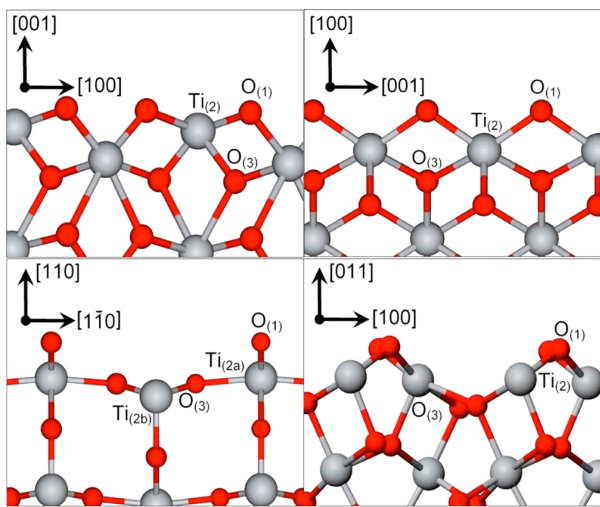


Figure 51. Relaxed rutile (001) surface (top left), (100) surface (top right), (110) surface (lower left), and (011) surface (lower right).¹²⁰ Reprinted figure with permission from ref 120. Copyright (2004) by the American Physical Society.

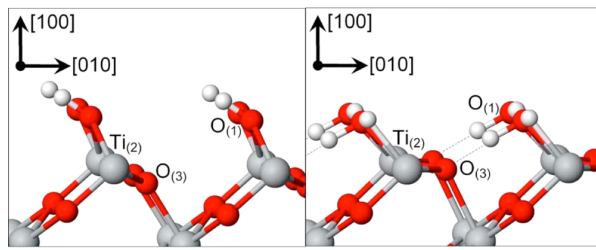


Figure 52. Relaxed, partially hydrogenated rutile (100) surface (left) and fully hydrogenated (100) surface (right).¹²⁰ Reprinted figure with permission from ref 120. Copyright (2004) by the American Physical Society.

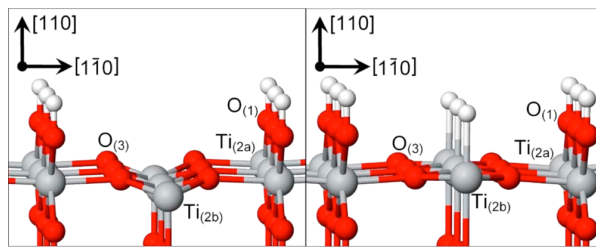


Figure 53. Relaxed, partially hydrogenated rutile (110) surface (left) and fully hydrogenated (110) surface (right).¹²⁰ Reprinted figure with permission from ref 120. Copyright (2004) by the American Physical Society.

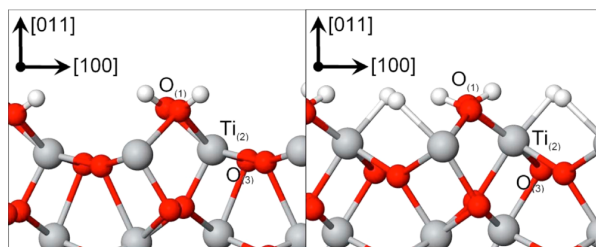


Figure 54. Relaxed, partially hydrogenated rutile (011) surface (left) and fully hydrogenated (011) surface (right).¹²⁰ Reprinted figure with permission from ref 120. Copyright (2004) by the American Physical Society.

the coverage by hydrogen is increased. This is an example demonstrating how the shape of the rutile nanocrystals is affected by the chemical environment, by the extent of hydrogenation of the surface.

In a previous section (2.7.3), we presented the theoretical studies of Barnard et al. on the morphology of the anatase nanoparticles in relation to the solution pH, recorded upon the generation-growth of the anatase nanocrystals via the sol–gel synthesis. A similar study was applied for the rutile nanocrystals.^{192,193} They calculated the surface relaxation, energy, and stress for each of the above-mentioned surface chemistries of low-index surfaces of rutile, (110), (100), and (011). The surface chemistry in each case is illustrated in Figures 26–30. Using these data, they predicted the morphology of the rutile nanoparticles for each surface chemistry and for a constant size of the nanoparticles (side length $A \leq 15 \text{ nm}$).¹⁹² The effect of surface chemistry upon the shape of the rutile nanoparticles is illustrated in Figure 55.¹⁹²

We observe that the application of highly acidic conditions increases the aspect ratio of the rutile nanoparticles with respect

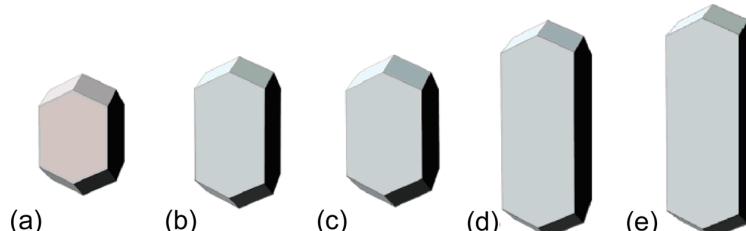


Figure 55. Morphology predicted for rutile with (a) hydrogenated surfaces, (b) hydrogenrich surfaces, (c) hydrated surfaces, (d) hydrogen-poor surfaces, and (e) oxygenated surfaces.¹⁹² Reprinted with permission from ref 192. Copyright 2005 American Chemical Society.

Table 5. Charge Localized above Each Surface Atom (e), the Charge Density Due to Its Kind of Atoms (e/nm, Second Figure), and the Total Charge Density of Each Anatase and Rutile Surface Studied (e/nm)¹⁰²

surface	Ti _{6C}	Ti _{5C}	Ti _{4C}	O _{3C}	O _{2C}	charge density
(101)	1.28/6.66	1.36/7.07		-0.70/3.64	-0.59/3.07	7.02
(100)	1.27/7.11	1.27/7.11		-0.62/6.92	-0.50/2.8	4.50
(001)		1.29/9.03		-0.67/4.69	-0.66/4.62	-0.28
(110)	1.26/9.95		1.36/5.37	-0.67/5.29	-0.64/5.06	4.98
(103) _f	1.29/4.64	1.34/9.65		-0.72/7.7	-0.6 ^a /2.16	2.09
(110) rut	1.23/	1.27/		-0.67/	-0.49/	3.48

^aIn the (103)_f, there are two kinds of surface O_{2C}. The figures for the one kind are illustrated in the table, whereas the corresponding figures for the other kind are equal to -0.65/2.34. Both figures were taken into account to calculate the total charge density of this surface.

to the shape predicted for the neutral conditions, namely with respect to the hydrated rutile surfaces. In contrast, the application of moderately or highly basic conditions, resulting in hydrogen-poor or oxygenated surfaces, decreases considerably the aspect ratio, leading to more elongated rutile nanoparticles. It is remarkable that the lowest value for the calculated surface free energy was obtained for the hydrated or hydrogenated surfaces. In contrast, the hydrogen-poor or oxygenated surfaces generally have the higher surface free energy value.¹⁹³

2.15. Charges Localized above the Surface Atoms Exposed by the Anatase and Rutile Surfaces Studied

As was already mentioned in the "Introduction", a very useful property of a surface that bridges the surface and the interface chemistry is the development of electrical charge on it, both before and after hydration. The charge causes the development of a potential, which, in turn, provokes the accumulation of ions with opposite charge close to the surface leading to the development of the interface. The latter is a very interesting region because inside the interface extremely critical processes for many applications take place, such as the synthesis of the supported catalysts. It is thus useful to know: (i) the charge localized on surface atoms exposed by the titanium oxide surfaces studied herein, (ii) the whole charge density of each surface, and (iii) the contribution to the latter of the charge density of each kind of surface atoms exposed by the surface in question. These parameters have been recently calculated by us in the context of the Density Functional Theory for the relaxed titanium oxide surfaces¹⁰² and are compiled in Table 5.

Inspection of this table shows that positive (negative) charge is localized above the Ti (O) surface atoms. For the same surface, the positive charge localized above the Ti_{5C} atoms is higher than that localized above the Ti_{6C} ones. Moreover, it may be seen that for the same surface the negative charge of the O_{3C} atoms is higher than that of the O_{2C} ones, because the former are surrounded by a greater number of Ti atoms, which have relatively low electronegativity as compared to the oxygen

atoms. It may be, moreover, seen that the charge above a certain kind of atoms does not considerably change from surface to surface, and this concerns even the (110) of rutile. Finally, it may be observed that only the (001) surface of anatase exhibits negative charge density.

The previous works provided the surface charge of the O_{2C} surface atoms, which is very useful for modeling the protonation/deprotonation equilibrium of these atoms when titanium oxide is in contact with an electrolytic solution (next part). For modeling this equilibrium for the O_{1C} terminal atoms, produced after the dissociation of the water molecules above the Ti_{5C} surface atoms of the surfaces studied, an estimation of their charge would be also useful. Following the procedure mentioned above, a value equal to -0.33 was found for the (101) termination of anatase.¹⁰² Taking into account the above considerations, this value seems reasonable as compared to the values illustrated for the O_{2C} and O_{3C} surface atoms. The above calculations were performed for the nonhydrated relaxed surfaces, in the framework of plane wave pseudopotential density functional theory (DFT) and assuming electrical neutrality for the whole slab of a given TiO₂ termination containing several layers.¹⁰²

A more systematic effort for estimating the charges of the surface atoms of the rutile (110) terminations has been recently reported by Bandura et al.⁶⁶ and Predota et al.⁶⁷ in the frame of a project for investigating the rutile (110) termination/electrolytic solution interface.^{65–73} Bandura et al.⁶⁶ have reported the charges for the bulk and surface titanium and oxygen atoms of different coordination obtained by HF-LCAO all-electron calculations using a three Ti-layer model (Table 6 in ref 66) or by DFT-LCAO calculations using a three or five Ti-layer model (Table 7 in ref 66). In both cases, the calculations were performed on the perfect (110) surface (bare surface) as well as on two model (110) surfaces (associatively and dissociatively hydroxylated). Selected values of charge determined by DFT-LCAO calculations and using a five Ti-layer slab are compiled in Table 6. For comparison, the values illustrated in the last line of Table 5 are also compiled in Table

Table 6. Charge Localized above Each Surface Atom (e) for the Bare Surface, Surface 1, and Surface 2 of the (110) Rutile Termination, Obtained by DFT-LCAO Calculations Using a Five Ti-Layer Model^a

symbol of the surface atom	bare surface	associatively hydroxylated	dissociatively hydroxylated
Ti _{6C}	1.758 (1.23) ^b	1.734	1.807
Ti _{5C}	1.813 (1.27)	1.793	1.802
O _{3C}	-0.969 (-0.67)	-0.943	-0.933
O _{2C}	-0.694 (-0.49)	-0.754	-0.760
O _{ter} or water O		-0.581	-0.689 (-0.33)
H _{ter} or water H		0.299	0.296
H _{br} or water H		0.312	0.320

^aSelected values from Table 7 of ref 66. ^bValues in parentheses are those illustrated in the last line of Table 5.

6 (values in parentheses). It may be seen that the same trends are obtained, although the absolute values obtained by us¹⁰² are smaller than the corresponding ones obtained by Bandura et al.⁶⁶ Values similar to those of Bandura et al. have been recently reported for the anatase (101) and rutile (110) terminations by Labat et al.¹²¹ It may be, moreover, seen that the values achieved lie in a reasonable range reflecting the partially covalent nature of the chemical bonds in the TiO₂. However, the HF method provides 25% larger absolute values than the DFT method.⁶⁶ It was, moreover, found that, concerning the bare surface, the deviations of the charges obtained for the surface atoms from their bulk values are less than 0.2 e.⁶⁶

As was already mentioned, Predota et al.⁶⁷ calculated surface charges in the frame of their effort to perform dynamic simulations of the rutile (110)/electrolyte solution interface. They, specifically, calculated surface charges for the surfaces presented in section 2.9.6 and compiled in Table 4. The values achieved are generally different from the corresponding values obtained by us¹⁰² and those reported in ref 66. These are compiled in Tables 3 and 5 of ref 67. Selected values from these tables are compiled in Table 7, whereas the corresponding surfaces are shown in Figure 56.

Table 7. Charge Localized above Each Surface Atom (e) for Four Model Surfaces of the (110) Rutile Termination⁶⁷

symbol of the surface atom	surface 1	surface 2	surface 3	surface 4
Ti _{6C}	2.196	2.196	2.121	2.134
Ti _{5C}	2.196	2.196	2.121	2.134
O _{3C}	-1.098	-1.098	-1.098	-1.098
O _{2C} unprotonated	-1.098		-1.053	-1.039
O _{2C} protonated		-1.035		-0.985
O _{ter}		-1.008	-0.974	-0.960
H _{ter}		0.459	0.394	0.409
H _{br}		0.486		0.434

The first column concerns surface 1, the rutile (110) surface with the Ti_{6C} surface atoms covered by the water molecules. It may be observed that, in contrast to the values compiled in Table 6, identical values were achieved for Ti_{6C} and Ti_{5C} surface atoms as well as for the O_{3C} and O_{2C} ones. These charges are compatible with the demand for the electrical neutrality of the surface. In fact, two O_{3C} surface atoms correspond to one Ti_{5C} surface atom (Figure 33). Thus, 2.196 + 2 × (-1.098) = 0 and the Ti_{5C}–O_{3C} layer is neutral. On the other hand, the positive charge of the Ti_{6C} atoms is compensated by the negative

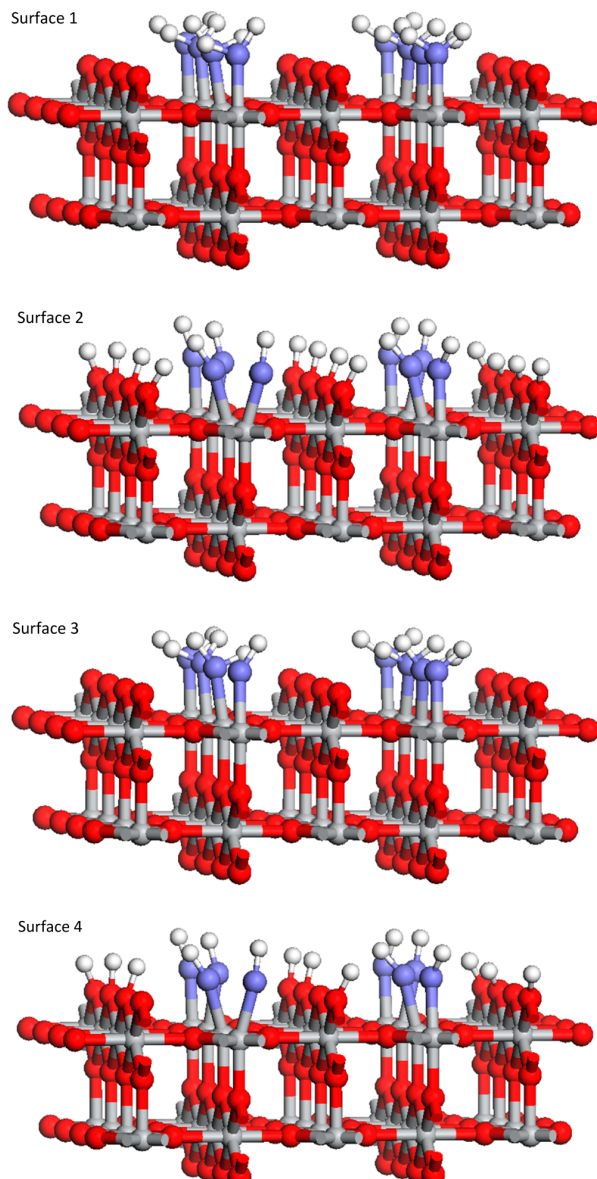


Figure 56. Schematic representation of the rutile (110) model surfaces adopted by Predota et al.⁶⁷ (Surface 1, neutral nonhydroxylated; Surface 2, neutral hydroxylated; Surface 3, negatively charged nonhydroxylated; Surface 4, negatively charged hydroxylated).

charges of one O_{2C} located above and one O_{3C} atom located below the Ti_{6C} atoms. The main comment here is that the adopted approach resulted in charges independent from the coordination of a given kind of atoms. The same is partly observed by inspecting the values achieved for surface 2, the rutile (110) surface with the Ti_{6C} surface atoms and the O_{2C} ones covered by the terminal hydroxyls and protons. On this surface, the sum of the charges of the atoms Ti_{5C} + 2 × O_{3C} + O_{ter} + H_{ter} is equal to -0.549 e, whereas the sum Ti_{6C} + O_{3C}(under the Ti_{6C} layer) + O_{2C}(protonated) + H_{br} is equal to 0.549 e. Therefore, the surface is neutral because the population of the terminal hydroxyls is equal to the population of the bridging ones. Three points are remarkable: (i) protonation changes the charge of the bridging oxygens, (ii) the charges of

the oxygen and hydrogen atoms of the terminal hydroxyls are different from the corresponding ones of the bridging hydroxyls, and (iii) the full hydroxylation of the surface does not change the charge of the Ti_{6C} , Ti_{5C} , and O_{3C} atoms. The latter is not valid when going from the neutral (surfaces 1 and 2) to the charged surfaces (surfaces 3 and 4). It was found that the charge localized above all of the surface atoms with the exception of the O_{2C} atoms depends on the charge of the surface, on the number of the terminal hydroxyls or the number of the unprotonated bridging surface hydroxyls. In surface 3, 25% of the Ti_{5C} surface atoms are bonded with terminal hydroxyls instead of water molecules, whereas in surface 4, 25% of the O_{2C} surface atoms are not protonated. The charges above the surface atoms in these surfaces are also illustrated in Table 7.

An interesting theoretical work, reported very recently by Zarzycki,²⁶¹ deals with the mode of the water adsorption on the rutile (110), (001), and (100) crystal faces, the charge of the terminal Ti_{5C} —OH surface groups developed on these crystal faces, and the protonation constants of these groups. The main purpose of the work was to compare the aforementioned surface charges and protonation constants with the corresponding ones assumed by the homogeneous “one site/one pK ” and “one site/two pK ” models or calculated in the context of the “multi site surface complexation model”, presented in the second part of this contribution. Adopting a molecular rather than a crystal orbital approach and considering isolated Ti_{5C} —OH surface groups, he calculated the aforementioned parameters using various calculation techniques and basis sets in the context of the Mulliken, Lowding, and Weinhold analysis. The energetic profiles of water adsorption on the aforementioned crystal faces suggested dissociative rather than molecular adsorption. The charges and the protonation constants calculated for the isolated Ti_{5C} —OH surface groups, formed upon the dissociative adsorption of water, are compiled in the Table 2 of ref 261. It was observed that the results provided by the Mulliken and Lowding analysis are basis set size-dependent; that is, they change rapidly when the basis sets are enlarged. It was, moreover, concluded that on the basis of the Mulliken charges we cannot distinguish the crystal face of the isolated Ti_{5C} —OH surface group. In contrast, the charges calculated by employing Lowding or Weinhold analysis vary considerably with the crystal face. It seems that the Weinhold analysis provided the most sensible results.

On the basis of selected values for the charge and the protonation constant of the aforementioned surface group, it was inferred that the values for the charge used in the homogeneous “one site/one pK ” model (-0.5 e) and “one site/two pK ” model (0.0) are not reliable for rutile. In contrast, most of the selected values obtained in this work for the charge and the protonation constant are similar although not identical to that calculated in the frame of the “multi site surface complexation model”. In the above analysis, it was not taken into account that on the surface of rutile the O_{2C} groups also exist, which may be protonated in aqueous suspensions. This renders rather difficult the comparison attempted concerning the number of the kinds of the Ti_{5C} —OH surface groups deduced from this work (at least one kind per crystal face) with the number of the kinds of surface hydroxyls inferred by exploiting the experimental proton affinity distribution curves.^{261,262}

2.16. Surface Chemistry and Phase Transitions of the Anatase and Rutile Polymorphs

Rutile is the thermodynamically stable phase, and anatase is a metastable one at ambient pressure and temperature.²⁶³ On the other hand, anatase has been found to be the majority product of industrial sol-gel and aerosol syntheses of titanium dioxide.²⁶⁴ Moreover, anatase is common in samples at nanoscale.^{265–267} The surface enthalpies of anatase and rutile are sufficiently different. Therefore, a crossover in thermodynamic stability can occur, and anatase is usually the stable phase at nanoscale.^{123,267} It has been reported several times that the anatase to rutile transformation depends on the size of nanocrystals, impurities, reaction atmosphere, and synthesis conditions.^{123,194,264,268–273} For example, the synthesis of titanium dioxide leads to anatase nanocrystals, which are transformed to rutile nanocrystals upon reaching a particular size greater than 14 nm . The rutile nanocrystals then grow remarkably faster.^{123,264} Zhang, Banfield, and colleagues have examined the size dependence of the phase transition from anatase to rutile nanocrystals through thermodynamic^{123,267,274} and kinetic^{267,270,275} approaches. The thermodynamic approach was based on a free energy model for the stability of spherical anatase and rutile nanoparticles as a function of the particle radius.¹²³ It was predicted that anatase will be thermodynamically preferred below, approximately, 14 nm . However, the model does not take into account the different number of atoms in anatase and rutile crystals of the same diameter.

The anatase to rutile transformation takes place inside a wide temperature range, depending on several of the above factors. For example, the phase transition for hydrothermally prepared samples takes place at about $500\text{ }^\circ\text{C}$, and the critical size is located between 11.4 and 17.6 nm , but it has been found to decrease with temperature.²⁶⁴ Different calorimetric values for the enthalpy of anatase to rutile transformation have been reported depending on size and experimental conditions.^{230,263,265,266,274,276–283} It has been reported that the different calorimetric data may reflect differences in nanocrystals morphologies.²⁷⁴ The nanocrystals’ morphology could be a factor that affects the phase stability, in addition to size.¹⁹⁵ The titanium dioxide nanoparticles are not necessarily spherical.¹¹⁴ For example, HRTEM study showed that the tetragonal bipyramidal morphology of anatase nanocrystals persists down to $3\text{--}5\text{ nm}$ that is in the size regime where anatase is thermodynamically preferred with respect to rutile.¹⁹⁵ Therefore, a general description of the phase stability requires the inclusion of the nanocrystals shape.¹²⁰

In view of the above, Barnard et al.¹²⁰ attempted to investigate the phase transition of the anatase to rutile using a suitable thermodynamic treatment that encompasses the morphological characteristics of nanocrystals as well as their size and accounts for the crystal terminations of the nanocrystals resulting from the various syntheses conditions. In other words, Barnard et al. attempted to relate surface chemistry and phase transition of the anatase and rutile polymorphs.¹²⁰

First, they studied the relative phase stability of clean nanoscale anatase and rutile, considering the effects of nanocrystals morphology on the phase transition. They found that the Wulff crystal shapes (top of Figure 25) correspond, in effect, to the minimum energy calculated for each morphology. They then calculated the free energy for each phase as a function of the number of titanium oxide units, proportional to atoms (Figure S7). We note that the free energy is the sum of

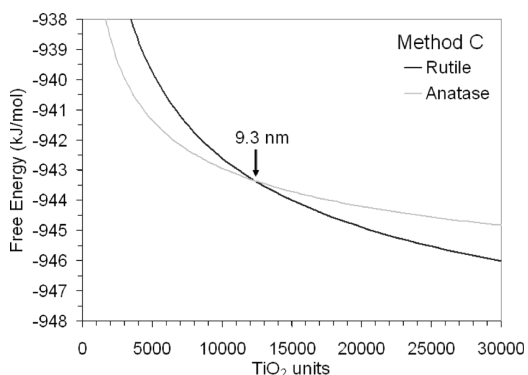


Figure 57. Free energy as a function of number of TiO₂ units for anatase and rutile, calculated using the shapes given at the top of Figure 25. The intersection points indicate the phase transition.¹²⁰ Reprinted figure with permission from ref 120. Copyright (2004) by the American Physical Society.

the bulk and surface free energy and the latter depends on the relative contribution of each orientation of the surface of the nanocrystals, which, in turn, is morphology dependent.

We may observe that the intersection point between anatase and rutile is located at about 9.3–9.4 nm in average diameter. This is in excellent agreement with the average diameter of 9.3 nm predicted by Zhang and Banfield,¹²³ although, as was already mentioned, they had assumed spherical scheme for the anatase and rutile nanocrystals, and the model did not account for the different number of atoms in anatase and rutile nanocrystals of the same diameter. We note that the findings of Zhang and Banfield¹²³ were obtained using empirical methods,¹¹⁸ whereas those of Barnard et al. using ab initio ones.¹²⁰ To investigate whether the agreement mentioned above is not fortuitous, Barnard et al. applied the model to spherical nanoparticles of anatase and rutile using values of surface energy and stress averaging over all of the low-index orientations of both polymorphs. The transition point is located at 2.6 nm in diameter, which is very different from that obtained assuming faceted nanoparticles and very far as compared to the experimental values.

The above clearly show that the assumption of faceted nanocrystals is crucial for obtaining a size at phase transition, which correlates quite well with experiment. More importantly, the above indicate the strong relation between the surface chemistry, morphology, and phase transition. However, even under this assumption, the experimental values mentioned above (11.4–17.6 nm)²⁶⁴ are somewhat greater than those obtained theoretically. This discrepancy was attributed to several factors.¹²⁰ The determination of the size of the nanoparticles takes place experimentally in the solution and at quite high temperatures, whereas the model is applied at 0 K considering the nanoparticles under vacuum. Moreover, nonequilibrium shapes may be involved in the transformation inside the solutions.

In previous sections (2.7 and 2.14), we have presented the work of Barnard et al.¹²⁰ concerning the influence of surface hydrogenation on the morphology of the anatase and rutile nanocrystals. Two cases have been considered. In the case of partially hydrogenated surfaces, the hydrogen atoms are located above the O_{2C} atoms, whereas in the case of the fully hydrogenated surfaces, the hydrogen atoms are located above both the O_{2C} and the Ti_{5C} atoms. It was predicted that the

partial or full hydrogenation does not have any considerable effect on the Wulff construction of anatase nanocrystals, whereas the aspect ratio increases in the case of rutile and the nanocrystals become squatter as the coverage by hydrogen is increased (Figure 25). Barnard et al. calculated the surface energy for each of the nanocrystals depicted in the figure and plotted it as a function of the TiO₂ units (Figure 58). As we

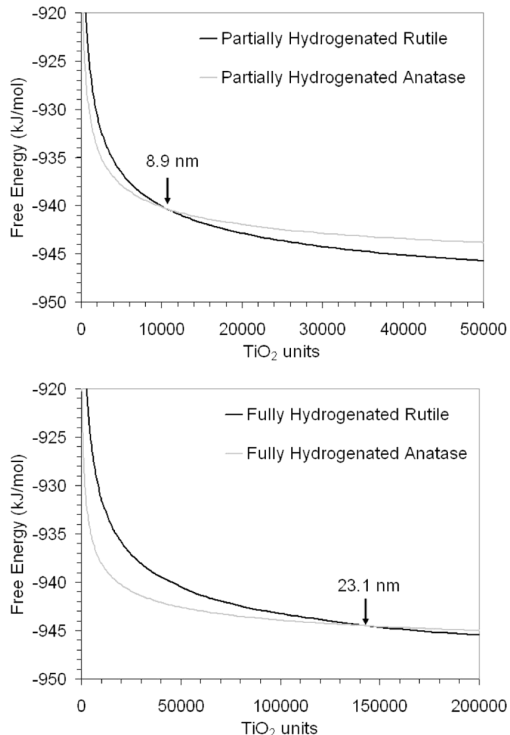


Figure 58. Free energy as a function of number of TiO₂ units for anatase and rutile, calculated using the shapes given in Figure 25. The intersection points indicate the phase transition. The sizes indicated by the arrows refer to the average diameters of anatase nanocrystals.¹²⁰ Reprinted figure with permission from ref 120. Copyright (2004) by the American Physical Society.

can see, the intersection points were determined at 8.9 and 23.1 nm for the partial and full hydrogenation, respectively. From the above, one may conclude that a change of the surface chemistry obtained by partial or full hydrogenation has critical effects not only on rutile morphology but, in addition, on phase transition. Specifically, the model predicted that full hydrogenation of the nanocrystal faces promotes the stability of anatase, whereas partial hydrogenation promotes that of rutile.¹²⁰

Barnard et al. continued their study by considering the influence of hydration of the low-index surface orientations of both anatase and rutile nanocrystals on their morphology and phase transition.¹²² Concerning anatase, dissociative adsorption of water was assumed for the (001) and (100) faces and molecular adsorption for the face (101). Concerning rutile, dissociative adsorption of water was adopted for the (100) and (011) surfaces and molecular adsorption for the majority (110) orientation. The influence of hydration on the morphology has been presented in previous sections (2.7 and 2.14). As to the phase transition, the main finding was the marked shift of the transition point from 9.6 nm, calculated for clean surfaces in

vacuum, to 15.1 nm, calculated for the hydrated surfaces. We note that the assumption that the nanocrystals are immersed in water is much more realistic than the assumption that the nanocrystals are in a vacuum. This perhaps justifies why the value obtained for the transition point under hydrated conditions is very close to those determined experimentally and mentioned above.²⁶⁴

The anatase and rutile nanocrystals are frequently in water solution of various pH's. The change in pH may cause considerable effects in the chemistry of the low-index crystal faces of the anatase and rutile nanocrystals, which, in turn, as was already mentioned in previous sections, affect their morphology. A reasonable question is whether the pH change may influence, in addition, the phase stability expressed by the phase transition size. Barnard et al.¹⁹² attempted to investigate the issue by studying the phase transition for five face configurations corresponding to different pH regions: (a) fully hydrogenated surfaces ("highly acidic conditions", Figure 26), (b) surfaces rich in hydrogen ("moderately acidic conditions", Figure 27), (c) hydrated surfaces ("neutral pH conditions", Figure 28), (d) hydrogen-poor surfaces ("moderately basic conditions", Figure 29), and (e) oxygenated surfaces ("highly basic conditions", Figure 30). It was found that the phase transitions of titanium dioxide nanoparticles with fully hydrogenated surfaces, surfaces rich in hydrogen, hydrated surfaces, hydrogen-poor surfaces, and oxygenated surfaces occur at sizes of approximately 22.7, 18.4, 15.1, 13.2, and 6.9 nm, respectively. These results do not indicate that anatase nanoparticles do not exist above these sizes. These simply indicate that above these sizes the anatase nanocrystals are metastable with respect to the transformation to rutile nanocrystals. More importantly, the above results show the strong relation between the surface chemistry of the faceted nanoparticles of titanium dioxide, presumably regulated by adjusting solution pH, with the phase transition size. The anatase nanocrystals are stabilized in acidic conditions, whereas the rutile nanocrystals are stabilized under basic conditions. These results explain why the anatase nanoparticles are typically grown under acidic conditions.^{183,284,285}

Closing this section, we have to note that the use of a quite accurate, *ab initio*, thermodynamic model^{120,122,191–193} showed that the phase stability of titanium dioxide nanoparticles depends strongly on the morphology of the nanocrystals and the hydration state. Faceting and hydration increase the stability of anatase nanocrystals. Moreover, it was found that pH may affect the phase stability through changes in the surface chemistry of the faceted nanoparticles with the anatase and rutile nanocrystals stabilized, respectively, in acidic and basic conditions.

In this section, we tried to show the close relation between the surface chemistry of the low-index faces of titanium dioxide nanoparticles (one of the three main issues of the present review) and the phase transition from rutile to anatase based on an accurate thermodynamic model. In this treatment, only the necessary experimental works have been mentioned. The reader is addressed to the excellent review of Chen and Mao¹¹ for more information concerning the experimental works dealing with the aforementioned phase transitions.

3. INTERFACIAL CHEMISTRY

3.1. A General Description of the Interfacial Region

Going from the surface to the interfacial chemistry, a concise description of the interfacial region developed between an oxide and an electrolytic solution seems to be useful. It is well-known that on the surface of a (hydr)oxide, more than one kind of unprotonated, singly protonated, and doubly protonated surface oxygens are developed. These are characterized by different electrical charge and basicity. Thus, depending on the pH of the impregnating solution, the whole surface charge may be negative or positive. The unique pH value where the whole surface charge is zero is called point of zero charge (pzc). Various methodologies have been developed for determining this parameter, which is quite important in many applications.^{286–295} Moreover, recent spectroscopic,²⁹⁶ computational,²⁹⁷ and electrochemical techniques²⁹⁸ have been applied to single crystal surfaces. Most of the above referenced techniques can also determine the surface charge, which is pH-dependent. The surface charge causes the development of surface potential. Under the influence of this potential, ions with opposite charges (counterions) are accumulated from the solution near the surface, forming thus the interfacial region. It should be noted that the size of the interface depends on the ionic strength of the impregnating solution. It is extended up to several nanometers for relatively low values of the ionic strength (e.g., 3 nm for $I = 0.01 \text{ M}$).¹⁰² Various models have been developed to describe the interfacial region.²⁹⁹ According to most of these models, the interface is divided into two regions, the compact region (extending up to 5–8 Å from the surface) and the diffuse one.

A more elaborate description of the interface requires the joint application of two models: one kind of surface ionization model describing the protonation-deprotonation equilibria of the surface oxygens and one kind of electrostatic model describing the whole interfacial region. The historical evolution of the models belonging to both classes has been involved in recent review articles.^{33,101,299} Therefore, in this Review, we focus on the four most modern models, one surface ionization model and three electrostatic models.

3.1.1. The Music Model. In 1989, Hiemstra et al.^{95,96} proposed the so-called "music model" (multi site surface complexation model). This has been redefined seven years later.⁹⁷ The model took advantage of the previous well-established knowledge that different kinds of oxo-/hydroxogroups are developed on the surface of solid oxides being in aqueous media. In fact, this model explicitly accounts for the various kinds of surface oxygen atoms known from surface structural analysis. Therefore, from this point of view, the music approach is much more realistic than the quite popular but rather hypothetical homogeneous models.^{91–94}

The latter assumed the development of only one kind of surface oxygen atoms on the surface of an oxide, which can undergo one or two protonation steps, resulting, respectively, in singly protonated or doubly protonated surface oxygen atoms ("one site/one pK", $\text{TiO}^{0.5-} + \text{H}_s^+ \leftrightarrow \text{TiOH}^{0.5+}, K_{\text{H}}$ and "one site/two pK", $\text{TiO}^- + \text{H}_s^+ \leftrightarrow \text{TiOH}^0, K_{\text{H},1}$ and $\text{TiOH}^0 + \text{H}_s^+ \leftrightarrow \text{TiOH}_2^+, K_{\text{H},2}$ models). The homogeneous models adopt rather arbitrary charges for the surface oxygen (-0.5 and -1 for the "one site/one pK" and "one site/two pK" model, respectively).

In contrast, the "music model" proposes a methodology for calculating the charges of the different kinds of surface oxygen atoms. This is based on the principle of local neutralization of

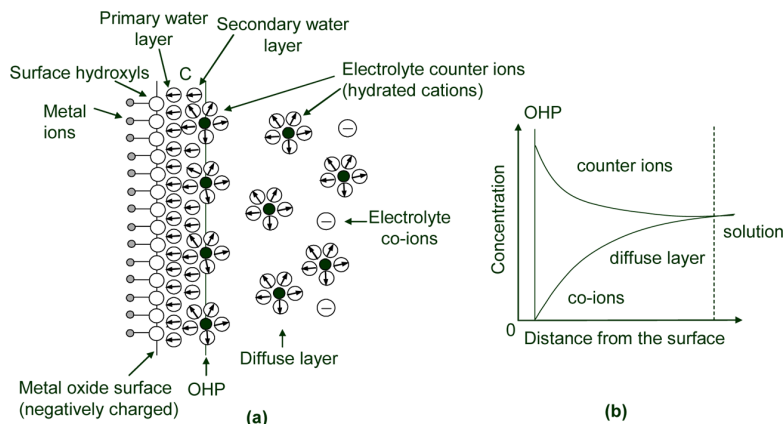


Figure 59. Basic Stern (BS) model: (a) arrangements of the ions at the interface, (b) variation of the concentration of the cations (counterions) and anions (co-ions) with the distance from the negatively charged surface of a metal (hydr)oxide. By OHP, we symbolize the so-called outer Helmholtz plane. For simplicity, we use the term “surface hydroxyls” to describe unprotonated, singly, or doubly protonated surface oxygens, and we consider only singly coordinated surface oxygens.

the charge, as introduced by Pauling³⁰⁰ and refined by Brown.^{301–303} The local neutralization of the charge is related to the concept of the bond valence. If the charge of a metal “ion”, being inside a solid metal oxide, is equally distributed over the surrounding oxygen atoms, the bond valence is defined as the typical charge of the metal ion divided by its coordination number. According to the local neutralization of the charge, the charge of an oxygen atom is calculated as the sum of its typical charge (-2) plus the bond valences of all coordinated metal ions. This calculation results always in a zero value for the bulk oxygen atoms. In contrast, for the surface oxygen atoms of a certain kind, the so calculated charge may be different from zero, if these oxygen atoms are coordinated by fewer metal ions than in the bulk. It is obvious that this approach provides different charges for the different kinds of surface oxygen atoms. More precisely, for such a calculation it is necessary to use the actual instead of the Pauling valence, when these parameters have different values. In fact, the former may be slightly different from the latter because for the determination of the actual valence we take into account the length of the cation–oxygen bonds for a certain kind of oxo- or hydroxo-group.

The music approach considers, moreover, that the protonation/deprotonation of a surface oxygen results in an increase/decrease of its charge by one unit. Furthermore, the refined music approach takes into account the hydrogen bonds formed between the surface oxygen and the hydrogen of a water molecule adsorbed on the surface, hydrogen-accepting bonds, as well as the hydrogen-donating bonds, which are hydrogen bonds formed between the surface hydrogen of a hydroxo-group and the oxygen atom of an adsorbed water molecule. Taking into account the accessible orbitals of the surface oxygen atoms, Hiemstra et al.⁹⁷ postulated that a singly coordinated surface group forms two hydrogen bonds: both accepting for an oxo-group, one donating and one accepting for a hydroxo-group. It was, moreover, postulated that a triply coordinated surface group may form only one hydrogen bond: accepting or donating for an oxo- or hydroxo-group, respectively. The doubly coordinated surface groups may form one or two hydrogen bonds. It has been estimated that (+0.2) charge units are transferred to (from) the surface oxygen

atom from (to) an adsorbed water molecule for each accepting (donating) hydrogen bond.

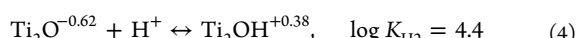
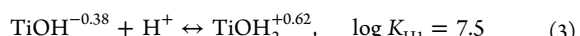
Following the above-mentioned approach, the excess oxygen charge is given by the algebraic sum of the actual valences (s_j) of the metal cations coordinated with the surface oxygen, the typical charge of the oxygen ($V = -2$), and the charge contribution to the oxygen due to the hydrogen bonds.

$$\text{excess oxygen charge} = \sum s_j + V \quad (1)$$

In the sum, $\sum s_j$, the actual valences of the hydrogen ions involved in the aforementioned hydrogen bonds are -0.2 ($+0.2$) charge units for each hydrogen bond in which the surface group donates (accepts) a hydrogen ion. The music model provided, moreover, the empirical equation:

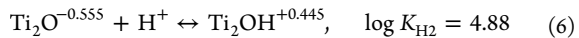
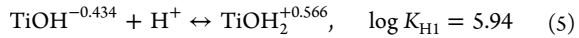
$$\log K = -19.8(\sum s_j + V) \quad (2)$$

for calculating the protonation constants of the surface oxygen atoms. It may be seen that the logarithm of the protonation constant changes linearly with the charge of the surface oxygen calculated following the aforementioned methodology. This relation indicates that the higher is the (negative) oxygen charge, the easier is its protonation. Application of eqs 1 and 2 to, for example, the (110) surface of rutile gives the following protonation equilibria:⁹⁷



This protonation scheme for the (110) surface of rutile was refined very recently by Machesky's group.³⁰⁴ The authors incorporated in the above-mentioned refined music model, on a quantitative basis, interfacial H-bond configurations, as obtained primarily from experimentally verified classical molecular dynamics simulations of the ab initio-optimized surface in contact with SPC/E water. They then used this obtained solvation structure, along with slight manual adjustments to interfacial Ti–O bond lengths that fall within the range of those determined via static DFT calculations and X-ray reflectivity measurements, to develop a surface protonation description consistent with experimentally determined pH_{pzc} value (5.4 ± 0.2) for a specific rutile powder dominated by the

(110) surface. The final obtained protonation scheme is represented by the following equilibria:



3.1.2. Basic Stern Model. A suitable interfacial model to describe electrostatic adsorption, one of the main processes of interfacial deposition, is the so-called Basic Stern (BS) model.³⁰⁵ According to this model, the interface is divided into two regions (Figure S9), the compact region (extending up to several angstroms from the surface) and the diffuse one. The compact region involves two charged planes: the surface (or zero plane) of the oxo- or hydroxo-surface groups and the head end of the diffuse part of the interface (outer Helmholtz plane (OHP) or plane 1). In this plane and in the diffuse layer, the counterions are accumulated compensating the surface charge. These ions are treated as point charges. The counterions located at OHP form ion pairs with the surface oxygens of opposite charge. The ion pairs are considered as outer-sphere complexes forming rather weak bonds with the surface oxygens. The uncharged space (layer) between the two planes is due to the fact that on the surface plane at least one layer of water molecules is adsorbed, whereas some of the counterions of the background electrolyte are hydrated (e.g., sodium or potassium cations). Therefore, according to this model, the electrostatically retained ions have a minimum distance of approach of the surface plane. The uncharged layer is treated as a plate condenser with a given capacitance, C . This parameter is related to the distance, d , between the surface plane and the OHP by the relationship:

$$C = \epsilon_0 \epsilon_r / d \quad (7)$$

whereby ϵ_0 and ϵ_r we denote, respectively, the absolute dielectric constant and the mean relative dielectric constant in the aforementioned layer. The BS model is indeed the simplest physically realistic model allowing the description of the interfacial region.⁹⁸

From one point of view, the older diffuse double layer (DDL) (or Gouy–Chapman (GC))³⁰⁶ and constant capacitance (CC)^{307,308} models are special cases of the BS model. In both cases, the hydration of the cations is ignored, whereas it is not taken into account that the surface of an oxide adsorbs, at least, one monolayer of oriented water molecules. In the first case, more suitable for solutions of relatively low ionic strength, the diffuse layer covers the whole interfacial region, whereas in the second, more convenient for solutions with relatively high ionic strength, the interface is reduced to its compact region.

A very popular interfacial model is the so-called Stern–Gouy–Chapman (SGC) model. The only difference with the BS model is that the formation of the aforementioned ion pairs is not assumed. As this model does not involve the formation constants of the ion pairs, it comprises a lower number of adjustable parameters.

3.1.3. Triple Layer Model (TLM). This model^{309,310} is more suitable for describing the adsorption of transition metal ionic species containing catalytically active elements. Usually, the TMIS are specifically adsorbed on oxidic supports. In most of the cases, they form inner-sphere surface complexes using one or more surface oxygens as ligands. In fewer cases, they form hydrogen bonds with surface oxygen or hydrogen atoms. Figure 60 illustrates the triple layer model for the case where specifically adsorbed cations form inner-sphere surface

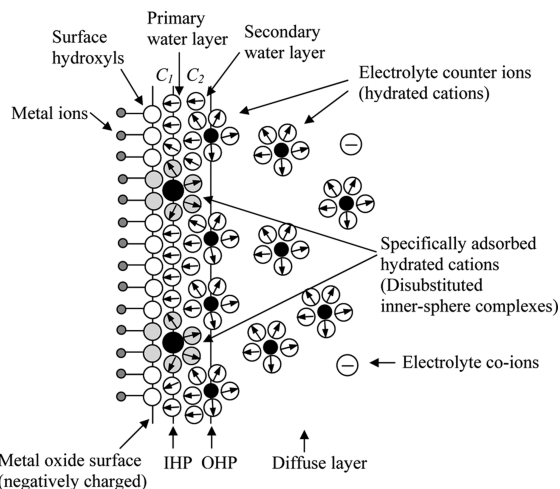


Figure 60. “Metal oxide/aqueous solution” interface in the presence of specifically adsorbed cations forming “inner-sphere complexes”, according to the triple layer model.^{309,310} For simplicity, we use the term “surface hydroxyls” to describe unprotonated, singly, or doubly protonated surface oxygens, and we consider only singly coordinated surface oxygens.

complexes. The only difference between the BS and the TL model is that in the latter model an additional charged plane, the so-called inner Helmholtz plane (now plane 1), is considered between the surface plane and the outer Helmholtz plane (now plane 2). The specifically adsorbed TMIS are located at the IHP, whereas the counterions of the background (indifferent) electrolyte are located at the OHP and in the diffuse layer. Therefore, in this model, the ions, also considered as point charges, are located at three planes: the surface plane, the IHP and the OHP, as well as in the diffuse layer. The name of this model implies that the interface is divided into three layers: the surface–IHP, the IHP–OHP, and the diffuse layer. It is obvious that following this model two capacitances should be considered, respectively, for the uncharged layers “surface–IHP” and “IHP–OHP”. The corresponding values C_1 and C_2 are related to the whole capacitance value.

$$1/C = 1/C_1 + 1/C_2 \quad (8)$$

Equations 9 and 10 relate the values of capacitance with the corresponding distances and the mean relative dielectric constants in the corresponding layers.

$$C_1 = \epsilon_0 \epsilon_r / d_1 \quad (9)$$

$$C_2 = \epsilon_0 \epsilon_r / d_2 \quad (10)$$

3.1.4. Three Plane Model. An important evolution of the triple layer model is the so-called Three Plane Model (TPM). This was proposed by Hiemstra and Van Riemsdijk⁹⁹ to overcome the nonrealistic assumption that the adsorbed species are simulated as point charges. They extended the Pauling valence bond concept initially to the specifically adsorbed TMIS. Moreover, they considered these species as a natural extension of the support surface and suggested a “distribution” of the positive charge of the transition metal to the surrounding ligands. The charge distribution (CD) concept,⁹⁹ introduced in the modeling of the interface, changed drastically the picture for the adsorbed TMIS. These species are not treated as point charges located at the IHP, but are considered to have a spatial

distribution of charge in the interfacial region. A schematic representation of the three plane model is illustrated in Figure 61. It concerns the formation of disubstituted and mono-

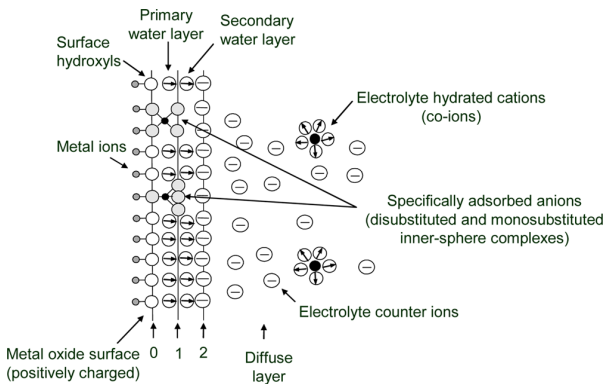


Figure 61. “Metal oxide/aqueous solution” interface in the presence of specifically adsorbed anions forming “inner-sphere complexes”, according to the three plane (TP) model.⁹⁹ For simplicity, we use the term “surface hydroxyls” to describe unprotonated, singly, or doubly protonated surface oxygens, and we consider only singly coordinated surface oxygens.

substituted inner-sphere complexes. According to this model, the positive charge of the central cation, for example, of the Mo^{6+} in MoO_4^{2-} , is distributed over the surface directed oxygen ligands as well as over the solution directed oxygen ligands. Such a distribution of the charge is compatible with three distinct charged planes: the surface plane (zero plane), the IHP of the triple layer model shifted to the right to meet the centers of the solution directed oxygen ligands (plane 1), and the OHP (plane 2) where the counterions form ion-pairs. The latter were initially treated as point charges, but very recently the charge distribution concept has been extended to the counterions, and their charge is considered to be distributed between plane 1 and plane 2.³¹¹

3.2. Studies on the Rutile (110) Crystal Termination/Electrolytic Solution Interface: A Bridge between the Surface and Interface Chemistry

3.2.1. Introductory Remarks. Few papers reported in the last years deal with the title interface.^{64,67–73,312} The electrolytic solutions studied in these works contain Na^+ , Rb^+ , Ca^{2+} , Sr^{2+} , Y^{3+} , Zn^{2+} , or Co^{2+} ions as well as Cl^- or Br^- ions. With the exception of cobalt, these ions are not of great catalytic interest. However, the results drawn from these works may be proved extremely useful for an in-depth understanding of the mode of deposition and the local structure of TMIS on the surface of titanium oxide. Most of these ions were considered in the past to be nonspecifically adsorbed. This is mainly the case for the alkali and alkaline earth ions as well as for halides. This is the reason for which these types of the background electrolytes, used to regulate the ionic strength, are called indifferent electrolytes. The main goal of these works is to examine the mode of interfacial deposition and the local structure of an eventually formed inner-sphere surface complex of the ions mentioned above on the (110) rutile termination. Specifically, the surfaces illustrated in Table 4 were studied.

3.2.2. Theoretical Calculations. Both theoretical and experimental methodologies were used but not for all ions. Concerning the theoretical methodologies, ab initio calcu-

lations in the frame of the density functional theory and then molecular dynamic simulations have been used.^{68,71,73} For the latter, as was already mentioned, they adopted a slab geometry with two parallel and identical surfaces based on the (110) rutile termination and water molecules between them. The separation of the two surfaces was assumed to be equal to 50 Å. It was proved that it is sufficient to prevent the interference of the two identical interfaces. Thus, the properties reported are averages over both interfaces. An amount of cations and anions to be studied in each case was considered in the impregnating solution. Very recently, the theoretical results that had been reported previously were properly corrected.²²¹ Presenting the adsorption of the various ions, we have taken into account these corrections.

3.2.3. X-ray Studies. In situ synchrotron X-ray studies including crystal truncation rod (CTR),^{69,72} Bragg X-ray standing wave (XSW),^{69–71} and X-ray absorption fine structure (EXAFS)⁷¹ spectroscopies were used together with macroscopic adsorption measurements and multisite modeling.

Starting with the CTR technique, we must first say that it is the interfacial analogue of the well-known bulk crystallography. Interfacial signals appear as continuously modulated rods of intensity extending from each Bragg peak due to the loss of translational invariance associated with the presence of the surface, and are known as crystal truncation rods.^{72,313} Typically, the strength of the CTR signal at the midpoint between Bragg peaks corresponds to one-half of a surface monolayer. The number of adsorbed species is comparable to one monolayer of the oxide. Therefore, the CTR measurement is expected to be directly sensitive to the oxide-aqueous interfacial structures.⁷² A brief analysis of the way of analyzing CTR data for mineral–water interface can be found in ref 72. An illustrative example is given in Figure 62. It concerns the adsorption of Rb^+ ions at the “rutile (110)/water” interface. The analysis of the CTR data revealed that some Rb^+ ions specifically adsorb at the interface, as it can be seen by the significant change in the shape of the CTR curve (Figure 62B) when this ion is present at high concentration.

Going from the CTR technique to the Bragg XSW spectroscopy, we have to say that there is no doubt that the last one has proved to be the most informative experimental methodology. In fact, to date the most direct probes of the interfacial regions are the X-ray standing wave spectroscopies. While the “total external reflection” XSW spectroscopy may be used for investigating the diffuse part of the interface, the Bragg XSW spectroscopy probes the compact region of the interface extended few angstroms from the surface. When an X-ray plane wave is Bragg-diffracted from a single crystal lattice, an XSW, a fluorescence signal, is generated as a result of a coherent superposition of the incident and reflected X-ray beams (see, for example, Figure 63A). The fluorescence signal is the product of the absorption of the X-ray photons of the standing wave. The normalized fluorescence yield is related to two parameters: the so-called “coherent position”, P_{H} , and “coherent fraction”, f_{H} . Thus, this technique allows the determination of these parameters. Both are unit less quantities ranging between 0 and 1.

The first parameter is related to the height of an ion from a surface plane considered as zero plane. As was already mentioned, the basal plane of the (110) termination has been considered as a zero one. This involves interconnected Ti_{SC} , Ti_{6C} , and O_{3C} atoms. The Ti_{6C} atoms are, moreover, connected with structural O_{2C} atoms protruded out from the basal plane,

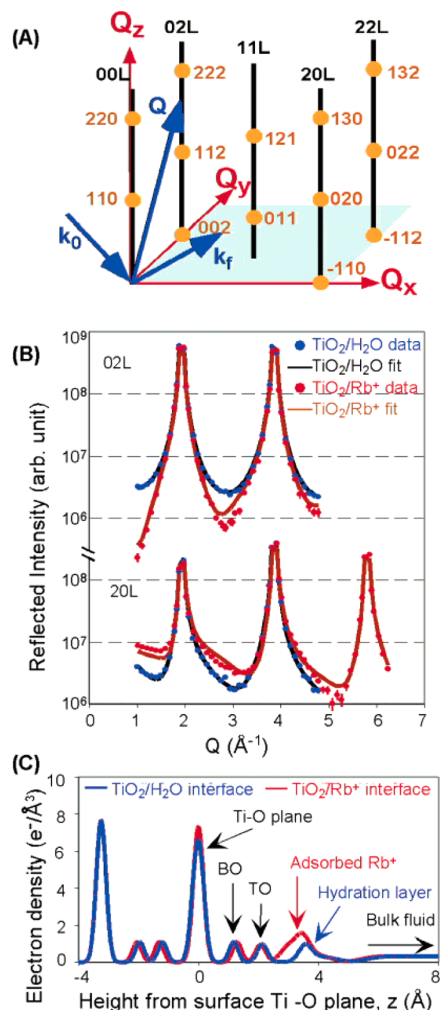


Figure 62. (A) Reciprocal space structure of the rutile (110) surface with crystal truncation rods and bulk Bragg reflections (labeled with surface Miller indices and bulk Miller indices, respectively). (B) Representative high-resolution XR results for the rutile (110)/water interface, showing the $(2,0,L)$ and $(0,2,L)$ crystal truncation rods for rutile in deionized water (blue ●) and $[\text{RbCl}] = 1 \text{ M}$ at pH 12 (red ●), with changes associated with Rb^+ adsorption. (C) The data were quantitatively compared to structural models and optimized to reveal the atomic arrangements at the rutile/water interface. The best fit model was then converted to a laterally averaged electron density profile.⁶⁹ Reprinted with permission from ref 69. Copyright 2004 American Chemical Society.

whereas after hydration the $\text{Ti}_{5\text{C}}$ atoms are bonded with $\text{O}_{1\text{C}}$ atoms of the terminal hydroxyls or water molecules, also protruding out from the basal plane (Figure 33).

On the other hand, under suitable conditions, the coherent fraction is equal to 0 or is related to the so-called “ordered fraction”, C . The latter is related to the surface coverage of the compact layer with respect to the surface coverage of the whole interfacial region. Therefore, using the Bragg XSW spectroscopy, the surface coverage of the compact layer and the distribution of the ions between the compact and the diffuse part of the interface may be deduced. For example, a value of the coherent fraction equal to 1 means that all ions are located at the same position, whereas a value of the coherent fraction

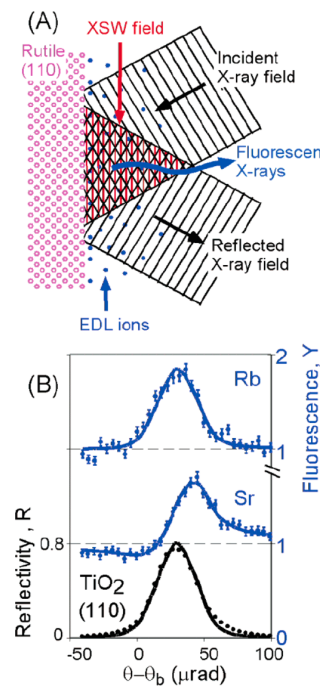


Figure 63. (A) A schematic of the XSW technique showing the incident and Bragg reflected X-ray beams, the electric double layer (EDL) ions (that maybe either adsorbed to the rutile surface or distributed within the diffuse layer), and the fluorescent X-rays. (B) Representative XSW data for adsorption of Rb^+ and Sr^{2+} at the rutile (110) surface. The fluorescent yield modulations indicate that Sr^{2+} specifically adsorbs to rutile under these conditions but that Rb^+ does not. More details can be found in ref 69. Reprinted with permission from ref 69. Copyright 2004 American Chemical Society.

equal to 0 means that the ions form a perfectly random distribution.

Closing this subsection, we should mention that also EXAFS spectroscopy has been used in conjunction with the above presented CTR and XSW techniques. In the following, we shall try to present very briefly the most important results concerning the adsorption of the ions mentioned in this section, which has been studied on the basis of both theoretical calculations and the use of the above-mentioned X-ray techniques.

3.2.4. Sodium Ions. It is well-known that these monovalent ions are hydrated in aqueous solutions. As was already mentioned, it was for years considered that these ions are located in the diffuse part and in the outer plane of the compact region of the interface (Stern plane, OHP, or plane 2, depending on the model adopted for the interface). It was, moreover, considered that these ions retain its hydration sphere upon adsorption. This picture had been elaborated on the basis of macroscopic adsorption data, potentiometric titrations, and microelectrophoresis results.

Theoretical calculations using the methodologies mentioned above indicate that the picture is presumably more complicated.^{68,69,221} In fact, the axial density (number of ions per cubic angstrom) profile of sodium ions, derived above the surfaces presented in Table 4, revealed adsorption of sodium ions on the negatively charged surfaces (surfaces 3 and 4) as well as on the neutral surface 2. Concerning surface 4, the lateral distribution of the sodium ions indicated formation of

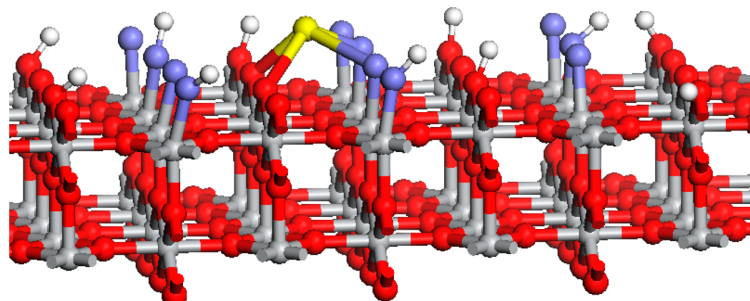


Figure 64. Formation of inner-sphere surface complex on a tetradeятate site (TD) involving two bridging oxygen (BO) and two terminal oxygen (TO) atoms. We note that the height of the O_{2C} atoms from the basal plane is calculated in the range 1.1–1.4 Å, whereas that of the terminal O_{1C} atoms is in the range 2.0–2.2 Å⁶⁹ (Na atoms: yellow balls).

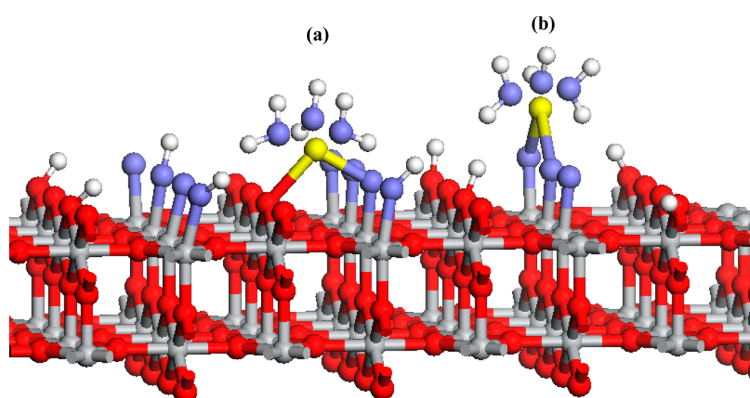


Figure 65. Formation of inner-sphere surface complex on bidentate site involving (a) one bridging and one terminal oxygen atom (BOTO) and (b) two terminal oxygen atoms (TOTO). We note that the height of the O_{2C} atoms from the basal plane is calculated in the range 1.1–1.4 Å, whereas that of the terminal O_{1C} atoms is in the range 2.0–2.2 Å⁶⁹ (Na atoms: yellow balls).

inner-sphere complex on a tetradeятate (TD) surface site (Figure 64). This site involves four oxygen atoms protruding out the basal plane, two bridging oxygen (BO) and two terminal oxygen (TO) atoms. These form a new plane above the basal one. The sodium ions are located above this plane (at about 2.9 Å), forming four bonds with the aforementioned oxygen atoms. The formation of the inner-sphere surface complex is accompanied by partial dehydration of the sodium ions and presumably by removal of the water molecules, which had formed hydrogen bonds with the receptor oxygen atoms. This happens because the bridging and terminal oxygen atoms substitute water molecules in the first hydration shell by the sodium ion. It should be observed that, due to the geometry of the tetradeятate site, the sodium ion is located above one O_{3C} atom of the basal plane. The presence of this oxygen presumably renders the tetradeятate site more favorable for the sodium adsorption. In fact, the development of electrostatic-attractive forces exerted between the sodium ion and the negatively charged triply coordinated oxygen (see Tables 5–7) may stabilize the inner-sphere surface complex.

The lateral distribution of the sodium ions indicated, moreover, formation of inner-sphere complexes on two bidentate surface sites, BOTO and TOTO. The first site involves one bridging oxygen (BO) and one terminal oxygen (TO) atom, whereas the second involves two terminal oxygen (TO) atoms (Figure 65). The sodium ions located at these sites at heights equal to 3.25 and 3.75 Å, respectively, above the basal plane. The formation of these bidentate sites may be also

accompanied by partial dehydration. The adsorbed sodium ions above the TD, BOTO, and TOTO sites are distributed as 28%, 16%, and 52%, respectively.

Concerning the charged surface 3, the formation of the TD (42%) and BOTO (46%) inner-sphere complexes was also found. In these complexes, the sodium ions are located at heights 2.9 and 3.4 Å, respectively. As in the charged surface 3, there is only one terminal hydroxyl group available for bonding with the adsorbed sodium ions; the coordinated water offers the fourth oxygen of the tetradeятate site. The presence of the hydrogen atoms bonded with the terminal and bridging (if present) oxygen atoms causes the development of repulsive forces upon the formation of the surface complexes. The stabilization of these complexes is obtained by moving the hydrogen atoms away from the adsorbed sodium ions. It seems that it is not possible for the uncharged surface 1, which contains only coordinated water molecules with two hydrogen atoms per terminal oxygen. This explains that the theoretical calculations do not predict formation of inner-sphere surface complexes for this surface. Finally, it should be mentioned that the tetradeятate complex is predicted to be formed in larger amounts on the charged surfaces 3 and 4 as compared to those on the uncharged surface 2.

The above findings were obtained by performing only theoretical calculations as no X-ray results on the structure of the sodium ion at the title interface are available. This is due to the greater difficulty of observing low-Z elements *in situ* at the solid–liquid interface.⁶⁸

3.2.5. Calcium Ions. The structure of the adsorption state of these ions on the (110) model rutile surfaces is also investigated using only theoretical methodologies.^{68,221} This is because experimental X-ray data are not available due to reasons similar to those mentioned for sodium ions. This structure is similar to that of the sodium ions. In fact, calcium ions form an inner-sphere surface complex above the tetradentate site at both negatively charged surfaces (surface 4 (31%), surface 3 (25%)). In this complex, the height of the calcium ions from the basal plane is equal to 3 Å, very close to that calculated for sodium. Moreover, at these surfaces, calcium ions form bidentate inner-sphere surface complexes (surface 4, BOTO (3.35 Å, 34%), TOTO (3.85 Å, 22%); surface 3, BOTO (3.5 Å, 65%).

The axial density profiles at charged surfaces revealed, in addition, nonspecific adsorption of fully hydrated calcium ions.^{68,221} This nonspecific adsorption is also predicted for the neutral surfaces. In both types of surfaces, the distances of the fully hydrated calcium ions from the basal plane are greater than 5 Å. It was found that in both cases the amount of the nonspecifically adsorbed calcium ions is 10% of partially dehydrated calcium ions, which are involved in the inner-sphere complexes formed at the charged surfaces.

3.2.6. Rubidium Ions. The adsorption of these ions on the model surfaces was studied applying both the theoretical calculations used for the study of the ions discussed before^{68,221} as well as crystal truncation rod (CTR) and Bragg X-ray standing wave (XSW) measurements.⁶⁹ Therefore, a comparison of the theoretical predictions with the experimental findings is now feasible.

The theoretical calculations suggested an adsorption behavior similar to that suggested for the sodium and calcium ions, which are characterized by the formation of inner-sphere complexes.^{68,221} Thus, the Rb⁺ ions are adsorbed on the negatively charged surface 4 over the tetradentate sites with the rubidium ions located at a distance 3.55 Å (79%) as well as over the BOTO (4.25 Å, 14%) and TOTO (4.25 Å, 14%) bidentate sites. Moreover, these ions are adsorbed on the negatively charged surface 3 over the tetradentate sites with the rubidium ions located at a distance 3.50 Å (58%) as well as over the BOTO bidentate sites (3.90 Å, 36%). Concerning the neutral surfaces, rubidium is adsorbed, in a smaller amount, at surface 2 over the tetradentate sites, whereas it is not adsorbed on surface 1.

A remarkable difference in the adsorption behavior of the Rb⁺ ions with respect to that of the Na⁺ and Ca²⁺ ions is that the heights from the basal plane calculated for the rubidium ions are greater than the corresponding ones calculated for the sodium and calcium ions.⁶⁸ This was attributed to the greater ionic radius of the Rb⁺ ions with respect to that of the Na⁺ and Ca²⁺ ions resulting in a larger ion–oxygen bond in the case of the former ions. In fact, the calculated lengths of the ion–oxygen bonds in the hydrated sodium, calcium, and rubidium ions are equal to 2.47, 2.46, and 2.95 Å, respectively. The role of the ionic radii, and thus of the lengths of the ion–oxygen bonds, in the structure of the inner-sphere complexes formed for each cation started to emerge. This role will be more pronounced after studying the adsorption of zinc ions.

Let us now examine whether the X-ray measurements confirmed the aforementioned theoretical findings. Bragg XSW measurements did not reveal any evidence for specific adsorption of Rb⁺, that is, for the formation of the aforementioned inner-sphere complexes, at the relatively low

Rb⁺ concentrations ($[Rb^+] < 10^{-3}$ M).⁶⁹ These concentrations are necessary to meet the requirements of the XSW measurements, that is, to maintain a small number of Rb⁺ ions in the bulk solution with respect to the number of adsorbed ions. However, the XSW measurements performed at the aforementioned and similar conditions suggested that the hydrated Rb⁺ ions are accumulated in the interfacial region (i.e., in a diffuse layer) but not specifically adsorbed on the surface at detectable concentrations under these conditions (Figure 63B).⁶⁹ In contrast, X-ray measurements performed at very high pH (pH = 12) and high rubidium concentrations ($[Rb^+] = 1$ M) revealed that some of the rubidium ions are adsorbed specifically in the compact region of the interface (see Figure 62) above the tetradentate sites suggested by the theoretical calculations. It is important to note even under these experimental conditions the X-ray measurements do not indicate specific adsorption over bidentate sites as it was suggested by the theoretical calculations for the charged surfaces 3 and 4.⁶⁸ On the other hand, at surface 4 the percentage occupancy of the tetradentate sites (79%) is considerably higher than the corresponding one found at surface 3 (58%). Thus, the charged surface 4, corresponding to fully dissociative adsorption of water molecules, seems to describe better the experimental data than the charged surface 3 corresponding to molecular adsorption of water molecules. This is a very strong evidence that in actual electrolytic solutions the rutile (110) surface is fully hydroxylated. The experimental data showed, moreover, that the height of the so coordinated Rb⁺ ions from the basal plane is equal to 3.44 Å, in fair agreement with the theoretical value for the charged surface 4 (3.55 Å).⁶⁹

The experimental results for this monovalent ion rather suggest the partitioning of the rubidium ions between two states: fully hydrated Rb⁺ ions accumulated in the diffuse layer and specifically adsorbed, partially dehydrated Rb⁺ ions over the tetradentate sites of the surface 4.⁶⁹ The experimental results rather indicate a preference for the former state in a broad range of experimental conditions. The similarity of the theoretical predictions for the Na⁺ and Rb⁺ monovalent ions could imply similar adsorption behavior for the sodium ions.

Finally, it must be mentioned that a recent experimental and more accurate CTR study of the “rutile (110)/RbCl solution” interface ($[Rb^+] = 1$ M, pH = 12) corroborated the previous finding that Rb⁺ ions can be adsorbed as inner-sphere complexes over tetradentate sites.⁷² However, as the authors state, the binding constant of such species on rutile surface is relatively low, and thus in normal experimental conditions these ions mainly behaved as indifferent background electrolyte ions.

3.2.7. Strontium Ions. The adsorption of these cations on the model surfaces was studied more extensively than the adsorption of the cations discussed before.^{68–70} Let us begin with the theoretical predictions.⁶⁸ In the axial density profiles of strontium ions calculated for both charged surfaces, an adsorption peak at 3.20–3.25 Å is illustrated. On the other hand, the lateral density profiles indicated that this peak concerns formation of inner-sphere surface complex over the tetradentate sites, similar to that formed in the case of adsorption of the Na⁺, Ca²⁺, and Rb⁺ ions. The calculated percentage occupancy is equal to 63% and 38%, for surfaces 4 and 3, respectively. These profiles showed, in addition, formation of inner-sphere surface complexes over bidentate sites in agreement with the predictions for the cations previously discussed (surface 4, BOTO (3.55 Å, 21%),

TOTO (4.05 Å, 11%); surface 3, BOTO (3.70 Å, 49%). The heights from the basal plane mentioned above are slightly greater than the corresponding ones calculated for the calcium (also divalent) ions. This is related to the larger ionic radius of the Sr^{2+} ions resulting in higher ion–oxygen bond length in hydrated Sr^{2+} ions (2.64 Å) with respect to the Ca^{2+} hydrated ions (2.46 Å).

The molecular dynamic simulations predicted, moreover, that only 10% of the strontium ions remain fully hydrated and accumulated in the diffuse part of the interface developed above the negative surfaces 3 and 4. These are located at 5.5–6.3 Å above the basal plane with preferred positions above the $\text{Ti}_{6\text{C}}$ atoms for surface 3 and above $\text{Ti}_{5\text{C}}$ atoms for surface 4.⁶⁸

The calculations have, moreover, predicted that the strontium ions do not form inner-sphere complexes on the neutral surfaces 1 and 2.⁶⁸ These ions remain fully hydrated at heights 5.5–6.0 Å from the basal plane of the (110) termination. The peak of the density profile is only 6 times the homogeneous density in the bulk. The lateral distribution of the Sr^{2+} ions is rather flat with increasing density above the $\text{Ti}_{6\text{C}}$ surface atoms. These predictions are in agreement with the observation that negligible adsorption occurs near pzc of polycrystalline rutile where the (110) termination predominates.⁶⁹

Let us now examine whether the X-ray measurements confirmed the aforementioned theoretical calculations.⁶⁹ These measurements showed that the Sr^{2+} ions actually form an inner-sphere complex above the tetradentate sites. The height determined was equal to 3.07 Å in excellent agreement with the theoretical predictions. In contrast, the formation of inner-sphere surface complex above bidentate sites, predicted theoretically for both charged surfaces, is not confirmed by the Bragg XSW study.⁶⁹ On the other hand, at surface 4 the percentage occupancy of the tetradentate sites (63%) is considerably higher than the corresponding one found at surface 3 (38%). This corroborates the view mentioned in the previous paragraph dealing with the adsorption of Rb^+ ions, that the charged surface 4, corresponding to fully dissociative adsorption of water molecules, describes better the experimental data than the charged surface 3, corresponding to molecular adsorption of water molecules, and that this is a very strong evidence that in actual electrolytic solutions the rutile (110) surface is fully hydroxylated.

The Bragg XWS technique was used, moreover, to investigate the sensitivity of Sr^{2+} ions adsorption to changes in the kind and concentration of the background electrolyte as well as in the Sr^{2+} ion coverage.⁷⁰ Measurements were performed at pH = 10.7. To control the ionic strength, NaCl or NaBr was used as background electrolytes over a broad range of concentrations (e.g., $[\text{NaCl}]$: 0, 10^{-2} , 10^{-1} , 1 M). The pH was adjusted with sodium hydroxide aqueous solutions. It was found that the Sr^{2+} height above the basal plane is insensitive to the choice of the background electrolyte and ionic strength. It was, moreover, found that the coherent fraction and thus the coverage of the Stern layer are also largely independent of ionic strength. The above could suggest that the compact region of the interface is mainly covered by the Sr^{2+} ions with respect to the sodium ions. In fact, it was found that the adsorption strength of sodium ions is 4 orders of magnitude lower than that of strontium ions. It was found that the maximum Stern-layer coverage for the Sr^{2+} ions is about 0.45 of the monolayer, with no significant change in the height with the Stern-layer coverage. A monolayer coverage is defined as 1 ion

per TiO_2 (110) surface unit cell.⁷⁰ It was found that the Sr^{2+} hydrated species retain part of the hydration shell upon adsorption, and this limits the coverage achieved. Assuming that the lateral size of the adsorbed hydrated Sr^{2+} ions is similar to that found in solution (6 Å), the maximum coverage in the Stern layer was estimated to be equal to 0.5 of the monolayer, in good agreement with the experimental value mentioned before.

3.2.8. Yttrium Ions. The adsorption state of the Y^{3+} ions was studied using X-ray measurements.⁶⁹ The structure of the adsorption state of these ions on the (110) model rutile surfaces is almost identical to that of the previously studied ions. In fact, these trivalent ions form an inner-sphere surface complex above the tetradentate site. As in the previous cases, the X-ray measurements do not reveal formation of inner-sphere complex above the bidentate sites. In the tetradentate complex, the height of the yttrium ions from the basal plane is equal to 2.75 Å. This value is smaller than the corresponding ones found for the surface complexes above the tetradentate sites discussed before for the Na^+ , Ca^{2+} , Rb^+ , and Sr^{2+} ions. Taking into account the value for the Y^{3+} ionic radius, this relatively low value is rather expected. This finding confirms the dependence on the ionic radius of the ion–oxygen bond length in the hydrated ions and thus of the height from the basal plane in the surface complex above the tetradentate site. This linear dependence is illustrated in Figure 66.⁶⁹ It, moreover, indicates

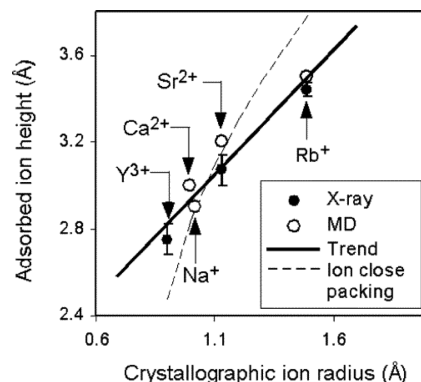


Figure 66. Plot of the values achieved for the height of the cations from the basal plane of the (110) unrelaxed rutile crystal surface versus bare cation radius, for cations adsorbed above a tetradentate site involving two bridging and two terminal oxygen atoms. “●” are X-ray results; “○” are molecular dynamic results for the charged surface 4 (see Table 4). The ions studied are indicated.⁶⁹ Reprinted with permission from ref 69. Copyright 2004 American Chemical Society.

that the height of a cation in the inner-sphere surface complex is rather independent of the ionic charge, as cations with different charges belong to the same line.

3.2.9. Zinc Ions. The adsorption behavior of these divalent cations on the model surfaces was studied more systematically than the adsorption of the cations discussed before by performing theoretical calculations and using X-ray-based techniques.^{68–71,73} Most of the experiments were performed at pH = 8, whereas some experiments were carried out at pH = 6 to test the sensitivity of the zinc adsorption to changes in pH. The adsorption behavior of the Zn^{2+} cations is completely different with respect to those exhibited by the previously presented cations. From the X-ray experiments, it was found that Zn^{2+} adsorbs as inner-sphere surface complex at two

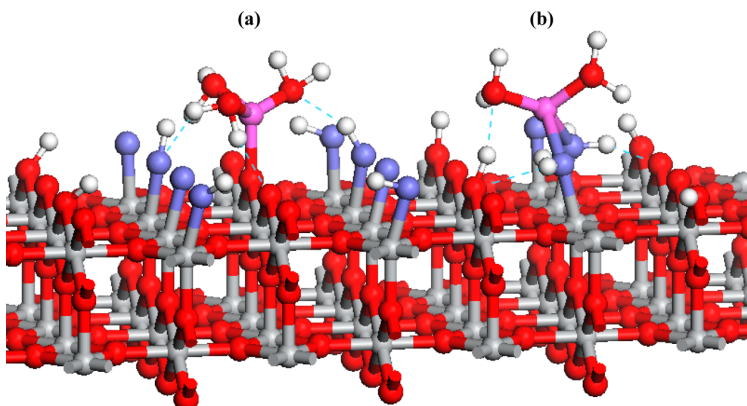


Figure 67. Adsorption of Zn²⁺ ions on the rutile (110) crystal surface deduced from X-ray experiments: (a) adsorption on a monodentate site (BO), (b) adsorption on a bidentate site (TOTO)⁷¹ (Zn atoms: lilac balls).

distinct sites. First, it forms a monodentate complex above one O_{2C} surface atom (BO) (Figure 67a). In this complex, the Zn²⁺ ions are located at 3.12–3.16 Å from the basal plane. Second, it is adsorbed between two neighboring terminal O_{1C} atoms (TOTO) forming a bidentate inner-sphere surface complex (Figure 67b). In this complex, the Zn²⁺ ions are located at 2.6 Å from the basal plane.

These experimental findings agree better with the theoretical predictions with respect to the charged surface 4, corresponding to dissociative water adsorption on the (110) rutile termination. In fact, the theoretical calculations at this surface suggested adsorption on two kinds of sites with bidentate structure (BOTO, 2.95 Å, 48%; and TOTO, 3.40 Å, 39%). In contrast, the theoretical calculations at surface 3 suggested exclusive adsorption over the BOTO sites (3.05 Å, 88%) not confirmed by the X-ray experiments. This again suggests that the negatively charged surface 4 represents better the actual surface configuration. As for the cations presented before, the axial density profiles calculated for zinc ions indicated that these ions are not practically adsorbed on the uncharged surfaces 1 and 2.

The change in the adsorption mechanism was related to the relatively small radius of the Zn²⁺ ions resulting in relatively small length of the ion–oxygen bond in the Zn²⁺ hydrated species (2.06 Å⁶⁸). This length is actually smaller than the minimum one (2.25 Å) required to achieve the bonding of the Zn²⁺ ions with the four oxygen atoms of the tetradeinate site.⁶⁸

The height of the Zn²⁺ ions above the basal planes in the monodentate complex is significantly greater than that in the bidentate complex. In fact, the height for the monodentate site obtained using XSW and EXAFS measurements was found to be equal to 3.12 and 3.16 Å, respectively, whereas the corresponding values for the bidentate sites were found to be equal to 2.6 and 2.51 Å. These heights are insensitive to the pH changes.

In contrast, the experimentally found partitioning of the Zn²⁺ ions between the two sites is sensitive to pH.⁷¹ The Zn²⁺ coverage at the monodentate site is almost 3 times as much as that at the bidentate site at pH = 8, whereas the relative coverage of the two sites is comparable at pH = 6. Moreover, the total Zn²⁺ coverage, which includes the coverages at the compact and the diffuse part of the interface, is also sensitive to pH. It was found to be equal to 0.5 and 0.08 of the monolayer at pH 8 and 6, respectively. This is expected if one takes into

account that the negative surface charge decreases with decreasing pH.

EXAFS results suggested for both sites a 4-fold or 5-fold first shell coordination environment for adsorbed Zn²⁺ ions instead of the 6-fold coordination found for aqueous species at this pH.⁷¹ This is obtained by the removal of more than one water ligand. Thus, Zn²⁺ is adsorbed in two distinct sites with an O coordination shell that it is perturbed from the octahedrally coordinated geometry in solution. In any case, Zn²⁺ aqueous species retain part of the hydration shell upon adsorption, and this limits the coverage achieved. Assuming that the lateral size of the adsorbed hydrated Zn²⁺ ions is similar to that found in solution (6 Å), the maximum coverage in the Stern layer was estimated to be equal to 0.5 of the monolayer, in full agreement with the experimental value mentioned before. Moreover, it was found that adsorption coincides with sorption-induced hydrolysis of the Zn²⁺ aqueous species. Assumption of the sorption-enhanced hydrolysis had facilitated the fitting of macroscopic adsorption and titration data of rutile powder suspensions.⁶⁹

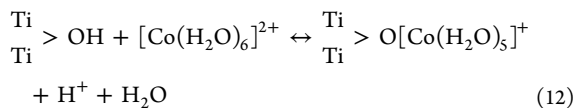
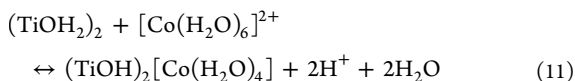
As in the case of the Sr²⁺ ions, the Bragg XWS technique was used to investigate the sensitivity of Zn²⁺ ions adsorption to changes in the kind and concentration of the background electrolyte and in the Zn²⁺ ion coverage as well.⁷⁰ Most of the measurements were performed at pH = 8, whereas some measurements were performed at pH = 10 and pH = 4.3. To control the ionic strength, NaCl or NaBr was used as background electrolytes over a broad range of concentrations (e.g., [NaCl]: 0, 10⁻², 10⁻¹, 1 M). The pH was adjusted with HTr aqueous solutions (where Tr⁻ is trifluoromethanesulfonate, a synthetic noncomplexing, monovalent ion) and buffered with the addition of tris (hydroxymethyl) aminomethane. It was found that the Zn²⁺ height above the basal plane is actually insensitive to the choice of the background electrolyte and ionic strength. It was, moreover, found that the coherent fraction and thus the coverage of the Stern layer are also largely independent of ionic strength. The above could suggest that the compact region of the interface is mainly covered by the Zn²⁺ ions with respect to the sodium ions. In fact, it was found that the adsorption strength of sodium ions is 5 orders of magnitude lower than that of zinc ions.

Finally, it should be mentioned a very recent and very interesting work coming from the same research group.⁷³ The authors studied again the adsorption of Zn²⁺ at the rutile

(110)/aqueous solution interface by performing DFT molecular dynamics simulations. The new significant point in the study was that the calculations were performed at 300 K, bringing thus their system close to the temperature used in the experiments. They were based on their previous experimental data^{70,71} and static calculations,⁷¹ which had concluded that the two most probable configurations were those of Figure 67. These previous results were taken into account when the initial structures were created for their DFMD simulations. The new results revealed almost the same configurations for the adsorbed Zn²⁺ ions. Moreover, the simulations showed that the tetrahedral zinc coordination is more stable than the octahedral one. The hydrolysis of H₂O molecules was observed in the first coordination shell of the adsorbed ions, resulting in formation of hydroxyl groups bonded to Zn. The analysis of MD trajectories showed that, on average, one OH group is bonded to Zn²⁺ in the tetrahedral monodentate site, but zero and two OH groups are also possible. Finally, the calculated energies showed that the tetrahedral bidentate structure of hydrated Zn²⁺ is favored on the rutile surface.

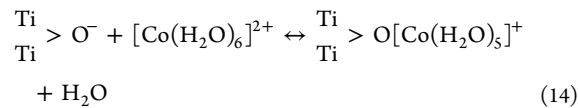
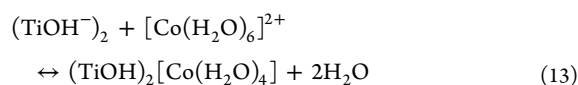
3.2.10. Cobalt(II) Ions. The cobalt(II) ions are important from the catalytic point of view. The adsorption behavior of these divalent cations on various powdered polycrystalline oxides is the subject of a quite recent review.²⁹⁹ The structure of the adsorption state on the (110) termination was studied by Towle et al.⁶⁴ They used a bond valence approach in combination with polarization-dependent grazing-incident X-ray absorption fine structure spectroscopy. The experiments were performed under ambient conditions in a humid atmosphere. The results indicate formation of inner-sphere surface complexes. Specifically, it was concluded that the [Co(H₂O)₆]²⁺ aqua complex is adsorbed above an O_{2C} surface atom by releasing one water ligand and forming a monodentate inner-sphere surface complex. Moreover, this aqua complex is adsorbed on two adjacent terminal oxygen atoms by releasing two water ligands and forming a bidentate inner-sphere surface complex. Thus, the adsorption behavior of the cobalt(II) ions is very similar, but not identical, to that found for the zinc(II) ions. In view of the previous considerations concerning the role of the ionic radii, this may be attributed to the fact that ionic radius of the cobalt(II) ions (0.79 Å) is very close to that of the zinc(II) ions (0.88 Å). The main difference in the sorptive behavior between zinc(II) and cobalt(II) ions is that in the latter case there is not so strong evidence for a decrease of the cobalt(II) coordination upon adsorption from 6-fold into 5-fold or 4-fold. It was, moreover, inferred that the surface reaction scheme is pH-dependent.

At low pH values (pH < 5), the terminal surface oxygen atoms were considered to be doubly protonated, whereas the bridging oxygen atoms are singly protonated. At these pH values, the adsorption is described by the following equilibria:



At pH > 7, the terminal surface oxygen atoms were considered to be singly protonated, whereas the bridging oxygen atoms

were unprotonated. Therefore, in this pH range, the adsorption is described by the following equilibria:



The fact that Co second neighbors are deduced by the X-ray absorption fine structure spectra indicates that some, but not all, adjacent surface sites may adsorb the Co(II) aqua complexes resulting in binuclear surface complexes. In the later, the monomeric units are presumably linked through hydroxo-bridging bonds. The formation of these bonds is accompanied by additional release of protons. This process takes place at relatively high Co(II) surface concentrations. The aforementioned location of the cobalt ions can be alternatively described as adsorption corresponding to Ti-equivalent positions in an extension of the rutile structure above the surface.

3.2.11. Chloride and Bromide Ions. The adsorption of the Cl⁻ ions on the model surfaces was studied by performing only theoretical calculations.⁶⁸ This is because X-ray data are not available due to the low energy of the characteristic X-ray fluorescence line. This line is too strongly absorbed in water to be seen.⁶⁸ In the axial profiles calculated for the neutral surfaces 1 and 2, a very weak peak located at about 5–5.5 Å above the basal plane for surface 1 and 6.5 Å for surface 2 is observed. For surface 2 an additional small peak at about 4.3 Å is also observed. Presumably, this peak is due to the direct attractive interactions of the chloride ions with the hydrogen atoms of the terminal and bridging hydroxyls. The location of these peaks is practically independent of the kind of cation present in the solution.

The lateral distribution of the chloride ions does not indicate any significant lateral ordering. This agrees with the widely accepted view that chloride ions are mainly present in the diffuse part of the interface as species of indifferent electrolyte. From the magnitude of the axial density distribution peaks, it was inferred that the affinity of the Cl⁻ ions for the rutile surfaces is significantly lower than those of the cations presented before. This is rather plausible even for neutral surfaces. In fact, due to the termination of the rutile surface by oxygen atoms, cations are expected to be adsorbed, whereas anions are expected to be repelled. This is expected to be more pronounced for the negatively charged surfaces. It was found a >10-fold weaker tendency of the chloride ions to be adsorbed at distances smaller than 7.5 Å than the cations.

In view of the above, the adsorption of the Cl⁻ ions was also studied at two additional, now positively charged, model surfaces (surfaces 5 and 6). In both surfaces, the surface charge is equal to +0.208 C/m². Titration data on powdered rutile samples indicate that this charge is very high corresponding to suspension pH lower than 2. Surface 5 was obtained from surface 1 by protonating 36 of the 144 unprotonated O_{2C}, whereas surface 6 was obtained from surface 2 by removal of 36 of the 144 terminal hydroxyls (see Table 4). Rb⁺ ions are assumed at the interface to compensate the surface charge.

In the axial density profile of the Cl⁻ ions at surface 5, it was observed a peak at 4.4 Å. It was concluded that this peak

indicates adsorption above the tetradeятate site mentioned before. The O_{2C} atoms of this site are now protonated. It seems that the interaction of the adsorbate with the hydrogen atoms of the coordinated water molecules and bridging oxygens is the factor that determines adsorption. The distance from the basal plane rather suggests that the Cl⁻ ions retain its hydration sphere. An additional peak was observed at 2.7 Å. This presumably corresponds to partially dehydrated Cl⁻ ions, which substitute chemisorbed water molecules above the Ti_{5C} surface atoms.

In the axial density profiles of surface 6, it was observed only one peak at 4.3 Å, reflecting also adsorption above the tetradeyatate site through interactions of the adsorbate with the hydrogen atoms of the bridging and terminal hydroxyls.

Unlike the adsorption of the chloride ions, the location of the bromide ions can be directly probed with XSW.^{69,70} Extrapolation of the experimental measurements at zero time when the sample was first exposed to the X-ray beam gave a surface coverage of 0.04 monolayer. This is approximately the expected value in the bulk solution. Thus, the experimental results indicated that Br⁻ ions are not significantly adsorbed at the compact region of the interface. Moreover, the experimental results indicated negligible ordering of this anion at the interface.⁷⁰

3.2.12. Final Remarks. The work presented in this section shed certainly more light on the structure of the adsorbed species at the "rutile (110) termination/aqueous solution" interface. The new insight that all cations, even those considered as cations of an indifferent electrolyte, may be specifically adsorbed near to the surface undergone partial dehydration could be proved quite useful for improving the modeling with respect to the adsorption at the "TiO₂/aqueous solution" interface in real systems. A first attempt to this direction was done by Ridley et al.³¹² The authors modeled surface charging curves of rutile in NaCl, KCl, and RbCl electrolyte solutions as well as titration curves of NaCl solution/TiO₂ in the presence of Ca²⁺ ions and of NaCl or RbCl solution/TiO₂ in the presence of Sr²⁺ ions. The modeling was based on a combination of the CD-MUSIC model with a Basic Stern approach for the double layer. The predominant crystallographic plane of the rutile used was the (110), and its surface ionization was described by equilibria 5 and 6. On the basis of the fitted CD values, they concluded that for all cations, above neutral pH, the principal adsorption complex is a tetradeyatate inner-sphere complex. In addition, a bidentate species was also fitted, which is predominant in the case of Na⁺, at pH values <10. Moreover, outer-sphere surface species improved the fit of K⁺ and Rb⁺. Concerning Cl⁻, an outer-sphere complex was found. The general conclusion of that work was that the model adopted shows outer-sphere complexation as the predominant mode of adsorption at pH values around pzc and inner-sphere complexation as the predominant mode of adsorption at increasing pH values. The results are generally in good agreement with the theoretical calculations and X-ray studies previously mentioned in this section.

However, some points should be commented. While there is no doubt that the bivalent and trivalent ions presented in the previous sections are mainly specifically adsorbed, located at a plane that is very close to the surface, the experimental results concerning the adsorption of the Rb⁺ ions indicate that only some of these ions are located at this plane even under quite extreme conditions favoring this adsorption mode (pH = 12, [Rb⁺] = 1 M). In contrast, at lower concentration and pH

values, the experimental results suggested that Rb⁺ ions are rather accumulated in the diffuse layer as hydrated species not in full agreement with the theoretical predictions. Taking into account that similar theoretical results were obtained for Rb⁺ and Na⁺ ions, one can not exclude that over a wide concentration and pH range, the latter are also (mainly) nonspecifically adsorbed. This would be in agreement with the observation that similar pzc and iep values are obtained in NaCl aqueous solutions.

Another issue is related to the term "inner-sphere surface complex". This is completely successful for the transition metal ions, which may form complexes, for example, for the cobalt ions that form aqua complexes in aqueous solutions. In these cases, we have actually an exchange of ligands with the surface oxygen atoms and formation of coordinative adsorption bonds. Yet for other ions, for example for alkaline ions present as hydrated species in aqueous solutions with a rather ionic ion–oxygen bond, the term simply describes the direct bonding of the adsorbed ion with the surface oxygen and not the character of the bond. In fact, in these cases the surface bonds are ionic rather than coordinative.

An additional remark concerns the improvement of the "ionization/interfacial" models for describing macroscopic adsorption data of cations on polycrystalline titanium oxide. This was attempted by incorporating some of the molecular scale findings presented in the previous sections (e.g., the location of the ions at the compact region of the interface, the structure of the reception site, the adsorption stoichiometry, the cation distances from the surface related to the extracted capacitance values, and the Ti–O bond lengths to improve the Pauling charge of the surface oxygen atoms). This effort was proved to be generally successful in describing adsorption edges and titration data in the presence of these cations.^{69,312} However, it is notable that the corrected values of the "Pauling" oxygen charges are used for applying the music model instead of the ab initio calculated values. Moreover, the finding of the formation of inner-sphere complexes³¹² might be different, if a three plane model (with a charge distribution of ions between the 1 and the 2 plane) instead of a Basic Stern one would be used.

Another point, also discussed in ref 69, concerns the size of the interface. As was already mentioned in the previous part, molecular dynamic simulations and X-ray experimental results^{67,71,222} indicated that the water exhibits diffusivity and viscosity as close as 15–20 Å from the surface plane, similar to those exhibited in the bulk solution. This finding, obtained over a wide range of ionic strengths, implies a relatively small size for the interface. In contrast, the Debye length of the diffuse layer varies from 3 to 547 Å over a wide range of ionic strengths.⁷⁰ The calculated values of the Debye length are in line with the distance determined between the surface and the "shear plane" of the interface (80 Å in 10⁻⁴ M NaCl solution). The determination of the latter was based on electrokinetic results on rutile powders.³¹⁴ In our opinion, the size deduced from molecular dynamic simulations and X-ray experimental results concerns principally the compact part of the interface and not the whole interfacial region.

Finally, it should be stressed again the finding that the charged surface 4, corresponding to fully dissociative adsorption of water molecules, describes better the adsorption data for cations than the charged surface 3 corresponding to molecular adsorption of water molecules. This is a very strong evidence that in actual electrolytic solutions the rutile (110)

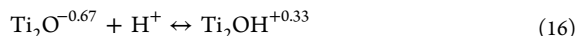
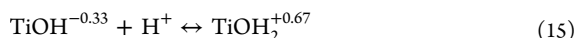
surface is fully hydroxylated though STM experiments,^{208,209} which indicated that water dissociation takes place exclusively on oxygen vacancies but not on the perfect (110) rutile termination. In view of the above, we consider that this critical issue should be further investigated.

3.3. The Polycrystalline Titanium Oxide/Background Electrolyte Solution Interface

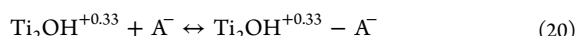
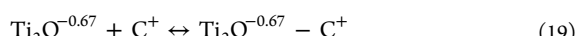
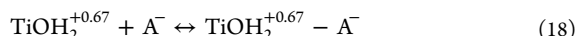
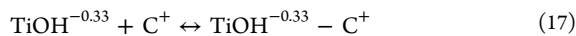
3.3.1. Historical Remarks. To the extent of our knowledge, the first study dealing with the “titanium oxide/electrolyte solution interface” was reported at 1968 by Berube and De Bruyn.³¹⁵ From that time to 2000, about 20 papers devoted to the same subject have been published.^{276,277,315–343} Pure anatase,^{316–321} titania rich in anatase (Degussa P25),^{318,322–327} and rutile^{315,318,328–334} have been used in these studies. In almost all cases, it was considered that specific adsorption of the studied electrolyte ions (Cs^+ , K^+ , Na^+ , Li^+ , NH_4^+ , I^- , NO_3^- , ClO_4^-) does not take place. As was already mentioned, this is the reason for which these types of the background electrolytes, used mainly to regulate the ionic strength, are called indifferent electrolytes. In 1997 Sahai and Sverjensky analyzed a lot of previous experimental results taken on various minerals, among which titanium oxide.³³⁵ However, their analysis was based on the nonrealistic “one site two/pK model”.

3.3.2. Description in Terms of the Music/Basic Stern Model: A Bond Valence Approach. In 2001, the accumulated experimental results on titanium oxide were analyzed by Bourikas et al., on the basis of the music/Basic Stern model.⁹⁸ The main interest in this popular work was focused on the investigation of the primary charging behavior of titanium oxide (pure anatase, titania rich in anatase (P25), and rutile) and on the ion pair formation of the electrolyte ions with the surface oxygen atoms exposed by the various forms of titanium oxide.

Using the music approach and on the basis of older crystallographic data, it was adopted that three kinds of surface groups are exposed on the surface of titanium oxide, irrespective of its crystallographic form. Specifically, it was adopted the development of singly, doubly, and triply coordinated surface oxygen atoms (TiO , Ti_2O , Ti_3O). Using the Pauling bond valence for the Ti^{4+} ions ($4/6 = 0.67$), they calculated the charge of the surface oxygen atoms equal to -1.33 , -0.67 , and 0 , respectively. From the aforementioned empirical equation, related to the music approach, it may be calculated that $pK = -\log K = 3.96$ for the Ti_3O surface oxygen atoms, which means that these oxygen atoms cannot be protonated in the actual pH range (pH: 3–12). Therefore, this group, considered as inactive, was not taken into account for describing the charging behavior of titanium oxide. Moreover, by applying the aforementioned equation to the singly coordinated oxygen atoms and taking into account that these oxygens form two accepting hydrogen bonds with water molecules, it can be calculated that $pK = -\log K = -18.41$, which means that the proton affinity of these oxygen atoms is so high that in contact with water the TiO group is immediately transformed into the TiOH group, in which the oxygen has a charge equal to $1 - 1.33 = -0.33$. In view of the above, it was considered that only the following protonation/deprotonation equilibria are responsible for the acid base behavior of the titanium oxide surface.



On the other hand, an approximate calculation of the logarithm of the protonation constants for reactions 15 and 16, by taking into account the number of the hydrogen bonds formed by each group and using the Pauling valence bond of the titanium atoms, resulted in 6.53 and 5.35, respectively. The similarity of the values of these constants, estimated following a slightly different way by Bourikas et al.,⁹⁸ allowed assuming equal values for the protonation constants, simplifying the modeling. In this modeling, the protonation constant was considered an adjustable parameter. The formation of ion pairs was formulated by considering the following equilibria:



where C^+ and A^- stand for the cation and anion, respectively. Taking into account that the singly and doubly coordinated oxygen atoms present almost equal affinities for the hydrogen ions, they also assumed equal affinities for the ion-pair formation involving the same ion. Therefore, they adopted, as adjustable parameters, only two equilibrium constants: one for the equilibria 17 and 19 and one for the equilibria 18 and 20. The capacitance of the “surface–OHP” layer (Stern layer) is also considered as adjustable parameter. In contrast, on the basis of crystallographic data, it was assumed the common value of 6 atoms/nm^2 for the surface density of $\text{O}_{1\text{C}}$ or $\text{O}_{2\text{C}}$ surface atoms for both anatase and rutile. The limited number of adjustable parameters (four parameters) allowed a more objective fitting of experimental data.

Using the above methodology, a large number of titration and electrokinetic results were successfully described. It was found that the interfacial charging parameters achieved for anatase do not differ significantly from the corresponding ones achieved for rutile, apart from the protonation constants that are slightly lower for rutile. In fact, the mean $\log K$ for rutile is equal to 5.2, whereas that of anatase is equal to 6.3. Taking into account that in the modeling adopted the pzc is equal to $\log K$, the above difference in the $\log K$ values is in agreement with the slightly lower pzc values determined for rutile than those determined for anatase.

The values achieved for the ion pair formation constants with respect to the cations and anions studied (equilibria 17–20) suggested that the interactions of the cations with the negatively charged oxygens are stronger than the interactions of the anions with the positively charged oxygen atoms. This explains the observed shift of the isoelectric point of titanium oxide (defined as the pH value where the potential at the shear plane takes a zero value) to higher pH values at high electrolyte concentrations.^{336,337} The values achieved for the ion pair formation constants indicated, moreover, that the affinity of the cations and anions follows the sequences $\text{Li}^+ > \text{Na}^+ > \text{K}^+ > \text{Cs}^+$ and $\text{Cl}^- > \text{NO}_3^- > \text{ClO}_4^- > \text{I}^-$, respectively. The fitting of the experimental data was related to various values of capacitance centered at two different mean values (0.9 and 1.6 F m^{-2}). The observation that the samples examined, irrespective of its crystallographic form, are classified into two different categories from the viewpoint of the capacitance was attributed to various

reasons such as the surface roughness, the protrusion of surface groups, the difference in $\log K$ between singly and doubly coordinated surface oxygen atoms, and the values of the relative dielectric constants.

3.3.3. The Influence of Temperature. In the last years, several very interesting articles have been published dealing with the subtitle interface.^{314,334,338–343} Most of them concern studies devoted to the investigation of the polycrystalline “rutile/background electrolyte solution” interface over a broad range of temperatures (25–250 °C). These have been reported by Machesky, Wesolowski, and their co-workers.^{314,334,338–340}

Specifically, they studied rutile aqueous suspensions containing NaCl or tertamethylammonium chloride in the aforementioned temperature range.³³⁴ It was found that temperature influences the protonation–deprotonation sites of rutile. It is mainly reflected in the change of the pzc values brought about by the variation of temperature. The pzc value decreased progressively from 5.4 to 4.2 upon increasing temperature from 25 to 250 °C. A “one site/three layer” model has been used to analyze the potentiometric titrations data. It was, moreover, concluded more efficient screening of the rutile surface by the sodium ions relative to chloride or tertamethylammonium ions. A stirred hydrogen electrode concentration cell has been used to perform potentiometric titrations.

In a subsequent article, they studied again the “rutile/aqueous suspension” interface containing NaCl in a temperature range 10–50 °C, now using a conventional glass-electrode autotitrator system.³³⁹ Completely compatible results with those mentioned above have been obtained in the aforementioned temperature range. The experimentally determined pzc values over the temperature range studied agree with the corresponding ones calculated from an extension of the music model. Moreover, the surface titration curves obtained from the titration data using the conventional glass-electrode at various temperatures were successfully analyzed using surface protonation constants derived from the “music/Basic Stern” model.

A recently developed high temperature microelectrophoresis cell was employed by Machesky, Wesolowski, and their co-workers to study the influence of temperature on the isoelectric point of rutile.³¹⁴ This cell allowed ζ -potential measurements at the “rutile/aqueous solution” interface containing NaCl. It was found that the isoelectric point also decreases upon increasing the suspension temperature. Thus, the values obtained at 25, 120, and 200 °C were, respectively, equal to 5.26, 5.13, and 4.50. The combination of the microelectrophoretic mobility measurements with the potentiometric titration data enabled the location of the shear plane to be estimated in the context of the “music/Basic Stern” model.

The adsorption of calcium ions on the “rutile/aqueous solution” interface containing NaCl as indifferent electrolyte was studied in the temperature range 25–250 °C by performing potentiometric titrations and adsorption measurements.³³⁸ It was found that the adsorption of the divalent Ca^{2+} ions is significantly higher than the adsorption of the Na^+ ions. Moreover, it was found that the adsorption of the Ca^{2+} ions increases considerably with temperature at pH values above pzc. This may be attributed to favorable entropic effects related to the increased release of the hydration-sphere water molecules with increasing temperature. The absence of a trend for the ratio “ Ca^{2+} ions adsorbed/ H^+ released” suggested that the mechanism of adsorption of calcium ions does not

change considerably as temperature increases. Finally, it was found that the increase of ionic strength from 0.03 to 0.3 M NaCl caused a decrease in the extent of Ca^{2+} ions adsorption at all temperatures studied. This is presumably due to the increasing competition from Na^+ ions or greater complexation of Ca^{2+} by Cl^- ions.

The adsorption of the neodymium trivalent ions on the “polycrystalline rutile/aqueous solution” interface, containing NaCl as indifferent electrolyte, has been recently studied in the temperature range 25–250 °C using potentiometric titrations and adsorption measurements.³⁴⁰ These ions are strongly adsorbed even at low temperatures and below pzc. The adsorption brings about considerable release of protons from the surface and thus a shift of the pzc to lower values. The extent of adsorption increased considerably with temperature. Although these results are similar to those presented above for the adsorption of Ca^{2+} ions, the magnitude of the negative surface charge enhancement due to the adsorption is much greater for the neodymium trivalent ions than for the calcium divalent ions. A local structure was assumed similar to that deduced by X-ray measurements for the Y^{3+} ions on the (110) rutile surface. According to this tetradentate configuration, the Nd^{3+} ions bond directly with two adjacent terminal and two adjacent bridging oxygen atoms. On the basis of this structure, the experimental results were successfully analyzed on the basis of the “music/Basic Stern” model. A significantly improved model fit at higher temperatures (above 50 °C) and pH values was achieved assuming hydrolysis of the inner-sphere tetradentate adsorption complex. The quality of the model fits was highest from 50 to 150 °C. Although the experimental data were fitted successfully assuming the aforementioned configuration and hydrolysis, one cannot exclude the possibility that some alternate inner-sphere adsorption complexes and/or hydrolysis products may also form.

In the previous paragraphs, we have concisely presented the work of Machesky, Wesolowski, et al. devoted to the study of the polycrystalline “rutile/electrolytic solution” interface over a wide temperature range. The contribution is important because the systematic study of adsorption phenomena at elevated temperatures and over a wide temperature range is very useful for both fundamental and practical reasons. In fact, this approach allows a more complete thermodynamic description of ion adsorption than can be achieved from isothermal data alone. Thus, a surface ionization/electrostatic model, like the “music/Basic Stern” model, can be tested over a broad temperature range. This allows the determination of adsorption equilibrium constants at various temperatures and thus the determination of adsorption enthalpies and entropies. On the other hand, quite important processes, in which adsorption of ions is involved, take place at temperatures higher than room temperature (several important examples are presented in ref 334).

Closing this subsection, we should mention a very recent relevant study of Kyriakopoulos et al.³⁴³ dealing with the influence of impregnation temperature on the pzc of titanium oxide and the loading of Ni upon synthesis of Ni/TiO₂ catalysts. Various titanium oxides were used in that study. It was found a decrease of about 1.5 pH unit in the pzc of the materials, when the temperature increases from 10 to 75 °C. Moreover, a considerable increase of the adsorbed amount of Ni on titanium oxide surface was obtained, by regulating the temperature of the impregnation suspension. This is due to the increase of the factor $\Delta\text{pH} = \text{pH} - \text{pzc}$, which renders the TiO₂

surface more negative. However, the extent of the increase is restricted by the exothermic character of the adsorption process.

3.3.4. Investigation of the Subtle Interface for Anatase of a Nanosized Structure and High Surface Area. A very interesting work reported recently deals with the investigation of the subtle interface for a high surface area anatase of nanosized structure.³⁴¹ The work was mainly motivated by the fact that in most applications the small particle size, tunable properties, and large surface areas of the titanium oxide nanomaterials have been advantageous. On the other hand, the investigation of the protonation/deprotonation properties of a nanosized anatase is also interesting from the viewpoint of fundamental research. In fact, as the size of nanoparticles decreases, more atoms become surface ones. This causes an increase of the broken surface bonds relative to the bulk Ti–O bonds. On the other hand, the large curvature of particles may modify the surface relaxation of surface atoms or their coordination geometry.^{230,276,277} Finally, the area of particle edges, which constitute regions of preferential charge accumulation, also increases with decreasing particle size.

This Review presents characterization and charging behavior results of about 4 nm anatase crystallites in aqueous solutions. The nanoparticles were characterized by small-angle neutron and ultrasmall-angle X-ray scattering, high-resolution transmission electron microscopy, laser diffraction techniques, and nitrogen adsorption–desorption isotherms. On the other hand, the interface was investigated using potentiometric titrations and microelectrophoresis. It was found that the anatase sample comprises primary nanoparticles of about 4 nm diameter. The nanoparticles are crystals with visible facets and lattice patterns. The predominant crystal face, apparent from the lattice spacing, is the (101) plane. These are assembled into larger clusters that exhibit a hierarchical structure. The size of the close-packed clusters of the discrete crystallites is centered in the range of 30–40 nm. In these clusters, the primary crystallites are oriented along specific crystallographic planes. Microscale structures centered at about 2 and 10 μm also exist. These are large aggregates of the smaller clusters and primary particles characterized by fractal surface geometry and porous structure. These structures are stable in aqueous suspensions, even under intense ultrasonic treatment.

It was found that the pzc value (6.85) is practically equal to iep. This value is considerably larger than that of the average (5.9) and median (5.5) values calculated very recently by Kosmulski,³⁴² taking into account 31 different values reported in the literature for anatase samples with quite smaller specific surface area. In contrast, it was found that the proton-induced charge curves, derived from the corresponding potentiometric titration curves, of nanocrystalline anatase were very similar to those of larger rutile crystallites when expressed relative to their pzc values. This indicates that the development of positive and relative charge away from pzc for nanocrystalline anatase is similar to that of TiO₂ larger crystallites.

3.3.5. Description in Terms of a Multisite/Three Plane Model: An Ab Initio Approach. In a previous subsection of this part entitled “Description in Terms of the Music/Basic Stern Model: A Bond Valence Approach”, we presented a popular work⁹⁸ dealing with the investigation of the charging behavior of polycrystalline titanium oxide. The music approach based on older crystallographic data had been used. In that context, it was adopted that on the surface of titanium oxide, three kinds of surface oxygen atoms are exposed (TiO^{1.33−},

Ti₂O^{0.67−}, and Ti₃O⁰) with charges calculated using the empirical Pauling bond valence method.

The recent developments in the surface chemistry of titanium oxide, presented in the first part of this Review, rendered necessary the reinvestigation of the charging behavior of polycrystalline titania on the basis of an even more realistic surface ionization model.¹⁰² In this work, undertaken by our group, the investigation of the whole interface was based on the recently developed “Three Plane” model, whereas “fine structured” potentiometric titration curves obtained at various ionic strengths and over a wide pH range have been used. Microelectrophoretic and streaming potential measurements have been also performed. The electrolytic solutions used contained sodium (or potassium) and nitrate ions. Ab initio calculations were performed in the frame of the DFT for estimating the charge of the titanium and oxygen atoms exposed on the (101), (100), (001), and (103)_f crystal faces of anatase as well as on the (110) crystal face of rutile. As these orientations have smaller surface energy with respect to other ones, it is more probable they are the real terminations of the anatase and rutile nanocrystallites in the titania polycrystalline powders.

On the basis of the ab initio calculations, and taking into account the relative contribution of each crystal face to the whole surface of the titania nanocrystals, we developed the three most probable surface ionization models. These models depict the number of the kinds of the surface atoms, mainly that of the surface (hydr)oxo-groups, the surface density, and the surface charge for each kind of surface atoms. These models and the music one were tested in the frame of the traditional “Stern–Gouy–Chapman” and “Basic Stern” interfacial models, which involve a relatively low number of adjustable parameters. The surface ionization model finally selected (model A) described very well the protonation/deprotonation behavior of titanium oxide in electrolytic solutions. This model is based on the dissociative adsorption of water molecules on the titania low-index crystal faces. It describes also very well the protonation/deprotonation behavior of titania in electrolytic solutions in the frame of the more detailed (but more adaptable to the experimental data) “Three Plane (TP)” model.

The application of the “A/(TP)” model allowed mapping the surface (hydr)oxo groups [TiOH(H) and Ti₂O(H)] of titanium oxide exposed in aqueous solutions. An example for a given ionic strength is illustrated in Figure 68. It may be seen that at

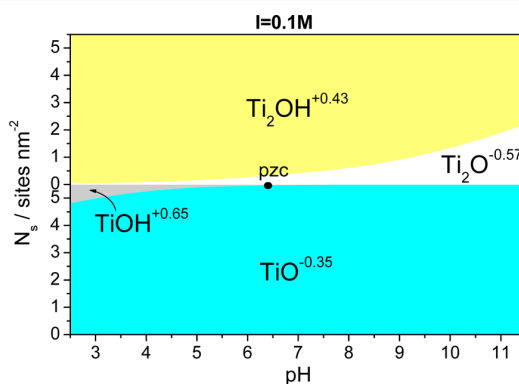


Figure 68. A map of the surface (hydr)oxo groups exposed by titanium oxide in electrolyte solution, at a given ionic strength.¹⁰² Reprinted with permission from ref 102. Copyright 2008 Elsevier.

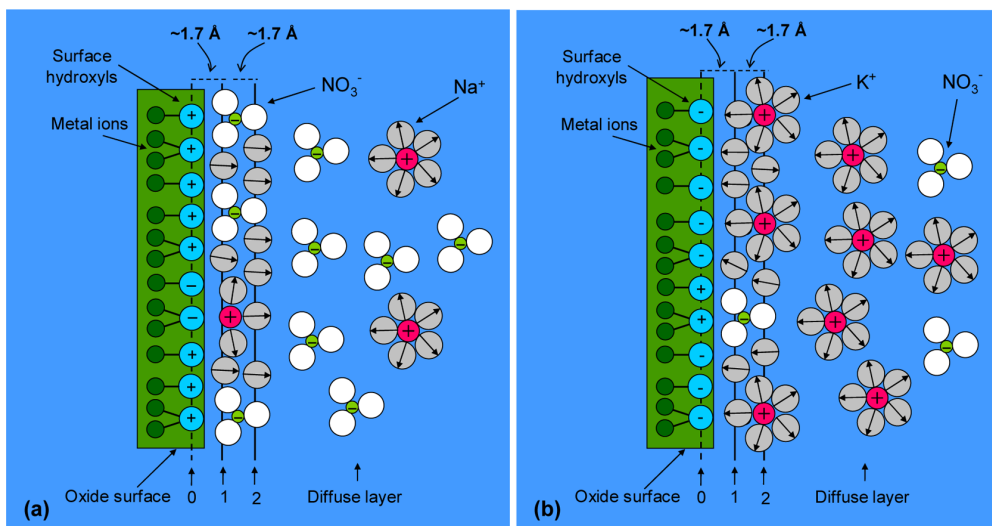


Figure 69. Arrangement of the ions at the (a) “NaNO₃/TiO₂” interface in the case of a positively charged surface and (b) “KNO₃/TiO₂” interface in the case of a negatively charged surface.¹⁰² Reprinted with permission from ref 102. Copyright 2008 Elsevier.

pH values higher than pzc almost all terminal oxygens [TiO] are nonprotonated, whereas even at low pH values the nonprotonated terminal oxygens predominate. The acid–base behavior of the bridging oxygens [Ti₂O] is somewhat different. Thus, even at pH = 10, the greater portion of the bridging oxygens is protonated. This portion increases as pH decreases. This mapping of the surface is very useful for determining the mode of interfacial deposition and the structure of a transition metal ionic species (containing the catalytically active element) deposited on the “titania/impregnation solution” interface at a given pH and ionic strength. Therefore, it is extremely useful for designing the synthesis of a supported catalyst.

Finally, the joint use of microelectrophoretic mobility measurements, streaming potential measurements, and potentiometric titrations in combination with the application of the “A/Three Plane” model provided a detailed structure for the “titanium oxide/electrolyte solution” interface, as well as the location and the distribution of the counterions inside the interface. An example is illustrated in Figures 69 and 70.

It may be observed (Figure 69) that the first (second) charged plane is located on the oxygen atoms of the first (second) water overlayer at a distance of 1.7 (3.4) Å from the surface. It was, moreover, concluded that the distance of the shear plane from the second plane depends strongly on the ionic strength, ranging from 20 Å (0.01 M) to 4 Å (0.3 M) (Figure 70). The width of the mobile-diffuse part of the interface depends also on the ionic strength ranging from 10 Å (0.01 M) to 2 Å (0.3M).

The mean concentration of the counterions is generally higher in the stagnant than in the mobile part of the diffuse layer. Removal of pH from the pzc brings about an increase of the mean concentration in the whole interfacial region as well as a displacement of the counterions from the mobile to the stagnant part of the diffuse layer. The mean concentration of the counterions in the compact layer is generally lower than the corresponding ones in the stagnant and mobile diffuse layers. This preference of the counterions could be attributed to the stereochemical hindrances related to the size of counterions and that of the compact layer. The sodium ions are generally located closer to the surface than the nitrate ions. The small

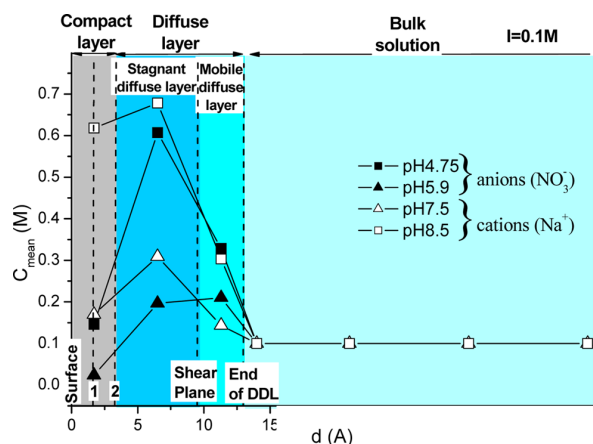


Figure 70. Structure of the “titanium oxide/electrolyte solution” interface as well as the location and the distribution of the counterions inside the interface (C_{mean} : mean concentration of the counterions inside each region/layer of the interface).¹⁰² Reprinted with permission from ref 102. Copyright 2008 Elsevier.

portion of the sodium and nitrate (potassium) ions being in the compact layer is located near the first (second) plane. The mobility of the counterions in the stagnant (diffuse stagnant plus compact) layer decreases as pH removes from pzc. This mobility also decreases with increasing ionic strength.

4. DEPOSITION OF TRANSITION METAL IONIC SPECIES ON THE “POLYCRYSTALLINE TITANIUM OXIDE/ELECTROLYTE SOLUTION” INTERFACE RELATED TO THE SYNTHESIS OF SUPPORTED CATALYSTS

4.1. Regulation of the Mode of Deposition for a Tailor-Made Synthesis of a Supported Catalyst Based on Titanium Oxide

A tailor-made synthesis of a supported catalyst based on titanium oxide is mainly related to the optimization of the size and the physicochemical characteristics of the supported

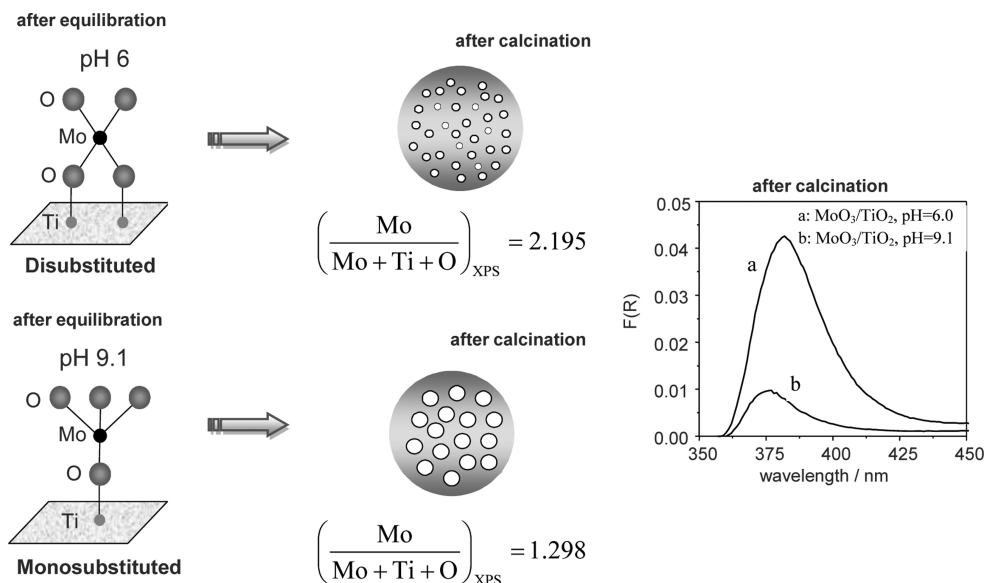


Figure 71. Influence of the mode of interfacial deposition and the type of the inner-sphere Mo complex formed at the interfacial region upon impregnation on the characteristics of the final supported phase (see text for details).³⁷

nanocrystallites of the active element.³⁴⁴ Such an optimization may be first achieved by selecting the impregnation method of deposition of the TMIS to be mounted on the titania surface. Following the conventional “pore volume” impregnation technique and relatively small aging time, the deposition takes mainly place through precipitation/crystallization in the bulk solution (inside or outside the pores of the support) during the drying step, which follows impregnation and aging. This mode of deposition, defined as bulk deposition, results frequently in relatively large supported nanoparticles in the final catalyst and thus in the supported catalysts with relatively low active surface and catalytic activity.^{345,346}

In contrast, following the “equilibrium deposition filtration (EDF)” technique,^{35,37,39,40,347–362} otherwise called equilibrium adsorption, or the “homogeneous deposition precipitation (HDP)” technique,^{363–367} the TMIS are deposited in the step of the equilibration of the suspension through interfacial deposition. This mode of deposition results in relatively small supported nanoparticles on the final catalyst and thus in catalysts with relatively high active surface and catalytic activity.^{33,344,345} In this case, the size of the supported nanoparticles is confined by the size and the parameters related to the interface developed between the support surface and the impregnating solution.³⁶⁸

An interesting idea to overcome, to a certain degree, the main drawback of the “pore volume” technique (the bulk deposition), was presented very recently by Zhu et al.³⁶⁹ They regulated appropriately the pH of the impregnation solution to favor interfacial deposition (deposition through adsorption) at the expense of bulk deposition. The result was the synthesis of supported catalysts (using various supports) with higher dispersion and smaller supported crystallites than the corresponding catalysts prepared with the conventional “pore volume” impregnation technique.

An excellent review dealing with the above-discussed subject has been very recently published by Mäki-Arvela and Murzin.³⁷⁰ The authors clearly show, through the literature survey, that the effect of the preparation technique is very

crucial on the metal particle size in the final catalysts. More specifically, it is illustrated that the preparation parameters are key factors in tuning the size of the supported nanoparticles. A characteristic example concerning the catalysts supported on titania are the gold catalysts (Au/TiO_2). Several studies have shown how the regulation of the impregnation parameters can lead to catalysts with high dispersion (supported gold nanoparticles with very small size) and therefore high efficiency in various reactions.^{371–381}

A much finer tuning of the size of the supported nanoparticles could be achieved by selecting the mode of interfacial deposition. Many relevant studies can be found in the literature, which show different ways for such an achievement.^{33,37,344,345,358,361,363–372,377,379–395} These studies concern synthesis of supported catalysts using various supports (including titanium oxide^{33,37,344,368,371,372,377,379–381}).

An illustrative example is presented in Figure 71.³⁷ It concerns two $\text{MoO}_3/\text{TiO}_2$ catalysts that were prepared by EDF: the first one at pH = 6.0 and $[\text{Mo}]_{\text{initial}} = 1.0 \times 10^{-2}$ M and the second one at pH = 9.1 and $[\text{Mo}]_{\text{initial}} = 1.8 \times 10^{-2}$ M. After drying and calcination (500 °C for 5 h), the catalysts, with almost the same Mo loading, were characterized using diffuse reflectance spectroscopy (DRS) and X-ray photoelectron spectroscopy (XPS). In Figure 71, we schematize the resulting final catalysts and the relevant characterization results. A disubstituted inner-sphere Mo complex is formed in the first catalyst upon impregnation, which is stronger bounded on the support surface than the monosubstituted one, formed in the second catalyst. Therefore, the former is expected to resist more effectively the sintering taking place during calcination, where the inner-sphere complexes are progressively transformed into supported MoO₃ nanoparticles. Thus, smaller MoO₃ supported nanoparticles stronger interacting with the support surface are expected to be obtained for the catalyst prepared at pH = 6.0 as compared to those obtained for the catalyst prepared at pH = 9.1. These are confirmed by the values of the surface atomic ratio $[\text{Mo}/(\text{Mo} + \text{Ti} + \text{O})]_{\text{XPS}}$ determined by XPS as well as by the $F(R_\infty)$ values at ~380

nm estimating the “support-supported particles” interactions (Figure 71). It is worth mentioning that the catalyst prepared at pH = 6.0 proved to be more active than the catalyst prepared at pH = 9.1 in the selective catalytic reduction (SCR) of NO by NH₃.³⁷ This example clearly shows how the regulation of the mode of interfacial deposition may result in supported catalysts with optimum surface characteristics and thus high activity.

However, it must be mentioned that this deposition is a complex procedure involving some kind of electrostatic adsorption, adsorption through hydrogen bonds, formation of inner-sphere surface complexes, interfacial polymerization and precipitation, as well as surface dissolution of the support and formation of a mixed phase with the TMIS. The electrostatically retained TMIS may be accumulated in the diffuse part of the interface and/or located inside the compact region of the interface, usually between planes 1 and 2 in terms of the “Three Plane” model or at OHP in terms of the “Triple Layer” model. On the other hand, the TMIS retained through hydrogen or coordinative bonds are usually located between the surface and plane 1, following the “Three Plane” model, or at IHP according to the “Triple Layer” model.

The relative contribution of each of the aforementioned processes to the whole interfacial deposition depends on the nature of the TMIS, the pH and the concentration of the impregnating solution, the ionic strength, the impregnation temperature, and the impregnation time. Interfacial chemistry provides the general strategy and the methodologies for determining the mode of interfacial deposition, which predominates under given impregnation conditions as well as the interfacial structure of the eventually formed inner-sphere complexes.³³ This allows the “selection” of the proper mode of interfacial deposition or the local structure mentioned above by adjusting the aforementioned impregnation parameters.

However, the determination of the mode of interfacial deposition and the local structure of the eventually formed inner-sphere complexes requires one to model some of the aforementioned interfacial processes using more and more realistic models for the titania surface (surface ionization models) and the interface (electrostatic or interfacial models). In the previous sections, we have realized that the development of realistic surface ionization models (e.g., the music model) requires the elucidation of the structure and energetics of the various surfaces exposed by the anatase and rutile nanocrystals as well as their interactions with the water molecules. The elucidation of the “water–titania surface” interactions and the structure of the adsorbed water molecules helps considerably in the understanding of the above processes. In fact, the structure of the first few water overlayers is indeed critical in the above processes for several reasons. For instance, it affects the ability of the dissolved species to reach the reactive surface atoms. It has been shown that the mode of the water adsorption affects the kind and the concentration of the surface hydroxyls produced by water dissociation and thus the acid–base behavior of the titania surface in aqueous solutions. This influences, in turn, the physicochemical characteristics of the interface developed between the titania surface and the aqueous solution. On the other hand, the structure and energetics of the various surfaces exposed by the anatase and rutile nanocrystals are closely related to their morphology, which, in turn, affects the porosity and the size of the resulting aggregates in the polycrystalline titania used in catalysis. The above considerations illustrate the usefulness of the surface chemistry and

the liquid–solid interfacial chemistry for controlling the synthesis of the supported catalysts.

4.2. Deposition of Transition Metal Ionic Species on the “Polycrystalline Titanium Oxide/Electrolyte Solution” Interface Containing Catalytically Active Elements

4.2.1. Introductory Remarks. In the previous section, we have explained how important it is (for a tailor-made synthesis of a supported catalyst) to elucidate the deposition mode and the structure of the deposited TMIS of a catalytically active element, over a broad range of impregnation parameters. Much effort has been done in the last three decades relative to this purpose from groups working in the field of catalysts synthesis. We have presented the role of the solid–liquid interface in the preparation of a supported catalyst in a recent review article.³³

Concerning the subtitle interface, systematic works related to the aforementioned purpose are not abundant in the literature. Moreover, most of them, even the most systematic ones, are based on the highly hypothetical, but very popular in interface science, “one site/two pK” model for the surface in combination with the “Triple Layer” model for the interface. Only one work of catalytic interest reported so far is based on the “music/Basic Stern” model and the bond valence approach for calculating the charge of surface groups. It concerns the deposition of molybdenum oxo-species on the “titania (rich in anatase)/electrolyte solution” interface.³⁹⁶ Preliminary results based on a modern mapping of the titania “protonation/deprotonation sites”, presented previously, have been only recently reported.³⁹⁷ In the following subsections, we shall present the efforts done so far for investigating the deposition of TMIS containing catalytically active elements on the subtitle interface.

4.2.2. Co(II) Aqua Complexes. Co(II) is present as an octahedral aqua complex $\text{Co}(\text{H}_2\text{O})_6^{2+}$ in the cobalt nitrate aqueous solutions usually used in the synthesis of cobalt supported catalysts. Most of the relevant works have been presented, rather in detail, in a quite recent review article reported by us.²⁹⁹ This is devoted to the adsorption of cobalt species on the interface, which is developed between aqueous solutions and metal oxides used for the synthesis of supported catalysts. Therefore, in this subsection, we will present very briefly these studies. These concern deposition on “polycrystalline rutile/electrolyte solution interface”.

Tewari and Lee reported the first paper dealing with the deposition of the $[\text{Co}(\text{H}_2\text{O})_6]^{2+}$ species.³⁹⁸ It was found that the extent of deposition increases with pH in the range 6–8. This was attributed to the increasing hydrolysis of the aforementioned species. It was also concluded that the increasing surface coverage by the cobalt species brings about interfacial precipitation of $\text{Co}(\text{OH})_2$ under conditions, which do not allow bulk precipitation. Finally, it has been reported that the deposition studied is endothermic.

A carefully study of the deposition of the $[\text{Co}(\text{H}_2\text{O})_6]^{2+}$ ions, also on rutile, has been reported by James³⁹⁹ and James and Healy.^{400,401} An abrupt increase of adsorption at pH just above pzc has been observed. On the other hand, all deposition isotherms converged to almost the same saturation value corresponding to monolayer coverage for hydrated Co(II). Both indicated electrostatic adsorption with the $[\text{Co}(\text{H}_2\text{O})_6]^{2+}$ species located outside the compact region of the interface. In contrast, the considerable deposition observed at pzc and a shift of the iep of the rutile to higher pH values in the presence of the $[\text{Co}(\text{H}_2\text{O})_6]^{2+}$ species strongly suggested specific adsorp-

tion, location of these ions inside the compact region of the interface and, presumably, retention through chemical forces (hydrogen and/or coordinative bonds in the modern terminology). It was, moreover, concluded that above a critical pH value, Co(OH)_2 could be formed on the rutile surface. The interfacial precipitation at pH values lower than those required for bulk precipitation was attributed to the electric field of the surface.

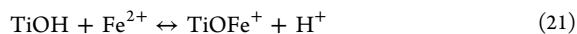
Chisholm-Brawse et al.⁴⁰² studied the subtle deposition using EXAFS. This important work shed more light on the deposition mode. It was found that in the sorption complexes the Co(II) ions are surrounded by six oxygen atoms at an average distance of 2.09 Å, similar to that found for the $[\text{Co}(\text{H}_2\text{O})_6]^{2+}$ ions in electrolytic solutions and for the solid Co(OH)_2 (2.10 Å). This implies octahedral coordination of these adsorbed Co(II) complexes. In the second coordination shell, concerning a Co(II) adsorbed ion, 0.8 Co(II) ions were detected instead of 6 for the model solid phase Co(OH)_2 . The Co–Co distance was found to be equal to 3.14 Å, very similar to that found for the model solid phase Co(OH)_2 . The EXAFS results are much better interpreted by assuming that in the second coordination shell 1.6 Ti atoms are also located at a distance equal to 3.29 Å. This suggests that the Co(II) ion loses one or two water ligands and bonds directly to the surface oxygen atoms of titanium oxide, forming an inner-sphere complex. Moreover, the small number of the Ti atoms in the second coordination shell suggested negligible diffusion of the Co(II) ions into the bulk of rutile. On the other hand, the presence of the second Co(II) neighbor probably indicates that a fraction of the adsorbed Co(II) species forms oligonuclear surface complexes. The finding that the coordination number in the third coordination shell is equal to zero, instead of six in the model Co(OH)_2 , indicates that no interfacial Co(OH)_2 precipitate is formed.

A subsequent more systematic study reported by the same group over a wider range of the Co(II) surface concentrations confirmed, more or less, the aforementioned results.⁴⁰³ It was concluded the formation of inner-sphere Co(II) complexes, the local structure of which depends on the Co(II) surface concentration. Specifically, it was reported that the adsorbed Co(II) forms mononuclear ($0.63 \mu\text{mol m}^{-2}$), small multinuclear ($1.38 \mu\text{mol m}^{-2}$), or larger multinuclear ($4.65\text{--}9.51 \mu\text{mol m}^{-2}$) surface complexes but not Co(OH)_2 surface precipitates.

A few years later, this research group performed a more detailed study of the $[\text{Co}(\text{H}_2\text{O})_6]^{2+}$ deposition on the rutile (110) and (001) crystal faces, using GI-XAFS spectroscopy and single crystals of rutile with specific crystallographic terminations. The main findings of this work concerning the majority (110) crystal surface have been presented in the section entitled “Studies on the Rutile (110) Crystal Termination/Electrolytic Solution Interface: A Bridge between the Surface and Interface Chemistry”.

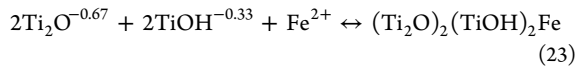
4.2.3. Fe(II) Aqua Complexes. Studies on the deposition of Fe(II) on titanium oxide are rare in the literature [refs 404, 405, and references therein]. A possible reason is the difficulty of working under well-defined conditions where Fe(II) is not oxidized to Fe(III). The first systematic study of the adsorption of Fe(II) on TiO_2 oxide (rich in anatase (P25)) was performed by Nano and Strathmann.⁴⁰⁴ The authors studied both the kinetics and the equilibrium of the adsorption by performing macroscopic adsorption experiments. Adsorption was found to be a very fast process because the majority of the total adsorbed

amount of Fe(II) occurs within the first few hours. Equilibrium adsorption measurements were carried out to quantify the effects of various variables, such as pH, total Fe(II) concentration, and ionic strength, on the extent of Fe(II) adsorption on titanium oxide. As expected, Fe(II) adsorption increases with increasing pH. A typical adsorption edge is observed, where the extent of Fe(II) adsorption increases from 0 to nearly 100% over a narrow pH window. Ionic strength had a negligible influence on the adsorption edge. Moreover, by performing surface complexation modeling (adopting the one site/two pK model in combination with the diffuse layer model), the authors resulted in the following equations, which describe the adsorption of Fe(II) on titanium oxide surface:



According to these equations, Fe(II) is deposited on titania surface, forming two monosubstituted inner-sphere complexes with the TiOH hydroxyls (the second is a hydrolyzed one). It should be mentioned that the model failed to predict adsorption at high initial Fe(II) concentrations and $\text{pH} > 8$, probably due to surface precipitation reactions.

One year later, Hiemstra and Van Riemsdijk⁴⁰⁵ modeled the data of the aforementioned study, using the most realistic CD-music model in combination with the Extended Stern layer model (a refinement of the Basic Stern model).^{311,406} The best fitting of the adsorption data was achieved assuming the formation of a tetradsulfate inner-sphere complex (see eq 23).



This outcome is in general agreement with spectroscopic findings for similar structures found for the adsorption of other divalent cations on the (110) surface of rutile (see section 3.2).

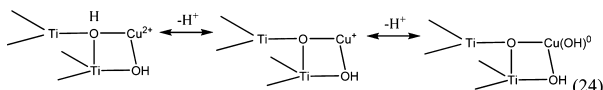
4.2.4. Cu(II) Aqua Complexes. Studies on the deposition of Cu(II) on titanium oxide are also not abundant in the literature.^{407–417} Cu(II) is present as an octahedral aqua complex $\text{Cu}(\text{H}_2\text{O})_6^{2+}$ in the copper nitrate aqueous solutions usually used in the synthesis of copper supported catalysts. Unfortunately, Cu(II) precipitates in relatively low pH values, as compared to other transition metals, thus limiting significantly the possibility of depositing adequate amounts on TiO_2 through an adsorption process.⁴¹⁷

Bleam and McBride⁴⁰⁷ studied the deposition of Cu(II) on titanium oxide using electron spin resonance (ESR) spectroscopy. They found that adsorption of Cu(II) on the surface of titanium dioxide begins at pH = 2 with the occupation of isolated sites having relatively high crystal fields. The adsorbed Cu(II) is in a tetragonal coordination. The sharp increase in the surface coverage of Cu(II) and the appearance of a composite ESR spectrum at pH = 4.4 indicate the formation of hydrous-Cu(II) clusters on the surface of the titanium oxide at that pH, and the surface coverage rises sharply in the pH range of 4.4–4.6. Adsorption is more gradual at pH's above 4.6 and, at the two lowest Cu(II) levels (4.52×10^{-5} and $9.04 \times 10^{-5} \text{ M}$), is complete by pH = 6.1. Precipitation occurs at pH = 6.2 in the systems with an initial Cu(II) concentration of $3.61 \times 10^{-4} \text{ M}$.

At almost the same period, Ottaviani et al.⁴⁰⁸ studied also the adsorption of Cu(II) on titanium oxide by ESR spectroscopy. The spectra revealed that Cu(II) is specifically adsorbed forming inner-sphere complexes at which one or two of its water ligands are substituted by surface hydroxyls. At relatively

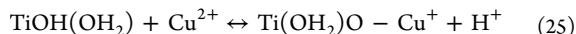
high pH values (~ 8), clusters of adsorbed Cu(II) seem to be formed, which is probably the result of a surface precipitation of hydrolyzed Cu(II).

Ludwig and Schindler⁴⁰⁹ studied the adsorption of Cu(II) on anatase based on potentiometric titrations and adsorption experiments. They explained the adsorption behavior in terms of a surface complexation model. The receptor surface groups were defined as pairs consisting of a terminal and a bridged hydroxyl group. They described satisfactorily their experimental results, proposing the following structures for the binary Cu(II) complexes formed on the titanium oxide surface:



The Cu(II) uptake increases with the pH of the suspension, and complete adsorption occurs at a pH of 7.0, where the predominant surface species is the right one, in the above schematic representation (eq 24). A similar bidentate inner-sphere complex was proposed later by Konstantinou and Pashalidis⁴¹⁶ to describe their results on the adsorption of Cu(II) on TiO₂.

Similar studies based on surface complexation modeling of the adsorption of Cu(II) on TiO₂ were performed by Yang et al.^{410–412} By adopting the “one site/two pK” and diffuse layer models, they described the adsorption experiments using the following surface reaction:



This equation suggests a monodentate inner-sphere type of complex formation between Cu(II) and the TiO₂ surface, in contrast to the bidentate structure proposed in the previous work. In addition to this species, the authors should have taken into account copper precipitation as Cu(OH)₂ occurred above pH 5 with 10⁻³ M Cu(II) concentration, to describe their adsorption experiments at high pH values and concentrations. Finally, the authors studied the influence of the ionic strength and the type of background electrolytes on the adsorption. They found that the adsorption behavior of Cu(II) was similar, independent of the type of background electrolyte ions, over the entire pH range. The adsorption curves shifted to a lower pH as the ionic strength increased due to the variation of electrostatic interaction. Later, Barakat⁴¹⁵ explained his results concerning the adsorption behavior of Cu(II) on TiO₂ assuming the same surface species, as it is described in eq 25. Moreover, this species can undergo surface hydrolysis reaction as pH increases, whereas at alkaline pH (>8), bulk precipitation of Cu(OH)₂ occurs rather than adsorption.

A very interesting and thorough study on the adsorption of Cu(II) onto titanium oxide was published by Poznyak et al.⁴¹³ The adsorption was performed on sol–gel-derived nanostructured TiO₂ thin films and powders and was studied using electrochemical methods, ESR, XPS, and electroreflection spectroscopies. The combined use of these techniques allowed one to obtain important information on the adsorption behavior of Cu(II) ions on the titanium oxide surface and on the nature of species formed as a result of the adsorption. It was found that at least four types of copper species formed on the TiO₂ surface after the adsorption of aqueous Cu²⁺ ions:

(a) Individual Cu²⁺ ions coupled to the surface Ti(IV) ions via oxygen. This type of surface species is dominant when

Cu(II) ions are adsorbed from the dilute solutions and at lower values of the pH.

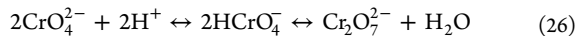
(b) Isolated ions of monovalent copper formed as a result of the partial reduction of the adsorbed Cu(II) ions by electrons of the TiO₂ matrix. The surface concentration of these species averages ca. 10% of the total surface concentration of the adsorbed copper ions.

(c) Clusters of Cu²⁺ ions. The amount of these species increases with increasing Cu²⁺ concentration in solution and pH.

(d) Copper hydroxide particles. These particles dominate when adsorbing from the concentrated Cu²⁺ solutions and at higher pH (>5). At pH = 6, they constitute most (80–90%) of the adsorbed copper.

Another study of the adsorption of Cu(II) onto anatase was performed by Kim et al.⁴¹⁴ This was a macroscopic-only study because the interest of the authors was focused on the removal of Cu(II), as a toxic element, from aqueous solutions. It was found that adsorption is a Langmuir type and the adsorbed amount of Cu²⁺ increases with pH from 2 to 5 and remains constant over pH 5. Moreover, the adsorption amount increases with increasing temperature from 15 to 40 °C.

4.2.5. Cr(VI) Oxo-species. Cr(VI) is present as oxo-species (CrO₄²⁻, HCrO₄⁻, and Cr₂O₇²⁻) in aqueous solutions. The relative concentration of these species depends on pH and Cr(VI) concentration. The following equations describe the equilibria between these species.



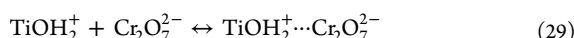
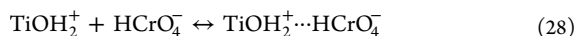
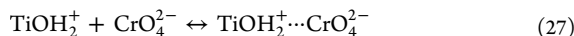
It is obvious that at low pH's and high Cr(VI) concentrations, the equilibrium is shifted to the right. Formation of Cr₃O₁₀²⁻ and other polyanions is also possible, but in very acidic solutions.⁴¹⁸ Interesting issues from the viewpoint of catalyst synthesis are the macroscopic adsorption behavior of titania (that is, the variation of its deposition capacity with pH and Cr(VI) concentration), the mode of interfacial deposition (the location of the adsorbed oxo-species inside the interface and the nature of the sorptive “bond”), the interface speciation, and, finally, the surface structure of the deposited surface species. These issues are examined in the following three works.

The first systematic study devoted to the deposition of the Cr(VI) ions on titania (anatase) is based on macroscopic deposition experiments.⁴¹⁹ This study revealed that the deposition is a quite slow process. Thus, more than 24 h was required for the saturation of the adsorptive sites to be achieved. The extent of deposition increases with decreasing pH, whereas measurable deposition occurs at pH values below 8. Inspecting the deposition isotherm obtained at pH = 5, it was inferred, rather qualitatively, that at very low Cr(VI) concentration the Cr(VI) oxo-species are deposited through irreversible strong adsorption. A concentration interval is followed where the adsorbed amount of the Cr(VI) ions depends weakly on the Cr(VI) concentration in the solution. It was concluded that at relatively high Cr(VI) concentration, the deposition proceeds via the adsorption of the Cr₂O₇²⁻ ions following a Langmuir-type isotherm. Finally, an increase of the titania depositing capacity was achieved by pretreating it with H₂O₂. The macroscopic observations were explained developing a deposition mechanism based on a charged surface comprised from negative sites (surface oxygen atoms) and positive ones (unsaturated Ti atoms). In view of the structure of the titania surface in contact with water molecules at room

temperature, described in this Review, such a surface model is obviously not realistic.

The second work dealing with the aforementioned deposition involved macroscopic deposition experiments, systematic thermodynamic analysis of the deposition isotherms, obtained at various pH's in the region 4.5–8.0, and microelectrophoretic mobility measurements.⁴²⁰ Titania containing 80% anatase and 20% rutile has been used. The “one site/two pK//triple layer” model was implied, although it is not explicitly stated. It was found that the extent of deposition increased with a pH decrease from 8.0 to 4.8. Further decrease in pH caused a considerable decrease in the extent of deposition. It was, moreover, concluded that the deposited Cr(VI) oxo-species are located on energetically equivalent surface sites at the IHP (plane 1) of the interface. The deposition sites are protonated and neutral surface hydroxyls, assumed to be present in the context of the adopted “one site/two pK” model. Strong lateral interactions are exerted between the deposited Cr(VI) oxo-species.

A step further toward the “interfacial speciation” of the deposited Cr(VI) oxo-species was pointed out after the publication of the third work.⁴²¹ The development of a quantitative thermodynamic methodology, based on the “one site/two pK//triple layer” model, allowed one to take advantage of the experimental results reported in ref 420 and successfully handle the various deposition equilibria of the Cr(VI) oxo-species. It was concluded that the deposition of these species takes place, on both anatase and rutile surfaces comprised of the titania used, following the equilibria:

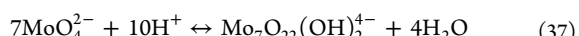
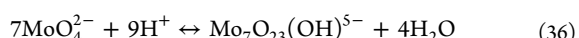
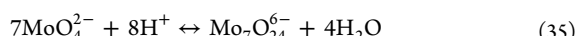


In the above equilibria, by “...” and “—” we denote, respectively, an electrostatic and a chemical (coordinative) bond. A detailed interface speciation has been obtained at various pH values. This speciation revealed that the deposition on the anatase regions is markedly greater than that on the rutile ones. Moreover, according to this speciation at pH's 7.5 and 8, the deposition takes place exclusively through the equilibria 30 and 31, by surface reactions with the neutral surface hydroxyls resulting in the formation of the surface species illustrated in the right-hand side of these equilibria. In the pH range 6.0–4.0, all equilibria contribute to the deposition. The only exception is that equilibrium 30 does not practically contribute at pH values lower than or equal to 4.5. However, in the pH range 6.0–4.0, the deposition through electrostatic adsorption (equilibria 27–29), mainly that of the HCrO_4^- ions, predominates. In all cases, it was inferred that the rhs parts of the surface species formed are located at the IHP (plane 1) of the interface whereas lateral attractive interactions are exerted between them, presumably through water molecules. The intensity of these interactions increases with the charge of the deposited Cr(VI) oxo-species. Although this work provided a more or less successful interface speciation, very useful for regulating the

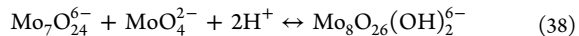
relative concentration of the deposited Cr(VI) oxo-species upon preparing Cr/TiO₂ catalysts via interfacial deposition, the surface structures achieved for these species strongly depend on the rather arbitrary “one site/two pK” model adopted. Very recently, we have reinvestigated the deposition of the Cr(VI) oxo-species on the aforementioned titania assuming the mapping of the titania protonation/deprotonation sites recently developed by us (described in a previous section) and the modern “Three Plane” model as well. The surface structures achieved are presented in the last section of this part.

4.2.6. Mo(VI) Oxo-species. Molybdenum species supported on various oxidic supports are used in several catalytic reactions (e.g., oxidation,^{422–426} metathesis,^{427,428} esterification and transesterification,^{429,430} hydrotreatment of oil fractions,^{353,358–360,431–439} ammonoxidation,⁴⁴⁰ etc.). Systematic studies devoted to the investigation of the deposition of the monomeric and polymeric Mo(VI) oxo-species on the “polycrystalline titania/electrolyte solution” interface are not abundant in the literature.^{396,441–444} As in the case of the Cr(VI) oxo-species, interesting issues from the viewpoint of catalyst synthesis are the macroscopic adsorption behavior of titanium oxide, the mode of interfacial deposition, the interface speciation, and, finally, the surface structure of the deposited surface species.

Mo(VI) is present as oxo-species in aqueous solutions. The presence and relative concentration of these species depend on pH and Mo(VI) concentration.^{445,446} The following equations describe the equilibria between these species:



At pH values above 6, the tetrahedral MoO_4^{2-} species are exclusively present in aqueous solutions. These can be protonated at lower pH values forming H_2MoO_4 , although the presence of HMnO_4^- ions is uncertain.⁴⁴⁵ A decrease of pH at Mo concentrations above 10^{-4} M results in the formation of the heptamolybdate polyanions, $\text{Mo}_7\text{O}_{24}^{6-}$. Further decrease of pH leads to the progressive protonation of these species (single, double, or even triple protonation). At pH values lower than those used in the usual impregnation procedures, other types of polymeric species are formed. For example, $\text{Mo}_8\text{O}_{26}(\text{OH})_2^{6-}$ polymeric species are formed following the equilibrium:

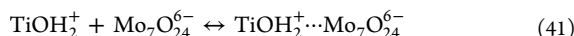
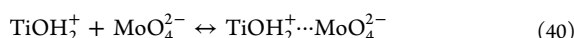


These species tend to polymerize presumably resulting in a precipitate.⁴⁴¹

A work dealing with the deposition of the subtitle species on the “polycrystalline titania (rich in anatase)/electrolyte solution” interface has been reported by us in 1992.⁴⁴² It was found that the extent of deposition increases with decreasing pH. The deposition mechanism was studied in the context of the “one site/two pK//triple layer” model, using deposition experiments in the pH range 9–4.6, pH measurements in the absence and presence of the species to be deposited, potentiometric titrations, and microelectrophoretic mobility measurements. Comparison of the deposition data with the

surface charge of titanium oxide determined at various pH values indicated that the groups responsible for the creation of the deposition sites are the neutral, but mainly the protonated surface hydroxyls. It has been, moreover, concluded that upon deposition the polymolybdates are transformed to a large extent into MoO_4^{2-} ions. The latter are deposited at energetically equivalent sites located at IHP (plane 1) of the triple layer, whereas relatively weak lateral interactions are exerted between the adsorbed molybdates.

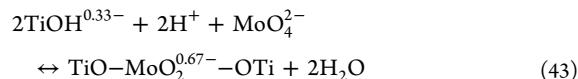
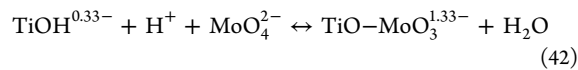
The development of the quantitative thermodynamic methodology, mentioned above with respect to the deposition of the Cr(VI) oxo-species, allowed us to take advantage of the experimental results reported in ref 442 and handle the various deposition equilibria of the Mo(VI) oxo-species to obtain an interface Mo speciation.⁴⁴³ It was found that the deposition of the MoO_4^{2-} and $\text{Mo}_7\text{O}_{24}^{6-}$ species on the surface of the anatase patches of the titania used takes place mainly by the following equilibria:



In the above equilibria, by “...” and “—” we denote, respectively, an electrostatic and a chemical (coordinative) bond. Specifically, it was found that in the pH range 9–7 the deposition takes place exclusively through the equilibrium 39 that is by reaction of the MoO_4^{2-} with the neutral surface hydroxyls. The deposition of the MoO_4^{2-} and $\text{Mo}_7\text{O}_{24}^{6-}$ species on the protonated surface hydroxyls through electrostatic adsorption (equilibria 40 and 41) starts, respectively, at pH 7.0 and 6.4. The same equilibria describe the deposition of the aforementioned Mo(VI) species on the rutile patches, although the extent of deposition is very small. A preference for deposition of the MoO_4^{2-} monomeric species with respect to the $\text{Mo}_7\text{O}_{24}^{6-}$ polymeric ones was found over the whole pH range studied. This was attributed to the negative charge located at IHP, which inhibits the deposition on it of the highly negatively charged $\text{Mo}_7\text{O}_{24}^{6-}$ ions. It was finally inferred that lateral, attractive, interactions are exerted between the deposited Mo(VI) species through water molecules located at IHP, whereas the magnitude of these interactions increases with the charge of the deposited Mo(VI) species. The validity of the interfacial speciation achieved is limited by the “one site/two pK//triple layer” model adopted, although it has been quite useful in the synthesis of supported Mo(VI)/ TiO_2 catalysts.

To overcome the aforementioned limitation in the validity of the interfacial Mo(VI) speciation and approach better the local structure of the deposited Mo(VI) oxo-species, the same system has been reinvestigated several years later using data drawn from potentiometric titrations, deposition experiments, and proton-ion titrations.³⁹⁶ The latter technique is a very effective experimental methodology that had been previously popularized by Hiemstra and Van Riemsdijk.^{447,448} The experimental data were analyzed on the basis of the “music model” applied for the titanium oxide surface.⁹⁸ This “two sites” surface ionization model has been presented in detail in the subsection entitled “Description in Terms of the Music/Basic Stern Model: A Bond Valence Approach”. As was already stated, the charges of the two different kinds of the surface protonation/deprotonation sites have been calculated using the Pauling bond valence approach. Concerning the interface, the

Three Plane model has been applied. In this model, the ions of the background electrolyte were located at plane 2 as point charges (Basic Stern approach), whereas the charge of the deposited MoO_4^{2-} and $\text{Mo}_7\text{O}_{24}^{6-}$ species is spatially distributed in the interface. It was found that the deposition of the MoO_4^{2-} and $\text{Mo}_7\text{O}_{24}^{6-}$ species may be successfully described on the basis of the aforementioned more realistic modeling over a large pH (4–9) and Mo(VI) concentration range. Concerning the interface speciation, it was found that in the entire parameters range, the monomeric MoO_4^{2-} species are adsorbed by reacting with the singly coordinated surface groups ($\text{TiOH}^{0.33-}$) forming inner-sphere surface complexes. At high pH values, a monodentate structure is favored, whereas a bidentate structure predominates at low pH values. In both cases, the Mo(VI) is located between the zero plane (surface plane) and plane 1 of the Three Plane model, whereas the oxygen atoms of the MoO_4^{2-} species directed to the solution side are located at plane 1. The formation of the inner-sphere complexes may be formulated as follows:



In the above equilibria, by “—” we denote a chemical (coordinative) bond. The charge of the deposited monomeric species is distributed between the surface plane and the plane 1.

At high Mo concentrations and below pH 5.5, the $\text{HM}_7\text{O}_{24}^{5-}$ polymeric species is additionally deposited as an outer-sphere surface complex covering approximately 12–14 reactive surface groups. These are retained through electrostatic/hydrogen-bonding forces. The charge of the $\text{Mo}_7\text{O}_{24}^{6-}$ part of the polymer is distributed symmetrically (−3, −3) between planes 1 and 2, whereas hydrogen is located at plane 1. A portion of the positive charge of the surface groups is transferred from the surface to plane 1, indicating the formation of hydrogen bonds between the surface hydroxyls and the oxygen atoms of the polyanion, acting as proton acceptors.

Comparison of the interface speciation achieved on the basis of the “one site/two pK//triple layer” model with that obtained on the basis of the “two sites/one pK//three plane model” shows that there are important differences. In the second case, it was inferred the formation of bidentate inner-sphere complexes, the absence of deposition through electrostatic adsorption of the MoO_4^{2-} species, and the deposition of the polymeric Mo(VI) through electrostatic/hydrogen-bonding forces on surface sites comprised from 12–14 reactive surface groups. Moreover, the second approach allows one to develop a clearer picture concerning the location of the deposited Mo(VI) oxo-species in the interface.

4.2.7. V(V) Oxo-species. It is well-known that the $\text{V}_2\text{O}_5/\text{TiO}_2$ catalysts are used industrially for the selective reduction of NO by NH_3 .^{35,36,38–41} V(V) is present as monomeric and polymeric oxo-species in aqueous solutions used in impregnations for the synthesis of the aforementioned catalysts (VO_4^{3-} , HVO_4^{2-} , H_2VO_4^- , $\text{V}_2\text{O}_7^{4-}$, $\text{V}_3\text{O}_9^{3-}$, $\text{V}_4\text{O}_{12}^{4-}$, $\text{V}_{10}\text{O}_{27}^{4-}$, $\text{V}_{10}\text{O}_{28}^{6-}$, and $\text{HV}_{10}\text{O}_{28}^{5-}$). The relative concentration of these species depends largely on pH and V(V) concentration, and this had rendered very difficult the achievement of an interfacial speciation. However, a systematic theoretical approach allowed finally the detailed study of the deposition

of the subtle species on a “polycrystalline anatase/electrolyte solution” interface.⁴⁴⁹ This deposition was studied over a wide pH (8.0–4.5) and V(V) concentration range using deposition experiments, potentiometric titrations, and microelectrophoretic mobility measurements. The extent of deposition increases with decreasing pH. The interface speciation was proved to be quite complicated, as 12 deposition equilibria were required to describe the whole deposition over the pH range studied. However, inspection of the deposition isotherms, derived for each of the surface species formed, shows that there is a preferential deposition of the monomeric species (mainly that for HVO_4^{2-} and H_2VO_4^-) with respect to the polymeric ones. These isotherms showed, in addition, that the electrostatic adsorption on TiOH_2^+ surface groups is predominant at relatively low pH values. In contrast, at relatively high pH values, the deposition proceeds mainly via surface reaction with the neutral surface hydroxyls (TiOH), resulting in surface oxo-species in which V(V) is retained to the surface through a chemical (coordinative) bond ($\text{Ti}-\text{O}-\text{V}$). The interfacial speciation achieved in this work proved to be very useful to control the synthesis procedure.³⁵

However, as was already mentioned for the deposition of the Cr(VI) and Mo(VI) oxo-species, the validity of the interfacial speciation achieved is limited by the “one site/two pK//triple layer” model adopted. Work is now in progress in our laboratory to investigate the deposition of the V(V) oxo-species assuming the mapping of the titania protonation/deprotonation sites recently developed by us¹⁰² and the modern “Three Plane” model as well.

4.2.8. Recent Efforts Based on a Modern Mapping of the Titanium Oxide Protonation/Deprotonation Sites and the Three Plane Model. In the last years, we attempt to elucidate the deposition mode and the surface structure of the Cr^{6+} , Mo^{6+} , W^{6+} , V^{5+} oxo-species as well as Co^{2+} , Ni^{2+} , and Cu^{2+} aqua complexes deposited on the “polycrystalline titanium oxide/electrolyte solution” interface.^{103–107,450,451} The work concerns a titania (rich in anatase) used industrially for the synthesis of supported catalysts and a broad range of impregnation parameters. This is based on a very modern mapping of the protonation/deprotonation sites developed on the titanium oxide surface (see the subsection entitled: “Description in Terms of a Multisite/Three Plane Model: An Ab Initio Approach”). Potentiometric titrations, microelectrophoresis, macroscopic adsorption experiments, UV-vis-NIR diffuse reflectance spectroscopy (DRS), laser Raman spectroscopy (LRS), and electron paramagnetic resonance (EPR) spectroscopy have been performed.

The interfacial deposition of the $[\text{Co}(\text{H}_2\text{O})_6]^{2+}$ and $[\text{Ni}(\text{H}_2\text{O})_6]^{2+}$ aqua complexes was studied at 25 °C, pH range 6.0–7.5, metal concentration range 10^{-4} to 2×10^{-2} M, and ionic strength $I = 0.1$ N.⁴⁵⁰ There was not any experimental evidence for interfacial precipitation or titania surface dissolution. It was, moreover, found considerable deposition even at pzc and considerable decrease of pH upon adsorption. Moreover, it was observed that the presence of the aqua complexes in the impregnating solution brings about an important shift of the pzc (iep) to lower (higher) values and a decrease of the electrokinetic charge or zeta potential values determined at various pH's. Finally, a value equal to ~2 was determined for the ratio “amount of H^+ ions released/amount of cationic species adsorbed”. The above indicated the formation of mainly mononuclear and a small quantity of oligonuclear inner-sphere complexes under our experimental

conditions. Moreover, the value for the aforementioned ratio suggested a disubstituted local structure for the deposited Co(II) and Ni(II) mononuclear precursor species (in the case of Ni(II), a monosubstituted structure is also formed).⁴⁵⁰ The application of these results in combination with UV-vis-NIR DR and EPR spectra recorded after impregnation and semiempirical quantum mechanical calculations allowed a quantitative modeling based on the above-described mapping of the protonation/deprotonation sites developed on the titania surface.^{103,104} This modeling provided clear pictures for the structure of the deposited Co(II) and Ni(II) species. Two representative pictures are illustrated in Figures 72 and 73.^{103,104}

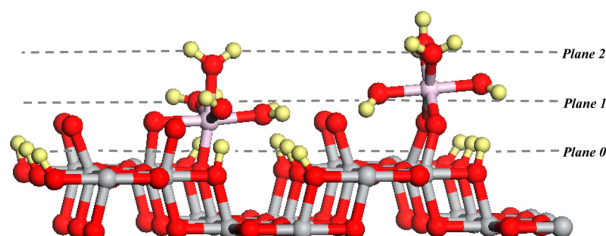


Figure 72. Schematic representations of the monohydrolyzed ($\text{TiO}-\text{Ti}_2\text{O}$) and the dihydrolyzed ($\text{TiO}-\text{TiO}$) disubstituted configurations on the anatase (100) crystal face formed upon deposition of the $[\text{Co}(\text{H}_2\text{O})_6]^{2+}$ ions onto the titania surface at low and medium Co(II) surface concentrations¹⁰³ (Ti atoms, gray balls; H atoms, yellow balls; O atoms, red balls; Co atoms, pink balls). Reprinted with permission from ref 103. Copyright 2009 Wiley-VCH.

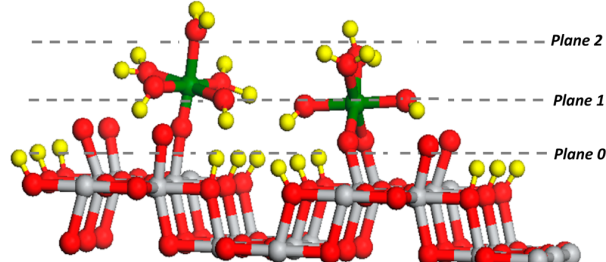


Figure 73. Schematic representations of the monosubstituted dihydrolyzed (TiO) and the disubstituted dihydrolyzed ($\text{TiO}-\text{TiO}$) configurations on the anatase (100) crystal face formed upon deposition of the $[\text{Ni}(\text{H}_2\text{O})_6]^{2+}$ ions onto the titania surface¹⁰⁴ (Ti atoms, gray balls; H atoms, yellow balls; O atoms, red balls; Ni atoms, green balls). Reprinted with permission from ref 104. Copyright 2011 Wiley-VCH.

The study of the interfacial deposition of the $[\text{Cu}(\text{H}_2\text{O})_6]^{2+}$ aqua complexes is still in progress. The first published macroscopic results⁴¹⁷ have shown that the adsorption of copper species on the titanium oxide surface is a rapid process, which is not affected by the ionic strength value. By increasing the pH, the adsorbed amount of Cu^{2+} ions increases. However, a significant limiting factor in the working pH is the bulk precipitation, which occurs at relatively low pH values (e.g., at a concentration of 10^{-3} M, Cu(II) precipitates at a pH value of 6.5). Moreover, preliminary results of the application of electrochemical techniques and adsorption experiments in combination with EPR spectroscopic results show that the Cu^{2+} species are presumably retained on the titania surface by coordinative bonds. The quantitative fitting of these results,

which is now performed, is expected to elucidate the exact local structure of the Cu(II) complexes formed on the titania surface.

The interfacial deposition of Cr⁶⁺, W⁶⁺, and Mo⁶⁺ oxo-species was studied at 25 °C, pH range 4.0–9.0, metal concentration range 2×10^{-5} to 3×10^{-2} M, and ionic strength $I = 0.1$ N.^{105–107} Surface dissolution of the support does not take place even in the presence of the Cr⁶⁺, W⁶⁺, or Mo⁶⁺ oxo-species in the impregnating solution.

Concerning the W⁶⁺ or Mo⁶⁺ oxo-species, it was found considerable deposition at pH > pzc, considerable (very small) increase of pH upon deposition of the W⁶⁺ or Mo⁶⁺ oxo-species at pH's > (<)6, significant shift of the pzc (iep) to higher (lower) values brought about by the presence of the W⁶⁺ or Mo⁶⁺ oxo-species in the impregnating solution, and relatively high values for the ratio “amount of H⁺ ions adsorbed/amount of W⁶⁺ (Mo⁶⁺) ions adsorbed” at various pH's.^{106,107} These results indicate deposition of the W⁶⁺ or Mo⁶⁺ oxo-species through coordinative and/or hydrogen bonds. The application of these results in combination with laser Raman spectra recorded after impregnation allowed a quantitative modeling based on the above-described mapping of the protonation/deprotonation sites developed on the titania surface. This modeling provided clear pictures for the structure of the deposited W⁶⁺ (Mo⁶⁺) oxo-species at various pH's. An example is given in Figure 74, where the local structures of the deposited

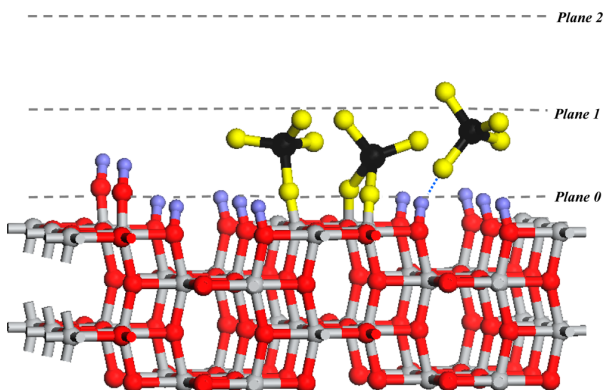


Figure 74. Local structures of the adsorbed W(VI) monomer oxo-species on the (100) crystal termination of anatase¹⁰⁶ (Ti atoms, gray balls; H atoms, blue balls; O atoms in TiO₂ cluster, red balls; O atoms in tungsten surface species, yellow balls; W atoms, black balls). The dashed line indicates H-bond. Reprinted with permission from ref 106. Copyright 2009 Elsevier.

W(VI) monomer oxo-species are illustrated.¹⁰⁶ A similar picture was obtained for the local structure of the deposited Mo(VI) monomer oxo-species.¹⁰⁷

Concerning the deposition of the Cr⁶⁺ oxo-species, we found a low extent deposition at pH > pzc, too small increase of pH upon adsorption, a slight shift of the pzc (iep) to higher (lower) pH values due to the presence of the Cr⁶⁺ oxo-species in the impregnating solution, and very small values for the ratio “amount of H⁺ ions adsorbed/amount of Cr⁶⁺ ions adsorbed” determined at various pH's.¹⁰⁵ These results indicate deposition of the Cr⁶⁺ oxo-species through electrostatic and/or hydrogen bonds. The joint use of these results, in conjunction with laser Raman spectra and the aforementioned quantitative modeling, provided the structures of the deposited Cr⁶⁺ oxo-species at various pH's. These are illustrated in Figure 75.¹⁰⁵

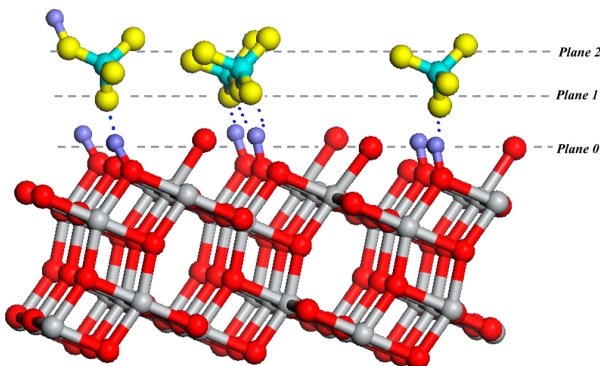


Figure 75. Schematic representation of the local structures of the deposited CrO₄²⁻, HCrO₄⁻, and Cr₂O₇²⁻ on the anatase (101) crystal termination¹⁰⁵ (Ti atoms, gray balls; H atoms, light blue; O atoms in TiO₂ cluster, red balls; O atoms in chromium species, yellow balls; Cr atoms, cyan balls). The dotted line indicates electrostatic bond between the chromium species and the anatase surface. Reprinted with permission from ref 105. Copyright 2009 Wiley-VCH.

Finally, concerning the V⁵⁺ oxo-species, as it has already been mentioned, the relevant study is still in progress. The first published results⁴⁵¹ show significant deposition at pH > pzc, considerable increase of pH upon deposition of the V⁵⁺ oxo-species, significant shift of the pzc (iep) to higher (lower) values brought about by the presence of the V⁵⁺ oxo-species in the impregnating solution, and relatively high values for the ratio “amount of H⁺ ions adsorbed/amount of V⁵⁺ ions adsorbed” at various pH's. These results indicate deposition of the V⁵⁺ oxo-species through coordinative and/or hydrogen bonds. The application of these results, in combination with laser Raman spectra recorded after impregnation and a quantitative modeling based on the above-described mapping of the protonation/deprotonation sites developed on the titania surface¹⁰² (which is now in progress), is expected to elucidate the exact local structure of the V⁵⁺ oxo-species formed on the titanium oxide surface.

5. CLOSING REMARKS

The main links of the chain that connects surface chemistry, interface chemistry, and scientific synthesis of supported catalysts based on titanium oxide may be visualized as follows:

The degree of rationalization of the synthesis of a supported catalyst based on titanium dioxide depends on our ability to control the interface speciation, the mode of interfacial deposition, and the surface structure of transition metal ionic species (containing the catalytically active element) deposited on the “polycrystalline titanium oxide/electrolyte solution” interface.

This, in turn, requires the determination of these features over a broad range of impregnation parameters (pH, TMIS concentration, ionic strength, impregnation temperature), and it is closely related to the regulation of the concentration of the protonation/deprotonation sites (receptor sites) exposed on the titania surface by adjusting these parameters.

Our ability for obtaining such a control increases with increasing the level of our understanding with respect to the “polycrystalline titanium oxide/electrolytic solution” interface, and it is related to the elaboration of more and more realistic surface ionization models describing the surface protonation/deprotonation behavior of the titania nanocrystals.

The progressive development of more and more realistic surface ionization models proceeds in line with the evolution of more and more clear pictures concerning: (a) the structure and energetics of anatase and rutile crystal faces exposed on the titanium oxide nanocrystals, (b) the “water–surface” and “water–water” interactions of the water molecules adsorbed on these faces, (c) the morphology of the anatase and rutile nanocrystals, (d) the charges and surface densities of the various titanium and oxygen surface atoms exposed on the aforementioned faces, and (e) the structure of the deposited ions of background electrolytes and TMIS on low-index crystal faces of anatase and rutile.

The above points underline the usefulness of findings drawn from the surface and interface chemistry for understanding fundamental aspects related to the synthesis of supported catalysts based on titanium oxide. In writing this Review, we realized that there is rather a long way until a severe control to be obtained concerning the synthesis of the aforementioned catalysts. In fact, some of the links of the aforementioned chain are rather weak at present. Thus, despite the fact that anatase is much more useful than rutile in the synthesis of supported catalysts, the largest majority of the surface chemistry studies and rather few interfacial chemistry studies have focused on the perfect (110) surface of rutile. In contrast, only in the last 10 years have been published several excellent surface chemistry studies devoted to low-index surfaces exposed by the anatase nanocrystals, principally to the most stable (101) anatase termination, whereas for the moment there is not any experimental or theoretical work dealing with an “anatase crystal termination/electrolytic solution” interface. This situation justifies, to some extent, the extensive application of the homogeneous, highly hypothetical, “one/site two pK” model for studying the “polycrystalline titanium oxide/electrolyte solution” interface both in the presence and in the absence of a TMIS containing a catalytically active element.

As was already mentioned, in the frame of our research program, we attempted the determination of the interfacial speciation, the mode of interfacial deposition, and the surface structure of transition metal ionic species, containing the most important catalytically active elements, deposited on the “polycrystalline titanium oxide/electrolytic solution” interface. In this work, it is taken into account the progress pointed out in the domain of the surface and interface chemistry. The central message drawn from this work is that for a scientific approach to the synthesis of supported catalysts based on titanium oxide, we must take into account the aforementioned progress.

AUTHOR INFORMATION

Corresponding Author

*Tel.: +302610997114. Fax: +302610994796. E-mail: alycour@chemistry.upatras.gr.

Notes

The authors declare no competing financial interest.

Biographies



Dr. Kyriakos Bourikas was born in Athens in 1971. He received his bachelor from the Department of Physics (1993) and his Ph.D. (1999) from the Department of Chemistry at the University of Patras, Greece. He then worked as a postdoctoral research fellow in the Department of Environmental Sciences at Wageningen University, Netherlands. In 2001 he obtained his certificate of post graduate studies in Open and Distance Learning (Hellenic Open University). From 2001–2005 he worked as a post doctoral researcher, and from 2005–2009 as an Adjunct Lecturer at the Department of Chemistry at University of Patras. From 2009–2014 he worked as a Lecturer Professor in the School of Science and Technology of the Hellenic Open University, and since 2014 he is an Assistant Professor, where he tutors in the M.Sc. program “Catalysis and Protection of the Environment”. His research interests are focused on the study of the liquid/solid interface developed at various important processes, such as the synthesis of supported catalysts, the photocatalytic degradation of various pollutants, the removal of toxic metal ions or organic pollutants through the use of sorbents, etc.



Dr. Christos Kordulis was born in Derveni Korinthias in 1957. He obtained his diploma (Chemistry) in 1980 and his Ph.D. (Catalysis) in 1985 from the University of Patras, Greece. He worked as a research fellow for one year at the Université Catholique de Louvain, Groupe de Physico-Chimie Minérale et de Catalyse (Louvain la Neuve, Belgium). He is now Professor of Catalysis in the Department of Chemistry of the University of Patras. He has been Dean of the School of Natural Sciences of the University of Patras (2010–2014). He is also a collaborating faculty member of the Institute of Chemical Engineering Sciences (FORTH/ICE-HT). His research interests are focused on heterogeneous catalyst development for catalytic processes such as oil upgrading and bio-fuels production.



Dr. Alexis Lycourghiotis was born in Athens in 1947. He received his bachelor (Chemistry) in 1971, his Ph.D. (Catalysis) in 1974, and his readership in 1978 from the University of Patras, Greece. He worked as a research fellow for one year at the Université Catholique de Louvain, Groupe de Physico-Chimie Minérale et de Catalyse (Louvain la Neuve, Belgium). He currently holds the position of Professor in the Department of Chemistry of the University of Patras in Greece. He has been Head of this Department (1987–1988), Rector of the University of Patras (1988–1994), President of the Board of Directors of the Hellenic Open University (1995–2004), and President of the National Council of Education, Greece (2010–2013). His research interests are focused on heterogeneous catalysis, molecular synthesis of supported catalysts, and environmental catalysis.

REFERENCES

- (1) Linsebigler, A.; Lu, G.; Yates, J. T. *Chem. Rev.* **1995**, *95*, 735.
- (2) Gratzel, M. *Nature* **2001**, *414*, 338.
- (3) Diebold, U. *Surf. Sci. Rep.* **2002**, *293*, 1.
- (4) Hoffmann, M. R.; Martin, S. T.; Choi, W.; Bahnemann, D. W. *Chem. Rev.* **1995**, *95*, 69.
- (5) Brown, G. E., Jr.; Hennrich, V. E.; Casey, W. H.; Clark, D. L.; Eggleston, C.; Felmy, A.; Goodman, D. W.; Grätzel, M.; Maciel, G.; McCarthy, M. I.; Nealson, K. H.; Sverjensky, D. A.; Toney, M. F.; Zachara, J. M. *Chem. Rev.* **1999**, *99*, 77.
- (6) Vittadini, A.; Selloni, A.; Rotzinger, F. P.; Gratzel, M. *Phys. Rev. Lett.* **1998**, *81*, 2954.
- (7) Kavan, L.; Gratzel, M.; Gilbert, S. E.; Klemenz, C.; Scheel, H. J. *J. Am. Chem. Soc.* **1996**, *118*, 6716.
- (8) Yates, J. T. *Surf. Sci.* **2009**, *603*, 1605.
- (9) Fujishima, A.; Zhang, X.; Tryk, D. A. *Surf. Sci. Rep.* **2008**, *63*, 515.
- (10) Kwon, S.; Fan, M.; Cooper, A. T.; Yang, H. *Crit. Rev. Environ. Sci. Technol.* **2008**, *38*, 197.
- (11) Chen, X.; Mao, S. S. *Chem. Rev.* **2007**, *107*, 2891.
- (12) Roy, P.; Berger, S.; Schmuki, P. *Angew. Chem., Int. Ed.* **2011**, *50*, 2904.
- (13) Leung, D. Y. C.; Fu, X.; Wang, C.; Ni, M.; Leung, M. K. H.; Wang, X.; Fu, X. *ChemSusChem* **2010**, *3*, 681.
- (14) Kitano, M.; Tsujimaru, K.; Anpo, M. *Top. Catal.* **2008**, *49*, 4.
- (15) Ni, M.; Leung, M. K. H.; Leung, D. Y. C.; Sumathy, K. *Renewable Sustainable Energy Rev.* **2007**, *11*, 401.
- (16) Zhu, J.; Zäch, M. *Curr. Opin. Colloid Interface Sci.* **2009**, *14*, 260.
- (17) Han, F.; Kambala, V. S. R.; Srinivasan, M.; Rajarathnam, D.; Naidu, R. *Appl. Catal., A* **2009**, *359*, 25.
- (18) Rauf, M. A.; Meetani, M. A.; Hisaindee, S. *Desalination* **2011**, *276*, 13.
- (19) Lu, S.-Y.; Wu, D.; Wang, Q.-L.; Yan, J.; Buekens, A. G.; Cen, K.-F. *Chemosphere* **2011**, *82*, 1215.
- (20) Khataee, A. R.; Kasiri, M. B. *J. Mol. Catal. A* **2010**, *328*, 8.
- (21) Kabra, K.; Chaudhary, R.; Sawhney, R. L. *Ind. Eng. Chem. Res.* **2004**, *43*, 7683.
- (22) O'Regan, B.; Gratzel, M. *Nature* **1991**, *353*, 737.
- (23) Akpan, U. G.; Hameed, B. H. *Appl. Catal., A* **2010**, *375*, 1.
- (24) Rehman, S.; Ullah, R.; Butt, A. M.; Gohar, N. D. *J. Hazard. Mater.* **2009**, *170*, 560.
- (25) Li Puma, G.; Bono, A.; Krishnaiah, D.; Collin, J. G. *J. Hazard. Mater.* **2008**, *157*, 209.
- (26) Ismail, A. A.; Bahnemann, D. W. *J. Mater. Chem.* **2011**, *21*, 11686.
- (27) Kumar, S. G.; Devi, L. G. *J. Phys. Chem. A* **2011**, *115*, 13211.
- (28) He, H.; Liu, C.; Dubois, K. D.; Jin, T.; Louis, M. E.; Li, G. *Ind. Eng. Chem. Res.* **2012**, *51*, 11841.
- (29) Wong, C. L.; Tan, Y. N.; Mohamed, A. R. *J. Environ. Manage.* **2011**, *92*, 1669.
- (30) Banerjee, A. N. *Nanotechnol., Sci. Appl.* **2011**, *4*, 35.
- (31) Kamat, P. V. *J. Phys. Chem. C* **2012**, *116*, 11849.
- (32) Jones, F. H. *Surf. Sci. Rep.* **2001**, *42*, 75.
- (33) Bourikas, K.; Kordulis, Ch.; Lycourghiotis, A. *Catal. Rev.* **2006**, *48*, 363.
- (34) Henderson, M. A. *Surf. Sci. Rep.* **2011**, *66*, 185.
- (35) Georgiadou, I.; Papadopoulou, Ch.; Matralis, H. K.; Voyatzis, G. A.; Lycourghiotis, A.; Kordulis, Ch. *J. Phys. Chem. B* **1998**, *102*, 8459.
- (36) Fountzoula, Ch.; Matralis, H. K.; Papadopoulou, Ch.; Voyatzis, G. A.; Kordulis, Ch. *J. Catal.* **1999**, *184*, 5.
- (37) Fountzoula, Ch.; Spanos, N.; Matralis, H. K.; Kordulis, Ch. *Appl. Catal., B* **2002**, *35*, 295.
- (38) Giakoumelou, I.; Fountzoula, Ch.; Kordulis, Ch.; Boghosian, S. *Catal. Today* **2002**, *73*, 255.
- (39) Bourikas, K.; Fountzoula, Ch.; Kordulis, Ch. *Appl. Catal., B* **2004**, *52*, 145.
- (40) Bourikas, K.; Fountzoula, Ch.; Kordulis, Ch. *Langmuir* **2004**, *20*, 10663.
- (41) Giakoumelou, I.; Fountzoula, Ch.; Kordulis, Ch.; Boghosian, S. *J. Catal.* **2006**, *239*, 1.
- (42) Ramirez, J.; Fuentes, S.; Diaz, G.; Vrinat, M.; Breyses, M.; Lacroix, M. *Appl. Catal.* **1989**, *52*, 211.
- (43) Breyses, M.; Portefaix, J. L.; Vrinat, M. *Catal. Today* **1991**, *10*, 489.
- (44) Ishihara, A.; Dumeignil, F.; Wang, D.; Li, X.; Arakawa, H.; Qian, E. W.; Inoue, S.; Muto, A.; Kabe, T. *Jpn. Pet. Inst. Spec.* **2005**, *48*, 37.
- (45) Ishihara, A.; Dumeignil, F.; Wang, D.; Li, X.; Arakawa, H.; Qian, E. W.; Inoue, S.; Muto, A.; Kabe, T. *Appl. Catal., A* **2005**, *292*, 50.
- (46) Kaneko, E. Y.; Pulcinelli, S. H.; Teixeira da Silva, V.; Santilli, C. V. *Appl. Catal., A* **2002**, *235*, 71.
- (47) Daly, F. P.; Ando, H.; Schmitt, J. L.; Sturm, E. A. *J. Catal.* **1987**, *108*, 401.
- (48) Zhaobin, W.; Qin, X.; Xiebian, G.; Sham, E. L.; Grange, P.; Delmon, B. *Appl. Catal.* **1990**, *63*, 305.
- (49) Zhaobin, W.; Qin, X.; Xiebian, G.; Sham, E. L.; Grange, P.; Delmon, B. *Appl. Catal.* **1991**, *75*, 179.
- (50) Pophal, C.; Kameda, F.; Hoshino, K.; Yoshinaka, S.; Segawa, K. *Catal. Today* **1997**, *39*, 21.
- (51) Zepeda, T. A.; Fierro, J. L. G.; Pawelec, B.; Nava, R.; Klimova, T.; Fuentes, G. A.; Halachev, T. *Chem. Mater.* **2005**, *17*, 4062.
- (52) Zepeda, T. A.; Halachev, T.; Pawelec, B.; Nava, R.; Klimova, T.; Fuentes, G. A.; Fierro, J. L. G. *Catal. Commun.* **2006**, *7*, 33.
- (53) Zepeda, T. A.; Pawelec, B.; Fierro, J. L. G.; Halachev, T. *J. Catal.* **2006**, *242*, 254.
- (54) Zepeda, T. A.; Pawelec, B.; Fierro, J. L. G.; Halachev, T. *Appl. Catal., B* **2007**, *71*, 223.
- (55) Roy, P.; Kim, D.; Lee, K.; Spiecker, E.; Schmuki, P. *Nanoscale* **2010**, *2*, 45.
- (56) Ladislav, K. *Adv. Sci. Technol.* **2006**, *51*, 20.
- (57) Junfeng, Y.; Feng, Z. *J. Mater. Chem.* **2011**, *21*, 9406.
- (58) Xu, M.; Gao, Y.; Moreno, E. M.; Kunst, M.; Muhler, M.; Wang, Y.; Idriss, H.; Woll, C. *Phys. Rev. Lett.* **2011**, *106*, 138302.
- (59) Henderson, M. A. *Surf. Sci. Rep.* **2002**, *46*, 1.
- (60) Lindan, P. J. D.; Harrison, N. M.; Gillan, M. J. *Phys. Rev. Lett.* **1998**, *80*, 762.

- (61) Schaub, R.; Thorstrup, P.; Laegsgaard, E.; Steensgaard, I.; Norskov, J. K.; Besenbacher, F. *Phys. Rev. Lett.* **2001**, *87*, 266104.
- (62) Langel, W. *Surf. Sci.* **2002**, *496*, 141.
- (63) Zhang, C.; Lindan, P. J. D. *J. Chem. Phys.* **2003**, *118*, 4620.
- (64) Towle, S. N.; Brown, G. E., Jr.; Parks, G. A. *J. Colloid Interface Sci.* **1999**, *217*, 299.
- (65) Bandura, A. V.; Kubicki, J. D. *J. Phys. Chem. B* **2003**, *107*, 11072.
- (66) Bandura, A. V.; Sykes, D. G.; Shapovalov, V.; Troung, T. N.; Kubicki, J. D.; Evgarostov, R. A. *J. Phys. Chem. B* **2004**, *108*, 7844.
- (67) Predota, M.; Bandura, A. V.; Cummings, P. T.; Kubicki, J. D.; Wesolowski, D. J.; Chialvo, A. A.; Machesky, M. L. *J. Phys. Chem. B* **2004**, *108*, 12049.
- (68) Predota, M.; Zhang, Z.; Fenter, P.; Wesolowski, D. J.; Cummings, P. T. *J. Phys. Chem. B* **2004**, *108*, 12061.
- (69) Zhang, Z.; Fenter, P.; Cheng, L.; Sturchio, N. C.; Bedzyk, M. J.; Predota, M.; Bandura, A.; Kubicki, J. D.; Lvov, S. N.; Cummings, P. T.; Chialvo, A. A.; Ridley, M. K.; Benezeth, P.; Anovitz, L.; Palmer, D. A.; Machesky, M. L.; Wesolowski, D. J. *Langmuir* **2004**, *20*, 4954.
- (70) Zhang, Z.; Fenter, P.; Cheng, L.; Sturchio, N. C.; Bedzyk, M. J.; Machesky, M. L.; Anovitz, L. M.; Wesolowski, D. J. *J. Colloid Interface Sci.* **2006**, *295*, 50.
- (71) Zhang, Z.; Fenter, P.; Kelly, S. D.; Catalano, J. G.; Bandura, A. V.; Kubicki, J. D.; Sofo, J. O.; Wesolowski, D. J.; Machesky, M. L.; Sturchio, N. C.; Bedzyk, M. J. *Geochim. Cosmochim. Acta* **2006**, *70*, 4039.
- (72) Zhang, Z.; Fenter, P.; Cheng, L.; Sturchio, N. C.; Bedzyk, M. J.; Machesky, M. L.; Wesolowski, D. J. *Surf. Sci.* **2007**, *601*, 1129.
- (73) Bandura, A. V.; Sofo, J. O.; Kubicki, J. D. *J. Phys. Chem. C* **2011**, *115*, 9608.
- (74) Diebold, U.; Ruzyczyk, N.; Herman, G. S.; Selloni, A. *Catal. Today* **2003**, *85*, 93.
- (75) Hengerer, R.; Kavan, L.; Gratzel, M. *J. Electrochem. Soc.* **2000**, *147*, 1467.
- (76) Hengerer, R.; Bolliger, B.; Erbudak, M.; Gratzel, M. *Surf. Sci.* **2000**, *460*, 162.
- (77) Hengerer, R.; Kavan, L.; Bolliger, B.; Erbudak, M.; Gratzel, M. *Mater. Res. Soc. Symp. Proc.* **2000**, *623*, 43.
- (78) Hebenstreit, W.; Ruzyczyk, N.; Herman, G. S.; Gao, Y.; Diebold, U. *Phys. Rev. B* **2000**, *64*, 162.
- (79) Dulub, O.; Diebold, U. *J. Phys.: Condens. Matter* **2010**, *22*, 084014.
- (80) Herman, G. S.; Gao, Y.; Tran, T. T.; Osterwalder, J. *Surf. Sci.* **1999**, *447*, 201.
- (81) Herman, G. S.; Gao, Y. *Thin Solid Films* **2001**, *397*, 157.
- (82) Chambers, S. A.; Wang, C. M.; Thevuthasan, S.; Droubay, T.; McCready, D. E.; Lea, A. S. *Thin Solid Films* **2002**, *418*, 197.
- (83) Chambers, S. A. *Surf. Sci. Rep.* **2000**, *39*, 105.
- (84) Gao, W.; Klie, R.; Altman, E. I. *Thin Solid Films* **2005**, *485*, 115.
- (85) Silversmit, G.; Poelman, H.; Fiermans, L.; De Cryse, R. *Solid State Commun.* **2001**, *119*, 101.
- (86) Poelman, H.; Fiermans, L. *Surf. Sci. Spectra* **1998**, *5*, 252.
- (87) Li, S.-C.; Dulub, O.; Diebold, U. *J. Phys. Chem. C* **2008**, *112*, 16166.
- (88) Vittadini, A.; Casarin, M.; Selloni, A. *Theor. Chem. Acc.* **2007**, *117*, 663.
- (89) Thiel, P. A.; Madey, T. E. *Surf. Sci. Rep.* **1987**, *7*, 211.
- (90) Liu, L.-M.; Crawford, P.; Hu, P. *Prog. Surf. Sci.* **2009**, *84*, 155.
- (91) Parks, G. A. *Chem. Rev.* **1965**, *65*, 177.
- (92) Bolt, G. H.; Van Riemsdijk, W. H. In *Soil Chemistry B: Physicochemical Models*, 2nd ed.; Bolt, G. H., Ed.; Elsevier: Amsterdam, 1982.
- (93) Van Riemsdijk, W. H.; Bolt, G. H.; Koopal, L. K.; Blaakmeer, J. *J. Colloid Interface Sci.* **1986**, *109*, 219.
- (94) Van Riemsdijk, W. H.; De Wit, J. C. M.; Koopal, L. K.; Bolt, G. H. *J. Colloid Interface Sci.* **1987**, *116*, 511.
- (95) Hiemstra, T.; Van Riemsdijk, W. H.; Bolt, G. H. *J. Colloid Interface Sci.* **1989**, *133*, 91.
- (96) Hiemstra, T.; De Wit, J. C. M.; Van Riemsdijk, W. H. *J. Colloid Interface Sci.* **1989**, *133*, 105.
- (97) Hiemstra, T.; Venema, P.; Van Riemsdijk, W. H. *J. Colloid Interface Sci.* **1996**, *184*, 680.
- (98) Bourikas, K.; Hiemstra, T.; Van Riemsdijk, W. H. *Langmuir* **2001**, *17*, 749.
- (99) Hiemstra, T.; Van Riemsdijk, W. H. *J. Colloid Interface Sci.* **1996**, *179*, 488.
- (100) Bourikas, K.; Kordulis, Ch.; Lycourghiotis, A. *J. Colloid Interface Sci.* **2006**, *296*, 389.
- (101) Bourikas, K.; Kordulis, Ch.; Lycourghiotis, A. *Adv. Colloid Interface Sci.* **2006**, *121*, 111.
- (102) Panagiotou, G. D.; Petsi, Th.; Bourikas, K.; Garoufalidis, Ch. S.; Tsevis, A.; Spanos, N.; Kordulis, Ch.; Lycourghiotis, A. *Adv. Colloid Interface Sci.* **2008**, *142*, 20.
- (103) Petsi, Th.; Panagiotou, G. D.; Garoufalidis, C. S.; Kordulis, Ch.; Stathi, P.; Deligiannakis, Y.; Lycourghiotis, A.; Bourikas, K. *Chem.—Eur. J.* **2009**, *15*, 13090.
- (104) Bourikas, K.; Stavropoulos, J.; Garoufalidis, C. S.; Kordulis, Ch.; Petsi, Th.; Lycourghiotis, A. *Chem.—Eur. J.* **2011**, *17*, 1201.
- (105) Petsi, Th.; Panagiotou, G. D.; Bourikas, K.; Kordulis, Ch.; Voyatzis, G. A.; Lycourghiotis, A. *ChemCatChem* **2011**, *3*, 1072.
- (106) Panagiotou, G. D.; Petsi, Th.; Bourikas, K.; Kordulis, Ch.; Lycourghiotis, A. *J. Catal.* **2009**, *262*, 266.
- (107) Panagiotou, G. D.; Petsi, Th.; Bourikas, K.; Kalampounias, A. G.; Boghosian, S.; Kordulis, Ch.; Lycourghiotis, A. *J. Phys. Chem. C* **2010**, *114*, 11868.
- (108) Burdett, K.; Hughbanks, T.; Miller, G. J.; Richardson, J. W., Jr.; Smith, J. V. *J. Am. Chem. Soc.* **1987**, *109*, 3639.
- (109) Schossberger, F. Z. *Kristallogr.* **1942**, *104*, 358.
- (110) Vegard, L. *Philos. Mag.* **1916**, *32*, 505.
- (111) Lazzeri, M.; Vittadini, A.; Selloni, A. *Phys. Rev. B* **2001**, *63*, 155409.
- (112) Labat, F.; Baranek, Ph.; Domain, C.; Minot, C.; Adamo, C. *J. Chem. Phys.* **2007**, *126*, 154703.
- (113) Burnside, S. D.; Shklover, V.; Barbe, C.; Comte, P.; Arendse, F.; Brooks, K.; Gratzel, M. *Chem. Mater.* **1998**, *10*, 2419.
- (114) Gao, Y.; Elder, S. A. *Mater. Lett.* **2000**, *44*, 228.
- (115) Chemseddine, A.; Moritz, T. *Eur. J. Inorg. Chem.* **1999**, 235.
- (116) Arrouvel, C.; Digne, M.; Breysse, M.; Toulhoat, H.; Raybaud, P. *J. Catal.* **2004**, *222*, 152.
- (117) Diebold, U. *Surf. Sci. Rep.* **2003**, *48*, 53.
- (118) Oliver, P. M.; Watson, G. W.; Kelsey, E. T.; Parker, S. C. *J. Mater. Chem.* **1997**, *7*, 563.
- (119) Lazzeri, M.; Vittadini, A.; Selloni, A. *Phys. Rev. B* **2002**, *65*, 119901.
- (120) Barnard, A. S.; Zapol, P. *Phys. Rev. B* **2004**, *70*, 235403.
- (121) Labat, F.; Baranek, Ph.; Adamo, C. *J. Chem. Theory Comput.* **2008**, *4*, 341.
- (122) Barnard, A. S.; Zapol, P.; Curtiss, L. A. *J. Chem. Theory Comput.* **2005**, *1*, 107.
- (123) Zhang, H.; Banfield, J. F. *J. Mater. Chem.* **1998**, *8*, 2073.
- (124) Ziolkowski, J. *Surf. Sci.* **1989**, *209*, 356.
- (125) Ceperley, D. M.; Alder, B. J. *Phys. Rev. Lett.* **1980**, *45*, 566.
- (126) Perdew, J. P.; Zunger, A. *Phys. Rev. B* **1981**, *23*, 5048.
- (127) Perdew, J. P.; Burke, K.; Ernzerhof, M. *Phys. Rev. Lett.* **1996**, *77*, 3865.
- (128) Becke, A. D. *Phys. Rev. A* **1988**, *38*, 3098.
- (129) Lee, C.; Yang, W.; Parr, R. C. *Phys. Rev. B* **1988**, *37*, 785.
- (130) Perdew, J. P.; Wang, Y. *Phys. Rev. B* **1992**, *45*, 13244.
- (131) Beltran, A.; Sambrano, J. R.; Calatayud, M.; Sensato, F. R.; Andres, J. *Surf. Sci.* **2001**, *490*, 116.
- (132) Ruzyczyk, N.; Herman, G.; Boatner, L. A.; Diebold, U. *Surf. Sci.* **2003**, *529*, L239.
- (133) Herman, G. S.; Sievers, M. R.; Gao, Y. *Phys. Rev. Lett.* **2000**, *84*, 3354.
- (134) Liang, Y.; Gan, S.; Champers, S. A.; Altman, E. I. *Phys. Rev. B* **2001**, *63*, 235402/1.
- (135) Tanner, R. E.; Sasahara, A.; Liang, Y.; Altman, E. I.; Onishi, H. *J. Phys. Chem. B* **2002**, *106*, 8211.
- (136) Lazzeri, M.; Selloni, A. *Phys. Rev. Lett.* **2001**, *87*, 266105.

- (137) Gong, X. Q.; Selloni, A.; Vittadini, A. *J. Phys. Chem. B* **2006**, *110*, 2804.
- (138) Thomas, A. G.; Flavell, W. R.; Kumarasinghe, A. R.; Mallick, A. K.; Tsoutsou, D.; Smith, G. C.; Stockbauer, R.; Patel, S.; Gratzel, M.; Hengerer, R. *Phys. Rev. B* **2003**, *67*, 035110.
- (139) Selloni, A.; Vittadini, A.; Gratzel, M. *Surf. Sci.* **1998**, *402–404*, 219.
- (140) Tilocca, A.; Selloni, A. *J. Phys. Chem. B* **2004**, *108*, 4743.
- (141) Tilocca, A.; Selloni, A. *Langmuir* **2004**, *20*, 8379.
- (142) Tilocca, A.; Selloni, A. *J. Chem. Phys.* **2003**, *119*, 7445.
- (143) Herman, G. S.; Dohnalek, Z.; Ruzycki, N.; Diebold, U. *J. Phys. Chem. B* **2003**, *107*, 2788.
- (144) Car, R.; Parrinello, M. *Phys. Rev. Lett.* **1985**, *55*, 2741.
- (145) Laasonen, K.; Pasquarello, A.; Car, R.; Lee, C.; Vanderbilt, D. *Phys. Rev. B* **1993**, *47*, 10142.
- (146) Perdew, J. P.; Chevary, J. A.; Vosko, S. H.; Jackson, K. A.; Pederson, M. R.; Singh, D. J.; Fiolhais, C. *Phys. Rev. B* **1992**, *46*, 6671.
- (147) Egashira, M.; Kawasumi, S.; Kagawa, S.; Seiyama, T. *Bull. Chem. Soc. Jpn.* **1978**, *51*, 3144.
- (148) Hamraoui, K.; Cristol, S.; Payen, E.; Paul, J.-F. *J. Phys. Chem. C* **2007**, *111*, 3963.
- (149) Mattioli, G.; Filippone, F.; Caminiti, R.; Amore Bonapasta, A. *J. Phys. Chem. C* **2008**, *112*, 13579.
- (150) Haas, K.; Schneider, W. F.; Curioni, A.; Andreoni, W. *Science* **1998**, *282*, 265.
- (151) Giordano, L.; Goniakowski, J.; Suzanne, J. *Phys. Rev. Lett.* **1998**, *81*, 1271.
- (152) Odelius, M. *Phys. Rev. Lett.* **1999**, *82*, 3919.
- (153) Feibelman, P. J. *Science* **2002**, *295*, 99.
- (154) Michaelides, A.; Alavi, A.; King, D. A. *J. Am. Chem. Soc.* **2003**, *125*, 2746.
- (155) Stirling, A.; Bernasconi, M.; Parrinello, M. *J. Chem. Phys.* **2003**, *118*, 8917.
- (156) Cheng, H.; Selloni, A. *J. Chem. Phys.* **2009**, *131*, 054703.
- (157) Cheng, H.; Selloni, A. *Phys. Rev. B* **2009**, *79*, 092101.
- (158) He, Y.; Dulub, O.; Cheng, H.; Selloni, A.; Diebold, U. *Phys. Rev. Lett.* **2009**, *102*, 106105.
- (159) Thomas, A. G.; Flavell, W. R.; Mallick, A. K.; Kumarasinghe, A. R.; Tsoutsou, D.; Khan, N.; Chatwin, C.; Rayner, S.; Smith, G. C.; Stockbauer, R. L.; Warren, S.; Johal, T. K.; Patel, S.; Holland, D.; Taleb, A.; Wiame, F. *Phys. Rev. B* **2007**, *75*, 035105.
- (160) Aschauer, U.; He, Y.; Cheng, H.; Li, S.-C.; Diebold, U.; Selloni, A. *J. Phys. Chem. C* **2010**, *114*, 1278.
- (161) Posternak, M.; Baldereschi, A.; Delley, B. *J. Phys. Chem. C* **2009**, *113*, 15862.
- (162) Gong, X.-Q.; Selloni, A.; Batzill, M.; Diebold, U. *Nat. Mater.* **2006**, *5*, 665.
- (163) Nosaka, A. Y.; Fujiwara, T.; Yagi, H.; Akutsu, H.; Nosaka, Y. *J. Phys. Chem. B* **2004**, *108*, 9121.
- (164) Beck, D. D.; White, J. M.; Radcliffe, C. T. *J. Phys. Chem.* **1986**, *90*, 3123.
- (165) Hugenschmidt, M. B.; Gamble, L.; Campbell, C. T. *Surf. Sci.* **1994**, *302*, 329.
- (166) Joseph, Y.; Ranke, W.; Weiss, W. *J. Phys. Chem. B* **2000**, *104*, 3224.
- (167) Jones, P.; Hockey, J. A. *J. Chem. Soc., Faraday Trans. 1* **1972**, *68*, 907.
- (168) He, Y.; Tilocca, A.; Dulub, O.; Selloni, A.; Diebold, U. *Nat. Mater.* **2009**, *8*, 585.
- (169) Bredow, T.; Jug, K. *Surf. Sci.* **1995**, *327*, 398.
- (170) Munuera, G.; Moreno, F.; Gonzalez, F. In *Reactivity of Solids*; Anderson, J. S., Roberts, M. W., Stone, F. S., Eds.; Chapman Hall: London, 1972; p 681.
- (171) Gong, X.-Q.; Selloni, A. *J. Phys. Chem. B* **2005**, *109*, 19560.
- (172) Busca, G.; Saussey, H.; Saur, O.; Lavallee, J.-C.; Lorenzelli, V. *Appl. Catal.* **1985**, *14*, 245.
- (173) Morterra, C. *J. Chem. Soc., Faraday Trans.* **1988**, *84*, 1617.
- (174) Veen, V.; R, J. A. *Z. Phys. Chem.* **1988**, *162*, 215.
- (175) Hadjiivanov, K. I.; Klissurski, D. *Chem. Soc. Rev.* **1996**, *25*, 61.
- (176) Travert, A.; Manoilova, O. V.; Tsyganenko, A. A.; Mauge, F.; Lavallee, J. C. *J. Phys. Chem. B* **2002**, *106*, 1350.
- (177) Dzwigaj, S.; Arrouvel, C.; Breysse, M.; Geantet, C.; Inoue, S.; Toulhoat, H.; Raybaud, P. *J. Catal.* **2005**, *236*, 245.
- (178) Chizallet, C.; Digne, M.; Arrouvel, C.; Raybaud, P.; Delbecq, F.; Costentin, G.; Che, M.; Sautet, P.; Toulhoat, H. *Top. Catal.* **2009**, *52*, 1005.
- (179) Inoue, S.; Muto, A.; Kudou, H.; Ono, T. *Appl. Catal., A* **2004**, *269*, 7.
- (180) Inoue, S.; Muto, A.; Ono, T.; Makabe, T.; Takatsuka, T.; Nomura, H. Patent US 2004/0238410 A1.
- (181) Shiroto, Y.; Ono, T.; Asaoka, S.; Nakamura, M. Patent USP 4,422,960.
- (182) Sugiyama, M.; Okazaki, H.; Koda, S. *J. Appl. Phys.* **2002**, *41*, 4666.
- (183) Sugimoto, T.; Okada, K.; Itoh, H. *J. Colloid Interface Sci.* **1997**, *193*, 140.
- (184) Sugimoto, T.; Zhou, X.; Muramatsu, A. *J. Colloid Interface Sci.* **2003**, *259*, 53.
- (185) Barnard, A. S.; Zapol, P. *J. Chem. Phys.* **2004**, *121*, 4276.
- (186) Wulff, G. Z. *Kristallogr.* **1901**, *34*, 449.
- (187) Herring, C. *Phys. Rev.* **1951**, *82*, 87.
- (188) Ziolkowski, J. *Surf. Sci.* **1989**, *209*, 536.
- (189) Ohno, T.; Sarukawa, K.; Tokieda, K.; Matsumura, M. *J. Catal.* **2001**, *203*, 82.
- (190) Stekolnikov, A. A.; Furthmuller, J.; Bechstedt, F. *Phys. Rev. B* **2002**, *65*, 115318.
- (191) Barnard, A. S.; Zapol, P. *J. Phys. Chem. B* **2004**, *108*, 18435.
- (192) Barnard, A. S.; Curtiss, L. A. *Nano Lett.* **2005**, *5*, 1261.
- (193) Barnard, A. S.; Zapol, P.; Curtiss, L. A. *Surf. Sci.* **2005**, *582*, 173.
- (194) Zaban, A.; Aruna, S. T.; Tirosh, S.; Gregg, B. A.; Mastai, Y. *J. Phys. Chem. B* **2000**, *104*, 4130.
- (195) Penn, R. L.; Banfield, J. F. *Geochim. Cosmochim. Acta* **1999**, *63*, 1549.
- (196) Barnard, A. S.; Erdin, S.; Lin, Y.; Zapol, P.; Halley, J. W. *Phys. Rev. B* **2006**, *73*, 205405.
- (197) Yu, N.; Halley, J. W. *Phys. Rev. B* **1995**, *51*, 4768.
- (198) Schelling, P. K.; Yu, N.; Halley, J. W. *Phys. Rev. B* **1998**, *58*, 1279.
- (199) Erdin, S.; Lin, Y.; Halley, J. W.; Zapol, P.; Redfern, P.; Curtiss, L. *J. Electroanal. Chem.* **2007**, *607*, 147.
- (200) Yang, H. G.; Sun, C. H.; Qiao, S. Z.; Zou, J.; Liu, G.; Smith, S. C.; Cheng, H. M.; Lu, G. Q. *Nature* **2008**, *453*, 638.
- (201) Jun, Y.-W.; Casula, M. F.; Sim, J.-H.; Kim, S. Y.; Cheon, J.; Alivisatos, A. P. *J. Am. Chem. Soc.* **2003**, *125*, 15981.
- (202) Selloni, A. *Nat. Mater.* **2008**, *7*, 613.
- (203) Fang, W. Q.; Gong, X.-Q.; Yang, H. G. *J. Phys. Chem. Lett.* **2011**, *2*, 725.
- (204) Liu, S.; Yu, J.; Jaroniec, M. *Chem. Mater.* **2011**, *23*, 4085.
- (205) Sun, C.; Liu, L.-M.; Selloni, A.; Lu, G.-Q. (Max); Smith, S. C. *J. Mater. Chem.* **2010**, *20*, 10319.
- (206) Hebenstreit, W.; Ruzycki, N.; Herman, G. S.; Gao, Y.; Diebold, U. *Phys. Rev. B* **2000**, *62*, R16334.
- (207) Xu, M.; Noei, H.; Fink, K.; Muhler, M.; Wang, Y.; Woll, C. *Angew. Chem., Int. Ed.* **2012**, *51*, 4731.
- (208) Brookes, I. M.; Muryn, C. A.; Thornton, G. *Phys. Rev. Lett.* **2001**, *87*, 266103/1.
- (209) Suzuki, S.; Fukui, K.-I.; Onishi, H.; Sasaki, T.; Iwasawa, Y. *Stud. Surf. Sci. Catal.* **2001**, *132*, 735.
- (210) Schaub, R.; Thostrup, P.; Lopez, N.; Lægsgaard, E.; Stensgaard, I.; Norskov, J. K.; Besenbacher, F. *Phys. Rev. Lett.* **2001**, *87*, 266104/1.
- (211) Henderson, M. A. *Langmuir* **1996**, *12*, 5093.
- (212) Kumar, N.; Neogi, S.; Kent, P. R. C.; Bandura, A. V.; Kubicki, J. D.; Wesolowski, D. J.; Cole, D.; Sofo, J. O. *J. Phys. Chem. C* **2009**, *113*, 13732.
- (213) Mamontov, E.; Vlcek, L.; Wesolowski, D. J.; Cummings, P. T.; Wang, W.; Anovitz, L. M.; Rosenqvist, J.; Brown, C. M.; Garcia Sakai, V. *J. Phys. Chem. C* **2007**, *111*, 4328.

- (214) Mamontov, E.; Wesolowski, D. J.; Vlcek, L.; Cummings, P. T.; Rosenqvist, J.; Wang, W.; Cole, D. R. *J. Phys. Chem. C* **2008**, *112*, 12334.
- (215) Kornherr, A.; Vogtenhuber, D.; Ruckenbauer, M.; Podloucky, R.; Zifferer, G. *J. Chem. Phys.* **2004**, *121*, 3722.
- (216) Wendt, S.; Schaub, R.; Matthiesen, J.; Vestergaard, E. K.; Wahlström, E.; Rasmussen, M. D.; Thostrup, P.; Molina, L. M.; Lægsgaard, E.; Stensgaard, I.; Hammer, B.; Besenbacher, F. *Surf. Sci.* **2005**, *598*, 226.
- (217) Wendt, S.; Matthiesen, J.; Schaub, R.; Vestergaard, E. K.; Lægsgaard, E.; Besenbacher, F.; Hammer, B. *Phys. Rev. Lett.* **2006**, *96*, 066107.
- (218) Matthiesen, J.; Hansen, JØ.; Wendt, S.; Lira, E.; Schaub, R.; Lægsgaard, E.; Besenbacher, F.; Hammer, B. *Phys. Rev. Lett.* **2009**, *102*, 226101.
- (219) Matthiesen, J.; Wendt, S.; Hansen, JØ.; Madsen, G. K. H.; Lira, E.; Galliker, P.; Vestergaard, E. K.; Schaub, R.; Lægsgaard, E.; Hammer, B.; Besenbacher, F. *ACS Nano* **2009**, *3*, 517.
- (220) Hammer, B.; Wendt, S.; Besenbacher, F. *Top. Catal.* **2010**, *53*, 423.
- (221) Predota, M.; Vlcek, L. *J. Phys. Chem. B* **2007**, *111*, 1245.
- (222) Predota, M.; Cummings, P. T.; Wesolowski, D. J. *J. Phys. Chem. C* **2007**, *111*, 3071.
- (223) Ramamoorthy, M.; Vanderbilt, D.; King-Smith, R. D. *Phys. Rev. B* **1994**, *49*, 16721.
- (224) Beck, T. J.; Klust, A.; Batzill, M.; Diebold, U.; Di Valentin, C.; Selloni, A. *Phys. Rev. Lett.* **2004**, *93*, 036104.
- (225) Rohrer, G. S. In *The Chemical Physics of Solid Surfaces*; Woodruff, D. P., Ed.; Elsevier: Amsterdam, 2001; Vol. 9, Chapter 12, p 485.
- (226) Kubo, T.; Orita, H.; Nozoye, H. *J. Am. Chem. Soc.* **2007**, *129*, 10474.
- (227) Torrelles, X.; Cabailh, G.; Lindsay, R.; Bikondoa, O.; Roy, J.; Zegenhagen, J.; Teobaldi, G.; Hofer, W. A.; Thornton, G. *Phys. Rev. Lett.* **2008**, *101*, 185501.
- (228) Farges, F.; Brown, G. E., Jr.; Rehr, J. *J. Phys. Rev. B* **1997**, *56*, 1809.
- (229) Roberts, M. A.; Sankar, G.; Thomas, J. M.; Jones, R. H.; Du, H.; Chen, J.; Pang, W.; Xu, R. *Nature (London)* **1996**, *381*, 401.
- (230) Rajh, T.; Nedeljkovic, J. M.; Chen, L. X.; Poluektov, O.; Thurnauer, M. C. *J. Phys. Chem. B* **1999**, *103*, 3515.
- (231) Redfern, P. C.; Zapol, P.; Curtiss, L. A.; Rajh, T.; Thurnauer, M. C. *J. Phys. Chem. B* **2003**, *107*, 11419.
- (232) Dulub, O.; Di Valentin, C.; Selloni, A.; Diebold, U. *Surf. Sci.* **2006**, *600*, 4407.
- (233) Gong, X.-Q.; Khorshidi, N.; Stierle, A.; Vonk, V.; Ellinger, C.; Dosch, H.; Cheng, H.; Selloni, A.; He, Y.; Dulub, O.; Diebold, U. *Surf. Sci.* **2009**, *603*, 138.
- (234) Beck, T. J.; Klust, A.; Batzill, M.; Diebold, U.; Di Valentin, C.; Tilocca, A.; Selloni, A. *Surf. Sci.* **2005**, *591*, L267.
- (235) Di Valentin, C.; Tilocca, A.; Selloni, A.; Beck, T. J.; Klust, A.; Batzill, M.; Losovyj, Y.; Diebold, U. *J. Am. Chem. Soc.* **2005**, *127*, 9895.
- (236) He, Y.; Li, W.-K.; Gong, X.-Q.; Dulub, O.; Selloni, A.; Diebold, U. *J. Phys. Chem. C* **2009**, *113*, 10329.
- (237) Raza, H.; Pang, C. L.; Haycock, S. A.; Thornton, G. *Phys. Rev. Lett.* **1999**, *82*, 5265.
- (238) Raza, H.; Pang, C. L.; Haycock, S. A.; Thornton, G. *Appl. Surf. Sci.* **1999**, *140*, 271.
- (239) Perron, H.; Domain, C.; Roques, J.; Drot, R.; Simoni, E.; Catalette, H. *Theor. Chem. Acc.* **2007**, *117*, 565.
- (240) Purton, J.; Bullett, D. W.; Oliver, P. M.; Parker, S. C. *Surf. Sci.* **1995**, *336*, 166–180.
- (241) Muscat, J.; Harrison, N. M.; Thornton, G. *Phys. Rev. B* **1999**, *59*, 2320.
- (242) Lo, W. J.; Chung, Y. W.; Somorjai, G. A. *Surf. Sci.* **1978**, *71*, 199.
- (243) Chung, Y. W.; Lo, W. J.; Somorjai, G. A. *Surf. Sci.* **1977**, *64*, 588.
- (244) Hardman, P. J.; Prakash, N. S.; Muryn, C. A.; Raikar, G. N.; Thomas, A. G.; Prime, A. F.; Thornton, G.; Blake, R. *J. Phys. Rev. B* **1993**, *47*, 16056.
- (245) Muryn, C. A.; Tirvengadum, G.; Crouch, J. J.; Warburton, D. R.; Raikar, G. N.; Thornton, G.; Law, D. S. L. *J. Phys.: Condens. Matter* **1989**, *1*, SB127.
- (246) Suda, Y.; Morimoto, T. *Langmuir* **1987**, *3*, 786.
- (247) Fahmi, A.; Minot, C. *Surf. Sci.* **1994**, *304*, 343.
- (248) Ferris, K. F.; Wang, L.-Q. *J. Vac. Sci. Technol., A* **1998**, *16*, 956.
- (249) Kamisaka, H.; Yamashita, K. *Surf. Sci.* **2007**, *601*, 4824.
- (250) Muscat, J.; Harrison, N. M. *Surf. Sci.* **2000**, *446*, 119.
- (251) Muscat, J.; Harrison, N. M.; Thornton, G. *Phys. Rev. B* **1999**, *59*, 15457.
- (252) Firment, L. E. *Surf. Sci.* **1982**, *116*, 205.
- (253) Nörenberg, H.; Dinelli, F.; Briggs, G. A. D. *Surf. Sci.* **1999**, *436*, L635.
- (254) Nörenberg, H.; Dinelli, F.; Briggs, G. A. D. *Surf. Sci.* **2000**, *446*, L83.
- (255) Poirier, G. E.; Hance, B. K.; White, J. M. *J. Vac. Sci. Technol., B* **1992**, *10*, 6.
- (256) Tait, R. H.; Kasowski, R. V. *Phys. Rev. B* **1979**, *20*, 5178.
- (257) Tero, R.; Fukui, K.; Iwasawa, Y. *J. Phys. Chem. B* **2003**, *107*, 3207.
- (258) Watson, B. A.; Barreau, M. A. *Chem. Mater.* **1994**, *6*, 771.
- (259) Smith, P. B.; Bernasek, S. L. *Surf. Sci.* **1987**, *188*, 241.
- (260) Morgan, B. J.; Watson, G. W. *J. Phys. Chem. C* **2009**, *113*, 7322.
- (261) Zarzycki, P. *J. Phys. Chem. C* **2007**, *111*, 7692.
- (262) Contescu, C.; Popa, V. T.; Schwarz, J. A. *J. Colloid Interface Sci.* **1996**, *180*, 149.
- (263) Muscat, J.; Swamy, V.; Harrison, N. M. *Phys. Rev. B* **2002**, *65*, 224112.
- (264) Gribb, A. A.; Banfield, J. F. *Am. Mineral.* **1997**, *82*, 717.
- (265) Navrotsky, A.; Kleppa, O. J. *J. Am. Ceram. Soc.* **1976**, *50*, 626.
- (266) Mitsuhashi, T.; Kleppa, O. J. *J. Am. Ceram. Soc.* **1979**, *62*, 356.
- (267) Zhang, H. Z.; Banfield, J. F. *J. Phys. Chem. B* **2000**, *104*, 3481.
- (268) Hwu, Y.; Yao, Y. D.; Cheng, N. F.; Tung, C. Y.; Lin, H. M. *Nanostruct. Mater.* **1997**, *9*, 355.
- (269) Kittaka, S.; Matsuno, K.; Takahara, S. *J. Solid State Chem.* **1997**, *132*, 447.
- (270) Zhang, H. Z.; Banfield, J. F. *J. Mater. Res.* **2000**, *15*, 437.
- (271) Yoshinaka, M.; Hirota, K.; Yamaguchi, O. *J. Am. Ceram. Soc.* **1997**, *80*, 2749.
- (272) Okada, K.; Yamamoto, N.; Kameshima, Y.; Yasumori, A. *J. Am. Ceram. Soc.* **2001**, *84*, 1591.
- (273) Yang, J.; Mei, S.; Ferreira, J. M. F. *J. Am. Ceram. Soc.* **2000**, *83*, 1361.
- (274) Rande, M. R.; Navrotsky, A.; Zhang, H. Z.; Banfield, J. F.; Elder, S. H.; Zaban, A.; Borse, P. H.; Kulkarni, S. K.; Doran, G. S.; Whitfield, H. J. *Proc. Natl. Acad. Sci. U.S.A.* **2002**, *99*, 6481.
- (275) Zhang, H.; Banfield, J. F. *Am. Mineral.* **1999**, *84*, 528.
- (276) Chen, L. X.; Rajh, T.; Jager, W.; Nedeljkovic, J.; Thurnauer, M. C. *J. Synchrotron Radiat.* **1999**, *6*, 445.
- (277) Rajh, T.; Chen, L. X.; Lucas, K.; Liu, T.; Thurnauer, M. C.; Tiede, D. M. *J. Phys. Chem. B* **2002**, *106*, 10543.
- (278) Zhang, W. F.; Zhang, M. S.; Yin, Z.; Chen, Q. *Appl. Phys. B: Lasers Opt.* **2000**, *70*, 261.
- (279) Paunesku, T.; Rajh, T.; Wiederrecht, G.; Maser, J.; Vogt, S.; Stojicevic, N.; Protic, M.; Lai, B.; Oryhon, J.; Thurnauer, M.; Woloschak, G. *Nat. Mater.* **2003**, *2*, 343.
- (280) Zhang, H.; Penn, R. L.; Hamers, R. J.; Banfield, J. F. *J. Phys. Chem. B* **1999**, *103*, 4656.
- (281) Jang, K. D.; Kim, S.-K.; Kim, S.-J. *J. Nanopart. Res.* **2001**, *3*, 141.
- (282) Bullen, H.; Garrett, S. *Nano Lett.* **2002**, *2*, 739.
- (283) Rao, C. N. R. *Can. J. Chem.* **1961**, *39*, 498.
- (284) Sugimoto, T.; Zhou, X.; Muramatsu, A. *J. Colloid Interface Sci.* **2003**, *259*, 43.
- (285) Sugimoto, T.; Zhou, X.; Muramatsu, A. *J. Colloid Interface Sci.* **2002**, *252*, 339.
- (286) Noh, J. S.; Schwarz, J. J. *Colloid Interface Sci.* **1989**, *130*, 157.

- (287) Lyklema, J. In *Adsorption from Solution at the Solid/Liquid Interface*; Parfitt, G. D., Rochester, C. H., Eds.; Academic Press: New York, 1983; Chapter 5.
- (288) Tewari, P.; Campbell, A. *J. Colloid Interface Sci.* **1982**, *55*, 531.
- (289) Berube, Y. G.; De Bruyn, P. L. *J. Colloid Interface Sci.* **1968**, *27*, 305.
- (290) Parks, G. A. *Chem. Rev.* **1965**, *65*, 177.
- (291) Vakros, J.; Kordulis, Ch.; Lycourghiotis, A. *Chem. Commun.* **2002**, *17*, 1980.
- (292) Bourikas, K.; Vakros, J.; Kordulis, Ch.; Lycourghiotis, A. *J. Phys. Chem. B* **2003**, *107*, 9441.
- (293) Park, J.; Regalbuto, J. R. *J. Colloid Interface Sci.* **1995**, *175*, 239.
- (294) Bourikas, K.; Kordulis, Ch.; Lycourghiotis, A. *Environ. Sci. Technol.* **2005**, *39*, 4100.
- (295) Svecova, L.; Cremel, S.; Sirguey, C.; Simonnot, M.-O.; Sardin, M.; Dossot, M.; Mercier-Bion, F. *J. Colloid Interface Sci.* **2008**, *325*, 363.
- (296) Fitts, J. P.; Machesky, M. L.; Wesolowski, D. J.; Shang, X.; Kubicki, J. D.; Flynn, G. W.; Heinz, T. F.; Eisenthal, K. B. *Chem. Phys. Lett.* **2005**, *411*, 399.
- (297) Cheng, J.; Sprik, M. *J. Chem. Theory Comput.* **2010**, *6*, 880.
- (298) Zarzycki, P.; Preocanin, T. *J. Colloid Interface Sci.* **2012**, *370*, 139.
- (299) Bourikas, K.; Kordulis, Ch.; Vakros, J.; Lycourghiotis, A. *Adv. Colloid Interface Sci.* **2004**, *110*, 97.
- (300) Pauling, L. *J. Am. Chem. Soc.* **1929**, *51*, 1010.
- (301) Brown, I. D. *Acta Crystallogr., Sect. B* **1977**, *33*, 1305.
- (302) Brown, I. D. *Chem. Soc. Rev.* **1978**, *7*, 359.
- (303) Brown, I. D.; Altermatt, D. *Acta Crystallogr., Sect. B* **1985**, *41*, 244.
- (304) Machesky, M. L.; Predota, M.; Wesolowski, D. J.; Vlcek, L.; Cummings, P. T.; Rosengvist, J.; Ridley, M. K.; Kubicki, J. D.; Bandura, A.; Kumar, N.; Sofo, J. O. *Langmuir* **2008**, *24*, 12331.
- (305) Hiemstra, T.; Van Riemsdijk, W. H. *Colloids Surf. A* **1991**, *59*, 7.
- (306) Stumm, W.; Huang, C. P.; Jenkins, S. R. *Croat. Chem. Acta* **1970**, *42*, 223.
- (307) Hohl, H.; Stumm, W. *J. Colloid Interface Sci.* **1976**, *55*, 281.
- (308) Kummert, R.; Stumm, W. *J. Colloid Interface Sci.* **1980**, *75*, 373.
- (309) Yates, D. E.; Levine, S.; Healy, T. W. *J. Chem. Soc., Faraday Trans. 1* **1974**, *70*, 1807.
- (310) Davis, J. A.; James, R. O.; Leckie, J. O. *J. Colloid Interface Sci.* **1978**, *63*, 480.
- (311) Rahnemaie, R.; Hiemstra, T.; Van Riemsdijk, W. H. *J. Colloid Interface Sci.* **2006**, *293*, 312.
- (312) Ridley, M. K.; Hiemstra, T.; Van Riemsdijk, W. H.; Machesky, M. L. *Geochim. Cosmochim. Acta* **2009**, *73*, 1841.
- (313) Robinson, I. K. *Phys. Rev. B: Condens. Matter Mater. Phys.* **1986**, *33*, 3830.
- (314) Fedkin, M. V.; Zhou, X. Y.; Kubicki, J. D.; Bandura, A. V.; Lvov, S. N.; Machesky, M. L.; Wesolowski, D. J. *Langmuir* **2003**, *19*, 3797.
- (315) Berube, Y. G.; De Bruyn, P. L. *J. Colloid Interface Sci.* **1968**, *28*, 92.
- (316) Sprycha, R. *J. Colloid Interface Sci.* **1984**, *102*, 173.
- (317) Kosmulski, M.; Matijevic, E. *Colloids Surf.* **1992**, *64*, 57.
- (318) Spanos, N.; Georgiadou, I.; Lycourghiotis, A. *J. Colloid Interface Sci.* **1995**, *172*, 374.
- (319) Janusz, W.; Kobal, I.; Sworska, A.; Szczypa, J. *J. Colloid Interface Sci.* **1997**, *187*, 381.
- (320) Kosmulski, M.; Gustafsson, J.; Rosenholm, J. B. *J. Colloid Interface Sci.* **1999**, *209*, 200.
- (321) Janusz, W.; Sworska, A.; Szczypa, J. *Colloids Surf., A* **1999**, *152*, 223.
- (322) Foissy, A.; M'Pandou, A.; Lamarche, J. M.; Jaffrezic-Renault, N. *Colloids Surf.* **1982**, *5*, 363.
- (323) Jamssen, M. J. G.; Stein, H. N. *J. Colloid Interface Sci.* **1986**, *111*, 112.
- (324) Girod, G.; Lamarche, J. M.; Foissy, A. *J. Colloid Interface Sci.* **1988**, *121*, 265.
- (325) Akratopulu, K. Ch.; Kordulis, Ch.; Lycourghiotis, A. *J. Chem. Soc., Faraday Trans.* **1990**, *86*, 3437.
- (326) Giacomelli, C.; Avena, M. J.; De Pauli, C. P. *Langmuir* **1995**, *11*, 3483.
- (327) Rodriguez, R.; Blesa, M. A.; Regazzoni, A. E. *J. Colloid Interface Sci.* **1996**, *177*, 122.
- (328) Yates, D. E.; Healy, T. W. *J. Chem. Soc., Faraday Trans. 1* **1980**, *76*, 9.
- (329) Jang, H. M.; Fuerstenau, D. W. *Colloids Surf.* **1986**, *21*, 235.
- (330) Szczypa, J.; Wasowska, L.; Kosmulski, M. *J. Colloid Interface Sci.* **1988**, *126*, 592.
- (331) Folkink, L. G. J.; De Keizer, A.; Lyklema, J. *J. Colloid Interface Sci.* **1989**, *127*, 116.
- (332) Gibb, A. W. M.; Koopal, L. *J. Colloid Interface Sci.* **1990**, *134*, 122.
- (333) Kallay, N.; Colic, M.; Fuerstenau, D. W.; Jang, H. M.; Matijevic, E. *Colloid Polym. Sci.* **1994**, *272*, 554.
- (334) Machesky, M. L.; Wesolowski, D. J.; Palmer, D. A.; Ichiro-Hayashi, K. *J. Colloid Interface Sci.* **1998**, *200*, 298.
- (335) Sahai, N.; Sverjensky, D. A. *Geochim. Cosmochim. Acta* **1997**, *61*, 2801.
- (336) Kosmulski, M.; Rosenholm, J. B. *J. Phys. Chem.* **1996**, *100*, 11681.
- (337) Kosmulski, M.; Durand-Vidal, S.; Gustafsson, J.; Rosenholm, J. B. *Colloids Surf., A* **1999**, *157*, 245.
- (338) Ridley, M. K.; Machesky, M. L.; Wesolowski, D. J.; Palmer, D. A. *Geochim. Cosmochim. Acta* **1999**, *63*, 3087.
- (339) Ridley, M. K.; Machesky, M. L.; Palmer, D. A.; Wesolowski, D. J. *Colloids Surf., A* **2002**, *204*, 295.
- (340) Ridley, M. K.; Machesky, M. L.; Wesolowski, D. J.; Palmer, D. A. *Geochim. Cosmochim. Acta* **2005**, *69*, 63.
- (341) Ridley, M. K.; Hackley, V. A.; Machesky, M. L. *Langmuir* **2006**, *22*, 10972.
- (342) Kosmulski, M. *Adv. Colloid Interface Sci.* **2002**, *99*, 255.
- (343) Kyriakopoulos, J.; Panagiotou, G.; Petsi, Th.; Bourikas, K.; Kordulis, Ch.; Lycourghiotis, A. *Stud. Surf. Sci. Catal.* **2010**, *175*, 643.
- (344) Bourikas, K.; Vakros, J.; Fountzoula, Ch.; Kordulis, Ch.; Lycourghiotis, A. *Catal. Today* **2007**, *128*, 138.
- (345) Ataloglu, Th.; Vakros, J.; Bourikas, K.; Fountzoula, Ch.; Kordulis, Ch.; Lycourghiotis, A. *Appl. Catal., B* **2005**, *57*, 299.
- (346) Lycourghiotis, A.; Kordulis, Ch.; Bourikas, K. *Encyclopedia of Surface and Colloid Science*; Marcel Dekker, Inc.: New York, 2002; pp 1366–1378.
- (347) Spanos, N.; Vordonis, L.; Kordulis, Ch.; Lycourghiotis, A. *J. Catal.* **1990**, *124*, 301.
- (348) Spanos, N.; Vordonis, L.; Kordulis, Ch.; Koutsoukos, P. G.; Lycourghiotis, A. *J. Catal.* **1990**, *124*, 315.
- (349) Karakstantis, L.; Kordulis, Ch.; Lycourghiotis, A. *Langmuir* **1992**, *8*, 1318.
- (350) Spanos, N.; Matralis, H. K.; Kordulis, Ch.; Lycourghiotis, A. *J. Catal.* **1992**, *136*, 432.
- (351) Georgiadou, I.; Slavov, S.; Papadopoulou, Ch.; Matralis, H. K.; Kordulis, Ch. *Bull. Soc. Chim. Belg.* **1995**, *104*, 143.
- (352) Lycourghiotis, A. *Stud. Surf. Sci. Catal.* **1995**, *91*, 95.
- (353) Papadopoulou, Ch.; Karakstantis, L.; Matralis, H. K.; Kordulis, Ch.; Lycourghiotis, A. *Bull. Soc. Chim. Belg.* **1996**, *105*, 247.
- (354) Karakstantis, L.; Matralis, H.; Kordulis, Ch.; Lycourghiotis, A. *J. Catal.* **1996**, *162*, 306.
- (355) Matralis, H. K.; Bourikas, K.; Papadopoulou, Ch.; Kordulis, Ch.; Lycourghiotis, A. *Pol. J. Appl. Chem.* **1998**, *41*, 275.
- (356) Kordulis, Ch.; Lappas, A. A.; Fountzoula, Ch.; Drakaki, K.; Lycourghiotis, A.; Vasalos, I. A. *Appl. Catal., A* **2001**, *209*, 85.
- (357) Vakros, J.; Kordulis, Ch.; Lycourghiotis, A. *Langmuir* **2002**, *18*, 417.
- (358) Vakros, J.; Bourikas, K.; Kordulis, Ch.; Lycourghiotis, A. *J. Phys. Chem. B* **2003**, *107*, 1804.
- (359) Papadopoulou, Ch.; Vakros, J.; Matralis, H. K.; Kordulis, Ch.; Lycourghiotis, A. *J. Colloid Interface Sci.* **2003**, *261*, 146.

- (360) Papadopoulou, Ch.; Vakros, J.; Matralis, H. K.; Voyatzis, G. A.; Kordulis, Ch. *J. Colloid Interface Sci.* **2004**, *274*, 159.
- (361) Ataloglu, Th.; Fountzoula, Ch.; Bourikas, K.; Vakros, J.; Lycourghiotis, A.; Kordulis, Ch. *Appl. Catal., A* **2005**, *288*, 1.
- (362) Sarella, A.; Niakolas, D.; Bourikas, K.; Vakros, J.; Kordulis, Ch. *J. Colloid Interface Sci.* **2006**, *295*, 165.
- (363) Van de Loosdrecht, J.; Van Dillen, A. J.; Van der Horst, A. A.; Van der Kraan, A. M.; Geus, J. W. *Top. Catal.* **1995**, *2*, 29.
- (364) Bitter, J. H.; Van der Lee, M. K.; Slotboom, A. G. T.; Van Dillen, A. J.; de Jong, K. P. *Catal. Lett.* **2003**, *89*, 139.
- (365) Toebe, M. L.; Van der Lee, M. K.; Tang, L. M.; Huis in't Veld, M. H.; Bitter, J. H.; Van Dillen, A. J.; de Jong, K. P. *J. Phys. Chem. B* **2004**, *108*, 11611.
- (366) Patil, N. S.; Uphade, B. S.; McCulloch, D. G.; Bhargava, S. K.; Choudhary, V. R. *Catal. Commun.* **2004**, *5*, 681.
- (367) Bezemer, G. L.; Radstake, P. B.; Koot, V.; Van Dillen, A. J.; Geus, J. W.; de Jong, K. P. *J. Catal.* **2006**, *237*, 291.
- (368) *Synthesis of Solid Catalysts*; de Jong, K. P., Ed.; Wiley-VCH: Weinheim, 2009.
- (369) Zhu, X.; Cho, H.-R.; Pasupong, M.; Regalbuto, J. R. *ACS Catal.* **2013** (in press), DOI: 10.1021/cs3008347.
- (370) Mäki-Arvela, P.; Murzin, D. Y. *Appl. Catal., A* **2013**, *451*, 251.
- (371) Zanella, R.; Delannoy, L.; Louis, C. *Appl. Catal., A* **2005**, *291*, 62.
- (372) Lim, S. H.; Phonthammachai, N.; Zhong, Z.; Teo, J.; White, T. J. *Langmuir* **2009**, *25*, 9480.
- (373) Tran, N. D.; Besson, M.; Descorne, C. *New J. Chem.* **2011**, *35*, 2095.
- (374) Ivanova, S.; Pitchon, V.; Petit, C. *J. Mol. Catal. A* **2006**, *256*, 278.
- (375) Murzin, D. Y.; Simakova, O. A.; Simakova, I. L.; Parmon, V. N. *React. Kinet., Mech. Catal.* **2011**, *104*, 259.
- (376) Chang, F.-W.; Ou, T.-C.; Roselin, L. S.; Chen, W.-S.; Lai, Z.-C.; Wu, H.-M. *J. Mol. Catal. A* **2009**, *313*, 55.
- (377) Soares, J. M. C.; Morral, O.; Crossley, A.; Harris, P.; Bokwer, M. J. *Catal.* **2003**, *219*, 17.
- (378) Dimitratos, N.; Villa, A.; Bianchi, C. L.; Prati, L.; Makkee, M. *Appl. Catal., A* **2006**, *311*, 185.
- (379) Moreau, F.; Bond, G. C.; Taylor, A. O. *J. Catal.* **2005**, *231*, 105.
- (380) Moreau, F.; Bond, G. C. *Appl. Catal., A* **2006**, *302*, 110.
- (381) Zanella, R.; Giorgio, S.; Shin, C.; Henry, C. R.; Louis, C. J. *Catal.* **2004**, *222*, 357.
- (382) Miller, J. T.; Schreier, M.; Kropf, A. J.; Regalbuto, J. R. *J. Catal.* **2004**, *225*, 203.
- (383) Jiao, L.; Regalbuto, J. R. *J. Catal.* **2008**, *260*, 329.
- (384) Jiao, L.; Regalbuto, J. R. *J. Catal.* **2008**, *260*, 342.
- (385) Toupanc, T.; Kermarec, M.; Lambert, J.-F.; Louis, C. *J. Phys. Chem. B* **2002**, *106*, 2277.
- (386) Toupanc, T.; Kermarec, M.; Louis, C. *J. Phys. Chem. B* **2000**, *104*, 965.
- (387) Guerreiro, E. D.; Gorri, O. F.; Larsen, G.; Arrúa, L. A. *Appl. Catal., A* **2000**, *204*, 33.
- (388) D' Souza, L.; Jiao, L.; Regalbuto, J. R.; Miller, J. T.; Kropf, A. J. *J. Catal.* **2007**, *248*, 165.
- (389) Lepetit, C.; Che, M. *J. Mol. Catal. A* **1995**, *100*, 147.
- (390) Lambert, J.-F.; Che, M. *J. Mol. Catal. A* **2000**, *162*, 5.
- (391) Négrier, F.; Marceau, E.; Che, M.; Giraudon, J.-M.; Gengembre, L.; Löfberg, A. *J. Phys. Chem. B* **2005**, *109*, 2836.
- (392) Marceau, E.; Che, M.; Čejka, J.; Zukal, A. *ChemCatChem* **2010**, *2*, 413.
- (393) Tarasov, K. A.; Isupov, V. P.; Bokhonov, B. B.; Gaponov, Y. A.; Tolochko, B. P.; Yulikov, M. M.; Yudanov, V. F.; Davidson, A.; Beaunier, P.; Marceau, E.; Che, M. *Microporous Mesoporous Mater.* **2008**, *107*, 202.
- (394) Dumond, F.; Marceau, E.; Che, M. *J. Phys. Chem. C* **2007**, *111*, 4780.
- (395) Sun, K.-Q.; Marceau, E.; Che, M. *Phys. Chem. Chem. Phys.* **2006**, *8*, 1731.
- (396) Bourikas, K.; Hiemstra, T.; Van Riemsdijk, W. H. *J. Phys. Chem. B* **2001**, *105*, 2393.
- (397) Panagiotou, G. D.; Petsi, Th.; Stavropoulos, J.; Bourikas, K.; Garoufalidis, C. S.; Kordulis, Ch.; Lycourghiotis, A. *Stud. Surf. Sci. Catal.* **2006**, *162*, 809.
- (398) Tewari, P. H.; Lee, W. *J. Colloid Interface Sci.* **1975**, *52*, 77.
- (399) James, R. O. Ph.D. Dissertation, University of Melbourne, 1971.
- (400) James, R. O.; Healy, T. W. *J. Colloid Interface Sci.* **1972**, *40*, 42.
- (401) James, R. O.; Healy, T. W. *J. Colloid Interface Sci.* **1972**, *40*, 53.
- (402) Chisholm-Brawse, C. J.; O'Day, P. A.; Brown, G. E., Jr.; Parks, G. A. *Nature* **1990**, *348*, 528.
- (403) O'Day, P. A.; Chisholm-Brawse, C. J.; Towle, S. N.; Parks, G. A.; Brown, G. E., Jr. *Geochim. Cosmochim. Acta* **1996**, *60*, 2515.
- (404) Nano, G. V.; Strathmann, T. J. *J. Colloid Interface Sci.* **2006**, *297*, 443.
- (405) Hiemstra, T.; Van Riemsdijk, W. H. *Geochim. Cosmochim. Acta* **2007**, *71*, 5913.
- (406) Hiemstra, T.; Van Riemsdijk, W. H. *J. Colloid Interface Sci.* **2006**, *301*, 1.
- (407) Bleam, W. F.; McBride, M. B. *J. Colloid Interface Sci.* **1986**, *110*, 335.
- (408) Ottaviani, M. F.; Ceresa, E. M.; Visca, M. *J. Colloid Interface Sci.* **1985**, *108*, 114.
- (409) Ludwig, C.; Schindler, P. W. *J. Colloid Interface Sci.* **1995**, *169*, 284.
- (410) Yang, J.-K.; Davis, A. P. *J. Colloid Interface Sci.* **1999**, *216*, 77.
- (411) Yang, J.-K.; Lee, S.-M. *J. Colloid Interface Sci.* **2005**, *282*, 5.
- (412) Yang, J.-K.; Lee, S.-M.; Davis, A. P. *J. Colloid Interface Sci.* **2006**, *295*, 14.
- (413) Poznyak, S. K.; Pergushov, V. I.; Kokorin, A. I.; Kulak, A. I.; Schläpfer, C. W. *J. Phys. Chem. B* **1999**, *103*, 1308.
- (414) Kim, M.-S.; Hong, K.-M.; Chung, J. G. *Water Res.* **2003**, *37*, 3524.
- (415) Barakat, M. *A. J. Colloid Interface Sci.* **2005**, *291*, 345.
- (416) Konstantinou, M.; Pashalidis, I. *Colloids Surf., A* **2008**, *324*, 217.
- (417) Georgaka, A.; Spanos, N. *Global NEST J.* **2010**, *12*, 239.
- (418) Bleam, W. F.; McBride, M. B. *J. Colloid Interface Sci.* **1986**, *110*, 335.
- (419) Vasileva, E.; Hadjiivanov, K.; Mandjukov, P. *Colloids Surf., A* **1994**, *90*, 9.
- (420) Spanos, N.; Slavov, S.; Kordulis, Ch.; Lycourghiotis, A. *Colloids Surf., A* **1995**, *97*, 109.
- (421) Bourikas, K.; Spanos, N.; Lycourghiotis, A. *Langmuir* **1997**, *13*, 435.
- (422) Heracleous, E.; Lee, A. F.; Vasalos, I. A.; Lemonidou, A. A. *Catal. Lett.* **2003**, *88*, 47.
- (423) Bertinchamps, F.; Gaigneaux, E. M. *Catal. Today* **2004**, *91*–92, 105.
- (424) Heracleous, E.; Vakros, J.; Lemonidou, A. A.; Kordulis, Ch. *Catal. Today* **2004**, *91*–92, 289.
- (425) Heracleous, E.; Machli, M.; Lemonidou, A. A.; Vasalos, I. A. *J. Mol. Catal. A* **2005**, *232*, 29.
- (426) Christodoulakis, A.; Heracleous, E.; Lemonidou, A. A.; Boghosian, S. *J. Catal.* **2006**, *242*, 16.
- (427) Handzlik, J.; Ogonowski, J.; Stoch, J.; Mikolajczyk, M. *Appl. Catal., A* **2004**, *273*, 99.
- (428) Handzlik, J.; Ogonowski, J.; Stoch, J.; Mikolajczyk, M. *Catal. Lett.* **2005**, *101*, 65.
- (429) Said, A. A.; Abd El-Wahab, M. M. *M. M. Oxid. Commun.* **2006**, *29*, 181.
- (430) Ma, X.; Gong, J.; Wang, S.; Gao, N.; Wang, D.; Yang, X.; He, F. *Catal. Commun.* **2004**, *5*, 101.
- (431) Senol, O. I.; Viljava, T.-R.; Krause, A. O. I. *Catal. Today* **2005**, *100*, 331.
- (432) Leckel, D. *Energy Fuels* **2006**, *20*, 1761.

- (433) Andonova, S.; Vladov, C.; Kunev, B.; Mitov, I.; Tyuliev, G.; Fierro, J. L. G.; Damyanova, S.; Petrov, L. *Appl. Catal., A* **2006**, *298*, 94.
- (434) Zepeda, T. A.; Halachev, T.; Pawelec, B.; Nava, R.; Klimova, T.; Fuentes, G. A.; Fierro, J. L. G. *Catal. Commun.* **2006**, *7*, 33.
- (435) Zepeda, T. A.; Pawelec, B.; Fierro, J. L. G.; Halachev, T. J. *Catal.* **2006**, *242*, 254.
- (436) Ferdous, D.; Bakhshi, N. N.; Dalai, A. K.; Adjaye, J. *Appl. Catal., B* **2007**, *72*, 118.
- (437) Leyva, C.; Ancheyta, J.; Rana, M. S.; Marroquin, G. *Fuel* **2007**, *86*, 1232.
- (438) Zepeda, T. A.; Pawelec, B.; Fierro, J. L. G.; Halachev, T. *Appl. Catal., B* **2007**, *71*, 223.
- (439) Vakros, J.; Papadopoulou, Ch.; Voyatzis, G. A.; Lycourghiotis, A.; Kordulis, Ch. *Catal. Today* **2007**, *127*, 85.
- (440) Chary, K. V. R.; Reddy, K. R.; Kumar, C. P. *Catal. Commun.* **2001**, *2*, 277.
- (441) Van Veen, J. A. R.; de Wit, H.; Emeis, C. A.; Hendriks, P. A. J. *M. J. Catal.* **1987**, *107*, 579.
- (442) Spanos, N.; Matralis, H. K.; Kordulis, Ch.; Lycourghiotis, A. *J. Catal.* **1992**, *136*, 432.
- (443) Bourikas, K.; Spanos, N.; Lycourghiotis, A. *J. Colloid Interface Sci.* **1996**, *184*, 301.
- (444) Vissenberg, M. J.; Joosten, L. J. M.; Heffels, M. M. E. H.; Van Welsenes, A. J.; (San) de Beer, V. H. J.; Van Santen, R. A.; Van Veen, J. A. R. *J. Phys. Chem. B* **2000**, *104*, 8456.
- (445) Baes, C. F., Jr.; Mesmer, R. E. *The Hydrolysis of Cations*; Wiley: New York, 1976.
- (446) Pope, M. T. In *Encyclopedia of Inorganic Chemistry*; King, B. R., Ed.; Wiley: New York, 1994; Vol. 6.
- (447) Rietra, P. J. J.; Hiemstra, T.; Van Riemsdijk, W. H. *Geochim. Cosmochim. Acta* **1999**, *63*, 3009.
- (448) Van Riemsdijk, W. H.; Hiemstra, T. In *Mineral-Water Interfacial Reactions*; Sparks, D. L., Grundl, T. J., Eds.; ACS Symposium Series 715; American Chemical Society: Washington, DC, 1999; p 68.
- (449) Bourikas, K.; Georgiadou, I.; Kordulis, Ch.; Lycourghiotis, A. *J. Phys. Chem. B* **1997**, *101*, 8499.
- (450) Panagiotou, G. D.; Petsi, Th.; Stavropoulos, J.; Garoufalidis, Ch. S.; Bourikas, K.; Kordulis, Ch.; Lycourghiotis, A. *Stud. Surf. Sci. Catal.* **2010**, *175*, 117.
- (451) Tella, E.; Panagiotou, G. D.; Petsi, Th.; Bourikas, K.; Kordulis, Ch.; Lycourghiotis, A. *Global NEST J.* **2010**, *12*, 231.